WARWICK
THE UNIVERSITY OF WARWICK

A Thesis Submitted for the Degree of PhD at the University of Warwick

Permanent WRAP URL:
http://wrap.warwick.ac.uk/89561

Copyright and reuse:
This thesis is made available online and is protected by original copyright.
Please scroll down to view the document itself.
Please refer to the repository record for this item for information to help you to cite it.
Our policy information is available from the repository home page.

For more information, please contact the WRAP Team at: wrap@warwick.ac.uk

warwick.ac.uk/lib-publications

Nanostructured Electroactive Materials: Applications in Electroanalysis and Electrocatalysis

By Peisan E (Sharel)

A thesis submitted for the degree of Doctor of Philosophy

Department of Chemistry
University of Warwick

September 2016

Table of contents

List of figures

List of tables

Acknowledgements

First I would like to thank my supervisors, Prof. Patrick Unwin and Prof. Julie Macpherson for their kindness in accepting me as a student transferring from Engineering. Their advice and guidance helped me a lot in the last four years, allowing me to grow as a research scientist. I really appreciate having had the opportunity to be a member of the group.

I have been fortunate to work with many gifted scientists on different projects -Yang-Rae, David, Minkyung, Paul, Andrew, Ashley, Tom, Lingcong, Guohui, Danqing, Rob, Jeremy, Marcio, Liz, Max and Jon. I would also like to thank the members of Warwick Electrochemistry and Interfaces Group past and present for their help and discussion, especially Yang-Rae Kim for his insightful comments and discussion which incentivized me to widen my research from various perspectives. A special thanks to the members of office C111, Ashley Page, David Perry, Tom Scott, Alexander Parker, they provided humor and entertainment in what could have otherwise been a stressful working environment.

I am thankful to Warwick Chancellors International scholarship for providing funding for my Ph.D. studies.

Thanks to all my friends in the UK, Malaysia and China. Thank for you the understanding and encouragement. Words cannot express how grateful I am to my parents and sisters. Without your love and support, I would not have achieved so much.

Declaration

The work in this thesis is original and my own except where carried out in collaboration, as outlined below.

Chapter 5 was developed by Marcio Vidotti, who kindly provided comments and discussion for this project. The $Ni(OH)_2$ electrodeposition using the indirect approach was conducted by Danqing Liu. HR-TEM images were taken with the help of Dr. Robert Lazenby and Dr. Jeremy Sloan (Warwick Physics); Chapter 6, the SECCM MATLAB script was kindly written by David Perry and the Raman MATLAB script by Ashley Page; Chapter 7 was developed by Dr. Andrew Basile, who kindly provided insight and expertize that greatly assisted the research. The polymer gel was developed by Dr. Paul Wilson. Galvanostatic discharging data and the HR-TEM image were collected by Minkyung Kang. I confirm that this thesis has not been submitted for any degree at another university.

Parts of this thesis have been published or to be submitted, as detailed below:

S. P. E, Y. R. Kim, D. Perry, C. L. Bentley and P. R. Unwin, *ACS Appl. Mater. Interfaces*, 2016, 8, 30458–30466.

S. P. E, D. Liu, R. A. Lazenby, J. Sloan, M. Vidotti, P. R. Unwin and J. V. Macpherson, *J. Phys. Chem. C*, 2016, 120, 16059-16068.

S. P. E, T. S. Miller, J. V. Macpherson and P. R. Unwin, *Phys. Chem. Chem. Phys.*, 2015, 17, 26394-26402.

S. P. E, T. S. Miller, J. V. Macpherson and P. R. Unwin. Quantitative Trace Level Electrochemical Detection in Complex Aqueous Media: Comparison of Single-Walled Carbon Nanotube Network Electrodes and Screen-Printed Carbon Electrodes as Voltammetric Electrochemical Sensors, *in preparation.*

S. P. E, M. Kang, Paul Wilson, A. Basile, L. Meng, D. Perry and P. R. Unwin. Nanoscale Visualization of Redox Activity of Li_2O_2 in Non-Aqueous Media: Conformal Layer *vs*. Toroid Structure, *in preparation.*

Side projects in collaboration with others:

T. S. Miller, S. Sansuk, **S. P. E**, S. C. Lai, J. V. Macpherson and P. R. Unwin, Catal. Today, 2015, 244, 136-145.

Y. R. Kim, **S. P. E** and P. R. Unwin. Nanoscale Electrocatalysis Imaging: Hydrogen Evolution Reaction at Electrochemically Activated Graphite, *in preparation.*

Abstract

Carbon materials, including single-walled carbon nanotubes (SWNT) and graphene, have gained great interest in electrochemistry. The advantages of carbon electrodes include chemical stability, biocompatibility, low background currents and good electrical conductivity. With the increasing importance of carbon electrode materials for biological and energy application, the systematic investigation and new applications is mandatory.

SWNT networks, with different densities, are firstly investigated using microscale capillary electrochemical (EC) methods. Pristine high density (HD) SWNT networks are shown to exhibit more facile electron transfer (ET) for dopamine (DA) electro-oxidation and are less susceptible to blocking by reaction products when compared to low density (LD) SWNT networks. Acid treatment of SWNT networks results in an enhancement of electrode kinetics and a reduction in their susceptibility to surface fouling. Further, a comparison is made between SWNT electrodes, with different densities and a commercial screen printed carbon electrode (SPCE), for the oxidation of ferrocenecarboxylic acid (FcCOOH) in complex aqueous media (polyethylene glycol (PEG) and albumin), to mimic conditions in which diagnostic devices might be used. SWNTs exceed the performance of SPCEs, with a detection limit that is 3 orders of magnitude lower. Finally, a $Ni(OH)_2$ nanoparticles (NPs) modified SWNT network is employed for the methanol oxidation reaction (MOR) and the ethanol oxidation reaction (EOR), showing improved ET processes with ~2.8 kA g^{-1} for MOR and ~3.7 kA g^{-1} for EOR, which are much higher than recent reports using other nanostructured catalysts.

A fundamental understanding of the structure-activity of "blistered" highly oriented pyrolytic graphite (HOPG), produced by electro-oxidation in $HClO_4$, is obtained using scanning EC cell microscopy (SECCM) coupled with multi-microscopy techniques. The disordered sp^2 carbon structure of the blister catalyzes the electro-oxidation of hydrazine compared to the basal surface. In this study, a potential sweep at each pixel of pre-defined scan area is recorded, providing potentiodynamic data with high resolution.

To demonstrate that the approaches are generally applicable, a fundamental study of the redox activity for Li_2O_2 product (toroidal and layer structure) in dimethyl sulfoxide (DMSO) non-aqueous media, is undertaken. A unique gel polymer organic electrolyte (polymer matrix, cross linker and organic electrolyte) is employed in a dual barrel nanopipette and the SECCM approach is carried out with cyclic voltammetry (CV) measurements performed at every pixel of a scan. The Li_2O_2 toroids outperforms the Li_2O_2 layer structure with a 9 times increase in the current response and *ca.* 80 % of charge efficiency. This work provides valuable information with regards to cathode materials for effective Li-air battery.

Abbreviations

Symbol	Abbreviation
AC	Alternating current
ADHD	Attention deficit hyperactivity disorder
AFM	Atomic force microscopy
AN	Acceptor number
AOR	Alcohol oxidation reaction
CE	Working electrode
CNT	Carbon nanotube
CV	Cyclic voltammetry
cCVD	Catalyzed chemical vapour deposition
DA	Dopamine
DI	Deionized
DMSO	Dimethyl sulfoxide
DN	Donor number
DOS	Density of state
DPV	Differential pulse voltammetry
EC	Electrochemical
EDS	Energy-dispersive X-ray spectroscopy

EGO	Electrochemically formed graphite oxide
EOR	Ethanol oxidation reaction
ET	Electron transfer
EtOH	Ethanol
FE-SEM	Field emission scanning electron microscopy
GC	Glassy carbon
HD	Highly density
HOPG	Highly oriented pyrolytic graphite
HR-TEM	High resolution-transmission electron microscopy
HZ	Hydrazine
LD	Low density
LOD	Limit of detection
LSV	Linear sweep voltammetry
MCEM	Micro-capillary electrochemical method
MeOH	Methanol
mSWNT	Metallic single-walled carbon nanotube
MOR	Methanol oxidation reaction
MWNT	Multi-walled carbon nanotube
NP	Nanoparticle
$Ni(OH)_2$	Nickel hydroxide
ORR	Oxygen reduction reaction

PBS	Phosphate-buffered solution
PEG	Polyethylene glycol
PCDF	Porous carbon derived from filter paper
PGMA	Poly(glycidyl methacrylate)
QRCE	Quasi reference counter electrode
QRE	Quasi reference electrode
RBM	Radial breathing mode
RE	Reference electrode
RGSs	Reduced graphene sheets
SA	Specific activity
SAED	Selected area electron diffraction
SECCM	Scanning electrochemical cell microscopy
SHD	Super high density
SPCE	Screen printed carbon electrode
SWNT	Single-walled carbon nanotube
sSWNT	Semiconducting single-walled carbon nanotube
WE	Working electrode

Glossary of Terms

Symbol	Abbreviation
j	Flux
D	Diffusion coefficient
c	Concentration of the electroactive species
v	Fluid velocity
z	Charge of the species
F	Faradaic constant
R	Gas constant
T	Temperature
$\emptyset$	Electric field
E	Electrode potential
$E^{o'}$	Formal electrode potential
O	Concentrations of the oxidized species
R	Concentrations of the reduced species
i	Faradic current
n	Number of electrons transferred
A	Electrode area
k_b	Electron transfer rate of the backward reaction

k_f	Electron transfer rate of the forward reaction
C_{ox}	Concentration of oxidized species
C_{red}	Concentration of reduced species
η	Electrode overpotential
α	Charge transfer coefficient
k_0	Heterogeneous standard rate constant
E_p^a	Anodic peak potential
E_p^c	Cathodic peak potential
ΔE_p	Peak separation
i_p^a	Anodic peak current
i_p^c	Cathodic peak current
$[R]_{bulk}$	Concentration of species R in bulk solution
D_R	Diffusion coefficient for R species
v	Scan rate
a	Radius of electrode
$E_{1/2}$	Half wave potential
$E_{3/4}$	Potential at current values at ¾ of i_{lim}
$E_{1/4}$	Potential at current values at ¼ of i_{lim}
E_0	Standard electrode potential
$\vec{C}$	Chiral vector defined as below
$\vec{a}_1$ and $\vec{a}_2$	Graphene lattice vectors defined as below

d_t	Nanotube's diameter
$a_{C\text{-}C}$	Carbon-carbon distance in graphene
μ	Mean of the CV response
σ	Standard deviation of the CV response
i_{lim}	Limiting current of disc UME
r	Radius of electrode
$\rho_{th(metallic)}$	Metallic percolation threshold
l	Length of SWNTs
C	Capacitance
i_{average}	Average current from forward and reverse sweep of CV
$A_{\text{geometric}}$	Geometrical area of the electrode
Γ	The amount of electroactive $Ni(OH)_2$
Q_{ox}	Oxidative charge
Q_{red}	Reductive charge
$M_{Ni(OH)_2}$	Molar mass of $Ni(OH)_2$
c_{o}	Inter-sheet distance
S	Saturation ratio
K_{sp}	Solubility constant
$a_{Ni^{2+}}$	Activities of Ni^{2+}
a_{OH^-}	Activities of OH^-

Co	Initial concentration
l	Separation of electrode surface and a parallel boundary
t	Time
x	Distance from electrode
m	Number of points used in the analytical expression
E_s	Working electrode potential defined as below
V_1	Substrate voltage
V_2	Bias voltage
I_{EC}	Working electrode current
I_{IC}	Ion conductance current

Chapter 1 Introduction

This introduction is concerned with the development of carbon electrodes for electroanalysis and electrocatalysis. The synthesis and modification of controlled growth of single-walled carbon nanotubes (SWNTs) is summarized. The uses of carbon electrodes for different applications such as biosensors for the detection of biological agents and alcohol oxidation for fuel cells are discussed. Finally, the fundamental understanding of the cathode electrode in Li-O_2 batteries is summarized.

1.1 Dynamic electrochemistry

Consider a simple electrochemical (EC) system, where an electrode is in contact with a solution containing reactant species. When there is an external driving force (a potential applied to the electrode), the reactant species at the electrode surface is consumed (oxidized or reduced) and a product species is produced.[1] An EC reaction usually involves at least two processes: Firstly, the electron transfer (ET) across the electrode surface and secondly, the mass transport of species from the bulk solution to the electrode surface, which is illustrated in Figure 1.1.[1] Each of the two stages of the EC reaction process may be further complicated by other events (adsorption/desorption, chemical reactions) and the slowest of which will limit the overall reaction rate (current).[1]

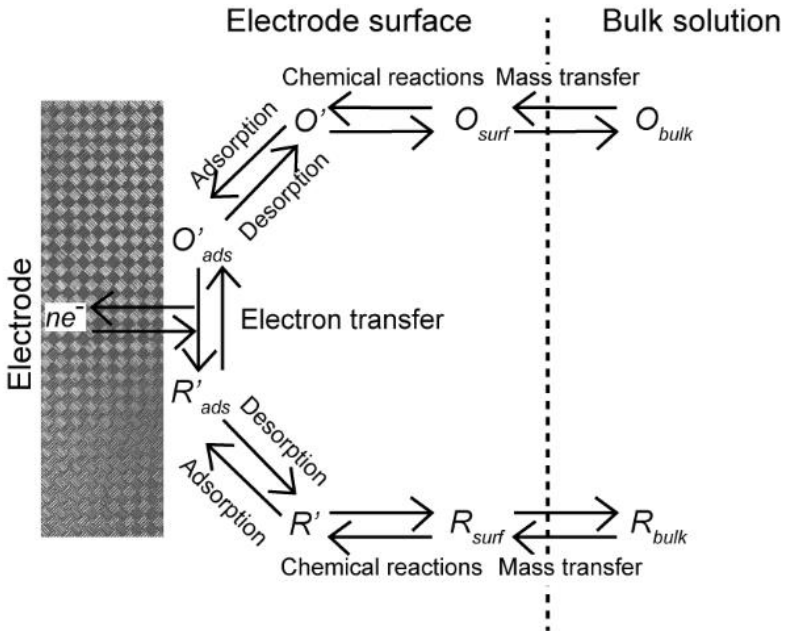

Figure 1.1 Schematic of a general electrode reaction. The mass transport occurs in series with other processes, such as chemical reactions, adsorption/desorption and ET.[1]

1.1.1 Mass transport

Mass transport involves a species in solution travelling between the electrode surface and bulk solution. The mass transfer coefficient, k_T, determines the rate of movement of species in solution. There are three mass transport modes: diffusion, convection and migration.[1, 2] The Nernst-Plank equation defines the contributions of all three modes to the steady state flux, J, as:[3]

$$J = -D\nabla c + vc - \frac{zF}{RT} D\nabla\emptyset \qquad (1)$$

where D is the diffusion coefficient, c is the concentration of the electroactive species, v is fluid velocity, z is charge of the species, F is Faraday's constant, R is the ideal gas constant, T is the temperature and $\emptyset$ is the electric field.

The movement of species driven by the presence of a concentration gradient is termed diffusion and is described by Fick's first law.[3] In an EC cell, the reactant

species is consumed and a product is formed, resulting in a low concentration of the reactant species and a high concentration of the product species close to electrode surface. Due to the uneven concentration distribution in the system, species tend to move between the electrode surface and bulk solution. The diffusion profile, which develops during an EC reaction, depends on the electrode size and on its geometry. As examples, planar diffusion is observed at a macroelectrode (Figure 1.2a) whereas a hemispherical diffusion profile develops at a microelectrode (or ultramicroelectrode, UME) under steady-state conditions (Figure 1.2b). UMEs offer advantages over macroelectrodes for the study of EC systems, as they have higher rates of mass transport (hemispherical diffusion profile), a small ohmic drop (due to the low current generated) and a low capacitance charge in time-dependant measurements (small surface area).[1, 4]

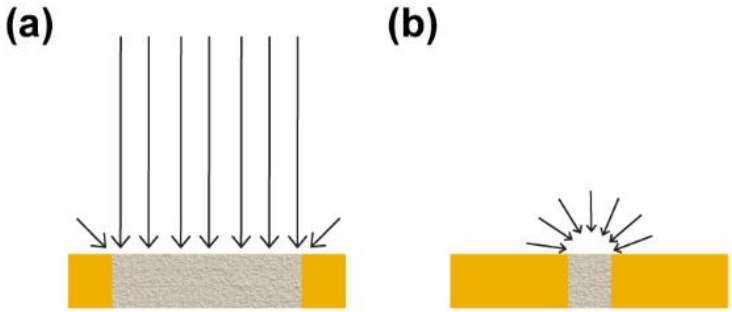

Figure 1.2 Schematic view of diffusion profiles for (a) macroelectrode and (b) microelectrode.

The movement of species due to an external force is termed convection. The most commonly used convection EC system is a rotating disk electrode, where an increased flux of species towards the electrode surface results from the convective flow of solution.

Migration is the movement of a charged species in an electrical field. In an EC cell, electrical fields exist due to the externally applied potential on the electrodes, with the charged species tending to move according to the electrical field, resulting in a complex mass transport. Typically, EC experiments are conducted under a large excess of background electrolyte where inert salt (KNO_3 or KCl) suppresses these migration effects. The concentration of supporting electrolyte added to solution is usually around 100 times greater than the concentration of the reactant species. Another benefit of the introduction of supporting electrolyte is the reduced solution resistance (reduced ohmic drop).[1, 3]

1.1.2 Electron transfer kinetics

For a reversible system, the ET at the electrode is fast when compared to the mass transport to the electrode surface so that the Nernst equation applies.[3]

$$E = E^{\circ\prime} + \frac{RT}{nF} ln \frac{[O]}{[R]} \tag{2}$$

where E is electrode potential, $E^{o'}$ is formal electrode potential, n is the number of electrons transferred per redox species, O and R are the concentrations of the oxidized and reduced species, respectively.

When kinetics operate, we may write:

$$O + ne^- \underset{k_b}{\overset{k_f}{\rightleftarrows}} R \tag{3}$$

where k_f and k_b are the ET reaction constants of the forward and backward reactions, respectively.

The faradic current, *i,* at the electrode is proportional to the flux of species at the electrode surface, *j*

$$i = nAFj \tag{4}$$

where *A* is the area of the electrode and *j* is defined by:

$$j = k_f C_{ox} - k_b C_{red} \tag{5}$$

k_f and k_b have an exponential dependence on the electrode overpotential, η, which is the potential difference between the applied potential and the equilibrium potential and act as a main driving force for a reaction. A good electrocatalyst can facilitate the EC reactions at low η.

$$\eta = E - E^o \tag{6}$$

$$k_f = k^0 e^{\frac{-\alpha nF\eta}{RT}} \tag{7}$$

$$k_b = k^0 e^{\frac{(1-\alpha)nF\eta}{RT}} \tag{8}$$

where α is the charge transfer coefficient. Substituting equations 7 and 8 into 5 yields the Butler-Volmer equation below (equation 9 and Figure 1.3a).[5]

$$i = nAFk_0\left[C_{ox}e^{\frac{-\alpha nF\eta}{RT}} - C_{red}e^{\frac{(1-\alpha)nF\eta}{RT}}\right] \tag{9}$$

If the system deviates from equilibrium, ($\left|\eta\right| \gg 0$) one reaction (either the cathodic or anodic reaction) will dominate and equation 9 can be written as

$$i = nAFk_0C_{ox}e^{\frac{-\alpha nF\eta}{RT}} \tag{10}$$

The Butler-Volmer equation can be simplified to the Tafel equation.[1]

$$\eta = \left(\frac{2.3RT}{\alpha nF}\right) log\ i_0 + \left(\frac{-2.3RT}{\alpha nF}\right) logi = a + b\ logi \qquad (11)$$

The Tafel equation reveals a linear relationship between η and log i, where i_o can be written as:

$$i_0 = nAFk_0C_{ox} \qquad (12)$$

and can be determined from the intercept of Tafel plot ($\eta = 0$) as shown in Figure 1.3b. The Tafel slope is proportional to α, which can be used to determine the possible reaction pathway and the rate determining step of the EC reactions.

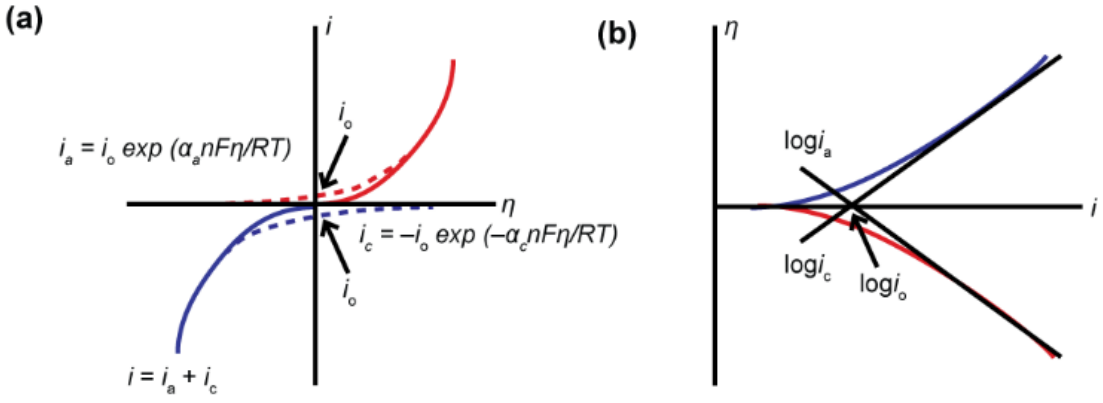

Figure 1.3 Schematic plots for (a) Butler–Volmer equation and (b) Tafel plots.

1.1.3 Cyclic voltammetry (CV)

One of the most commonly used dynamic EC techniques is voltammetry, where the current is recorded as a function of applied potential. Figure 1.4 shows a schematic of an example CV measurement. In a CV measurement, the potential applied to the working electrode (WE) is swept from E_1 to E_2 and then back to E_1, in a triangular waveform (Figure 1.4a) and the current flowing through the WE is measured. The CV is then represented as a plot of current as a function of the potential. A typical CV recorded at a macroelectrode (diameter in millimetre range) is shown in Figure 1.4b. For macroelectrode measurements a 3-electrode setup is necessary (Figure 1.4c)

where the potential is applied between the WE and reference electrode (RE) and the current is measured between the WE and counter electrode (CE).

The CV recorded at a macroelectrode exhibits some important key features: (1) the current value recorded is usually large in magnitude due to the large electrode area, hence the 3-electrode setup is necessary. The CE (typically a Pt wire) is used to pass the current resulting in negligible current being drawn through the RE to maintain a constant potential; and (2) peak shaped CV signature. The potential is swept from E_1, where no EC reaction occurs, to a value where a faradaic process, in this case the ET process of *R* to *O*, takes place, resulting in an increase in the current magnitude. As the potential scans towards E_2, the current increases exponentially until reaching a peak, i_p^a at potential of E_p^a, after which the current drops. The current signature is dependent on the relationship between the mass transport coefficient and the ET rate.[3] Scanning backwards, a similar current signature is observed; a cathodic peak, i_p^c at potential of E_p^c. The peak to peak separation, ΔE_p,

$$\Delta E_p = E_p^a - E_p^c \tag{13}$$

can be used to determine the reversibility of an EC reaction and it is 59 mV for a reversible (diffusion limited) one electron reaction. The anodic peak current, i_p^a is described by Randles-Sevcik equation:[6]

$$i_p^a = 0.446nFA[R]_{bulk}\left(\frac{nFD_R v}{RT}\right)^{\frac{1}{2}} \tag{14}$$

For the solution is at 298 K,

$$i_p^a = (2.69\times10^5)n^{\frac{3}{2}}AD_R^{\frac{1}{2}}[R]_{bulk}v^{\frac{1}{2}} \tag{15}$$

where D_R is the diffusion coefficient for R species; $[R]_{bulk}$ is concentration of R in bulk solution; T and v represent the temperature in K and scan rate in V s^{-1}.

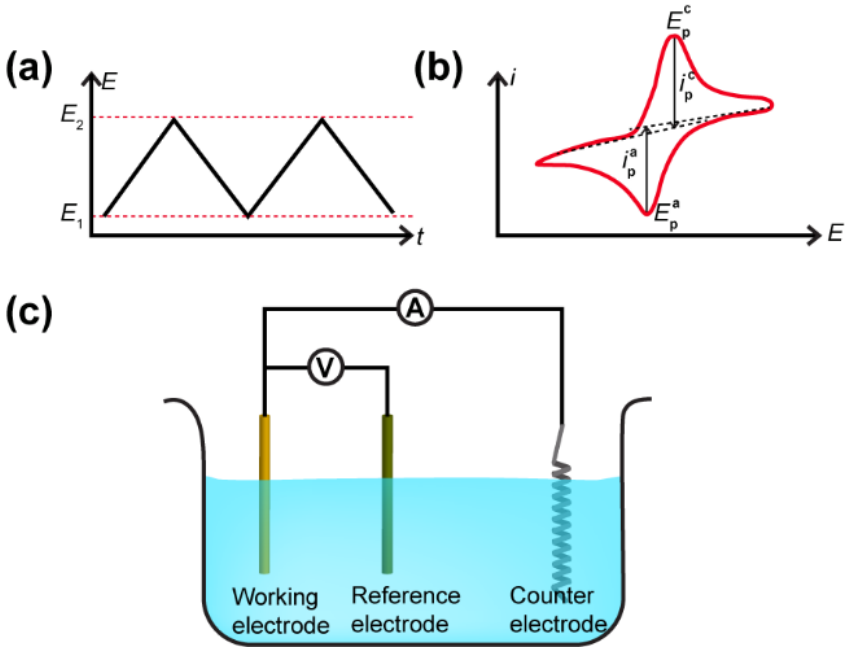

Figure 1.4 (a) $E - t$ plot for a CV; (b) A typical CV where i_p^c and E_p^c are the cathodic peak current and potential, respectively and i_p^a and E_p^a are the anodic peak current and potential, respectively for a reversible reaction; (c) A typical 3 electrode cell.

The CV for a UME (diameter in µm range) is somewhat different to that obtained from a macroelectrode (Figure 1.5) and exhibits (1) a much reduced current magnitude due to the smaller electrode area, hence, 2-electrode setup can often be used; (2) a steady-state current-potential response due to the enhanced mass transport rate which results from the hemispherical diffusion. The limiting current (i_{lim}) obtained for a disc UME is described by:

$$i_{lim} = 4naFD_R[R]_{bulk} \quad (16)$$

where a is the radius of the disc UME. For a reversible process in a microelectrode system,[1]

$$E_{3/4} - E_{1/4} = \frac{59}{n}\ mV \qquad (17)$$

where $E_{3/4}$ and $E_{1/4}$ are the potentials at which current values are at ¾ and ¼ of i_{lim}, respectively.[7]

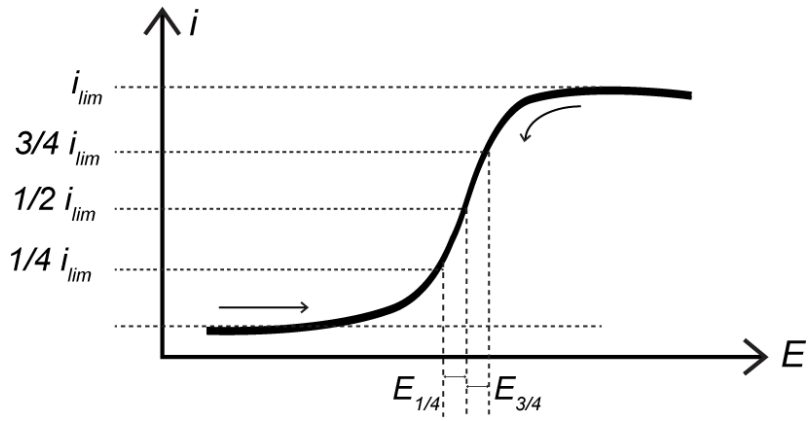

Figure 1.5 CV of a microdisk electrode. i_{lim} is the limiting current, $E_{3/4}$ and $E_{1/4}$ is the potential at current values equals to ¾ and ¼ of i_{lim}, respectively.

1.1.4 Scanning electrochemical cell microscopy

SECCM is part of the family of scanning probe microscopy techniques which utilizes a nanoscale (or microscale) liquid meniscus formed at the end of a dual barrel nanopipette, as an EC cell capable of achieving high resolution and localized EC measurements.[8-10] This setup enables high mass transport rates by manipulating the potential bias between the two barrels and is capable for studying ion transfer and ET.[8] Droplet cells were first developed in the mid-1990s for corrosion studies,[11, 12] and was greatly improved through the invention of SECCM to facilitate the simultaneous study of topography and the electroactivity of the electrode in the 2010.[8]

A schematic illustrating the SECCM method is shown in Figure 1.6 and the working mechanism will be discussed in detail in Chapter 2. Briefly, SECCM employs a dual-barrel theta nanopipette containing electrolyte solution of interest and quasi-

reference counter electrodes (QRCE) in each barrel. A bias is applied between the QRCEs to induce an ionic conductance current flow across of the droplet which is used as a feedback parameter for controlling the tip-to-substrate separation.[9] The tip is oscillated normal to the surface to induce an alternating the AC component which is detected through the use of lock-in techniques and the resulting AC ion current served as the feedback signal.[13]

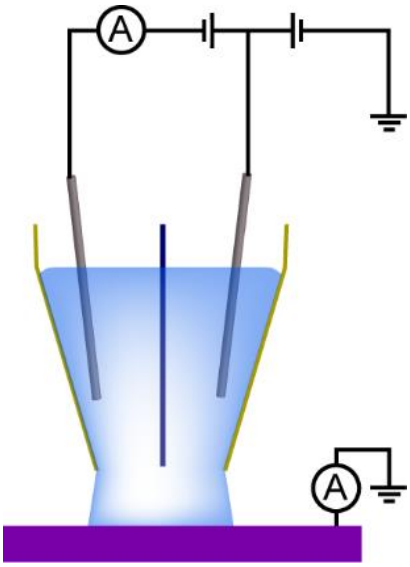

Figure 1.6 Schematic depicting SECCM operation. A bias is applied between the QRCEs in the electrolyte to introduce an ionic conductance current flow across the meniscus at the end of the nanopipette, which is used as the feedback signal for nanopipette positioning on the electrode surface. A substrate voltage is applied to one of the QRCEs to drive the EC reactions at the (semi)conducting electrode and the WE current was measured.

SECCM was employed to study complex structure-activity and provided considerable new insight on some key electrode processes, including graphene,[14-16] HOPG,[17-19] CNT,[20-22] polycrystalline Pt,[23-25] and conducting diamond.[26, 27] SECCM has become a powerful technique for electrochemistry and coupled with complementary microscopy techniques (*i.e.* atomic force microscopy (AFM) and field

emission-scanning electron microscope (FE-SEM)), it allows for a correlation between structure and activity at the nanoscale to be obtained.

1.2 Introduction to carbon materials

Carbon, an abundant element in nature, occurs in different allotropes *i.e.* three-dimensional (3D) graphite, two-dimensional (2D) graphene and one-dimensional (1D) carbon nanotubes (CNT). The structure of these allotropes, with different carbon atoms arrangements, greatly impacts on the material properties and their discovery and study has helped progress new technologies. For instance, Iijima discovered CNTs in 1991[28] and single layer graphene was isolated from graphite in 2004.[29] Carbon is the most commonly used electrode material in electroanalytical chemistry since early 1960s due to its promising physical[30] and chemical[31] properties such as chemical stability,[20] biocompatibility[32] and availability.[32] The development of nanotechnology has led to an increased level of understanding of carbon materials ranging from the macroscopic scale to the nanoscale. These nanoscale materials, with their possible perfect crystal lattice, show intriguing and tunable properties with graphene serving as a basic building block for other graphitic materials. In particular, it has been shown that the perturbation to the perfect graphene structure such as defects can aid its catalytic properties.[33] Even so, there are still questions remaining with regard to the structure-activity relationship of the EC performance of carbon materials. This section aims to highlight the potential future opportunities of nanocarbon materials and the challenges they face in term of fundamental understanding and their development for electrocatalytic applications.

1.2.1 Structural properties of carbon nanotubes

CNTs consists of sp^2-hybridized carbon atoms and can be constructed in two forms: SWNT and multi-walled carbon nanotube (MWNT).[34] SWNT can be described as a layer graphene rolled into a hollow cylinder whereas MWNT consist of several tubes of graphene fitted one inside the other (0.34 nm interlayer distance of graphite).[30, 34] A vast variety of possible nanotube geometries provides nanotubes of different diameters and chirality, uniquely described by a chiral vector ($\vec{C}$), which is the result of the graphene lattice vectors $\vec{a}_1$ and $\vec{a}_2$ correspond to a pair of integers (*n*, *m*),[35]

$$\vec{C} = n\vec{a}_1 + m\vec{a}_2 \quad (18)$$

Figure 1.7 shows three types of SWNTs: zigzag (*n*, 0), armchair (*n* = *m*) and chiral (n ≠ m > 0). The chiral angle is the angle between the direction of chiral $\vec{a}_1$, such as $0° > \theta > 30°$. The tube diameter, d_t, can be calculated by dividing $|\vec{C}|$ by π.[36]

$$d_t = \frac{\sqrt{3}a_{c-c}}{\pi}\sqrt{n^2 + m^2 + nm} \quad (19)$$

where $a_{C\text{-}C}$ is the carbon-carbon distance in graphene, 1.42 Å. T_a is known as the translational vector of the nanotube with the same origin as $\vec{C}$ but runs orthogonal to it, which defines as the length of the SWNT. Thus, T_a and $\vec{C}$ define the area of graphene sheet to form a SWNT. The typical diameter of CNT is 0.7 – 3 nm and 2 – 30 nm, for SWNT and MWNT, respectively.[34] Both SWNTs and MWNTs can range from microns to centimeters in length.[37] MWNTs and graphite (*i.e.* highly oriented pyrolytic graphite (HOPG)) are 3D structures comprised of terraces and step edges (Figure 1.8a), with point and other surface and subsurface defects.[38] SWNTs and graphene consist of surface atoms and defects. Defects in SWNT structure are inclusions of five-

or seven-membered rings (at the kinked side), sp^3 hybridized carbon and the open tube end. The open tube ends formed during chemical processing are often decorated with oxygen functionalities (Figure 1.8b).[39] These defects in CNTs are important in covalent chemistry as they serve as potential sites for adsorption of electroactive species which could bring new performance, an aspect that we discuss below.

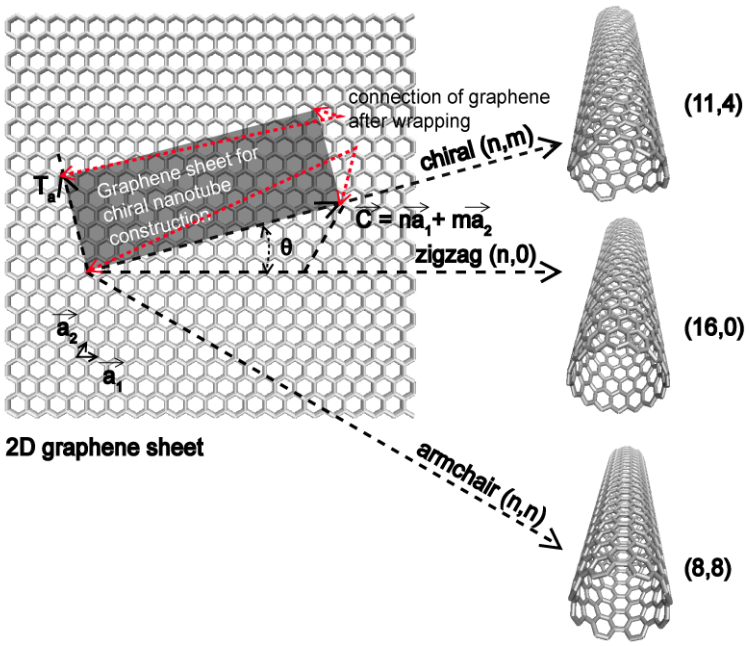

Figure 1.7 Schematic diagram showing roll-up of a 2D graphene sheet leading to the three different types of CNT: chiral (11, 4), zigzag (16, 0) and armchair (8, 8) orientations.

CNTs can be either metallic or semiconducting depending on the diameter and chirality of the tube, which corresponds to the (*n*, *m*) indices.[40, 41] The rule of thumb for electronic properties of nanotubes:[42] if (*n* – *m*) is a multiple of 3, it suggests the tube exhibits a metallic behavior (finite value of charge carriers in density of state (DOS) at the Fermi energy; Figure 1.9a) and otherwise it is semiconducting (no charge carriers in DOS at the Fermi energy; Figure 1.9b).[42] Nanotube networks typically exhibit a mixture of one third metallic SWNTs (mSWNTs) and two thirds semiconducting SWNTs (sSWNTs), with a band gap inversely proportional to the

diameter of the tube.[43] Sharp spikes (van Hove singularities), which arise from one-dimensional (1D) electronic structure, predict the electronic state densities for the CNTs.[36] The 1D electronic structure causes the electronic transport in mSWNTs and MWNTs to occur ballistically, where electrons can move freely over long nanotube lengths without scattering from atoms or defects.[44, 45] The introduction of defects into the CNT network results in fascinating properties and can enhance their potential application as electrocatalysts.[22, 46]

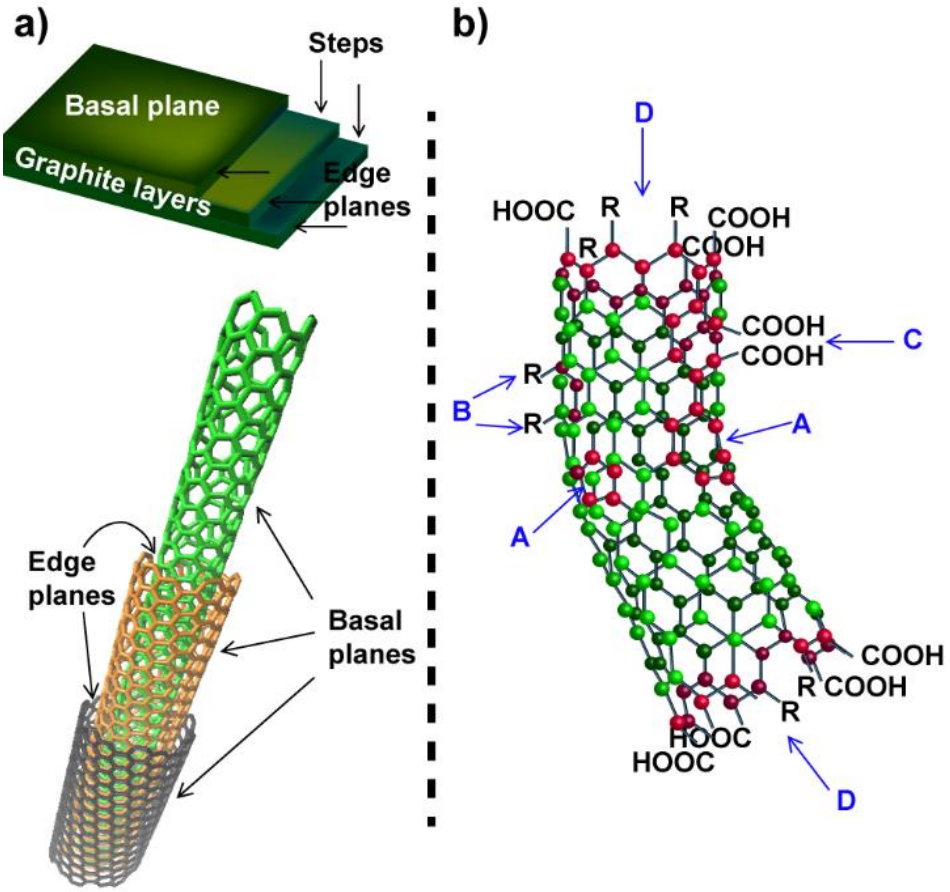

Figure 1.8 (a) Schematic illustrating edge plane and basal plane like sites on graphite and MWNTs. (b) Typical defects in a SWNT; A) five- or seven-membered rings, leading to a bend in the tube, B) sp^3-hybridized defects (R=H and OH), C) sidewall damaged by oxidative process, functionalizing the hole lined with -COOH groups and D) open end of the SWNT terminated with -R and -COOH groups.[39]

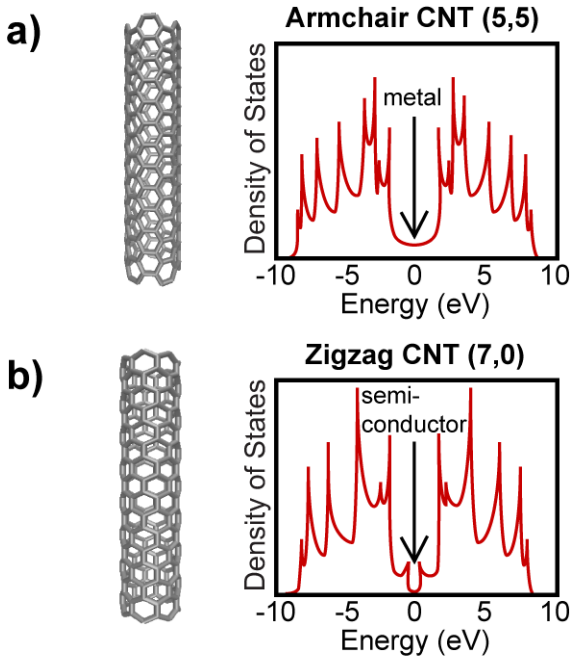

Figure 1.9 Electronic properties of two CNTs: (a) armchair (5,5) CNT exhibits metallic behavior (reveals charge carrier in DOS at the Fermi energy) and (b) zigzag (7,50) CNT exhibits semiconductor behavior (no charge carrier in DOS at the Fermi energy).[42]

1.2.2 Carbon nanotube network growth

High temperature CNTs growth techniques (arc discharge and laser ablation; $T > 3000$ ℃) have been replaced by relatively low temperature techniques (chemical vapor deposition (CVD); $T < 1000$ ℃).[47, 48] Arc discharge results in CNT formation by harvesting energy from electrical arc between cathode and anode electrodes, in the presence of metal catalyst (*i.e.* Co, Ni and Fe).[49] Laser ablation produces CNTs from condensation of laser-vaporized carbon/metal catalyst mixture at high pressures.[50] The CNTs synthesized using both laser ablation and arc discharge experience significant levels of contamination from amorphous carbon and metal nanoparticle (NP)

catalysts.[30, 51, 52] These impurities often interfere with the electrochemistry of CNTs.[53-55] Thus, a clean-up procedure after growth is necessary.[56-58]

Alternatively, with carefully optimization of the catalyzed CVD (cCVD) conditions, CNTs grown have been shown to exhibit a low defect density,[46, 59] negligible amorphous carbon content and to be relatively free of catalytic NPs (metal NPs encapsulated at the end of the CNT).[60] In this approach, the CNT is precipitated from the decomposition of a gaseous hydrocarbon source (alkane or CO) on the catalytic metal NPs (Co and Fe).[61] The CNTs are attached to an inert substrate (*e.g.* Si/SiO_2 or quartz).[62] It is possible to grow CNTs of different geometries (isolated CNTs,[63] 2D random networks,[64] and vertically aligned CNT forests[65]) by means of controlling the growth time and metal catalyst used. Another appealing feature of this method is the capability to control the diameter of CNTs by adapting the size of the catalyst NP.[66]

1.2.3 Modification of carbon nanotubes

The surface structure of CNT electrodes is crucial to EC applications. CNTs act as a support material for various organic and inorganic materials due to their large active surface[63] and stability[20]. The rapid development of these composite materials, used as EC sensors, has been successfully witnessed.[67] The role of oxygen containing groups and metal NPs functionalization in enhancing the catalytic activities of CNTs are highlighted in this section.

1.2.3.1 Oxygen containing groups functionalization

There has been great interest in techniques capable of removing the impurities from CNTs. A typical purification protocol is depicted in Figure 1.10. The first step involves thermal oxidation and annealing at high temperature (~ 350 ^{o}C) to remove amorphous

carbon. Next, the metal catalyst NPs are removed by refluxing the CNTs in HNO_3, H_2SO_4, HCl or mixtures of these acids.[68-70] A final annealing at high temperature (1000 ^oC) in vacuum eliminates residual surface defects.[71-73]

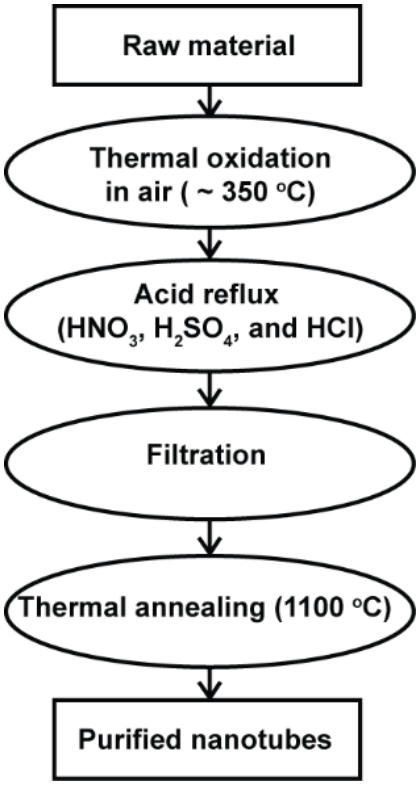

Figure 1.10 Typical purification process for CNTs.[58]

The use of this purification process can introduce defects, possibly resulting in CNT "cutting", opening the end of the CNTs and oxidative damage to the sidewalls.[57, 74] These cut ends and defects are functionalized with oxygen containing groups, such as carboxylic acids, ketones and alcohols.[75] These groups can further bind to other units, which could aid certain EC reactions.[67] Many redox processes (inner sphere) need to bind to an electrode surface to facilitate efficient ET.[1] Functionalization with oxygen containing groups has been shown to promote the EC oxidation of dopamine (DA),[60] hydrazine (HZ),[76] and metal ions (*i.e.* Cd(II) and Pb(II)).[77] However, the sidewall defects cause an increase in the resistivity of the CNT due to resonant back-

scattering.[78, 79] Hence, careful control of the purification procedure is needed to optimize the performance of CNT-based electrodes.

1.2.3.2 Modification with metal nanoparticles

The modification of CNT structures with metal NPs for EC-based sensor has also received great attention.[80] Noble metal NPs-modified CNTs can be constructed which give an excellent EC response as a consequence of improved catalytic activities and chemical stability. For instances, Au/SWNTs hybrid materials shows increased electrocatalytic activity towards hydroxylamine detection,[81] whilst Pt/SWNTs composites shows remarkably improved sensitivity towards hydrogen peroxide.[82] Pd/SWNTs hybrid composites acts as a novel non-enzymatic electrocatalyst for glucose oxidation.[83] These noble catalysts are rather expensive and scarce metals. Thus, there is a need to find an alternative method, using cheaper materials, which perform well in terms of electrocatalytic activity. Metal oxide nanostructures have also been applied as EC sensors, however, they are limited by poor electrical conductivity. This limitation can be overcome by anchoring the metal oxides on CNTs in which the CNT matrix provides electrons with conducting pathways.[67] Nickel and its hydroxide has been the subject of investigation as electrocalatysts for fuel cell applications[84] and glucose sensors.[85, 86] A variety of synthetic routes are available for making different $Ni(OH)_2$ morphologies.[87, 88] The electrocatalytic activity arises from unpaired d electrons or empty d-orbitals resulting from the oxidized form of Ni(OOH)[89-91] which is available to bond with adsorbed species.

Recent efforts have been focused on the synthesis of carbon materials with design flexibility (with or without modification) as electrocatalysts for various applications, particularly as biosensors and for alcohol oxidation reactions (AOR).

1.2.4 Applications of carbon-based nanostructures for electrocatalysis

1.2.4.1 Dopamine detection

Biosensors plays a vital role in medical diagnosis and detection of biological agents in the environment.[92] The discovery of novel, efficient electrocatalysts is highly desirable in the development of new biosensors. EC sensing holds great promise in this area due to their high sensitivity and fast response time.[93] Carbon-based materials of different structures and dimensionalities are important electrode materials for EC biosensors due to the wide potential window, chemical inertness and hence biocompatibility, as well as their low cost.[94] However, conventional EC biosensors based on glassy carbon (GC) electrodes and screen printed carbon electrodes (SPCE) have several limitations, such as slow ET rates, poor sensitivity and stability.[30] In contrast, CNTs could overcome some of these issues owing to their high surface area,[95] biocompatibility,[96, 97] ease of functionalization[98-100] and facile ET for different redox couples.[58]

DA is an important catecholamine neurotransmitter that plays a key role in the function of the central nervous, renal and hormonal systems.[101, 102] Indeed, abnormal level of DA has been linked to neurological diseases, such as Parkinson's disease, schizophrenia, autism and attention deficit hyperactivity disorder (ADHD).[103-105] Detection of these abnormal changes of DA in vitro and in vivo is highly desirable, for better understanding of neuronal function and developing diagnostic tools. CNT network electrodes have been used to detect DA.[60, 64, 106] For instance, acid treated CNT network electrodes have been shown to enhance the ET kinetics for the oxidation of inner-sphere DA (Figure 1.11a).[60] This is due to the creation of defect sites, which improves adsorption or electrostatic attraction of DA to the SWNT surface.[107] There

is a strong correlation between increasing functionalization and decreasing conductivity, hence, a balance must be obtained between the two in order to enhance the performance of a SWNT network electrode. However, the extent of acid treatment in relation to the SWNT density required for optimal EC performance has not been fully addressed.

The oxidation of DA tends to produce the by-product, leucodopaminechrome,[108, 109] and eventually melanin-like compounds are formed, which may block the electrode surface, inhibiting ET and restrain the sensitivity of the electrode.[110-112] High density (HD) SWNT network electrodes have been shown to enhance sensitivity and stability of DA oxidation (Figure 1.11b).[64] The HD SWNT networks with low resistivity and background current, show promise in biosensor applications especially in challenging biological media where fouling is evident on conventional electrodes.[113, 114]

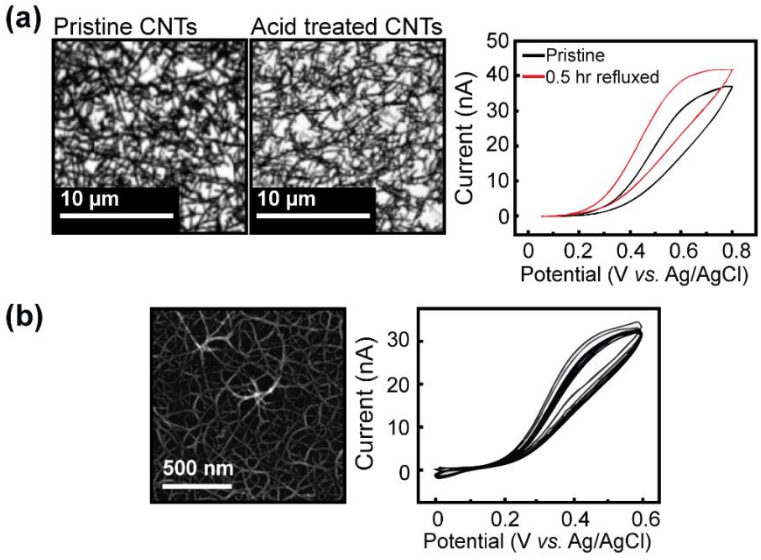

Figure 1.11 (a) FE-SEM images of pristine and 2 hours acid treated SWNT networks, CVs for the oxidation of 1 mM DA in 0.1 M citric acid pH 7.2 PBS, showing kinetically favored after acid treatment of SWNT network electrode.[60] (b) FE-SEM image of HD SWNT network, showing good electrode stability with 10 consecutive CVs for the oxidation of 1 mM DA in PBS.[64]

1.2.4.2 Hydrazine detection

HZ is a widely used in the chemical and pharmaceutical industries. However, HZ is a carcinogenic and hepatotoxic compound which is harmful to human health.[115-117] Thus, the development of strategies for sensitive and reliable HZ detection is becoming more important, with EC detection showing promise.[23, 118]

The overall reaction of HZ oxidation depends on the pH. For instance, in acidic media the reaction can be stated as:[119, 120]

$$N_2H_5^+ \rightarrow N_2 + 5H^+ + 4e^- \qquad E^o = -0.23 \text{ V (vs. NHE)} \quad (20)$$

whereas in alkaline media it is:[121]

$$N_2H_4 + 4OH^- \rightarrow N_2 + 4H_2O + 4e^- \qquad E^o = -0.33 \text{ V (vs. NHE)} \quad (21)$$

The use of porous carbon, derived from filter paper (PCDF), can electrocatalyze the HZ oxidation reaction.[122] The intertwined structure of the cellulose matrix in the filter paper is beneficial to serve as a self-template, the cellulose material and the metal-amine complexes act as precursors and the silica coating around cellulose structure as a protecting shell, the nanoporous carbon electrocatalysts were eventually formed (Figure 1.12a), showing good electrocatalytic activity towards HZ oxidation reaction. Besides, the reduced graphene sheets (RGSs) possess excellent electrocatalytic properties towards the HZ oxidation in alkaline media (Figure 1.12b).[123] These electrodes were shown to outperform conventional GC.

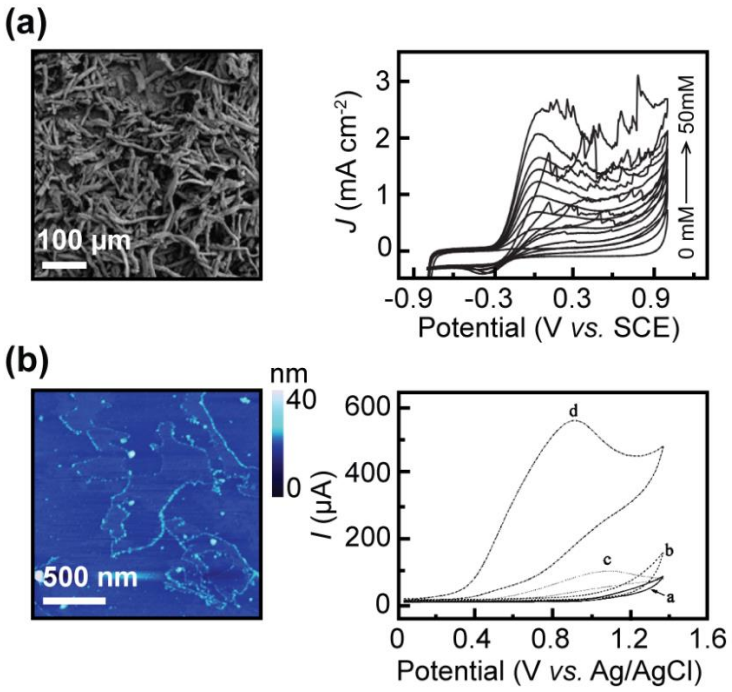

Figure 1.12 (a) FE-SEM image of PCDF, CVs for HZ oxidation with different concentration (0 to 50 mM) in 0.1 M PBS (pH 7.4).[122] (b) AFM image of RGSs deposited on the mica substrate, CVs at (a and c) the bare GC and (b and d) RGSs/GC electrode (a and b) in the absence and (c and d) in the presence of 10 mM HZ in 0.1 M KOH solutions. RGSs/GC electrode displays high electrocatalytic activity towards the oxidation of HZ with lower overpotential and a higher peak current as compared to bare GC.[123]

1.2.4.3 Carbon-based electrocatalysts for the alcohol oxidation reaction (AOR)

Understanding of the AOR (methanol oxidation reaction (MOR) and ethanol oxidation reaction (EOR)) is vitally important in fuel cell research. The commercial success of fuel cells is hindered by the high cost associated with noble metal electrocatalysts (*i.e.* Pt), typically used to facilitate these reactions.[124, 125] Additional problems include that Pt catalysts are readily poisoned by intermediate carbonaceous species (*i.e.* CO) produced during the AOR, which serve to reduce their electrocatalytic activity.[126, 127] Despite the tremendous efforts that have been made towards developing nanostructured Pt materials with increased mass activity for tackling the former issue,

through allowing the use of smaller amount of the expensive Pt, the electrode performance so far has been limited in success.[124, 128, 129] Pristine CNTs are ineffective as AOR catalysts as the reaction requires adsorption sites for the intermediates reaction, which are not readily available in the pure sp^2 structure. However, CNTs which exhibit a high surface area can act as a support material for metal or metal oxides catalysts and CNT networks provide a high electric conductivity for fast electrocatalysis of AOR.[130, 131] For instance, CNT supported Pt NPs have demonstrated significant enhancement of catalytic activity in MOR.[132, 133]

There is a need to find alternative and cheaper materials, which perform well in terms of electrocatalytic activity. Nickel hydroxide ($Ni(OH)_2$) is one such material that exhibits high EC activity and cost effectiveness and so this electrode has been the focus of considerable attention.[88, 134-137] $Ni(OH)_2$ prepared at low temperatures usually contains defects, which are particularly active for the dissociative adsorption of water molecules to form OH_{ad} species in alkaline electrolytes.[138] The interaction between $Ni(OH)_2$ and OH_{ad} species is neither too strong nor too weak, which has the maximum activity to participate in electrocatalytic reactions.[139] Besides, it is well known that the electrocatalytic activity of $Ni(OH)_2$ results from the oxidized form, Ni(OOH):[89]

$$Ni(OH)_2 + OH^- \rightleftharpoons NiOOH + H_2O + e^- \quad (22)$$

The interconversion of $Ni(OH)_2$/NiOOH acts as an electronic mediator, contributing to the superior catalytic activity for the AOR:[140]

$$NiOOH + \text{organic compound} \rightarrow Ni(OH)_2 + \text{byproduct} \quad (23)$$

In view of its attractive inherent properties, the incorporation of defective $Ni(OH)_2$ NPs play the pivotal role in prompting the dissociative adsorption of water

molecules and removing the carbonaceous product from poisoning the Pt electrode.[131] For instance, Pt-Ni(OH)$_2$–graphene ternary hybrids which were produced *via* a two-step solution method, as shown in Figure 1.13a, exhibit excellent activity and durability towards the MOR as shown in Figure 1.13b.

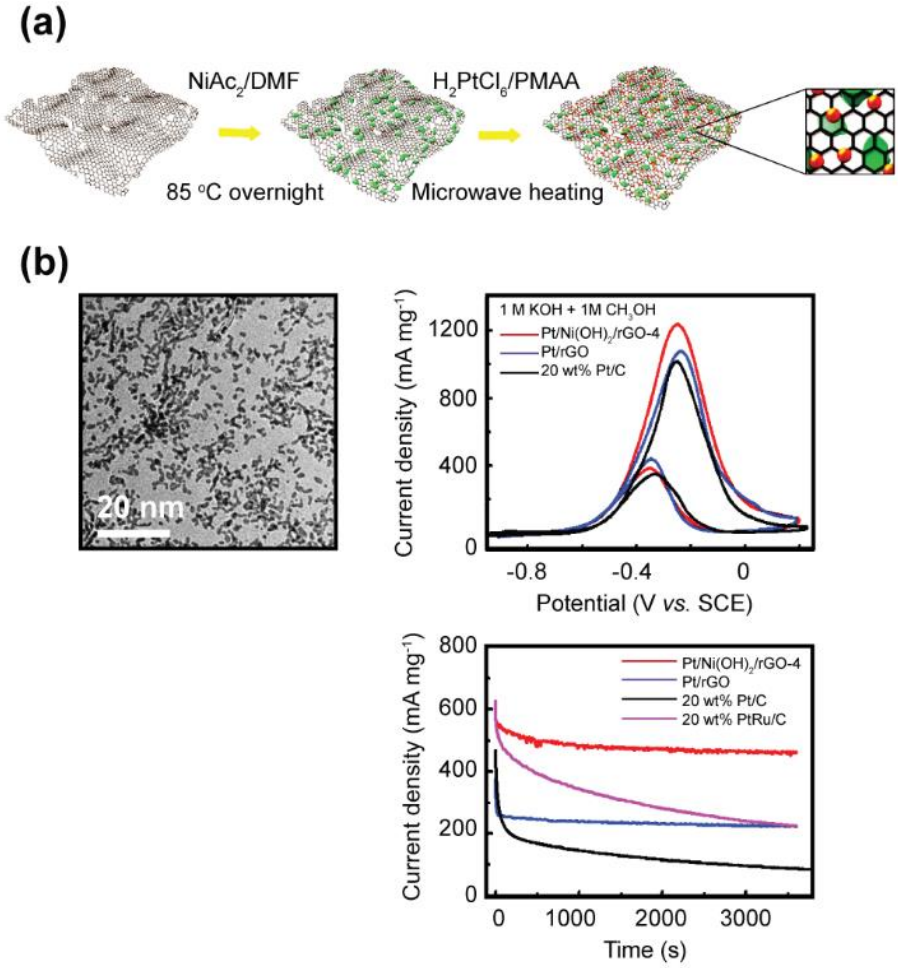

Figure 1.13 (a) A schematic depicting the two-step solution method to prepare the Pt/Ni(OH)$_2$/rGO-4 materials. (b) Corresponding transmission electron microscopy (TEM) image of ternary hybrid materials, CV curves of Pt/Ni(OH)$_2$/rGO-4, Pt/rGO hybrid and standard 20 wt % Pt/C in 1 M methanol/1 M KOH, short-term durability measurement at –0.30 V_{SCE} for Pt/Ni(OH)$_2$/rGO-4, Pt/rGO, standard 20 wt % Pt/C and 20 wt % PtRu/C. Pt/Ni(OH)$_2$/rGO-4 electrode displays exceptional activity and durability towards efficient MOR.[131]

1.3 Introduction to Li-O_2 batteries

The nonaqueous rechargeable Li- O_2 battery has been of great interest in developing practical device for road transportation owing to its high theoretical energy density of 3,458 Wh kg^{-1}.[141]

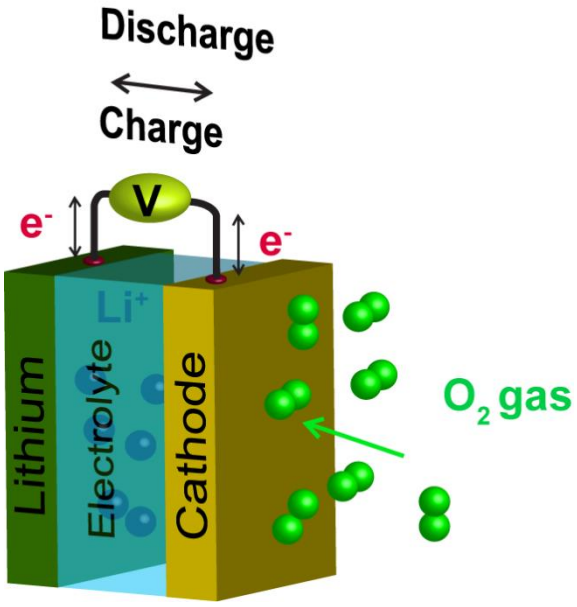

Figure 1.14 Schematic of nonaqueous Li-O_2 battery design.

The fundamental EC reaction of the Li-O_2 battery (Figure 1.14) can be written as,[142]

Anode:

$$Li \rightleftharpoons Li^+ + e^- \quad (24)$$

Cathode:

$$2Li^+ + 2e^- + O_2 \rightleftharpoons Li_2O_2 \quad E^o = 2.96\ V\ (vs.\ Li/Li^+) \quad (25)$$

whilst the net EC reaction is:

$$2Li + O_2 \rightleftharpoons Li_2O_2 \quad (26)$$

with the forward process corresponding to discharge of the battery and the backward reaction describing charge reaction.[143-145] Significant efforts, dedicated to the design of cathodes for Li-O_2 batteries, which give a uniform supply of O_2 throughout discharge have been made.[146] However, the formidable challenge arises from the electrical passivation of the cathode material during battery cycling,[147, 148] resulting in poor rechargeability and lower capacity.[149] The Li_2O_2 is an electronic insulator[150] and hinders charge transfer from cathode to Li_2O_2-electrolyte once the build-up of Li_2O_2 has a thickness of above 10 nm.[151] To alleviate this, better ways of controlling the discharge product morphology and engineering different cathode structures have to be pursued, to allow for extended cycling and to yield higher capacities for the battery. Li_2O_2 toroid is believed to circumvent the charge transport limitations.[149] This is an interesting structure, but their electrocatalytic properties have not been widely studied to date.

1.3.1 Formation of Li_2O_2 toroid

There are two EC pathways for Li_2O_2 growth, namely surface and solution mechanisms as shown in the schematic in Figure. 1.15. The surface mechanism can be written as:[152]

$$O_2^* + Li^+(sol) + e^- \rightarrow LiO_2^* \xrightarrow{Li^+(sol)+e^-} Li_2O_2(s) \qquad (27)$$

where * describes a surface-adsorbed species. The surface growth results in a homogenous Li_2O_2 layer, which terminates beyond the electron tunnelling thickness (~ 10 nm of discharge products).[147]

The slower pathway for the growth of Li_2O_2 crystal is a solution-mediated mechanism, which is induced by soluble oxygen species (O_2^-) in the presence of water[149] or at relatively low overpotentials,[153] and can be written as:

$$LiO_2^* \rightarrow Li^+(sol) + O_2^-(sol) \quad (28)$$

The $O_2^-(sol)$ undergoes reaction on a growing Li_2O_2 crystal on top of the existing Li_2O_2 conformal layer which is O-rich surface (primarily at kink site or defects on an already nucleated layer),[152, 154] which is given by:[149]

$$2Li^+(sol) + 2O_2^-(sol) \rightleftharpoons Li_2O_2(s) + O_2(g) \quad (29)$$

The proposed mechanism[149] as shown in Figure 1.15a is that: (a) LiO_2^* solvates from the O-rich Li_2O_2 conformal layer, (b) $O_2^-(sol)$ diffuses to the growing crystal and form LiO_2^*, (c) the disproportionation of two LiO_2^* results in formation of Li_2O_2 on a growing crystal and eventually toroidal Li_2O_2 particles are generated and (d) LiO_2^* is restored *via* the reaction in equation 27.

The stability of Li^+ and O_2^- ions depends on the Gutman donor number (DN) and acceptor number (AN).[149] The addition of water with a high AN of ~ 55 kcal mol^{-1} enhances the dissolution of O_2^-, encouraging the solution mechanism to form Li_2O_2 toroid structures. For instance, Li_2O_2 toroids grew as the water content increased from 500 ppm (Figure 1.15b) to 2000 ppm (Figure 1.15c). The resulting discharged capacity also increases with the water content (Figure .1.5d) due to the solution mediated Li_2O_2 toroids. However, the addition of water also introduces the parasitic side reactions caused by an increase in charging potential.[155] Therefore, water is not a good additive. A good additive must have high DN and/or AN for prompting the solution mechanism.

Dimethyl sulfoxide (DMSO) has high DNs (29.8 kcal mol^{-1}) and thus, it stabilizes Li^+ and is effective in promoting solution mechanism.

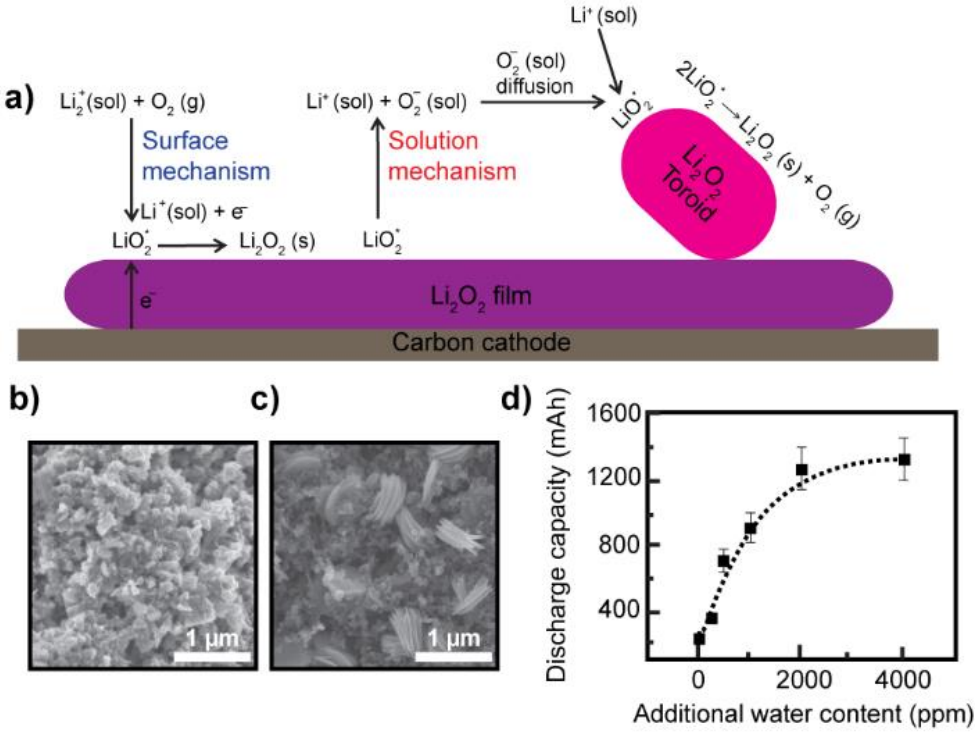

Figure 1.15 (a) Schematic of the Li_2O_2 crystal growth *via* a surface mechanism and solution mechanism. FE-SEM image of the discharged cathodes (capacity of 1 mAh at a rate of 50 μA) using 1 M LiTFSI in DME with water of (b) 500 ppm and (c) 2000 ppm. (c) Discharge capacities (discharge to a reductive potential of 2.3 V (vs. Li/Li^+) at a discharge rate of 250 μA) for the batteries with varying water content.[149]

1.4 Aims of thesis

This thesis presents fundamental studies on practically important electrodes through the application of microscopic and nanoscopic methods – both EC and structural/spectroscopic. Further, to demonstrate the general applicability of the approach, materials and electrodes with applications in sensing and energy systems will be considered.

First, carbon electrodes are important for EC sensing and analysis, their EC properties can be further improved in term of detection sensitivity and reduce fouling effect. Second, Li-O_2 batteries have received great attention for the development of a safe and cost-effective secondary batteries with high specific energy, yet fundamental aspects of their behaviour are unclear. This works highlights the importance of the precise control over the surface functionalization and surface nano-architectures, to optimize and to design the EC sensor and the cathode material for effective Li-O_2 battery. After describing the experimental methods and details, the following results and discussion chapters are presented.

Chapter 2 introduces the technical and experimental fundamentals of this thesis.

Chapter 3 is concerned with surface functionalization of the SWNT networks for effective DA electro-oxidation in terms of facile ET and making the electrodes less susceptible to blocking.

Chapter 4 compares the SWNT network electrodes of different densities and commercially available SPCE for trace level detection in challenging media.

Chapter 5 explores the electrodeposition of $Ni(OH)_2$ NPs on SWNT network electrodes for effective AOR.

Chapter 6 explores the surface properties and HZ electro-oxidation of surface "blistered" HOPG produced after electro-oxidation in $HClO_4$.

Chapter 7 investigates the fundamental behavior of redox activity at Li_2O_2 toroids in non-aqueous media.

Chapter 8 provides brief conclusions and ideas for future work.

1.5 References

1. Bard, A. J.; Faulkner, L. R. *Electrochemical Methods: Fundamentals and Applications*; Wiley, 2002.

2. Fisher, A. C. *Electrode Dynamics*; Oxford University Press, 1996.

3. Brett, C. M. A.; Brett, A. M. O. *Electroanalysis*; Oxford University Press, 1998.

4. Bard, A. J.; Denuault, G.; Lee, C.; Mandler, D.; Wipf, D. O. Scanning Electrochemical Microscopy – a New Technique for the Characterization and Modification of Surfaces. *Acc. Chem. Res.* **1990**, *23*, 357-363.

5. Bard, A. J.; Faulkner, L. R.; Leddy, J.; Zoski, C. G. *Electrochemical Methods: Fundamentals and Applications*; Wiley New York, 1980.

6. Randles, J. E. B. A Cathode Ray Polarograph. Part II. The Current-Voltage Curves. *Trans. Faraday Soc.* **1948**, *44*, 327-338.

7. Compton, R. G.; Banks, C. E. *Understanding Voltammetry*; Imperial College Press, 2011.

8. Ebejer, N.; Güell, A. G.; Lai, S. C. S.; McKelvey, K.; Snowden, M. E.; Unwin, P. R. Scanning Electrochemical Cell Microscopy: A Versatile Technique for Nanoscale Electrochemistry and Functional Imaging. *Annu. Rev. Anal. Chem.* **2013**, *6*, 329-351.

9. Ebejer, N.; Schnippering, M.; Colburn, A. W.; Edwards, M. A.; Unwin, P. R. Localized High Resolution Electrochemistry and Multifunctional Imaging: Scanning Electrochemical Cell Microscopy. *Anal. Chem.* **2010**, *82*, 9141-9145.

10. Rodolfa, K. T.; Bruckbauer, A.; Zhou, D. J.; Korchev, Y. E.; Klenerman, D. Two-Component Graded Deposition of Biomolecules with a Double-Barreled Nanopipette. *Angew. Chem. Int. Edit* **2005**, *44*, 6854-6859.

11. Suter, T.; Böhni, H. A New Microelectrochemical Method to Study Pit Initiation on Stainless Steels. *Electrochim. Acta* **1997**, *42*, 3275-3280.

12. Hassel, A. W.; Lohrengel, M. M. The Scanning Droplet Cell and Its Application to Structured Nanometer Oxide Films on Aluminum. *Electrochim. Acta* **1997**, *42*, 3327-3333.

13. Snowden, M. E.; Güell, A. G.; Lai, S. C. S.; McKelvey, K.; Ebejer, N.; O'Connell, M. A.; Colburn, A. W.; Unwin, P. R. Scanning Electrochemical Cell Microscopy: Theory and Experiment for Quantitative High Resolution Spatially-

Resolved Voltammetry and Simultaneous Ion-Conductance Measurements. *Anal. Chem.* **2012**, *84*, 2483-2491.

14. Güell, A. G.; Ebejer, N.; Snowden, M. E.; Macpherson, J. V.; Unwin, P. R. Structural Correlations in Heterogeneous Electron Transfer at Monolayer and Multilayer Graphene Electrodes. *J. Am. Chem. Soc.* **2012**, *134*, 7258-7261.

15. Unwin, P. R.; Güell, A. G.; Zhang, G. Nanoscale Electrochemistry of Sp^2 Carbon Materials: From Graphite and Graphene to Carbon Nanotubes. *Acc. Chem. Res.* **2016**, ASAP, **DOI:** 10.1021/acs.accounts.6b00301.

16. Güell, A. G.; Cuharuc, A. S.; Kim, Y.-R.; Zhang, G.; Tan, S.-Y.; Ebejer, N.; Unwin, P. R. Redox-Dependent Spatially Resolved Electrochemistry at Graphene and Graphite Step Edges. *ACS Nano* **2015**, *9*, 3558-3571.

17. Kirkman, P. M.; Güell, A. G.; Cuharuc, A. S.; Unwin, P. R. Spatial and Temporal Control of the Diazonium Modification of Sp^2 Carbon Surfaces. *J. Am. Chem. Soc.* **2014**, *136*, 36-39.

18. Zhang, G.; Kirkman, P. M.; Patel, A. N.; Cuharuc, A. S.; McKelvey, K.; Unwin, P. R. Molecular Functionalization of Graphite Surfaces: Basal Plane Versus Step Edge Electrochemical Activity. *J. Am. Chem. Soc.* **2014**, *136*, 11444-11451.

19. Patel, A. N.; Tan, S. Y.; Unwin, P. R. Epinephrine Electro-Oxidation Highlights Fast Electrochemistry at the Graphite Basal Surface. *Chem. Commun.* **2013**, *49*, 8776-8778.

20. Güell, A. G.; Ebejer, N.; Snowden, M. E.; McKelvey, K.; Macpherson, J. V.; Unwin, P. R. Quantitative Nanoscale Visualization of Heterogeneous Electron Transfer Rates in 2D Carbon Nanotube Networks. *P. Natl. Acad. Sci. USA* **2012**, *109*, 11487-11492.

21. Güell, A. G.; Meadows, K. E.; Dudin, P. V.; Ebejer, N.; Macpherson, J. V.; Unwin, P. R. Mapping Nanoscale Electrochemistry of Individual Single-Walled Carbon Nanotubes. *Nano Lett.* **2014**, *14*, 220-224.

22. Byers, J. C.; Güell, A. G.; Unwin, P. R. Nanoscale Electrocatalysis: Visualizing Oxygen Reduction at Pristine, Kinked, and Oxidized Sites on Individual Carbon Nanotubes. *J. Am. Chem. Soc.* **2014**, *136*, 11252-11255.

23. Chen, C.-H.; Jacobse, L.; McKelvey, K.; Lai, S. C. S.; Koper, M. T. M.; Unwin, P. R. Voltammetric Scanning Electrochemical Cell Microscopy: Dynamic Imaging of Hydrazine Electro-Oxidation on Platinum Electrodes. *Anal. Chem.* **2015**, *87*, 5782-5789.

24. Aaronson, B. D. B.; Chen, C.-H.; Li, H.; Koper, M. T. M.; Lai, S. C. S.; Unwin, P. R. Pseudo-Single-Crystal Electrochemistry on Polycrystalline Electrodes: Visualizing Activity at Grains and Grain Boundaries on Platinum for the Fe^{2+}/Fe^{3+} Redox Reaction. *J. Am. Chem. Soc.* **2013**, *135*, 3873-3880.

25. Chen, C.-H.; Meadows, K. E.; Cuharuc, A.; Lai, S. C. S.; Unwin, P. R. High Resolution Mapping of Oxygen Reduction Reaction Kinetics at Polycrystalline Platinum Electrodes. *Phys. Chem. Chem. Phys.* **2014**, *16*, 18545-18552.

26. Patel, A. N.; Unwin, P. R.; Macpherson, J. V. Investigation of Film Formation Properties during Electrochemical Oxidation of Serotonin (5-HT) at Polycrystalline Boron Doped Diamond. *Phys. Chem. Chem. Phys.* **2013**, *15*, 18085-18092.

27. Patten, H. V.; Meadows, K. E.; Hutton, L. A.; Iacobini, J. G.; Battistel, D.; McKelvey, K.; Colburn, A. W.; Newton, M. E.; Macpherson, J. V.; Unwin, P. R. Electrochemical Mapping Reveals Direct Correlation between Heterogeneous Electron-Transfer Kinetics and Local Density of States in Diamond Electrodes. *Angew. Chem. Int. Edit* **2012**, *51*, 7002-7006.

28. Iijima, S. Helical Microtubules of Graphitic Carbon. *Nature* **1991**, *354*, 56-58.

29. Novoselov, K. S.; Geim, A. K.; Morozov, S. V.; Jiang, D.; Zhang, Y.; Dubonos, S. V.; Grigorieva, I. V.; Firsov, A. A. Electric Field Effect in Atomically Thin Carbon Films. *Science* **2004**, *306*, 666-669.

30. Dumitrescu, I.; Unwin, P. R.; Macpherson, J. V. Electrochemistry at Carbon Nanotubes: Perspective and Issues. *Chem. Commun.* **2009**, *45*, 6886-6901.

31. Dudin, P. V.; Unwin, P. R.; Macpherson, J. V. Electrochemical Nucleation and Growth of Gold Nanoparticles on Single-Walled Carbon Nanotubes: New Mechanistic Insights. *J. Phys. Chem. C* **2010**, *114*, 13241-13248.

32. Smart, S. K.; Cassady, A. I.; Lu, G. Q.; Martin, D. J. The Biocompatibility of Carbon Nanotubes. *Carbon* **2006**, *44*, 1034-1047.

33. Deng, D.; Novoselov, K. S.; Fu, Q.; Zheng, N.; Tian, Z.; Bao, X. Catalysis with Two-Dimensional Materials and Their Heterostructures. *Nat. Nanotechnol.* **2016**, *11*, 218-230.

34. Dresselhaus, M. S.; Jorio, A.; Hofmann, M.; Dresselhaus, G.; Saito, R. Perspectives on Carbon Nanotubes and Graphene Raman Spectroscopy. *Nano Lett.* **2010**, *10*, 751-758.

35. Odom, T. W.; Huang, J. L.; Kim, P.; Lieber, C. M. Atomic Structure and Electronic Properties of Single-Walled Carbon Nanotubes. *Nature* **1998**, *391*, 62-64.

36. Dresselhaus, M. S.; Dresselhaus, G.; Saito, R. Physics of Carbon Nanotubes. *Carbon* **1995**, *33*, 883-891.

37. Zheng, L. X., et al. Ultralong Single-Wall Carbon Nanotubes. *Nat. Mater.* **2004**, *3*, 673-676.

38. Banks, C. E.; Compton, R. G. New Electrodes for Old: From Carbon Nanotubes to Edge Plane Pyrolytic Graphite. *Analyst* **2006**, *131*, 15-21.

39. Hirsch, A. Functionalization of Single-Walled Carbon Nanotubes. *Angew. Chem. Int. Edit* **2002**, *41*, 1853-1859.

40. Rossouw, D.; Botton, G. A.; Najafi, E.; Lee, V.; Hitchcock, A. P. Metallic and Semiconducting Single-Walled Carbon Nanotubes: Differentiating Individual SWCNTs by Their Carbon 1s Spectra. *ACS Nano* **2012**, *6*, 10965-10972.

41. Dresselhaus, M. S.; Dresselhaus, G.; Saito, R.; Jorio, A. Raman Spectroscopy of Carbon Nanotubes. *Phys. Rep.* **2005**, *409*, 47-99.

42. Charlier, J. C. Defects in Carbon Nanotubes. *Acc. Chem. Res.* **2002**, *35*, 1063-1069.

43. Saito, R.; Fujita, M.; Dresselhaus, G.; Dresselhaus, M. S. Electronic-Structure of Chiral Graphene Tubules. *Appl. Phys. Lett.* **1992**, *60*, 2204-2206.

44. Javey, A.; Guo, J.; Wang, Q.; Lundstrom, M.; Dai, H. Ballistic Carbon Nanotube Field-Effect Transistors. *Nature* **2003**, *424*, 654-657.

45. White, C. T.; Todorov, T. N. Carbon Nanotubes as Long Ballistic Conductors. *Nature* **1998**, *393*, 240-242.

46. Fan, Y. W.; Goldsmith, B. R.; Collins, P. G. Identifying and Counting Point Defects in Carbon Nanotubes. *Nat. Mater.* **2005**, *4*, 906-911.

47. Eatemadi, A.; Daraee, H.; Karimkhanloo, H.; Kouhi, M.; Zarghami, N.; Akbarzadeh, A.; Abasi, M.; Hanifehpour, Y.; Joo, S. W. *Nanoscale Res. Lett.* **2014,** *9*, 393-393.

48. Mishra, A. K., *Carbon Nanotubes : Synthesis and Properties*; New York, Nova Publishers, 2013.

49. Iijima, S.; Ichihashi, T. Single-Shell Carbon Nanotubes of 1 nm Diameter. *Nature* **1993**, *363*, 603-605.

50. Kokai, F.; Takahashi, K.; Yudasaka, M.; Iijima, S. Laser Ablation of Graphite−Co/Ni and Growth of Single-Wall Carbon Nanotubes in Vortexes Formed in an Ar Atmosphere. *J. Phys. Chem. B* **2000**, *104*, 6777-6784.

51. Hiura, H.; Ebbesen, T. W.; Tanigaki, K. Opening and Purification of Carbon Nanotubes in High Yields. *Adv. Mater.* **1995**, *7*, 275-276.

52. Montoro, L. A.; Rosolen, J. M. A Multi-Step Treatment to Effective Purification of Single-Walled Carbon Nanotubes. *Carbon* **2006**, *44*, 3293-3301.

53. Pumera, M. Carbon Nanotubes Contain Residual Metal Catalyst Nanoparticles Even after Washing with Nitric Acid at Elevated Temperature Because These Metal Nanoparticles Are Sheathed by Several Graphene Sheets. *Langmuir* **2007**, *23*, 6453-6458.

54. Banks, C. E.; Crossley, A.; Salter, C.; Wilkins, S. J.; Compton, R. G. Carbon Nanotubes Contain Metal Impurities Which Are Responsible for the "Electrocatalysis" Seen at Some Nanotube-Modified Electrodes. *Angew. Chem. Int. Edit* **2006**, *45*, 2533-2537.

55. Pumera, M.; Iwai, H. Multicomponent Metallic Impurities and Their Influence upon the Electrochemistry of Carbon Nanotubes. *J. Phys. Chem. C* **2009**, *113*, 4401-4405.

56. Jurkschat, K.; Ji, X.; Crossley, A.; Compton, R. G.; Banks, C. E. Super-Washing Does Not Leave Single Walled Carbon Nanotubes Iron-Free. *Analyst* **2007**, *132*, 21-23.

57. Vairavapandian, D.; Vichchulada, P.; Lay, M. D. Preparation and Modification of Carbon Nanotubes: Review of Recent Advances and Applications in Catalysis and Sensing. *Anal. Chim. Acta* **2008**, *626*, 119-129.

58. Balasubramanian, K.; Burghard, M. Chemically Functionalized Carbon Nanotubes. *Small* **2005**, *1*, 180-192.

59. Dai, H. J. Carbon Nanotubes: Opportunities and Challenges. *Surf. Sci.* **2002**, *500*, 218-241.

60. Dumitrescu, I.; Wilson, N. R.; Macpherson, J. V. Functionalizing Single-Walled Carbon Nanotube Networks: Effect on Electrical and Electrochemical Properties. *J. Phys. Chem. C* **2007**, *111*, 12944-12953.

61. Prasek, J.; Drbohlavova, J.; Chomoucka, J.; Hubalek, J.; Jasek, O.; Adam, V.; Kizek, R. Methods for Carbon Nanotubes Synthesis – Review. *J. Mater. Chem.* **2011**, *21*, 15872-15884.

62. Ivanov, V.; Nagy, J. B.; Lambin, P.; Lucas, A.; Zhang, X. B.; Zhang, X. F.; Bernaerts, D.; Vantendeloo, G.; Amelinckx, S.; Vanlanduyt, J. The Study of Carbon Nanotubules Produced by Catalytic Method. *Chem. Phys. Lett.* **1994**, *223*, 329-335.

63. Heller, I.; Kong, J.; Heering, H. A.; Williams, K. A.; Lemay, S. G.; Dekker, C. Individual Single-Walled Carbon Nanotubes as Nanoelectrodes for Electrochemistry. *Nano Lett.* **2005**, *5*, 137-142.

64. Dumitrescu, I.; Edgeworth, J. P.; Unwin, P. R.; Macpherson, J. V. Ultrathin Carbon Nanotube Mat Electrodes for Enhanced Amperometric Detection. *Adv. Mater.* **2009**, *21*, 3105-3109.

65. Miller, T. S.; Ebejer, N.; Güell, A. G.; Macpherson, J. V.; Unwin, P. R. Electrochemistry at Carbon Nanotube Forests: Sidewalls and Closed Ends Allow Fast Electron Transfer. *Chem. Commun.* **2012**, *48*, 7435-7437.

66. Li, Y.; Kim, W.; Zhang, Y.; Rolandi, M.; Wang, D.; Dai, H. Growth of Single-Walled Carbon Nanotubes from Discrete Catalytic Nanoparticles of Various Sizes. *J. Phys. Chem. B* **2001**, *105*, 11424-11431.

67. Gao, C.; Guo, Z.; Liu, J.-H.; Huang, X.-J. The New Age of Carbon Nanotubes: An Updated Review of Functionalized Carbon Nanotubes in Electrochemical Sensors. *Nanoscale* **2012**, *4*, 1948-1963.

68. Li, Y., et al. Purification of CVD Synthesized Single-Wall Carbon Nanotubes by Different Acid Oxidation Treatments. *Nanotechnology* **2004**, *15*, 1645-1649.

69. Moon, J.-M.; An, K. H.; Lee, Y. H.; Park, Y. S.; Bae, D. J.; Park, G.-S. High-Yield Purification Process of Single walled Carbon Nanotubes. *J. Phys. Chem. B* **2001**, *105*, 5677-5681.

70. Moonoosawmy, K. R.; Kruse, P. To Dope or Not to Dope: The Effect of Sonicating Single-Wall Carbon Nanotubes in Common Laboratory Solvents on Their Electronic Structure. *J. Am. Chem. Soc.* **2008**, *130*, 13417-13424.

71. Dillon, A. C.; Gennett, T.; Jones, K. M.; Alleman, J. L.; Parilla, P. A.; Heben, M. J. A Simple and Complete Purification of Single-Walled Carbon Nanotube Materials. *Adv. Mater.* **1999**, *11*, 1354-1358.

72. Park, T.-J.; Banerjee, S.; Hemraj-Benny, T.; Wong, S. S. Purification Strategies and Purity Visualization Techniques for Single-Walled Carbon Nanotubes. *J. Mater. Chem.* **2006**, *16*, 141-154.

73. Dujardin, E.; Ebbesen, T. W.; Krishnan, A.; Treacy, M. M. J. Purification of Single-Shell Nanotubes. *Adv. Mater.* **1998**, *10*, 611-+.

74. Liu, J., et al. Fullerene Pipes. *Science* **1998**, *280*, 1253-1256.

75. Marshall, M. W.; Popa, N. S.; Shapter, J. G. Measurement of Functionalized Carbon Nanotube Carboxylic Acid Groups Using a Simple Chemical Process. *Carbon* **2006**, *44*, 1137-1141.

76. Musameh, M.; Lawrence, N. S.; Wang, J. Electrochemical Activation of Carbon Nanotubes. *Electrochem. Commun.* **2005**, *7*, 14-18.

77. Wei, Y.; Liu, Z. G.; Yu, X. Y.; Wang, L.; Liu, J. H.; Huang, X. J. O_2-Plasma Oxidized Multi-Walled Carbon Nanotubes for Cd(II) and Pb(II) Detection: Evidence of Adsorption Capacity for Electrochemical Sensing. *Electrochem. Commun.* **2011**, *13*, 1506-1509.

78. Zhao, J.; Park, H.; Han, J.; Lu, J. P. Electronic Properties of Carbon Nanotubes with Covalent Sidewall Functionalization. *J. Phys. Chem. B* **2004**, *108*, 4227-4230.

79. Choi, H. J.; Ihm, J.; Louie, S. G.; Cohen, M. L. Defects, Quasibound States, and Quantum Conductance in Metallic Carbon Nanotubes. *Phys. Rev. Lett.* **2000**, *84*, 2917-2920.

80. Wildgoose, G. G.; Banks, C. E.; Compton, R. G. Metal Nanoparticles and Related Materials Supported on Carbon Nanotubes: Methods and Applications. *Small* **2006**, *2*, 182-193.

81. Bui, M. P. N.; Pham, X. H.; Han, K. N.; Li, C. A.; Lee, E. K.; Chang, H. J.; Seong, G. H. Electrochemical Sensing of Hydroxylamine by Gold Nanoparticles on Single-Walled Carbon Nanotube Films. *Electrochem. Commun.* **2010**, *12*, 250-253.

82. Hrapovic, S.; Liu, Y. L.; Male, K. B.; Luong, J. H. T. Electrochemical Biosensing Platforms Using Platinum Nanoparticles and Carbon Nanotubes. *Anal. Chem.* **2004**, *76*, 1083-1088.

83. Meng, L.; Jin, J.; Yang, G. X.; Lu, T. H.; Zhang, H.; Cai, C. X. Nonenzymatic Electrochemical Detection of Glucose Based on Palladium-Single-Walled Carbon Nanotube Hybrid Nanostructures. *Anal. Chem.* **2009**, *81*, 7271-7280.

84. Sarantaridis, D.; Atkinson, A. Redox Cycling of Ni-Based Solid Oxide Fuel Cell Anodes: A Review. *Fuel Cells* **2007**, *7*, 246-258.

85. Lin, K.-C.; Lin, Y.-C.; Chen, S.-M. A Highly Sensitive Nonenzymatic Glucose Sensor Based on Multi-Walled Carbon Nanotubes Decorated with Nickel and Copper Nanoparticles. *Electrochim. Acta* **2013**, *96*, 164-172.

86. Shamsipur, M.; Najafi, M.; Hosseini, M.-R. M. Highly Improved Electrooxidation of Glucose at a Nickel(II) Oxide/Multi-Walled Carbon Nanotube Modified Glassy Carbon Electrode. *Bioelectrochemistry.* **2010**, *77*, 120-124.

87. Oliva, P.; Leonardi, J.; Laurent, J. F.; Delmas, C.; Braconnier, J. J.; Figlarz, M.; Fievet, F.; Deguibert, A. Review of the Structure and the Electrochemistry of Nickel Hydroxides and Oxy-Hydroxides. *J. Power Sources* **1982**, *8*, 229-255.

88. Li, H. B.; Yu, M. H.; Wang, F. X.; Liu, P.; Liang, Y.; Xiao, J.; Wang, C. X.; Tong, Y. X.; Yang, G. W. Amorphous Nickel Hydroxide Nanospheres with Ultrahigh Capacitance and Energy Density as Electrochemical Pseudocapacitor Materials. *Nat. Commun.* **2013**, *4*.

89. Hutton, L. A.; Vidotti, M.; Patel, A. N.; Newton, M. E.; Unwin, P. R.; Macpherson, J. V. Electrodeposition of Nickel Hydroxide Nanoparticles on Boron-Doped Diamond Electrodes for Oxidative Electrocatalysis. *J. Phys. Chem. C* **2011**, *115*, 1649-1658.

90. Reim, R. E.; Vaneffen, R. M. Determination of Carbohydrates by Liquid-Chromatography with Oxidation at a Nickel(III) Oxide Electrode. *Anal. Chem.* **1986**, *58*, 3203-3207.

91. Dai, W.; Li, H.; Li, M.; Li, C.; Wu, X.; Yang, B. Electrochemical Imprinted Polycrystalline Nickel-Nickel Oxide Half-Nanotube-Modified Boron-Doped Diamond Electrode for the Detection of L-Serine. *ACS Appl. Mater. Inter.* **2015**, *7*, 22858-22867.

92. Turner, A. P. F. Biosensors: Sense and Sensibility. *Chem. Soc. Rev.* **2013**, *42*, 3184-3196.

93. Ronkainen, N. J.; Halsall, H. B.; Heineman, W. R. Electrochemical Biosensors. *Chem. Soc. Rev.* **2010**, *39*, 1747-1763.

94. Wang, Z. Y.; Dai, Z. H., Carbon Nanomaterial-Based Electrochemical Biosensors: An Overview. *Nanoscale* **2015**, *7*, 6420-6431.

95. Peigney, A.; Laurent, C.; Flahaut, E.; Bacsa, R. R.; Rousset, A. Specific Surface Area of Carbon Nanotubes and Bundles of Carbon Nanotubes. *Carbon* **2001**, *39*, 507-514.

96. Liu, Z.; Davis, C.; Cai, W.; He, L.; Chen, X.; Dai, H. Circulation and Long-Term Fate of Functionalized, Biocompatible Single-Walled Carbon Nanotubes in Mice Probed by Raman Spectroscopy. *Proc. Natl. Acad. Sci.* **2008**, *105*, 1410-1415.

97. Saito, N., et al. Safe Clinical Use of Carbon Nanotubes as Innovative Biomaterials. *Chem. Rev.* **2014**, *114*, 6040-6079.

98. Sun, Y.-P.; Fu, K.; Lin, Y.; Huang, W. Functionalized Carbon Nanotubes: Properties and Applications. *Acc. Chem. Res.* **2002**, *35*, 1096-1104.

99. Georgakilas, V.; Otyepka, M.; Bourlinos, A. B.; Chandra, V.; Kim, N.; Kemp, K. C.; Hobza, P.; Zboril, R.; Kim, K. S. Functionalization of Graphene: Covalent and Non-Covalent Approaches, Derivatives and Applications. *Chem. Rev.* **2012**, *112*, 6156-6214.

100. Yang, K.; Feng, L.; Hong, H.; Cai, W.; Liu, Z. Preparation and Functionalization of Graphene Nanocomposites for Biomedical Applications. *Nat. Protocols* **2013**, *8*, 2392-2403.

101. Weng, J.; Xue, J. M.; Wang, J.; Ye, J. S.; Cui, H. F.; Sheu, F. S.; Zhang, Q. Q. Gold-Cluster Sensors Formed Electrochemically at Boron-Doped-Diamond Electrodes: Detection of Dopamine in the Presence of Ascorbic Acid and Thiols. *Adv. Funct. Mater.* **2005**, *15*, 639-647.

102. Barras, A.; Lyskawa, J.; Szunerits, S.; Woisel, P.; Boukherroub, R. Direct Functionalization of Nanodiamond Particles Using Dopamine Derivatives. *Langmuir* **2011**, *27*, 12451-12457.

103. Asanuma, M.; Miyazaki, I.; Ogawa, N. Dopamine- or L-Dopa-Induced Neurotoxicity: The Role of Dopamine Quinone Formation and Tyrosinase in a Model of Parkinson's Disease. *Neurotox. Res.* **2003**, *5*, 165-176.

104. Venton, B. J.; Wightman, R. M. Psychoanalytical Electrochemistry: Dopamine and Behaviour. *Anal. Chem.* **2003**, *75*, 414-421.

105. Wu, K.; Fei, J.; Hu, S. Simultaneous Determination of Dopamine and Serotonin on a Glassy Carbon Electrode Coated with a Film of Carbon Nanotubes. *Anal. Biochem.* **2003**, *318*, 100-106.

106. Sansuk, S.; Bitziou, E.; Joseph, M. B.; Covington, J. A.; Boutelle, M. G.; Unwin, P. R.; Macpherson, J. V. Ultrasensitive Detection of Dopamine Using a Carbon Nanotube Network Microfluidic Flow Electrode. *Anal. Chem.* **2013**, *85*, 163-169.

107. DuVall, S. H.; McCreery, R. L. Self-Catalysis by Catechols and Quinones during Heterogeneous Electron Transfer at Carbon Electrodes. *J. Am. Chem. Soc.* **2000**, *122*, 6759-6764.

108. Bernsmann, F.; Ball, V.; Addiego, F.; Ponche, A.; Michel, M.; Gracio, J. J. d. A.; Toniazzo, V.; Ruch, D. Dopamine−Melanin Film Deposition Depends on the Used Oxidant and Buffer Solution. *Langmuir* **2011**, *27*, 2819-2825.

109. Hawley, M. D.; Tatawawadi, S. V.; Piekarski, S.; Adams, R. N. Electrochemical Studies of the Oxidation Pathways of Catecholamines. *J. Am. Chem. Soc.* **1967**, *89*, 447-450.

110. Hou, S.; Zheng, N.; Feng, H.; Li, X.; Yuan, Z. Determination of Dopamine in the Presence of Ascorbic Acid Using Poly(3,5-Dihydroxy Benzoic Acid) Film Modified Electrode. *Anal. Biochem.* **2008**, *381*, 179-184.

111. Lane, R. F.; Hubbard, A. T. Differential Double Pulse Voltammetry at Chemically Modified Platinum Electrodes for in Vivo Determination of Catechol Amines. *Anal. Chem.* **1976**, *48*, 1287-1293.

112. Alwarappan, S.; Butcher, K. S. A.; Wong, D. K. Y. Evaluation of Hydrogenated Physically Small Carbon Electrodes in Resisting Fouling During Voltammetric Detection of Dopamine. *Sensor Actuat. B-Chem.* **2007**, *128*, 299-305.

113. Dumitrescu, I.; Unwin, P. R.; Wilson, N. R.; Macpherson, J. V. Single-Walled Carbon Nanotube Network Ultramicroelectrodes. *Anal. Chem.* **2008**, *80*, 3598-3605.

114. Patel, A. N.; Tan, S. Y.; Miller, T. S.; Macpherson, J. V.; Unwin, P. R. Comparison and Reappraisal of Carbon Electrodes for the Voltammetric Detection of Dopamine. *Anal. Chem.* **2013**, *85*, 11755-11764.

115. Zhou, W. H.; Xu, L.; Wu, M. J.; Xu, L. J.; Wang, E. Determination of Hydrazines by Capillary Zone Electrophoresis with Amperometric Detection at a Platinum Particle-Modified Carbon-Fiber Microelectrode. *Anal. Chim. Acta* **1994**, *299*, 189-194.

116. Ding, W.; Wu, M.; Liang, M. L.; Ni, H. M.; Li, Y. Sensitive Hydrazine Electrochemical Biosensor Based on a Porous Chitosan-Carbon Nanofiber Nanocomposite Modified Electrode. *Anal. Lett.* **2015**, *48*, 1551-1569.

117. Fang, B.; Feng, Y. H.; Liu, M.; Wang, G. F.; Zhang, X. J.; Wang, M. F. Electrocatalytic Oxidation of Hydrazine at a Glassy Carbon Electrode Modified with Nickel Ferrite and Multi-Walled Carbon Nanotubes. *Microchim. Acta* **2011**, *175*, 145-150.

118. Channon, R. B.; Joseph, M. B.; Bitziou, E.; Bristow, A. W. T.; Ray, A. D.; Macpherson, J. V. Electrochemical Flow Injection Analysis of Hydrazine in an Excess of an Active Pharmaceutical Ingredient: Achieving Pharmaceutical Detection Limits Electrochemically. *Anal. Chem.* **2015**, *87*, 10064-10071.

119. Harrison, J. A.; Khan, Z. A. Oxidation of Hydrazine on Platinum in Acid Solution. *J. Electroanal. Chem.* **1970**, *28*, 131-138.

120. Harrison, J. A.; Khan, Z. A. Oxidation of Hydrazine in Alkaline Solution at Platinum and Mercury. *J. Electroanal. Chem.* **1970**, *26*, 1-11.

121. Rosca, V.; Duca, M.; de Groot, M. T.; Koper, M. T. M. Nitrogen Cycle Electrocatalysis. *Chem. Rev.* **2009**, *109*, 2209-2244.

122. Martins, A. C.; Huang, X. X.; Goswami, A.; Koh, K.; Meng, Y.; Almeida, V. C.; Asefa, T. Fibrous Porous Carbon Electrocatalysts for Hydrazine Oxidation by

Using Cellulose Filter Paper as Precursor and Self-Template. *Carbon* **2016**, *102*, 97-105.

123. Wang, Y.; Wan, Y.; Zhang, D. Reduced Graphene Sheets Modified Glassy Carbon Electrode for Electrocatalytic Oxidation of Hydrazine in Alkaline Media. *Electrochem. Commun.* **2010**, *12*, 187-190.

124. Zhao, X.; Yin, M.; Ma, L.; Liang, L.; Liu, C.; Liao, J.; Lu, T.; Xing, W. Recent Advances in Catalysts for Direct Methanol Fuel Cells. *Energ. & Environ. Sci.* **2011**, *4*, 2736-2753.

125. Huang, H.; Wang, X. Recent Progress on Carbon-Based Support Materials for Electrocatalysts of Direct Methanol Fuel Cells. *J. Mater. Chem. A* **2014**, *2*, 6266-6291.

126. Halder, A.; Sharma, S.; Hegde, M. S.; Ravishankar, N. Controlled Attachment of Ultrafine Platinum Nanoparticles on Functionalized Carbon Nanotubes with High Electrocatalytic Activity for Methanol Oxidation. *J. Phys. Chem. C* **2009**, *113*, 1466-1473.

127. Kang, Y.; Pyo, J. B.; Ye, X.; Gordon, T. R.; Murray, C. B. Synthesis, Shape Control, and Methanol Electro-Oxidation Properties of Pt–Zn Alloy and Pt_3Zn Intermetallic Nanocrystals. *ACS Nano* **2012**, *6*, 5642-5647.

128. Reddington, E.; Sapienza, A.; Gurau, B.; Viswanathan, R.; Sarangapani, S.; Smotkin, E. S.; Mallouk, T. E. Combinatorial Electrochemistry: A Highly Parallel, Optical Screening Method for Discovery of Better Electrocatalysts. *Science* **1998**, *280*, 1735-1737.

129. Spendelow, J. S.; Wieckowski, A. Electrocatalysis of Oxygen Reduction and Small Alcohol Oxidation in Alkaline Media. *Phys. Chem. Chem. Phys.* **2007**, *9*, 2654-2675.

130. Kumar, L. V.; Ntim, S. A.; Sae-Khow, O.; Janardhana, C.; Lakshminarayanan, V.; Mitra, S. Electro-Catalytic Activity of Multiwall Carbon Nanotube-Metal (Pt or Pd) Nanohybrid Materials Synthesized Using Microwave-Induced Reactions and Their Possible Use in Fuel Cells. *Electrochim. Acta* **2012**, *83*, 40-46.

131. Huang, W., et al. Highly Active and Durable Methanol Oxidation Electrocatalyst Based on the Synergy of Platinum-Nickel Hydroxide-Graphene. *Nat Commun* **2015**, *6*.

132. Maiyalagan, T.; Viswanathan, B.; Varadaraju, U. Nitrogen Containing Carbon Nanotubes as Supports for Pt–Alternate Anodes for Fuel Cell Applications. *Electrochem. Commun.* **2005**, *7*, 905-912.

133. Liu, H. S.; Song, C. J.; Zhang, L.; Zhang, J. J.; Wang, H. J.; Wilkinson, D. P. A Review of Anode Catalysis in the Direct Methanol Fuel Cell. *J. Power Sources* **2006**, *155*, 95-110.

134. Gong, M., et al. Nanoscale Nickel Oxide/Nickel Heterostructures for Active Hydrogen Evolution Electrocatalysis. *Nat. Commun.* **2014**, *5*.

135. Mu, Y.; Jia, D.; He, Y.; Miao, Y.; Wu, H.-L. Nano Nickel Oxide Modified Non-Enzymatic Glucose Sensors with Enhanced Sensitivity through an Electrochemical Process Strategy at High Potential. *Biosens. Bioelectron.* **2011**, *26*, 2948-2952.

136. Casas-Cabanas, M.; Canales-Vazquez, J.; Rodriguez-Carvajal, J.; Rosa Palacin, M. Deciphering the Structural Transformations during Nickel Oxyhydroxide Electrode Operation. *J. Am. Chem. Soc.* **2007**, *129*, 5840-5842.

137. Liu, J.; Chen, M.; Zhang, L.; Jiang, J.; Yan, J.; Huang, Y.; Lin, J.; Fan, H. J.; Shen, Z. X. A Flexible Alkaline Rechargeable Ni/Fe Battery Based on Graphene Foam/Carbon Nanotubes Hybrid Film. *Nano Lett.* **2014**, *14*, 7180-7187.

138. Subbaraman, R.; Tripkovic, D.; Strmcnik, D.; Chang, K. C.; Uchimura, M.; Paulikas, A. P.; Stamenkovic, V.; Markovic, N. M. Enhancing Hydrogen Evolution Activity in Water Splitting by Tailoring Li^+–$Ni(OH)_2$–Pt Interfaces. *Science* **2011**, *334*, 1256-1260.

139. Subbaraman, R.; Tripkovic, D.; Chang, K. C.; Strmcnik, D.; Paulikas, A. P.; Hirunsit, P.; Chan, M.; Greeley, J.; Stamenkovic, V.; Markovic, N. M. Trends in Activity for the Water Electrolyser Reactions on 3d M (Ni,Co,Fe,Mn) Hydr(oxy)Oxide Catalysts. *Nat. Mater.* **2012**, *11*, 550-557.

140. El-Shafei, A. A. Electrocatalytic Oxidation of Methanol at a Nickel Hydroxide/Glassy Carbon Modified Electrode in Alkaline Medium. *J. Electroanal. Chem.* **1999**, *471*, 89-95.

141. Bruce, P. G.; Freunberger, S. A.; Hardwick, L. J.; Tarascon, J. M. Li-O_2 and Li-S Batteries with High Energy Storage. *Nat. Mater.* **2012**, *11*, 19-29.

142. Shao, Y.; Park, S.; Xiao, J.; Zhang, J.-G.; Wang, Y.; Liu, J. Electrocatalysts for Nonaqueous Lithium–Air Batteries: Status, Challenges, and Perspective. *ACS Catal.* **2012**, *2*, 844-857.

143. Ogasawara, T.; Debart, A.; Holzapfel, M.; Novak, P.; Bruce, P. G. Rechargeable Li_2O_2 Electrode for Lithium Batteries. *J. Am. Chem. Soc.* **2006**, *128*, 1390-1393.

144. Laoire, C. O.; Mukerjee, S.; Abraham, K. M.; Plichta, E. J.; Hendrickson, M. A. Elucidating the Mechanism of Oxygen Reduction for Lithium-Air Battery Applications. *J. Phys. Chem. C* **2009**, *113*, 20127-20134.

145. Laoire, C. O.; Mukerjee, S.; Abraham, K. M.; Plichta, E. J.; Hendrickson, M. A. Influence of Nonaqueous Solvents on the Electrochemistry of Oxygen in the Rechargeable Lithium-Air Battery. *J. Phys. Chem. C* **2010**, *114*, 9178-9186.

146. Grande, L.; Paillard, E.; Hassoun, J.; Park, J. B.; Lee, Y. J.; Sun, Y. K.; Passerini, S.; Scrosati, B. The Lithium/Air Battery: Still an Emerging System or a Practical Reality? *Adv. Mater.* **2015**, *27*, 784-800.

147. Luntz, A. C.; Viswanathan, V.; Voss, J.; Varley, J. B.; Norskov, J. K.; Scheffler, R.; Speidel, A. Tunneling and Polaron Charge Transport through Li_2O_2 in Li-O_2 Batteries. *J. Phys. Chem. Lett.* **2013**, *4*, 3494-3499.

148. Radin, M. D.; Siegel, D. J. Charge Transport in Lithium Peroxide: Relevance for Rechargeable Metal-Air Batteries. *Energ. & Environ. Sci.* **2013**, *6*, 2370-2379.

149. Aetukuri, N. B.; McCloskey, B. D.; Garcia, J. M.; Krupp, L. E.; Viswanathan, V.; Luntz, A. C. Solvating Additives Drive Solution-Mediated Electrochemistry and Enhance Toroid Growth in Non-Aqueous Li-O_2 Batteries. *Nat. Chem.* **2015**, *7*, 50-56.

150. Albertus, P.; Girishkumar, G.; McCloskey, B.; Sanchez-Carrera, R. S.; Kozinsky, B.; Christensen, J.; Luntz, A. C. Identifying Capacity Limitations in the Li/Oxygen Battery Using Experiments and Modelling. *J. Electrochem. Soc.* **2011**, *158*, A343-A351.

151. Viswanathan, V.; Thygesen, K. S.; Hummelshoj, J. S.; Norskov, J. K.; Girishkumar, G.; McCloskey, B. D.; Luntz, A. C. Electrical Conductivity in Li_2O_2 and Its Role in Determining Capacity Limitations in Non-Aqueous Li-O_2 Batteries. *J. Chem. Phys.* **2011**, *135*.

152. Hummelshoj, J. S.; Luntz, A. C.; Norskov, J. K., Theoretical Evidence for Low Kinetic Overpotentials in Li-O_2 Electrochemistry. *J. Chem. Phys.* **2013**, *138*.

153. Zhang, Y.; Zhang, X.; Wang, J.; McKee, W. C.; Xu, Y.; Peng, Z., Potential-Dependent Generation of O_2^- and LiO_2 and Their Critical Roles in O_2 Reduction to Li_2O_2 in Aprotic Li–O_2 Batteries. *J. Phys. Chem. C* **2016**, *120*, 3690-3698.

154. Radin, M. D.; Tian, F.; Siegel, D. J., Electronic Structure of Li_2O_2 [3] Surfaces. *J. Mater. Sci.* **2012**, *47*, 7564-7570.

155. McCloskey, B. D.; Speidel, A.; Scheffler, R.; Miller, D. C.; Viswanathan, V.; Hummelshoj, J. S.; Norskov, J. K.; Luntz, A. C. Twin Problems of Interfacial

Carbonate Formation in Nonaqueous Li–O_2 Batteries. *J. Phys. Chem. Lett.* **2012**, *3*, 997-1001.

Chapter 2 Experimental

This chapter introduces the chemicals, materials and the experimental procedures used throughout the work described in this thesis.

2.1 Chemicals

All chemicals were used as received. All aqueous solutions were prepared freshly using deionized water produced by a Purite Select HP system (resistivity of 18.2 MΩ cm at 25 ^{o}C). A detailed list of chemicals and materials used in this thesis is shown in Table 2.1.

Table 2.1 Materials and chemicals used for the work described in this thesis.

Chemicals/ Materials	**Suppliers & Details**
Chemicals	-------
Ferritin (horse-spleen)	50 – 150 mg mL^{-1} in 150 mM aqueous NaCl, Sigma-Aldrich Co., U.K.
Ferrocenylmethyltrimethylamm -onium iodide ($FCTMA^{+}I^{-}$)	Strem Chemical Co., 99 %
Silver hexafluorophosphate ($Ag^{+}PF_{6}^{-}$) (Strem Chemical Co., 99.5 %)	Strem Chemical Co., 99.5 %

(Ferrocenyl-methyl) trimethylammonium hexafluorophosphate $(FCTMA^+)PF_6^-$	Prepared *via* metathesis of $FCTMA^+I^-$ with $Ag^+PF_6^-$
Potassium nitrate (KNO_3)	Fisher Scientific, 99 %
Dopamine hydrochloride	Sigma Aldrich, 98 %
HZ	Acros Organics, 64 %
Ferrocenecarboxylic acid (FcCOOH)	VWR International Ltd., 98 %
Polyethylene glycol (PEG) 2K	VWR International Ltd., Laboratory reagent
Sodium phosphate dibasic heptahydrate ($Na_2HPO_4{\cdot}7H_2O$)	Sigma-Aldrich, 98 – 102 %
Sodium dihydrogen orthophosphate dihydrate ($NaH_2PO_4{\cdot}2H_2O$)	Fisher Scientific, 99 – 101 %
Albumin	Sigma-Aldrich, 99 %
Nickel nitrate ($Ni(NO_3)_2$	Sigma-Aldrich, 99.999 %
Nickel sulphate ($NiSO_4$)	Sigma-Aldrich, 99 %
Potassium hydroxide (KOH)	Sigma-Aldrich, 90 %
EtOH	Fisher Scientific, 99.99 %
MeOH	VWR International Ltd., 99 %
Propan-2-ol	Fisher Scientific, 99.99 %
Acetone	Fisher Scientific, 99 %
Dichlorodimethylsilane	Fisher Scientific, ≥ 99 %
Citric acid	Sigma-Aldrich, 99.5 %
Sulfuric acid (H_2SO_4)	Sigma-Aldrich, 99.999 %
Perchloric acid ($HClO_4$)	Acros Organics, 70 %
Nitric acid (HNO_3)	Fisher Scientific Ltd., U.K., 70 %
Water	≥18 MΩ resistivity, Purite Select HP system
Lithium perchlorate ($LiCO_4$)	Sigma-Aldrich, 99.99 %
Dimethyl sulfoxide (DMSO)	Sigma-Aldrich, analytical reagent
4, 7, 10-trioxa-1, 13 tridecanediamine	Sigma-Aldrich, 97 %

Tetrabutylammonium hexafluorophosphate ($TBAPF_6$)	Sigma-Aldrich, ≥99 %
Argon (Ar)	BOC Gases, U.K., 99.9995 %
Hydrogen (H_2)	BOC Gases U.K., 99.95 %
Oxygen (O_2)	BOC Gases, U.K., 99.5 %
Materials	-------
Cobalt (Co) target	Testbourne Ltd., U.K., 99.95 %
Chromium (Cr) coated tungsten bar	Good fellow Cambridge Ltd., 99.9 %
Gold (Au) wire for thermal evaporation	MaTeck, 99.995 %
Palladium (Pd) wire	MaTeck, > 99.95 %
Platinum (Pt) wire	MaTeck, > 99.95 %
Silver (Ag) wire	Good fellow Cambridge Ltd., 99.99 %
AM-grade HOPG	Originating from Dr. A. Moore, Union Carbide (now GE Advanced Ceramics) and kindly provided by Prof. Richard L. McCreery (University of Alberta, Canada).
Si/SiO_2 substrates	IDB Technologies Ltd. (n-type, 525 µm thickness with 300 nm of thermally grown SiO_2 on both sides)
SPCE	Kanichi Research, UK. It consists of circular graphite as the WE with 3 mm in diameter, a large surface area of graphite as CE and a Ag/AgCl RE printed onto polyvinyl chloride.
Borosilicate glass capillary	Harvard Apparatus Ltd. (outer diameter (OD) = 1.2 mm, internal diameter (ID) = 0.69 mm)
Dual channel borosilicate theta capillary	Harvard Apparatus Ltd. (ID = 1.0 mm, OD = 1.5 mm)
Lacey carbon TEM grid	Agar Scientific

2.2 Single-walled carbon nanotube network growth

SWNT networks were grown on 2 cm × 2 cm Si/SiO_2 substrates (IDB Technologies Ltd., n-type, 525 µm thick with 300 nm of thermally grown SiO_2 on both sides) using cCVD (Figure 2.1).[1] Fe NPs[2] were used as catalysts for the growth of low density (LD) SWNT network whereas Co NPs[3] were employed as catalysts for both HD and super HD (SHD) SWNT networks growth. Fe NPs were deposited by soaking the substrate in 1 % ferritin (50-150 mg mL^{-1}, Aldrich) aqueous solution for 1 hour, followed by 2 min exposure to 100 W oxygen plasma (Emitech K1050X plasma asher). Co NPs were deposited by sputtering (SC7640 sputter coater, Quorum Technologies Ltd., U.K.) at 1 kV for 20 s and 30 s with respect to the growth of HD and SHD SWNT networks.

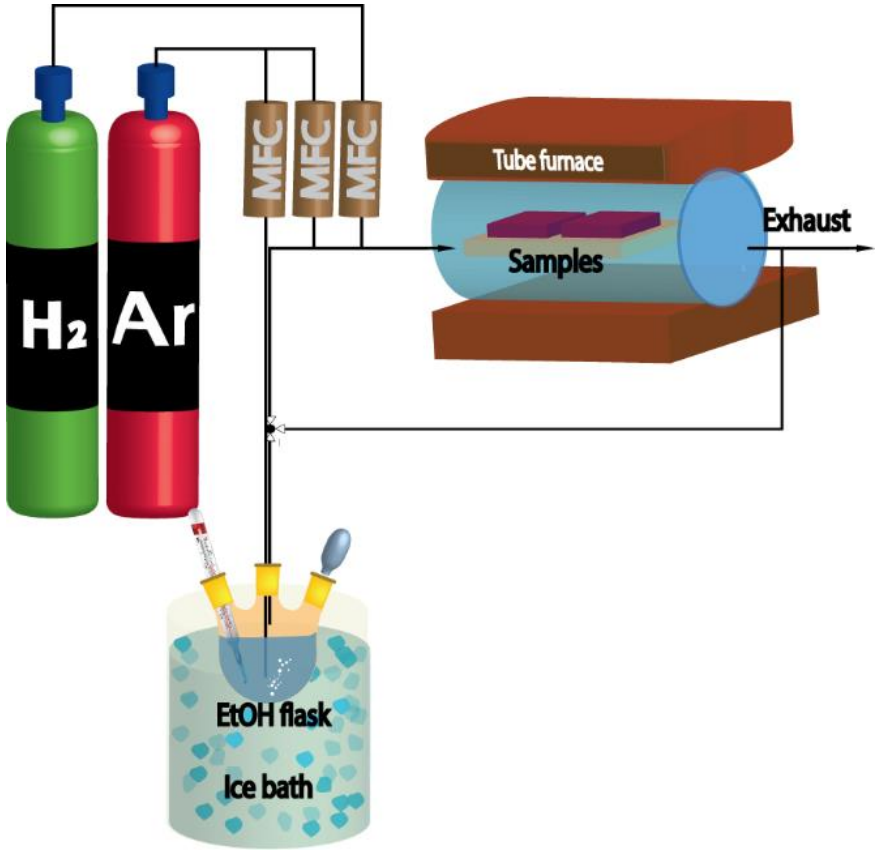

Figure 2.1 Schematic of the cCVD systems used to grow SWNT network.

The cCVD procedure (Figure 2.2) began with the substrate being heated from room temperature to 850 ^{o}C in 14 min under H_2 (BOC Gases, 99.95 %) atmosphere at a flow rate of 150 sccm, followed by stabilization at 850 ^{o}C for 1 min. The growth of SWNT networks was initiated by bubbling Ar (BOC Gases, 99.9995 %) (850 sccm) through EtOH (Fisher, 99.99 %) held at 0 ^{o}C. Growth was carried out for 10, 20 and 30 mins with respect to LD, HD and SHD SWNT networks. The system was left to cool under just H_2 gas.

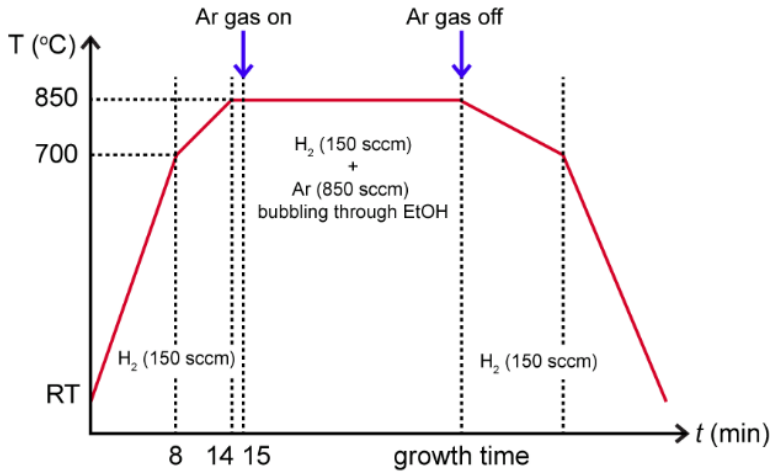

Figure 2.2 Graphical representation of cCVD for SWNT network growth.

2.3 Functionalization of Single-walled carbon nanotube networks

SWNT networks were treated with 3 M HNO_3 (70 %, Fisher) heated to 70 ^{o}C for 20, 120, 300 and 600 mins. After removal from solution, the substrates were rinsed with distilled water and dried under N_2 gas before use. These medium strength acid treatments were employed to enable good control over the acid etching of SWNT networks and to avoid etching of the insulating substrate[4] compared to strong acid treatments[5] (concentrated H_2SO_4/HNO_3) which are typically employed to purify as-

grown nanotubes. A similar medium acid treatment has been shown previously to oxidatively attack SWNTs.[6]

2.4 Gold evaporation

Electrical contact to the SWNT networks was achieved by evaporating Cr (3 nm), followed by Au (60 nm) through a shadow mask on the side of the Si/SiO_2 substrate using a Moorfield MiniLab deposition system (Moorfield Associates).

2.5 Droplet experiments

EC measurements using the droplet method[7] were carried out in a 3-electrode setup, with the SWNT network (Figure 2.3a) and freshly cleaved HOPG (Figure 2.3b) acting as the WE. Electrical contact to the Au band side contact was made *via* a pin for SWNT network electrode or conductive Ag paint for HOPG. A drop of electrolyte solution (~15 µL, ~ 4 mm diameter) was placed on the electrode surface, fairly close to the gold band but without making contact. A platinum wire was used as a CE. AgCl-coated Ag wire acted as a quasi-reference electrodes (QRE) for all droplet experiment in this thesis, except where a Pd-H_2 wire was used for the EC formation of blisters on HOPG in 0.1 M $HClO_4$, all potentials are quoted against the QRE used. The QREs used were found to be sufficiently stable under the experimental conditions and timescale.[8-9] Both the CE and QRE were positioned within the droplet of solution to complete the circuit. The EC measurements were performed with a CHI 730 EC workstation (CH Instruments, TX, USA).

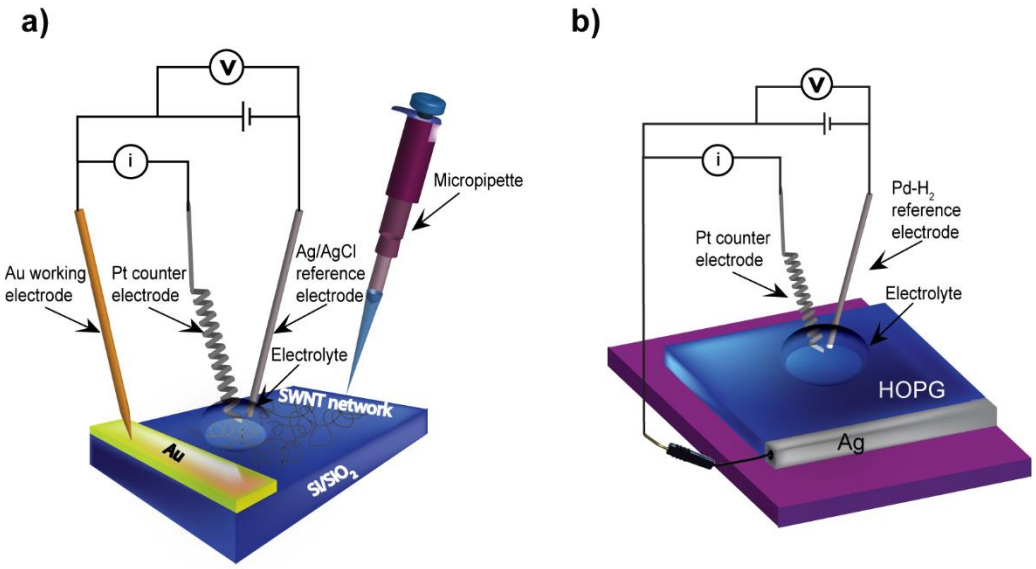

Figure 2.3 Schematic of a 3-electrode droplet experimental setup for the EC analysis on (a) SWNT network and (b) HOPG electrode.

2.6 Micro-capillary electrochemical method (MCEM)

Contact to the Au band was made *via* a Au pin. Neither came into contact with solution (Figure 2.4). To perform MCEM measurements,[10] SWNT networks were mounted inside a humidity cell (de-aerated with N_2) and connected as a WE. The MCEM cell was fabricated from a borosilicate glass capillary (1.2 mm outer diameter, 0.69 mm internal diameter, Harvard Apparatus Ltd.), pulled to a small opening using a laser pipet puller (P-2000, Sutter Instrument Co.). The end was polished flat with an inner diameter of 50 µm (for DA detection), 70 µm (for $FcTMA^+$ oxidation), 60 – 62 µm (for MOR and EOR) and rendered hydrophobic through immersion in dichlorodimethylsilane (Fisher, ≥99 %) for 90 s, with Ar gas flowing through to prevent any internal silanization.

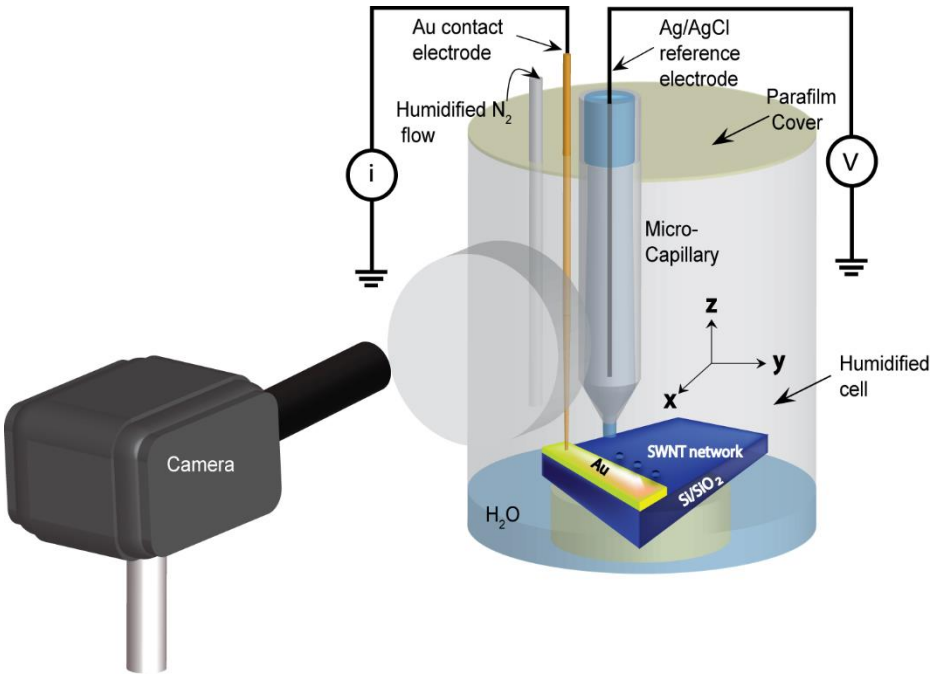

Figure 2.4 Schematic of a 2-electrode setup MCEM.

The capillary was then filled with the aqueous solution of interest and fitted with a AgCl-coated Ag wire QRCE. The capillary was mounted on an *x*-*y*-*z* micropositioner (Newport 433 series) above the SWNT network substrate. With the aid of a camera (PixeLINK PL-B776U) the capillary was moved so that the meniscus landed on the SWNT network, without the capillary itself making contact to the electrode surface. EC measurements were made in the 2-electrode arrangement owing to small current (small droplet size).

2.7 Hopping scanning electrochemical cell microscopy experiments

Dual channel borosilicate theta capillaries (ID = 1.0 mm, OD = 1.5 mm, Harvard Apparatus, UK) were pulled using a laser pipette puller to produce nanopipettes with diameter of around 400 nm (200 nm each channel; HZ detection) and 200 nm (100 nm each barrel; Li_2O_2 scanning). For experiments conducted in aqueous media,

nanopipettes were silanized to produce a hydrophobic outer surface. This ensured confined aqueous meniscus contact during SECCM experiments.[11]

A schematic illustrating the hopping SECCM method is shown in Figure 2.5a. Briefly, a dual barrel nanopipette filled with solution of interest and a QRCE (Pd-H_2 (HZ detection) and Ag/AgCl (Li_2O_2 scanning)) wire in each channel, functions as both a conductimetric cell and voltammetric cell. The nanopipette was approached towards the electrode surface until the meniscus just made contact (without contact from the nanopipette itself). The nanopipette was used to make a series of measurements by landing the capillary at a set of predefined locations. Electrolyte residues from the SECCM meniscus were visualized after experiments using FE-SEM to provide key information about the meniscus size and scanning location. The hopping distance between each pixel was 2 μm (HZ detection) and 3 μm (Li_2O_2 scanning) to avoid overlap of the probed areas, ~ 900 nm and ~ 2.5 μm in diameter, for HZ detection and Li_2O_2 scanning, respectively.

High precision control of the meniscus contact was achieved by applying a bias voltage (V_2) between the two QRCEs to produce a direct ion current (I_{IC}) across the meniscus. The nanopipette was oscillated perpendicular to the surface (267 Hz, 14 nm peak-to-peak amplitude for HZ detection and 276 Hz, 5 nm peak-to-peak amplitude for Li_2O_2 scanning) to induce an alternating component (AC) to the ion current between two barrels when the meniscus came into contact with the surface. 3 changes are detected upon meniscus contact with the electrode surface (Figure 2.5b): (1) development of an EC current originated from the substrate (I_{EC}), an increase in the (2) DC conductance current between the two channels and (3) AC component conductance current. I_{EC} describes surface activity of the electrode. An increase in the DC conductance current upon contact owing to an increase in meniscus size (wetting

effect) on the electrode surface and decrease of local resistance. A tip modulation scheme is used and the resulting AC signal at the generated oscillation frequency was detected using a lock-in amplifier (SR380, Stafford Research System). The reversible deformation of the liquid meniscus induced the changes in the AC ion current and it served as the feedback signal for positioning the nanopipette at a set distance from the electrode surface.[12]

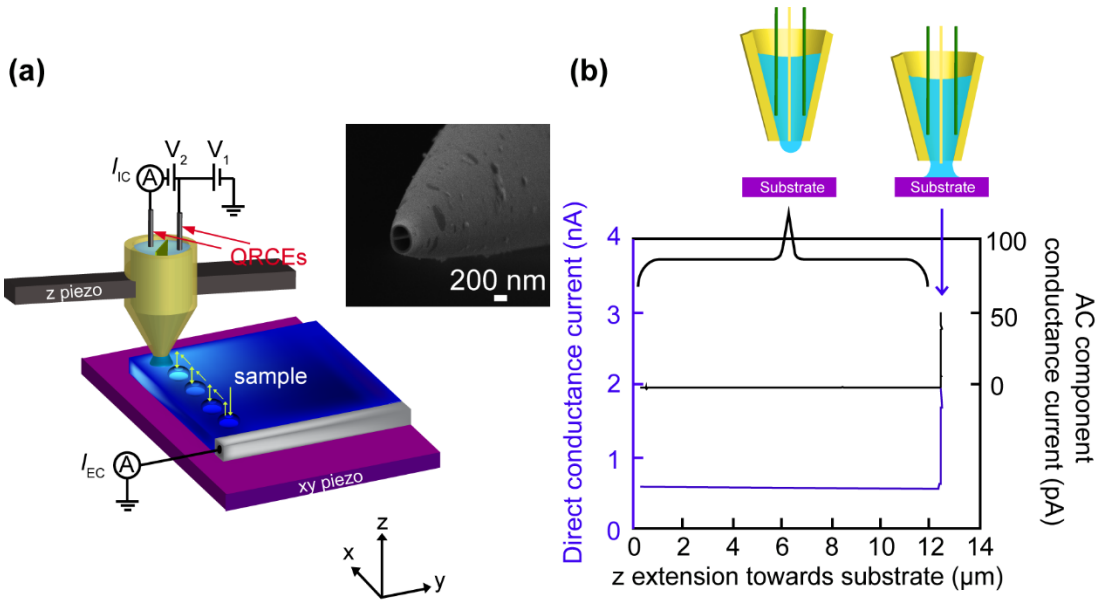

Figure 2.5 (a) Nanoscopic electrocatalytic measurement using voltammetric hopping mode SECCM. For SECCM, a bias voltage (V_2) was applied between two QRCEs and the resulting ion conductance current (I_{IC}) was measured and used for nanopipette positioning. A substrate voltage (V_1) was applied to one of the QRCEs to control the WE potential ($E_s = -(V_1 + V_2/2)$) and the WE current (I_{EC}) was measured. Small amount of residues were left after withdrawing the nanopipette from each position, which aided location identification by other techniques. The arrows show the movement of the nanopipette. (b) A typical SECCM approach curve showing the change in DC conductance current (blue) and the AC conductance current (black) as the nanopipette approaches and forms a meniscus on the substrate surface.

The WE potential (E_s) was $-(V_1 + V_2/2)$, against which all the I_{EC} were measured using a custom built, high-sensitivity, current-to-voltage converter. The voltammetric

scan rate was 0.5 V s^{-1} (HZ detection) and 1.0 V s^{-1} (Li_2O_2 scanning), applied at each point of meniscus contact, giving a spatial array of voltammograms. Data analysis was performed in Matlab (R2014b, Mathworks Inc.) to provide I_{EC} spatial maps over a set of potentials which could also be presented as movies.[11, 13]

2.8 Environmental scanning electrochemical cell microscopy

In the case environmental control[14-15] in Chapter 7 the experiments needed to be made without the interference of moisture. To achieve this, the sample and scanning probe were placed in a home-made environmental cell (polyether ether ketone) containing silica gel (Figure 2.6). The environmental cell incorporated a glass window on the top of the cover and on the sidewall for optical observation using both camera and light source. The cell was closed with finger clot, allowing the free movement of the nanopipette. Ar gas was flowed into the environmental cell and out through paraffin oil with constant bubbling. This procedure was used to remove moisture in the environmental cell. All SECCM imaging was performed after continuous Ar gas flow for at least an hour.

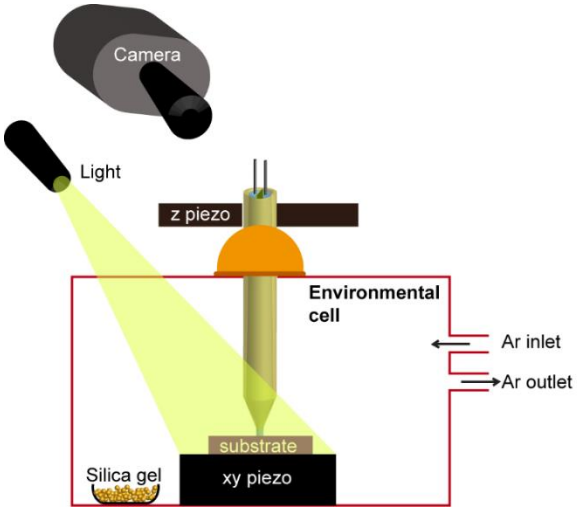

Figure 2.6 Schematic (not to scale) illustrating the home-made environmental chamber used in a SECCM setup. The red box represent the environmental cell made from polyether ether ketone. The chamber was continuously flushed with Ar gas and the excess gas was lead to the gas outlet through paraffin oil with constant bubbling. Silica gel was used to absorb moisture and keep the cell dry.

2.9 Characterization techniques

2.9.1 Optical microscopy

Optical microscopy was performed using an Olympus BH2 light microscope fitted with lenses in the magnification range ×5 to ×100.

2.9.2 Atomic force microscopy

AFM imaging was carried out in tapping mode (Innova, Veeco and Nano Enviroscope, Bruker) and Bruker MPP-21100-10 AFM tips were used. AFM image allows the determination of SWNT diameters and size/height of particles.

2.9.3 Field emission-scanning electron microscopy

Samples were characterized using FE-SEM (Zeiss Supra 55-VP) 1 kV (carbon electrodes) or 5 kV acceleration voltages (metal NPs). SWNT network density was determined using FE-SEM images (n = 3) with magnification of ×10000. These

images were cropped to leave only the image area followed by thresholding the images using the ImageJ software. The resulting binary image of SWNT networks was analyzed using in-house written software "Nanotube Analyzer" (courtesy of Anthony Holmes) to calculate the length of SWNT. The total length of nanotubes can be determined by calculating the principal axes of the CNTs in a skeletonize binary image and divided by the image area to give CNTs density ($\mu m_{SWNT}\ \mu m^{-2}$) value, as shown in Figure 2.7.

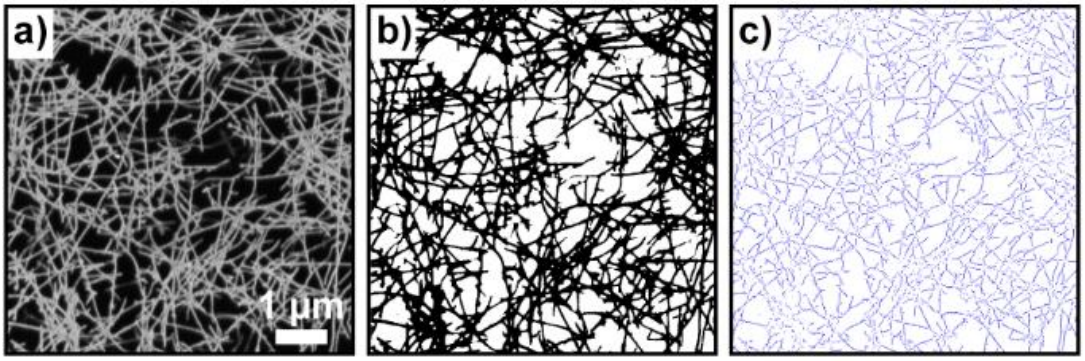

Figure 2.7 Calculating the density of a SWNT network using (a) FE-SEM images, (b) binary image produced by thresholding the original FE-SEM image and (c) skeletonize binary image using "Nanotube Analyzer" to determine of total nanotube length. The density of this LD SWNT sample was 4.7 $\mu m_{SWNT}\ \mu m^{-2}$.

2.9.4 High resolution-transmission electron microscopy (HR-TEM)

Crystalline formation of $Ni(OH)_2$ NPs in Chapter 6 was characterized by HR-TEM. For TEM sample preparation, $Ni(OH)_2$ NPs were mechanically scratched from the growth substrate using a blade and dispersed in absolute EtOH (Fisher Scientific) solution. The suspension underwent sonication for 4 minutes and centrifugation for 15 minutes (Eppendorf, 10 000 rpm) to cause particle sedimentation. A drop of solution (3 µL), containing the sedimented particles, was then placed onto a lacey carbon TEM

grid (Agar Scientific) and left until the EtOH had evaporated. HR-TEM was conducted (n = 3) using a JEM 2100 TEM (JEOL, LaB_6 filament, operated at 200 kV) equipped with energy-dispersive X-ray spectroscopy (EDS) and selected area electron diffraction (SAED) technique.

2.9.5 Micro-Raman microscopy

Micro-Raman spectra were recorded (Renishaw inVia Raman microscope; either a 633 nm HeNe or a 514.5 nm Ar laser, 10 mW, spot size of ~ 2.5 μm) with calibration against the Si peak (from the substrate) at 950 cm^{-1}.

2.10 References

1. Edgeworth, J. P.; Wilson, N. R.; Macpherson, J. V. Controlled Growth and Characterization of Two-Dimensional Single-Walled Carbon-Nanotube Networks for Electrical Applications. *Small* **2007**, *3*, 860-870.

2. Dudin, P. V.; Unwin, P. R.; Macpherson, J. V. Electrochemical Nucleation and Growth of Gold Nanoparticles on Single-Walled Carbon Nanotubes: New Mechanistic Insights. *J. Phys. Chem. C* **2010**, *114*, 13241-13248.

3. Dudin, P. V.; Unwin, P. R.; Macpherson, J. V. Electro-Oxidation of Hydrazine at Gold Nanoparticle Functionalised Single Walled Carbon Nanotube Network Ultramicroelectrodes. *Phys. Chem. Chem. Phys.* **2011**, *13*, 17146-17152.

4. Dumitrescu, I.; Wilson, N. R.; Macpherson, J. V. Functionalizing Single-Walled Carbon Nanotube Networks: Effect on Electrical and Electrochemical Properties. *J. Phys. Chem. C* **2007**, *111*, 12944-12953.

5. Marshall, M. W.; Popa, N. S.; Shapter, J. G. Measurement of Functionalised Carbon Nanotube Carboxylic Acid Groups Using a Simple Chemical Process. *Carbon* **2006**, *44*, 1137-1141.

6. Azamian, B. R.; Coleman, K. S.; Davis, J. J.; Hanson, N.; Green, M. L. H. Directly Observed Covalent Coupling of Quantum Dots to Single-Wall Carbon Nanotubes. *Chem. Commun.* **2002**, *4*, 366-367.

7. Bertoncello, P.; Edgeworth, J. P.; Macpherson, J. V.; Unwin, P. R. Trace Level Cyclic Voltammetry Facilitated by Single-Walled Carbon Nanotube Network Electrodes. *J. Am. Chem. Soc.* **2007**, *129*, 10982-10983.

8. Zhang, G.; Cuharuc, A. S.; Güell, A. G.; Unwin, P. R. Electrochemistry at Highly Oriented Pyrolytic Graphite (HOPG): Lower Limit for the Kinetics of Outer-Sphere Redox Processes and General Implications for Electron Transfer Models. *Phys. Chem. Chem. Phys.* **2015**, *17*, 11827-11838.

9. Cuharuc, A. S.; Zhang, G.; Unwin, P. R. Electrochemistry of Ferrocene Derivatives on Highly Oriented Pyrolytic Graphite (HOPG): Quantification and Impacts of Surface Adsorption. *Phys. Chem. Chem. Phys.* **2016**, *18*, 4966-4977.

10. Day, T. M.; Unwin, P. R.; Macpherson, J. V. Factors Controlling the Electrodeposition of Metal Nanoparticles on Pristine Single Walled Carbon Nanotubes. *Nano Lett.* **2007**, *7*, 51-57.

11. Ebejer, N.; Güell, A. G.; Lai, S. C. S.; McKelvey, K.; Snowden, M. E.; Unwin, P. R. Scanning Electrochemical Cell Microscopy: A Versatile Technique for Nanoscale Electrochemistry and Functional Imaging. *Annu. Rev. Anal. Chem.* **2013**, *6*, 329-351.

12. Snowden, M. E.; Güell, A. G.; Lai, S. C. S.; McKelvey, K.; Ebejer, N.; O'Connell, M. A.; Colburn, A. W.; Unwin, P. R. Scanning Electrochemical Cell Microscopy: Theory and Experiment for Quantitative High Resolution Spatially-Resolved Voltammetry and Simultaneous Ion-Conductance Measurements. *Anal. Chem.* **2012**, *84*, 2483-2491.

13. Ebejer, N.; Schnippering, M.; Colburn, A. W.; Edwards, M. A.; Unwin, P. R. Localized High Resolution Electrochemistry and Multifunctional Imaging: Scanning Electrochemical Cell Microscopy. *Anal. Chem.* **2010**, *82*, 9141-9145.

14. Aaronson, B. D. B.; Garoz-Ruiz, J.; Byers, J. C.; Colina, A.; Unwin, P. R. Electrodeposition and Screening of Photoelectrochemical Activity in Conjugated Polymers Using Scanning Electrochemical Cell Microscopy. *Langmuir* **2015**, *31*, 12814-12822.

15. Chen, C.-H.; Jacobse, L.; McKelvey, K.; Lai, S. C. S.; Koper, M. T. M.; Unwin, P. R. Voltammetric Scanning Electrochemical Cell Microscopy: Dynamic Imaging of Hydrazine Electro-Oxidation on Platinum Electrodes. *Anal. Chem.* **2015**, *87*, 5782-5789.

Chapter 3 Controlled functionalization of single-walled carbon nanotube network electrodes for the enhanced voltammetric detection of dopamine

Voltammetric studies of dopamine (DA) oxidation on pristine and acid-treated single-walled carbon nanotube (SWNT) network electrodes are undertaken in order to investigate both the effect of network density and acid treatment times on the voltammetric characteristics for DA oxidation and the susceptibility of the electrodes to fouling. Through careful control of catalyzed chemical vapour deposition growth parameters, multiply interconnected and randomly oriented SWNT networks of two significantly different densities are grown (high density, HD, coverage >>10 μm length of SWNT per μm^2 and low density, LD, coverage = 5 (±1) $\mu m_{SWNT}\ \mu m^{-2}$). Acid treatment is performed to provide materials with different electrochemical (EC) properties and SWNT coverage, as determined by field emission-scanning electron microscopy, atomic force microscopy and micro-Raman spectroscopy. A high concentration of DA (100 μM) is deliberately employed to accelerate the fouling phenomenon associated with DA oxidation in order to evaluate the lifetime of the electrodes. HD pristine SWNT networks are found to promote more facile electron transfer (ET) and are less susceptible to blocking, compared to LD pristine SWNT networks. Acid treatment results in both a further enhancement of the ET rate and a reduction in susceptibility towards electrode fouling. However, lengthy acid treatment detrimentally affects ET, due to a decrease in network density and significant damage

to the SWNT network structure. These studies highlight the subtle interplay between SWNT coverage and degree of acid functionalization when seeking to achieve the optimal SWNT electrode for the voltammetric detection of DA.

3.1 Introduction

Dopamine (DA) is one of the most important catecholamine neurotransmitters in the human central nervous system and is widely studied in clinical research.[1, 2] Abnormal levels of DA can be an indicator of a neurological disorder; insufficient DA may be linked to a loss of neurons and can indicate Parkinson's disease, whereas schizophrenia is associated with elevated levels of DA in the prefrontal cortex.[2-4] The concentration of DA in the extracellular fluid of the caudate nucleus, which is involved in motor processes, is *ca*. 0.01 – 1 µM for a healthy person and in the nM range for a person with Parkinson's disease.[5]

The early detection of abnormal DA concentration is critical and there has been significant investment in finding effective measurement methods at the levels required. Electrochemistry represents a very effective measurement methodology owing to the low cost, simplicity, short measurement time and high sensitivity.[6] DA can be oxidized to dopamine-*o*-quinone, allowing the use of traditional electrochemical (EC) techniques for detection.[2, 7] However, the redox inactive decomposition products of DA oxidation, leucodopaminechrome and 5,6-dihydroxyindole, are known to adsorb on traditional metal or carbon electrodes, including electrodes formed from carbon nanotubes (CNTs),[8, 9] forming an insulating layer and leading to reduced stability and sensitivity. Electrode fouling will eventually lead to significant inhibition of electron transfer (ET) at the electrode surface.[10-12] The

density of CNTs on the electrode surface has also been shown to play a role in the extent of electrode fouling.[13]

CNTs are a useful electrode material due to various promising physical[14] and chemical[15] properties, which include chemical stability,[16] biocompatibility,[14] low background currents,[17] good intrinsic electrical conductivity[18] and nanoscopic dimensions.[19] These properties make them promising for a wide range of applications in electrochemistry[15, 20, 21] and electroanalysis.[22] The use of CNTs as an electrode material in biological applications has attracted significant interest, particularly for the EC detection of neurotransmitters.[2, 10, 23-26] The EC detection of norepinephrine,[27] epinephrine,[28] serotonin,[10] and DA[10, 26, 29] have been reported. However, many of the aforementioned studies employed unpurified, as-grown CNTs synthesized using arc discharge, meaning that they were heavily contaminated with amorphous carbon[14] and metal nanoparticles (NPs).[30] The presence of these impurities has been shown to contribute to the EC behaviour of the CNT electrodes.[14]

CNT electrodes are often prepared by randomly dispersing CNTs onto a conducting electrode either by spin-coating or drop casting.[31, 32] There are a number of limitations associated with these CNT electrodes, including uneven CNT coverage[33] and EC influence from the supporting substrate.[34] In contrast, the direct growth of single-walled CNTs (SWNTs) on *insulating substrates* using catalyzed chemical vapour deposition (cCVD) allows the use of SWNTs as an electrode without the influence of the underlying substrate.[19] SWNTs grown using this method have also been shown to have a low defect density,[35] negligible amorphous carbon content and to be relatively free of catalytic NPs.[36]

The deliberate introduction of defects into CNTs may positively influence the EC response towards "inner sphere" electrode reactions, for example, defects may create adsorption sites.[36, 37] Covalent functionalization of SWNTs is a viable approach towards defect creation,[38-41] serving to change the surface hybridization from sp^2 to sp^3,[36] with the formation of surface functional groups such as carboxylic acids and alcohols.[41] For inner sphere DA oxidation, these groups have been postulated to act as catalytic sites,[36, 42] which enhance DA adsorption, as DA is protonated (*i.e*. positively charged) at physiological pH.[24] One simple method for creating defects in SWNTs is acid treatment, however the question as to the extent of acid treatment in relation to the density required for optimal EC performance has not yet been fully addressed. In this work we investigate the effect of nitric acid treatment on both high density (HD) and low density (LD) SWNT network electrodes towards DA oxidation.

To negate the use of lithographic processing procedures, which can leave residue on the surface and therefore block potential sites for ET,[19] a micro-capillary EC method (MCEM),[43, 44] is employed. Here, the EC cell is formed by simply landing the meniscus of a solution-filled micro-capillary on the SWNT network electrode. This method allows multiple measurements to be made on the same surface in a combinatorial approach, simply by re-landing the capillary at different locations. This is extremely beneficial when investigating a redox process which may foul an electrode surface, especially when the electrode surface is not amenable to conventional electrode polishing in order to re-clean the surface, common with disposable-type electrodes. Here, the electrode can be refreshed simply by repositioning the capillary in a new spot on the substrate. By using this method we are

able to investigate in detail the effect of SWNT density and level of SWNT functionalization on DA electro-oxidation.

3.2 Experimental

3.2.1 Single-walled carbon nanotube network growth

SWNT networks were grown on 2 cm × 2 cm Si/SiO_2 substrates (IDB Technologies Ltd., n-type, 525 µm thick with 300 nm of thermally grown SiO_2 on both sides) using cCVD. Fe^{15} and Co^{45} NPs were used as catalysts for the growth of LD and HD SWNT networks, respectively. Fe NPs were deposited by soaking the substrate in 1:100, ferritin (50 – 150 mg mL^{-1}, Aldrich) aqueous solution for 1 hour, followed by 2 min exposure to 100 W oxygen plasma (Emitech K1050X plasma asher). Co was deposited by sputtering (SC7640 sputter coater, Quorum Technologies Ltd., UK) at 1 kV for 20 s.

The cCVD procedure began with the substrate being heated from room temperature to 850 ^oC in 14 min under H_2 (BOC Gases, 99.95 %) atmosphere at a flow rate of 150 sccm, followed by stabilization at 850 ^oC for 1 min. The growth of SWNT networks was initiated by bubbling Argon (Ar, BOC Gases, 99.9995 %) (850 sccm) through ethanol (EtOH) (Fisher, 99.99 %) held at 0 ^oC. Growth was carried out for 20 min. The system was allowed to cool under H_2 only.

3.2.2 Functionalization of single-walled carbon nanotube networks

SWNT networks were treated with 3 M HNO_3 (70 %, Fisher) heated to 70 ^oC for 20, 120, 300 and 600 min. After removal from solution, the substrates were rinsed with distilled water and dried under N_2 gas before use. These medium strength acid treatments were employed to enable good control over the acid etching of SWNT networks and to avoid etching of the insulating substrate[36] compared to strong acid treatments[33] (concentrated H_2SO_4/HNO_3) which are typically employed to purify as-grown nanotubes. A similar medium acid treatment has been shown previously to oxidatively attack SWNTs.[46]

3.2.3 Single-walled carbon nanotube networks characterization

SWNT networks were characterized using both field emission-scanning electron microscopy (FE-SEM, Zeiss Supra 55-VP, 1 kV acceleration voltage) and atomic force microscopy (AFM, tapping mode, Bruker-Nano Enviroscope). Micro-Raman spectra were recorded (Renishaw inVia Raman microscope; 514.5 nm Ar laser, 10 mW) with calibration against the Si peak (from the substrate) at 950 cm^{-1}. For each electrode and after different treatments, three representative FE-SEM, AFM and micro-Raman measurements (n = 3) were recorded.

3.2.4 Single-walled carbon nanotube electrode fabrication and micro-capillary electrochemical method setup

Electrical contact to the SWNT networks was achieved by evaporating Cr (3 nm) followed by Au (60 nm) through a shadow mask on the side of the Si/SiO_2 substrate using a Moorfield MiniLab deposition system (Moorfield Associates). Contact to the Au band was made *via* a Au pin. Neither came into contact with solution (Figure 3.1). To perform MCEM measurements, SWNT networks were mounted inside a humidity cell (de-aerated with N_2) and connected as a working electrode. The MCEM cell was formed from a borosilicate glass capillary (1.2 mm outer diameter, 0.69 mm internal diameter, Harvard Apparatus Ltd.), pulled to a small opening using a laser pipet puller (P-2000, Sutter Instrument Co.). The end was polished flat with an inner diameter of 50 µm (for DA detection) and 70 µm (for ferrocenylmethyltrimethylammonium ($FcTMA^+$) oxidation) and rendered hydrophobic through immersion in dichlorodimethylsilane (Fisher, ≥99 %) for 90 s, with Ar gas flowing through to prevent any internal silanization. Next, the capillary was filled with the aqueous solution of interest and fitted with a AgCl-coated Ag wire quasi-reference/counter electrode (QRCE). The capillary was mounted on an *x-y-z* micropositioner (Newport 433 series) above the SWNT network substrate. With the aid of a camera (PixeLINK PL-B776U) the capillary was moved so that the meniscus landed on the SWNT network, without the capillary itself making contact to the electrode surface. EC measurements were made in the 2-electrode arrangement using a CH Instruments (Austin, TX; model 730A) potentiostat.

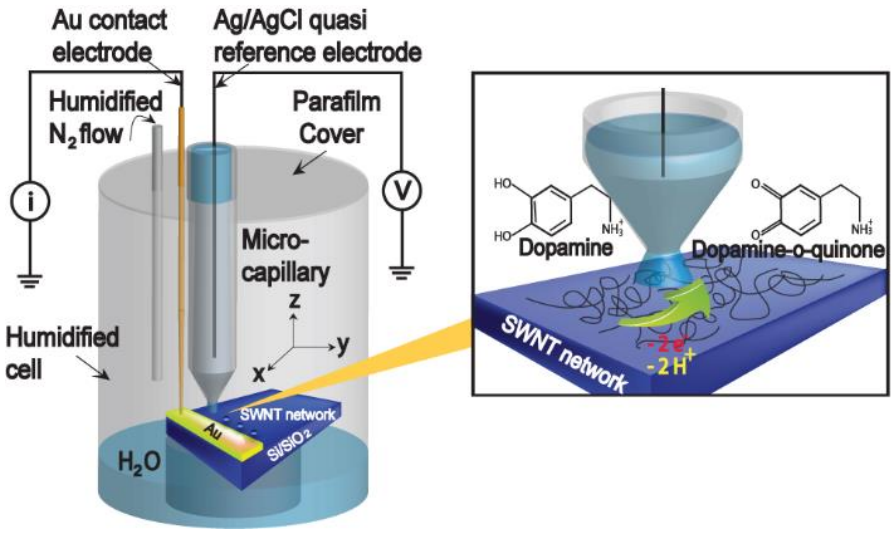

Figure 3.1 Schematic of the experimental setup for the electro-oxidation of DA.

3.2.5 Chemicals and solutions

All chemicals were used as received. Aqueous solutions were prepared using deionized water (resistivity of 18.2 MΩ cm at 25 °C). $FcTMA^+$ hexafluorophosphate was prepared in-house *via* metathesis of ferrocenylmethyltrimethylammonium iodide (Strem Chemical Co., 99 %) and silver hexafluorophosphate, $AgPF_6$ (Strem Chemical Co., 99.5 %). Potassium nitrate, KNO_3 (99 %) was purchased from Fisher. Dopamine hydrochloride was prepared in 0.01 M phosphate buffer aqueous solution (pH 7.4) and the pH was adjusted to 7.0 by adding 0.01 M citric acid (99.5 %, Sigma-Aldrich).[36] 100 µM DA was used throughout the experiments, as we were particularly interested in investigating potential blocking and/or fouling effects and this provides a reasonable concentration where such effects are 'accelerated'.[2, 47]

3.3 Results and discussion

3.3.1 Growth, functionalization and characterization of low density and high density single-walled carbon nanotube networks

Depending on their structure, SWNTs can be either metallic (mSWNT) or semiconducting (sSWNT).[48] In a randomly grown SWNT network, the ratio of mSWNTs to sSWNTs is approximately 1:3.[14] Hence, increasing the SWNT network density will change the electrical nature of the network resulting from increasing the number of mSWNT-mSWNT contacts. For all EC studies the as-grown (pristine) SWNT network density was above the metallic percolation threshold.[36]

The FE-SEM and AFM images shown in Figure 3.2a (i) and (ii), respectively, are of a typical pristine LD SWNT network; density in the range 4 – 6 $\mu m_{SWNT}\ \mu m^{-2}$. Similarly the FE-SEM and AFM images shown in Figure 3.2b (i) and (ii), respectively, are of a pristine HD SWNT network which has a density of >>10 $\mu m_{SWNT}\ \mu m^{-2}$. It is difficult to determine the precise density as there are many SWNT bundles (evidenced by the apparent thicker widths in the AFM image) and several SWNT layers. Note that the SWNTs appear much broader in the FE-SEM images due to charging effects. Both networks have a connectivity much greater than the metallic percolation threshold ($\rho_{th(\text{metallic})}$), since $\rho_{th(\text{metallic})}$ is 1.4 – 2.4 $\mu m_{SWNT}\ \mu m^{-2}$ (based on typical SWNTs lengths, l, of 7 – 12 μm) and calculated from:[49]

$$\rho_{th(\text{metallic})} = 3\left[\frac{17.94}{l\pi}\right] \quad (1)$$

Figure 3.2c shows representative micro-Raman spectra of both HD and LD SWNT networks. The intensity of each spectrum was normalized with respect to the Si/SiO_2 peak at 950 cm^{-1}. The peaks marked with an (*) at 303 cm^{-1}, 521 cm^{-1} and 950 cm^{-1} originate from the Si/SiO_2 substrate and provided a useful reference against which other peak intensities could be compared. In both spectra, the *G*-band (1565-1595 cm^{-1}) indicative of sp^2 carbon is clearly evident, containing a peak at 1595 cm^{-1} (G_p) and a shoulder, on the left-hand side, at 1574 cm^{-1}, due to mSWNT contributions.[50, 51] There are also radial breathing modes[52] (100 to 350 cm^{-1}) present which also confirm that the networks consist of SWNTs. The HD SWNT network gave a higher relative intensity of the *G*-band due to the increased number of SWNTs in resonance with the Raman laser excitation.[52]

The *D*-peak at 1350 cm^{-1} refers to defects in breaking up the symmetry of the carbon lattice, originating from sp^3 carbon at defects or in amorphous carbon deposits breaks;[53,54] the intensity difference of the *G*-peak to that of the *D*-peak is often used as an indicator of the quality of SWNTs.[55] G_p was *ca*. 30 times the intensity of the *D*-peak for the HD SWNT networks and 40 times the intensity for the LD SWNT networks, showing that in both cases the as-grown pristine SWNTs were extremely clean and had low intrinsic defect densities and/or amorphous carbon content.

Representative FE-SEM and AFM images of LD and HD SWNT networks after exposure to 3 M HNO_3 at 70 ^oC for 20, 120, 300 and 600 min are shown in Figure 3.3 and Figure 3.4, respectively. It is clear from these images that the acid treatment acts to cut and shorten the SWNTs within the network, in line with previous reports where acid treatment has been shown to open tube ends,[14] and cut SWNTs.[39] The LD SWNT network density (Figure 3.3) decreases from 4 – 6 μm_{SWNT} μm^{-2} for the pristine sample to (i) 3.8 – 5.2 μm_{SWNT} μm^{-2} after 20 min acid treatment, with further decreases to (ii)

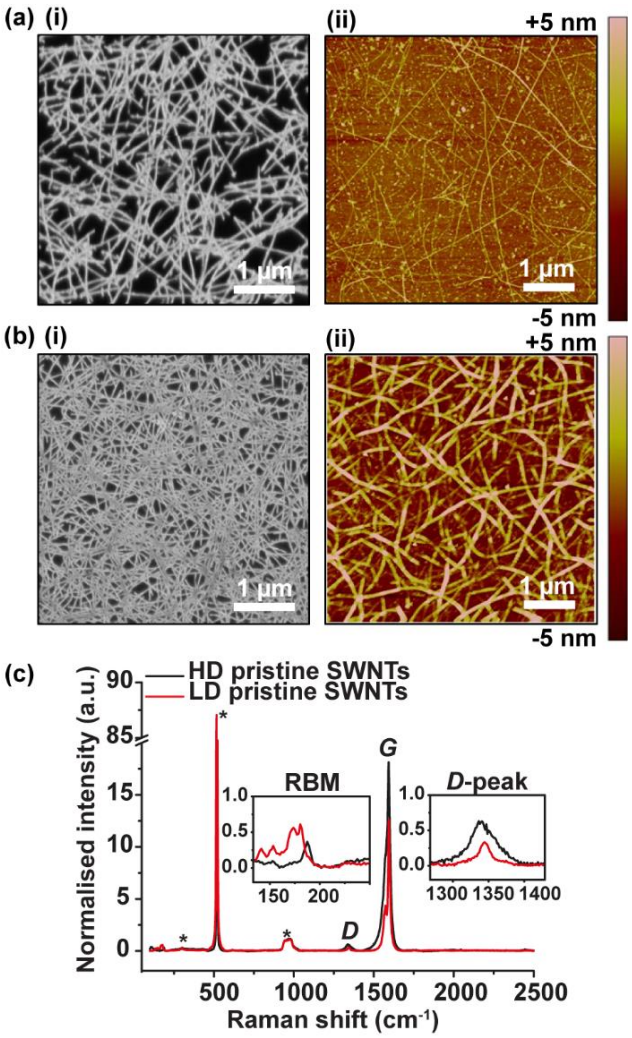

Figure 3.2 Typical (i) FE-SEM and (ii) AFM images of (a) LD and (b) HD SWNT networks. (c) Corresponding micro-Raman spectra of LD (red) and HD (black) SWNT networks normalised to the Si/SiO_2 peak at 950 cm^{-1}.

3.7 – 4.7 μm_{SWNT} μm^{-2}, (iii) 3.3 – 4.3 μm_{SWNT} μm^{-2} and (iv) 2.3 – 3.3 μm_{SWNT} μm^{-2} after 120 min, 300 min and 600 min acid treatment, respectively.

It is important to note that as the length of SWNTs in the network becomes reduced, $\rho_{th(metallic)}$ is significantly increased. For example, from equation (1), $\rho_{th(metallic)}$ is calculated to be 1.7 μm_{SWNT} μm^{-2} when l = 10 μm, increasing to 8.6 μm_{SWNT} μm^{-2} when l = 2 μm. After 600 min acid treatment, the mean SWNT length in the LD SWNT networks had decreased to 1 – 4 μm (2.3 – 3.3 μm_{SWNT} μm^{-2}), meaning that the network density is now below $\rho_{th(metallic)}$ (4 – 17 μm_{SWNT} μm^{-2}), greatly jeopardizing the ability of this material to function as an electrode material.[56] This highlights that functionalization must be carefully undertaken, with due attention to the impact on the electronic properties of the SWNT network electrode.

The acid-treated HD SWNT networks (Figure 3.4) show the same trend of reduced density with increasing acid treatment time as observed for the LD samples. Again, it can be seen how the SWNT network is acid etched, in particular in the AFM

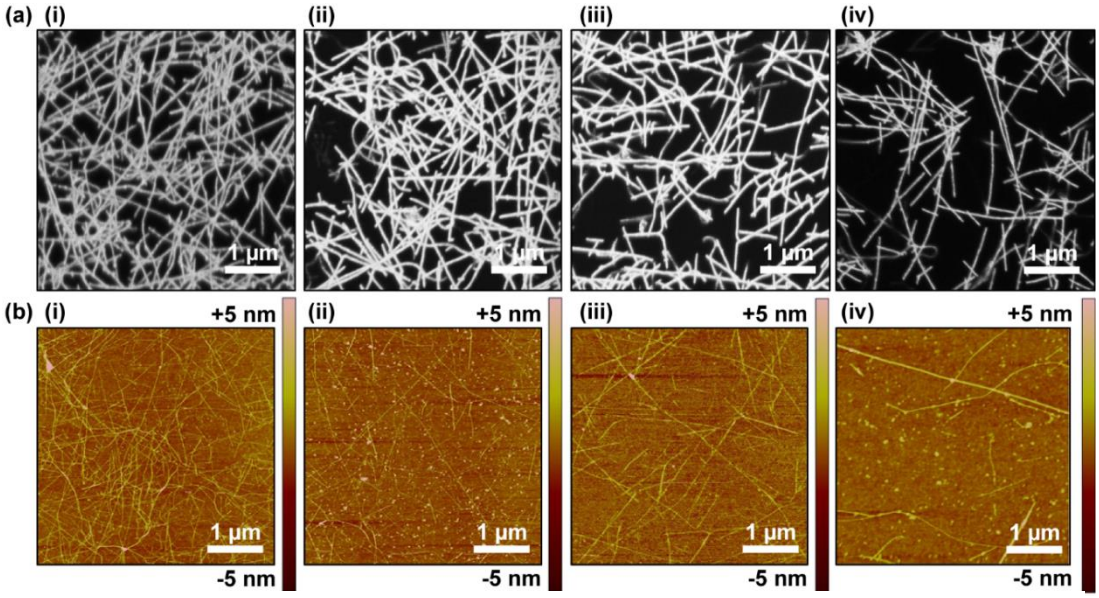

Figure 3.3 Typical (a) FE-SEM and (b) AFM images of LD SWNT networks after (i) 20 min, (ii) 120 min, (iii) 300 min and (iv) 600 min treatment with 3 M HNO_3 at 70 °C.

images in Figure 3.4b, where it is evident that SWNTs have been cut into smaller fragments. Importantly, as the network density was significantly higher than the LD SWNT networks, even after lengthy 600 min acid treatments the network density remained reasonable, in the range 5.5 – 6.5 μm_{SWNT} μm^{-2} (Figure 3.4b (iv)).

Typical micro-Raman spectra of HD and LD SWNT networks after different acid treatment times, focusing on the *D*- and *G*-bands, are shown in Figure 3.5(a) and (b), respectively. The spectra in Figures 3.5a-c were normalized with respect to the intensity of Si at 950 cm^{-1}. To highlight relative changes in *G*-band intensity, the intensity of the *G*-band *vs.* acid treatment time is plotted as $i_{G\mathrm{p}\,(t)}/i_{G\mathrm{p}\,(\mathrm{pristine})}$ (Figure 3.5c (i)), where *t* is the acid treatment time. The intensity of G_p, which is also indicative of SWNT network density (Figure 3.2c), shows a decreasing $i_{G\mathrm{p}\,(t)}/i_{G\mathrm{p}\,(\mathrm{pristine})}$ signal with time, for both low and high density networks, as expected based on Figures 3.3 and 3.4. Specifically, for the HD sample, the intensity of G_p (Figure 3.5c (i)) decreases to 96 %, 83 %, 78 % and 72 % relative to the $G_{p\,(\mathrm{pristine})}$ intensity after 20, 120, 300 and

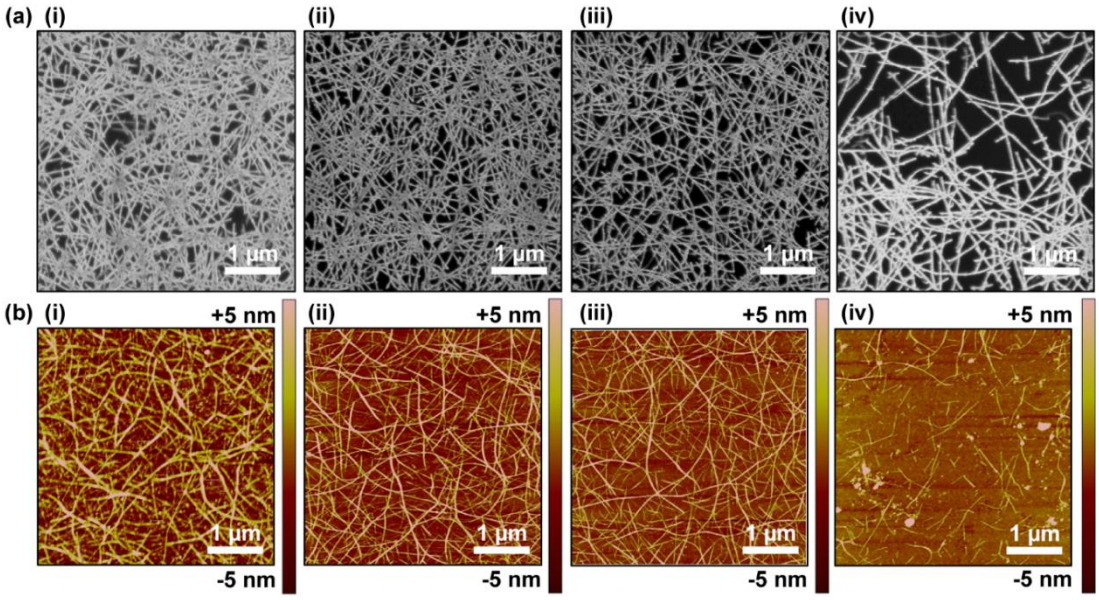

Figure 3.4 Typical (a) FE-SEM and (b) AFM images of HD SWNT networks after (i) 20 min, (ii) 120 min, (iii) 300 min and (iv) 600 min treatment with 3 M HNO_3 at 70 °C.

600 min acid treatment, respectively. The same scenario is apparent for LD SWNT samples, but with more severe changes in the intensity of G_p, which reduces to 83 %, 61 %, 40 % and 18 % of $G_{p\ (pristine)}$, after 20, 120, 300 and 600 min acid treatment, respectively.

The intensity of the *D* peak with respect to i_{Gp} *i.e.* (i_D /i_{Gp}) is used for the evaluation of the defect density in SWNT networks.[57] The spectra were normalized to the G_p peak at 1595 cm^{-1} (Figures 3.5c (ii)) so that relative changes in *D*-band intensities were easily observed. It is apparent that the intensity of i_D/i_{Gp} in Figure 3.5c (ii) increases with acid treatment time for both LD and HD SWNT networks as more defects are added to the SWNTs, during the etching and shortening of the SWNTs.

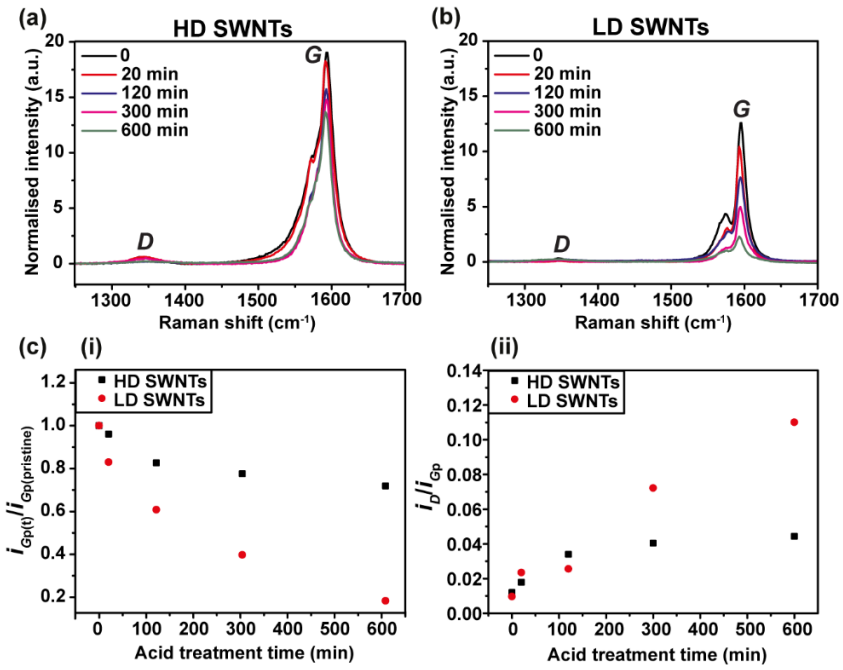

Figure 3.5 Typical micro-Raman spectra of (a) HD and (b) LD SWNT networks before and after acid treatment, in 3 M HNO_3 at 70 °C for different times. (c) Effect of acid treatment time on (i) SWNT network density as expressed in the $i_{Gp\ (t)}/i_{Gp\ (pristine)}$ ratio and (ii) defect density as expressed in the i_D /i_{Gp} ratio for HD SWNT networks (black) and LD SWNT networks (red).

3.3.2 $FcTMA^+$ oxidation

Before investigating the effect of SWNT network density and acid treatment on the oxidation of DA, preliminary studies were carried out using the one-electron outer sphere redox mediator (1 mM) $FcTMA^+$ in 100 mM KNO_3. The response of this mediator is unaffected by chemical changes to the surface of the SWNT.[37]

Figure 3.6 shows cyclic voltammograms (CVs) for $FcTMA^+$ oxidation at (a) HD and (b) LD pristine SWNT networks before and after acid treatment with 3M HNO_3 at 70 ^oC for 20, 120, 300 and 600 min. All CVs for HD SWNT networks displayed fast ET with ΔE_p in the range 59 mV to 63 mV and peak currents (i_p) close to those expected for the oxidation of 1 mM $FcTMA^+$ at a planar disk electrode, as predicted by the Randles-Sevcik equation.[58] LD pristine SWNT networks after short acid treatment (20 min, 120 min and 300 min) also showed fast ET with ΔE_p of 59 mV, 64 mV and 70 mV. These data are consistent with previous studies employing outer sphere redox couples, where SWNTs have been shown to support fast ET.[16, 19, 59-61] However, longer acid treatment of LD SWNT networks showed increased values of ΔE_p to 100 mV after 600 min acid treatment. The treatment lengths are sufficient to reduce the network density below the metallic percolation threshold, most likely resulting in an increased network resistance which produces ohmic drop effects in the CV response.

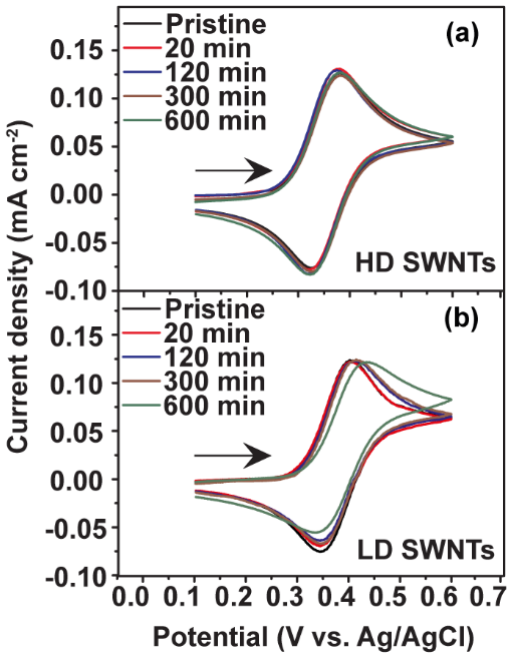

Figure 3.6 Typical CVs for the oxidation of 1 mM $FcTMA^+$ in 100 mM KNO_3 (50 mV s^{-1}) at (a) HD and (b) LD pristine SWNT networks and after 20 min, 120 min, 300 min, 600 min acid treatment in 3 M HNO_3 at 70 °C.

The data confirms that in all acid-treated cases of HD SWNT networks, the SWNT density is sufficiently high to achieve diffusional overlap between neighbouring SWNTs, with the electrode acting like a homogenous disk electrode with an equivalent geometry.[58, 62] It is also notable that for HD SWNT networks even after the 600 min acid exposure, the SWNT network has not become prohibitively resistive, despite the significant cutting of SWNTs.

3.3.3 Dopamine detection

Figure 3.7 shows the first cycle of a CV for the oxidation of 100 μM DA in 0.01 M citric acid pH 7.0 phosphate buffer at both HD and LD pristine SWNT networks. It is immediately apparent that the redox behaviour of DA is different on the SWNT networks of different densities, with the response on the HD SWNT networks showing

a peak to peak separation (ΔE_p) of 508 ± 6 mV while the value of the LD SWNT networks is 591 ± 4 mV. This could be due to the higher surface coverage of the HD SWNT networks providing more sites for reaction and/or the lower DA flux per SWNT length, also leading to less potential blocking.

Short time scale acid treatment, for 20 min, leads to a significant decrease in the overpotential for DA oxidation by 140 mV for HD SWNT networks (ΔE_p = 368 mV) and by 100 mV for LD SWNT networks (ΔE_p = 491 mV). This means that the intrinsic ET kinetics (per unit length of SWNT) is more facile. This behaviour is attributed to acid treatment opening the end of the SWNTs and introducing functional groups, such as carboxylic acid,[33, 41] into the sidewall and at the ends of the opened SWNTs. These groups on the modified surface serve as potential sites for DA adsorption,[36, 42, 62] leading to enhanced overall apparent ET kinetics. It is also important to point out, however, that the apparently fast kinetics could be due to less susceptibility to blocking reactions, an aspect that we consider below.

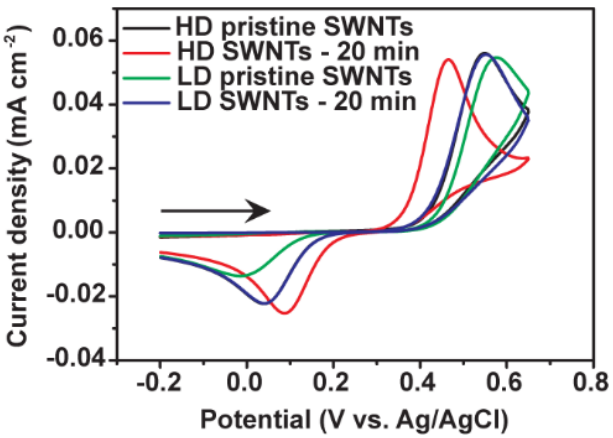

Figure 3.7 CVs for the oxidation of 100 µM DA in 0.01 M citric acid pH 7.0 phosphate buffer (100 mV s^{-1}) at HD (black) and LD (green) pristine SWNT networks and after 20 min acid treatment on HD (red) and LD (blue) SWNT networks.

As it is well-known that DA oxidation can lead to rapid fouling and blocking of the electrode surface, the extent of fouling on both HD and LD SWNT network electrodes was investigated by recording ten consecutive CVs as shown in Figure 3.8a and b, respectively. It is obvious from Figure 3.8b that the LD SWNT networks appear to be more susceptible to fouling than the HD SWNT networks (Figure 3.8a), with a drop in the oxidative peak current, i_p by 20 % after ten CVs for the LD SWNT networks compared to an 8 % drop for the HD SWNT networks. However, after just 20 min acid treatment, i_p falls by only 8.3 % for the LD SWNT networks (Figure 3.8d) and 6.5 % for the HD SWNT networks (Figure 3.8c), both after ten CV cycles.

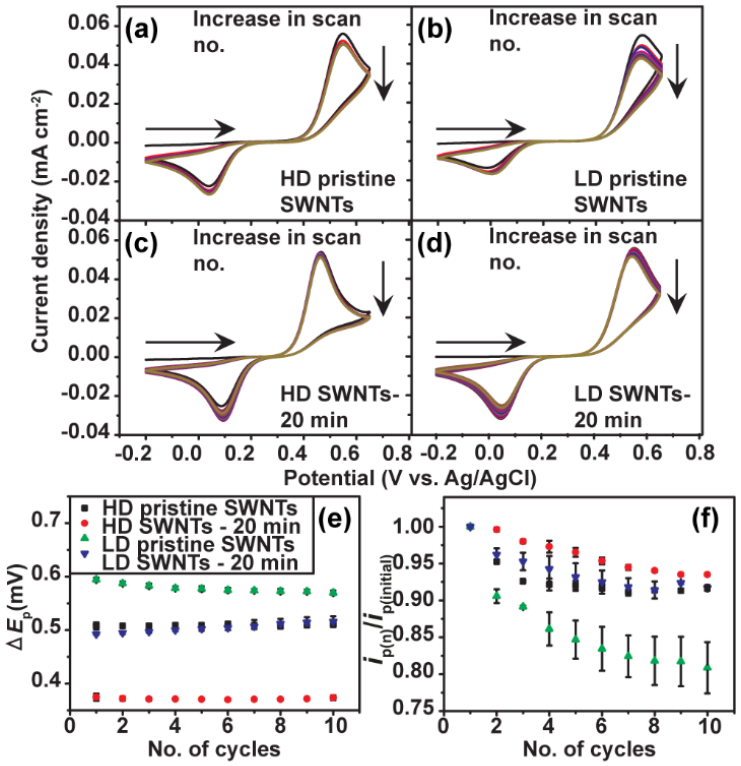

Figure 3.8 Ten consecutive CVs, recorded at a scan rate of 100 mV s^{-1}, for the oxidation of 100 µM DA in 0.01 M citric acid pH 7.0 phosphate buffer at (a) HD and (b) LD pristine SWNT networks and 20 min acid-treated (c) HD and (d) LD SWNT network electrodes. Plot of (e) ΔE_p versus number of cycles (n = 3) and (f) $i_{p(n)}/i_{p(initial)}$ versus number of cycles (n = 3): HD (black) and LD (green) pristine SWNT networks, 20 min acid treatment on HD (red) and LD (blue) SWNT networks.

Summary data of ΔE_p and i_p normalized by the initial scan are shown in Figure 3.8e and f (extracted from the data in Figure 3.8a, b, c and d), where $i_{p(n)}$ is the peak current per cycle number and "initial" indicates the first cycle.

It is apparent from the above studies that HD SWNT networks are superior for the detection of DA, showing faster apparent ET and little decrease in electrode performance, even after several cycles. These data also provide a reliable baseline, from which the effect of acid treatment on DA oxidation can be extracted. Based on these finding, we did not study further LD acid-treated SWNT networks but instead investigated the effect of acid treatment time on the DA EC response of HD SWNT networks.

Figure 3.9a shows CVs for the oxidation of 100 µM DA at acid-treated (3 M HNO_3, 70 ^oC) for 120, 300 and 600 min HD SWNT network electrodes, to see whether the performance towards DA detection could be optimized further. Three measurements were recorded for each experiment. 120 min acid-treated HD SWNT networks showed an even smaller ΔE_p of 353 ± 4 mV compared to pristine and 20 min acid treatment (Figure 3.7). However, after longer acid treatments, ΔE_p for DA oxidation increased, reaching 470 ± 12 mV and 598 ± 12 mV after 300 min and 600 min, respectively.

The studies with $FcTMA^+$ indicate that this is not due to the network increasing significantly in resistance. Rather, it indicates that there is an optimal balance required, trading off the creation of defects (functionalization) of SWNTs which enhances the ET kinetics (and/or serves to inhibit blocking side-reactions), with the loss of active

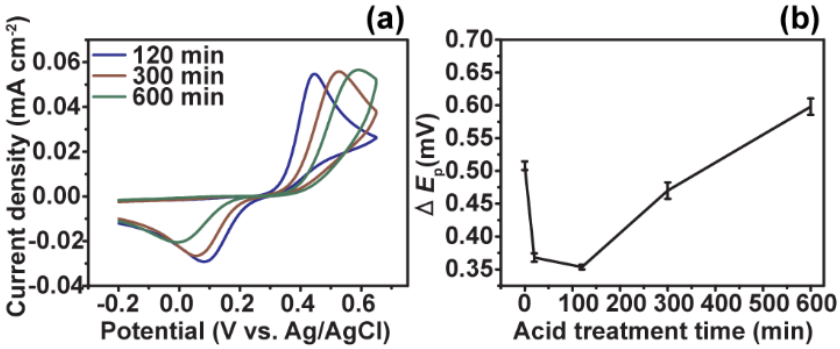

Figure 3.9 (a) CVs for the oxidation of 100 µM DA, recorded at a scan rate of 100 mV s^{-1}, in 0.01 M citric acid pH 7.0 phosphate buffer (100 mV s^{-1}) at HD SWNT networks after acid treatment for 120 min (blue), 300 min (brown) and 600 min (green) with 3 M HNO_3 at 70 °C; (b) plot of ΔE_p versus acid treatment times (n = 3).

electrode material by etching, which reduces the overall fraction of active electrode area, placing stronger kinetic demands on the remaining material.

Figure 3.10a, b and c show repeat cycling CVs (ten cycles) for DA oxidation on HD SWNT networks treated with acid for times in the range 120 min to 600 min. Figure 3.10d shows summary data for ΔE_p as a function of treatment time and number of CV cycles. It can be seen that ΔE_p remains relatively stable over ten consecutive scans for all acid-treated networks, even after lengthy acid treatments. However, i_p decreases with each consecutive scan (Figure 3.10e), with the extent depending on the acid treatment conditions (and hence SWNT coverage). i_p is reduced by 6.5 % after 20 min acid treatment (Figure 3.8c), falling to 5.5 % after 120 min (Figure 3.10a) (after ten scans for each). However, longer acid treatment on SWNT networks caused i_p to fall by 13 % and 22 % for 300 and 600 min (after ten scans), respectively, indicating that these treatment lengths are sufficient to reduce the network density enough to create a fouling effect similar to that of LD SWNT networks (Figure 3.8b).

For this study, we show that a 120 min acid treatment on a HD SWNT network is optimum for maximizing ET and minimizing electrode fouling. These data also highlight that there is a subtle interplay of acid treatment and overall SWNT coverage (intrinsic and after acid treatment) on both the ET kinetics and blocking effects that need to be taken into account to produce the optimal SWNT network electrode for DA detection.

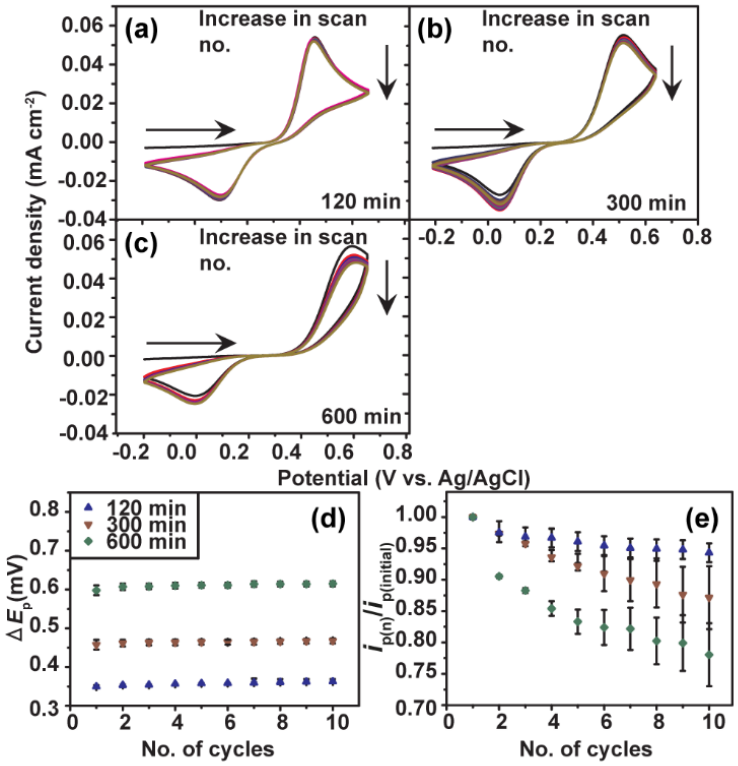

Figure 3.10 Ten consecutive CVs, recorded at a scan rate of 100 mV s^{-1}, for the oxidation of 100 µM DA in 0.01 M citric acid pH 7.0 phosphate buffer with acid treatment times of: (a) 120 min, (b) 300 min and (c) 600 min. Plot of (d) ΔE_p versus number of cycles (n = 3) and (e) $i_{p(n)}/i_{p(initial)}$ versus number of cycles (n = 3): HD SWNT networks after different acid treatment times of 120 min, 300 min and 600 min.

3.4 Conclusions

This work has shown that chemical acid treatment paves the way for the preparation of functionalized SWNT networks, which enhance the ET characteristics for the oxidation of the neurotransmitter DA. It has also been demonstrated that it is essential that the advantages brought by acid treatment are not offset by adversely decreasing the density of SWNT networks. Hence, a balance must be struck between chemical treatment and overall SWNT coverage to optimize the performance of SWNT electrodes. The local combinatorial approach outlined herein provides a route to screening and identifying the best conditions for DA detection.

Both LD and HD SWNT network electrodes were successfully obtained by cCVD growth. HD SWNT networks exhibit more facile ET for DA oxidation and are less susceptible to blocking, owing to more active surface area over the same geometrical area, leading to a lower flux (mass transport) per unit length of SWNT. It was found that a controlled (120 min) acid treatment significantly improved the apparent oxidation kinetics of DA (and/or less electrode blocking), as manifested by a decrease in ΔE_p. Repetitive CV cycling confirmed that acid-treated SWNT networks suffered much less from the effects of surface blocking, with i_p only reducing by 5.5 % over ten cycles (HD SWNT networks). However, longer acid treatments (300 and 600 min) caused SWNTs to cut and etch too much which adversely affected the overall response.

The SWNT configuration we use involving a sparse arrangement on an insulating support, differs greatly from the usual use of SWNTs in electrochemistry.[14] The arrangement we adopt is beneficial in enhancing detection limits,[64] due to the very

low background current of the network. The studies herein further enhance the capability of this type of arrangement by showing how SWNT networks can be tailored to perform a particular function. The MCEM is a particularly attractive means of quickly assessing the impact of functionalization and is expected to find wider use in electrochemistry.

3.5 References

1. Gao, F.; Cai, X.; Wang, X.; Gao, C.; Liu, S.; Gao, F.; Wang, Q. Highly Sensitive and Selective Detection of Dopamine in the Presence of Ascorbic Acid at Graphene Oxide Modified Electrode. *Sensor Actuat. B-Chem.* **2013**, *186*, 380-387.

2. Patel, A. N.; Tan, S. Y.; Miller, T. S.; Macpherson, J. V.; Unwin, P. R. Comparison and Reappraisal of Carbon Electrodes for the Voltammetric Detection of Dopamine. *Anal. Chem.* **2013**, *85*, 11755-11764.

3. Jacobs, C. B.; Peairs, M. J.; Venton, B. J. Review: Carbon Nanotube Based Electrochemical Sensors for Biomolecules. *Anal. Chim. Acta* **2010**, *662*, 105-127.

4. Alothman, Z. A.; Bukhari, N.; Wabaidur, S. M.; Haider, S. Simultaneous Electrochemical Determination of Dopamine and Acetaminophen Using Multiwall Carbon Nanotubes Modified Glassy Carbon Electrode. *Sensor Actuat. B-Chem.* **2010**, *146*, 314-320.

5. Venton, B. J.; Wightman, R. M. Psychoanalytical Electrochemistry: Dopamine and Behavior. *Anal. Chem.* **2003**, *75*, 414-421.

6. Zhang, M. N.; Gong, K. P.; Zhang, H. W.; Mao, L. Q. Layer-by-Layer Assembled Carbon Nanotubes for Selective Determination of Dopamine in the Presence of Ascorbic Acid. *Biosens. Bioelectron.* **2005**, *20*, 1270-1276.

7. Alwarappan, S.; Butcher, K. S. A.; Wong, D. K. Y. Evaluation of Hydrogenated Physically Small Carbon Electrodes in Resisting Fouling During Voltammetric Detection of Dopamine. *Sensor Actuat. B-Chem.* **2007**, *128*, 299-305.

8. Güell, A. G.; Meadows, K. E.; Unwin, P. R.; Macpherson, J. V. Trace Voltammetric Detection of Serotonin at Carbon Electrodes: Comparison of Glassy Carbon, Boron Doped Diamond and Carbon Nanotube Network Electrodes. *Phys. Chem. Chem. Phys.* **2010**, *12*, 10108-10114.

9. Patel, A. N.; McKelvey, K.; Unwin, P. R. Nanoscale Electrochemical Patterning Reveals the Active Sites for Catechol Oxidation at Graphite Surfaces. *J. Am. Chem. Soc.* **2012**, *134*, 20246-20249.

10. Swamy, B. E. K.; Venton, B. J. Carbon Nanotube-Modified Microelectrodes for Simultaneous Detection of Dopamine and Serotonin in Vivo. *Analyst* **2007**, *132*, 876-884.

11. Zhao, H.; Zhang, Y. Z.; Yuan, Z. B. Electrochemical Determination of Dopamine Using a Poly(2-Picolinic Acid) Modified Glassy Carbon Electrode. *Analyst* **2001**, *126*, 358-360.

12. Bernsmann, F.; Voegel, J. C.; Ball, V. Different Synthesis Methods Allow to Tune the Permeability and Permselectivity of Dopamine-Melanin Films to Electrochemical Probes. *Electrochim. Acta* **2011**, *56*, 3914-3919.

13. Dumitrescu, I.; Edgeworth, J. P.; Unwin, P. R.; Macpherson, J. V. Ultrathin Carbon Nanotube Mat Electrodes for Enhanced Amperometric Detection. *Adv. Mater.* **2009**, *21*, 3105-3109.

14. Dumitrescu, I.; Unwin, P. R.; Macpherson, J. V. Electrochemistry at Carbon Nanotubes: Perspective and Issues. *Chem. Commun.* **2009**, *45*, 6886-6901.

15. Dudin, P. V.; Unwin, P. R.; Macpherson, J. V. Electrochemical Nucleation and Growth of Gold Nanoparticles on Single-Walled Carbon Nanotubes: New Mechanistic Insights. *J. Phys. Chem. C* **2010**, *114*, 13241-13248.

16. Güell, A. G.; Ebejer, N.; Snowden, M. E.; McKelvey, K.; Macpherson, J. V.; Unwin, P. R. Quantitative Nanoscale Visualization of Heterogeneous Electron Transfer Rates in 2D Carbon Nanotube Networks. *P. Natl. Acad. Sci. USA* **2012**, *109*, 11487-11492.

17. Rutkowska, A.; Bawazeer, T. M.; Macpherson, J. V.; Unwin, P. R. Visualisation of Electrochemical Processes at Optically Transparent Carbon Nanotube Ultramicroelectrodes (OT-CNT-UMEs). *Phys. Chem. Chem. Phys.* **2011**, *13*, 5223-5226.

18. Dumitrescu, I.; Dudin, P. V.; Edgeworth, J. P.; Macpherson, J. V.; Unwin, P. R. Electron Transfer Kinetics at Single-Walled Carbon Nanotube Electrodes Using Scanning Electrochemical Microscopy. *J. Phys. Chem. C* **2010**, *114*, 2633-2639.

19. Heller, I.; Kong, J.; Heering, H. A.; Williams, K. A.; Lemay, S. G.; Dekker, C. Individual Single-Walled Carbon Nanotubes as Nanoelectrodes for Electrochemistry. *Nano Lett.* **2005**, *5*, 137-142.

20. Day, T. M.; Unwin, P. R.; Wilson, N. R.; Macpherson, J. V. Electrochemical Templating of Metal Nanoparticles and Nanowires on Single-Walled Carbon Nanotube Networks. *J. Am. Chem. Soc.* **2005**, *127*, 10639-10647.

21. Wildgoose, G. G.; Banks, C. E.; Compton, R. G. Metal Nanopartictes and Related Materials Supported on Carbon Nanotubes: Methods and Applications. *Small* **2006**, *2*, 182-193.

22. Gooding, J. J. Nanostructuring Electrodes with Carbon Nanotubes: A Review on Electrochemistry and Applications for Sensing. *Electrochim. Acta* **2005**, *50*, 3049-3060.

23. Hocevar, S. B.; Wang, J.; Deo, R. P.; Musameh, M.; Ogorevc, B. Carbon Nanotube Modified Microelectrode for Enhanced Voltammetric Detection of Dopamine in the Presence of Ascorbate. *Electroanal.* **2005**, *17*, 417-422.

24. Zhao, J.; Zhang, W.; Sherrell, P.; Razal, J. M.; Huang, X. F.; Minett, A. I.; Chen, J. Carbon Nanotube Nanoweb-Bioelectrode for Highly Selective Dopamine Sensing. *ACS Appl. Mater. Inter* **2012**, *4*, 44-48.

25. Bi, H.; Li, Y.; Liu, S.; Guo, P.; Wei, Z.; Lv, C.; Zhang, J.; Zhao, X. S. Carbon-Nanotube-Modified Glassy Carbon Electrode for Simultaneous Determination of Dopamine, Ascorbic Acid and Uric Acid: The Effect of Functional Groups. *Sensor Actuat. B-Chem.* **2012**, *171*, 1132-1140.

26. Britto, P. J.; Santhanam, K. S. V.; Ajayan, P. M. Carbon Nanotube Electrode for Oxidation of Dopamine. *Bioelectroch. Bioener.* **1996**, *41*, 121-125.

27. Wang, J. X.; Li, M. X.; Shi, Z. J.; Li, N. Q.; Gu, Z. N. Electrocatalytic Oxidation of Norepinephrine at a Glassy Carbon Electrode Modified with Single Wall Carbon Nanotubes. *Electroanal.* **2002**, *14*, 225-230.

28. Valentini, F.; Palleschi, G.; Morales, E. L.; Orlanducci, S.; Tamburri, E.; Terranova, M. L. Functionalized Single-Walled Carbon Nanotubes Modified Microsensors for the Selective Response of Epinephrine in Presence of Ascorbic Acid. *Electroanal.* **2007**, *19*, 859-869.

29. Rivas, G. A.; Rubianes, M. D.; Rodriguez, M. C.; Ferreyra, N. E.; Luque, G. L.; Pedano, M. L.; Miscoria, S. A.; Parrado, C. Carbon Nanotubes for Electrochemical Biosensing. *Talanta* **2007**, *74*, 291-307.

30. Banks, C. E.; Crossley, A.; Salter, C.; Wilkins, S. J.; Compton, R. G. Carbon Nanotubes Contain Metal Impurities Which Are Responsible for the "Electrocatalysis" Seen at Some Nanotube-Modified Electrodes. *Angew. Chem. Int. Edit* **2006**, *45*, 2533-2537.

31. Luo, H. X.; Shi, Z. J.; Li, N. Q.; Gu, Z. N.; Zhuang, Q. K. Investigation of the Electrochemical and Electrocatalytic Behavior of Single-Wall Carbon Nanotube Film on a Glassy Carbon Electrode. *Anal. Chem.* **2001**, *73*, 915-920.

32. Paolucci, D.; Marcaccio, M.; Bruno, C.; Paolucci, F.; Tagmatarchis, N.; Prato, M. Voltammetric Quantum Charging Capacitance Behaviour of Functionalised Carbon Nanotubes in Solution. *Electrochim. Acta* **2008**, *53*, 4059-4064.

33. Marshall, M. W.; Popa, N. S.; Shapter, J. G. Measurement of Functionalised Carbon Nanotube Carboxylic Acid Groups Using a Simple Chemical Process. *Carbon* **2006**, *44*, 1137-1141.

34. Zhao, J.; Yu, Y.; Weng, B.; Zhang, W.; Harris, A. T.; Minett, A. I.; Yue, Z.; Huang, X.; Chen, J. Sensitive and Selective Dopamine Determination in Human Serum with Inkjet Printed Nafion/MWCNT Chips. *Electrochem. Commun.* **2013**, *37*, 32-35.

35. Fan, Y. W.; Goldsmith, B. R.; Collins, P. G. Identifying and Counting Point Defects in Carbon Nanotubes. *Nat. Mater.* **2005**, *4*, 906-911.

36. Dumitrescu, I.; Wilson, N. R.; Macpherson, J. V. Functionalizing Single-Walled Carbon Nanotube Networks: Effect on Electrical and Electrochemical Properties. *J. Phys. Chem. C* **2007**, *111*, 12944-12953.

37. Miller, T. S.; Macpherson, J. V.; Unwin, P. R. Electrochemical Activation of Pristine Single Walled Carbon Nanotubes: Impact on Oxygen Reduction and Other Surface Sensitive Redox Processes. *Phys. Chem. Chem. Phys.* **2014**, *16*, 9966-9973.

38. Lurlo, M.; Paolucci, D.; Marcaccio, M.; Paolucci, F. Electron Transfer in Pristine and Functionalised Single-Walled Carbon Nanotubes. *Chem. Commun.* **2008**, *40*, 4867-4874.

39. Gooding, J. J.; Chou, A.; Liu, J.; Losic, D.; Shapter, J. G.; Hibbert, D. B. The Effects of the Lengths and Orientations of Single-Walled Carbon Nanotubes on the Electrochemistry of Nanotube-Modified Electrodes. *Electrochem. Commun.* **2007**, *9*, 1677-1683.

40. Chou, A.; Bocking, T.; Singh, N. K.; Gooding, J. J. Demonstration of the Importance of Oxygenated Species at the Ends of Carbon Nanotubes for Their Favourable Electrochemical Properties. *Chem. Commun.* **2005**, *7*, 842-844.

41. Flavin, K.; Kopf, I.; Del Canto, E.; Navio, C.; Bittencourt, C.; Giordani, S. Controlled Carboxylic Acid Introduction: A Route to Highly Purified Oxidised Single-Walled Carbon Nanotubes. *J. Mater. Chem.* **2011**, *21*, 17881-17887.

42. DuVall, S. H.; McCreery, R. L. Self-Catalysis by Catechols and Quinones during Heterogeneous Electron Transfer at Carbon Electrodes. *J. Am. Chem. Soc.* **2000**, *122*, 6759-6764.

43. Day, T. M.; Unwin, P. R.; Macpherson, J. V. Factors Controlling the Electrodeposition of Metal Nanoparticles on Pristine Single Walled Carbon Nanotubes. *Nano Lett.* **2007**, *7*, 51-57.

44. Miller, T. S.; Sansuk, S.; E, S. P.; Lai, S. C. S.; Macpherson, J. V.; Unwin, P. R. Pt Nanoparticle Modified Single Walled Carbon Nanotube Network Electrodes for Electrocatalysis: Control of the Specific Surface Area over Three Orders of Magnitude. *Catal. Today* **2014**, *244*, 136-145.

45. Dudin, P. V.; Unwin, P. R.; Macpherson, J. V. Electro-Oxidation of Hydrazine at Gold Nanoparticle Functionalised Single Walled Carbon Nanotube Network Ultramicroelectrodes. *Phys. Chem. Chem. Phys.* **2011**, *13*, 17146-17152.

46. Azamian, B. R.; Coleman, K. S.; Davis, J. J.; Hanson, N.; Green, M. L. H. Directly Observed Covalent Coupling of Quantum Dots to Single-Wall Carbon Nanotubes. *Chem. Commun.* **2002**, *4*, 366-367.

47. Patel, A. N.; Unwin, P. R.; Macpherson, J. V. Investigation of Film Formation Properties during Electrochemical Oxidation of Serotonin (5-HT) at Polycrystalline Boron Doped Diamond. *Phys. Chem. Chem. Phys.* **2013**, *15*, 18085-18092.

48. Holloway, A. F.; Toghill, K.; Wildgoose, G. G.; Compton, R. G.; Ward, M. A. H.; Tobias, G.; Llewellyn, S. A.; Ballesteros, B.; Green, M. L. H.; Crossley, A. Electrochemical Opening of Single-Walled Carbon Nanotubes Filled with Metal Halides and with Closed Ends. *J. Phys. Chem. C* **2008**, *112*, 10389-10397.

49. Hu, L.; Hecht, D. S.; Gruner, G. Percolation in Transparent and Conducting Carbon Nanotube Networks. *Nano Lett.* **2004**, *4*, 2513-2517.

50. Yang, C. M.; Park, J. S.; An, K. H.; Lim, S. C.; Seo, K.; Kim, B.; Park, K. A.; Han, S.; Park, C. Y.; Lee, Y. H. Selective Removal of Metallic Single-Walled Carbon Nanotubes with Small Diameters by Using Nitric and Sulfuric Acids. *J. Phys. Chem. B* **2005**, *109*, 19242-19248.

51. Li, J.; Huang, Y.; Chen, P.; Chan-Park, M. B. In Situ Charge-Transfer-Induced Transition from Metallic to Semiconducting Single-Walled Carbon Nanotubes. *Chem. Mater.* **2013**, *25*, 4464-4470.

52. Dresselhaus, M. S.; Dresselhaus, G.; Jorio, A.; Souza, A. G.; Saito, R. Raman Spectroscopy on Isolated Single Wall Carbon Nanotubes. *Carbon* **2002**, *40*, 2043-2061.

53. Skakalova, V.; Kaiser, A. B.; Dettlaff, W. U.; Hrncarikova, K.; Roth, S. Effect of Chemical Treatment on Electrical Conductivity, Infrared Absorption, and Raman Spectra of Single-Walled Carbon Nanotubes. *J. Phys. Chem. B* **2005**, *109*, 7174-7181.

54. Ferrari, A. C.; Meyer, J. C.; Scardaci, V.; Casiraghi, C.; Lazzeri, M.; Mauri, F.; Piscanec, S.; Jiang, D.; Novoselov, K. S.; Roth, S.; Geim, A. K. Raman Spectrum of Graphene and Graphene Layers. *Phys. Rev. Lett.* **2006**, *97*, 187401.

55. Jorio, A.; Saito, R.; Dresselhaus, G.; Dresselhaus, M. S. Determination of Nanotubes Properties by Raman Spectroscopy. *Philos. T. Roy. Soc. A* **2004**, *362*, 2311-2336.

56. Edgeworth, J. P.; Wilson, N. R.; Macpherson, J. V. Controlled Growth and Characterization of Two-Dimensional Single-Walled Carbon-Nanotube Networks for Electrical Applications. *Small* **2007**, *3*, 860-870.

57. Dresselhaus, M. S.; Jorio, A.; Souza Filho, A. G.; Saito, R. Defect Characterization in Graphene and Carbon Nanotubes Using Raman Spectroscopy. *Philos. T. Roy. Soc. A* **2010**, *368*, 5355-5377.

58. Bertoncello, P.; Edgeworth, J. P.; Macpherson, J. V.; Unwin, P. R. Trace Level Cyclic Voltammetry Facilitated by Single-Walled Carbon Nanotube Network Electrodes. *J. Am. Chem. Soc.* **2007**, *129*, 10982-10983.

59. Miller, T. S.; Ebejer, N.; Güell, A. G.; Macpherson, J. V.; Unwin, P. R. Electrochemistry at Carbon Nanotube Forests: Sidewalls and Closed Ends Allow Fast Electron Transfer. *Chem. Commun.* **2012**, *48*, 7435-7437.

60. Güell, A. G.; Meadows, K. E.; Dudin, P. V.; Ebejer, N.; Macpherson, J. V.; Unwin, P. R. Mapping Nanoscale Electrochemistry of Individual Single-Walled Carbon Nanotubes. *Nano Lett.* **2014**, *14*, 220-224.

61. Kim, J.; Xiong, H.; Hofmann, M.; Kong, J.; Amemiya, S. Scanning Electrochemical Microscopy of Individual Single-Walled Carbon Nanotubes. *Anal. Chem.* **2010**, *82*, 1605-1607.

62. Dumitrescu, I.; Unwin, P. R.; Wilson, N. R.; Macpherson, J. V. Single-Walled Carbon Nanotube Network Ultramicroelectrodes. *Anal. Chem.* **2008**, *80*, 3598-3605.

63. Jacobs, C. B.; Vickrey, T. L.; Venton, B. J. Functional Groups Modulate the Sensitivity and Electron Transfer Kinetics of Neurochemicals at Carbon Nanotube Modified Microelectrodes. *Analyst* **2011**, *136*, 3557-3565.

64. Sansuk, S.; Bitziou, E.; Joseph, M. B.; Covington, J. A.; Boutelle, M. G.; Unwin, P. R.; Macpherson, J. V. Ultrasensitive Detection of Dopamine Using a Carbon Nanotube Network Microfluidic Flow Electrode. *Anal. Chem.* **2013**, *85*, 163-169.

Chapter 4 Quantitative trace level electrochemical detection in complex aqueous media: comparison of single-walled carbon nanotube network electrodes and screen-printed carbon electrodes as voltammetric electrochemical sensors

This contribution is concerned with the use of carbon electrodes for trace voltammetric analysis in complex aqueous media containing polymers (polyethylene glycol) and bovine serum albumin to mimic conditions in which diagnostic devices might be used. A comparison is made between single-walled carbon nanotube (SWNT) electrodes grown by catalyzed chemical vapour deposition as networks on Si/SiO_2 surfaces at different coverages and commercial screen printed carbon electrodes (SPCEs), using the oxidation of ferrocenecarboxylic acid (FcCOOH) as an example system. SWNT electrodes outperform SPCEs using both cyclic voltammetry (CV) and differential pulse voltammetry (DPV) detection, with a detection limit that can be up to 3 orders of magnitude lower than SPCEs. Further, while low density (LD) SWNT electrodes show some deterioration in response to cycling, high density (HD) SWNT electrodes perform at least as well as SPCEs, showing little deterioration, even with 100 voltammetric sweeps (0.1 V s^{-1}). With DPV, detection limits down to 1 nM FcCOOH are realizable with SWNTs, making this electrode format highly suitable for applications where trace level detection is needed.

4.1 Introduction

Carbon-based electrochemical (EC) sensors have become the subject of intense investigation in many areas including the biotechnological[1] and clinical[2] fields. In particular, screen-printed carbon electrodes (SPCEs) have become a prominent material for biosensors in various real-life, high-volume applications.[3-5] The low cost, disposability and high reproducibility are the primary driving forces for SPCE development.[6] However, a limitation of SPCEs is that the commercial ink formulations are usually unknown and the ink components may affect the EC properties.[7] In contrast, carbon nanomaterials have been utilized for the EC analysis of important biomolecules[8] and offer improvements in stability, sensitivity and selectivity.[9, 10] Single-walled carbon nanotubes (SWNTs) have attracted particular interest in EC analysis because of their promising physical[11] and chemical[12] properties, including chemical stability,[13] biocompatibility[11] and low background currents.[14] SWNT network electrodes are often prepared by dispersing carbon nanotubes (CNTs) on a conducting substrate by spin-coating or drop casting.[15, 16] The disadvantages are EC interference from the supporting material,[17] large background current[18, 19] and uneven SWNT coverage.[20] In contrast, the direct growth of SWNTs on insulating substrates using catalytic chemical vapour deposition (cCVD)[21] provides electrodes that have a low defect density,[22] low amorphous carbon content and are relatively free of catalytic nanoparticles (NPs).[23]

EC sensing is used for a wide variety of applications in pharmaceutical[24-26] and clinical[27-30] systems. EC instrumentation is relatively inexpensive and with minimal effort, sensors can be designed that are of high sensitivity and selectivity.[31] However, non-faradaic or background current is an important issue for the practical sensitivity

of amperometric/voltammetric sensors and this detrimental factor typically scales with the electrode area.[32] A further issue is electrode fouling which can also impact the detection limit and the lifetime over which EC sensors can be used. By careful control of the growth parameters using cCVD, it is possible to produce SWNT networks that can address both of these issues.[23, 32-34]

In this study, we examine SWNT electrodes for trace level detection in complex polymeric solutions. We prepare SWNT network electrodes with a range of coverages on an insulating surface and compare the response to that obtained on commercial SPCEs, the most frequently used electrodes for electroanalysis. As well as using cyclic voltammetry (CV), we consider differential pulse voltammetry (DPV) which is often employed to circumvent capacitive charging currents as it takes the difference in current at two potentials where the charging current contribution is nearly equal,[35] allowing the determination of trace level redox components in biological and clinical environments.[36]

Ferrocene (Fc) and its derivatives[37] as well as other electroactive moieties such as inorganic ruthenium[38] and osmium complexes[39] are often used as EC redox labelling owing to their well-understood electrochemistry, good stability and simplicity for synthesis.[40] Typically, redox labelled molecules are used for DNA hybridization detection[37, 41] and to promote electron transfer (ET) between electrodes and enzymes.[40] Hence, the detection of Fc is the system we consider herein.

Polyethylene glycol (PEG) surfactant is a highly water-soluble and nontoxic polymer that is approved by the Food and Drug Administration (FDA) for human consumption,[42] and is used in the biomedical industry for a wide range of applications.

The conjugation of small proteins, peptides and oligonucleotides with PEG, known as PEGylation, is a common biological process.[43] Protein drugs created using PEGylation approach can minimise proteolytic cleavage and mask immunogenic sites. Therefore, it can prolong the circulation time in the human body and improve therapeutic efficacy.[44, 45] However, the adsorption of PEG on CNTs can cause surface passivation and eventually limit the detection sensitivity.[46] Also, it is very challenging to get a low limit of detection (LOD) due to the reduced mass transport caused by the high viscosity of PEG. For these reasons we have chosen to make measurements in such solutions, to test the electrode response.

Finally, we investigated the EC detection of Fc under conditions that mimic the *in vivo* environment with the presence of 4 % albumin. Albumin is the most abundant protein found in blood plasma and is a good model to investigate the influence of bio-fouling.[34]

4.2 Experimental

4.2.1 Chemicals and solutions

All chemicals were used as received. Aqueous solutions were prepared using deionized water produced by Purite Select HP system (resistivity of 18.2 MΩ cm at 25 ^{o}C). Ferrocenecarboxylic acid (FcCOOH, VWR International Ltd., 98 %) was prepared in 8 % (weight/weight (*w/w*)) of either PEG 2K, or PEG 20K (VWR International Ltd., UK) and 0.01 M phosphate-buffered solution (PBS, pH 7). PBS was prepared in-house from sodium phosphate dibasic heptahydrate ($Na_2HPO_4{\cdot}7H_2O$, Sigma-Aldrich, 98 – 100 %, UK) and sodium dihydrogen orthophosphate dihydrate

($NaH_2PO_4{\cdot}2H_2O$, Fisher Scientific, 99 – 100 %, UK). 4 % (*w/w*) albumin (Sigma-Aldrich, 97 %, UK) electrolyte was prepared in 0.01 M PBS.

4.2.2 Electrode materials

SPCE. Figure 4.1a shows a typical three-electrode SPCE (Kanichi Research, UK). The SPCE consists of a 3 mm diameter graphite disk as the working electrode (WE), a large surface area of graphite as the counter electrode (CE) and an Ag/AgCl reference electrode (RE) printed onto polyvinyl chloride.

SWNT networks. SWNT networks were grown on 2 cm × 2 cm Si/SiO_2 substrates (IDB Technologies Ltd., n-type, 525 µm thick with 300 nm of thermally grown SiO_2 on both sides) using cCVD. Fe NPs were used as catalysts[12] for the growth of low density (LD) SWNT network, whereas Co NPs were employed as catalysts[25] for both high density (HD) and super HD (SHD) SWNT network growth. Fe NPs were deposited by soaking the substrate in 1 % ferritin (50 – 150 mg mL^{-1}, Aldrich, UK) aqueous solution for an hour, followed by a 2 min exposure to 100 W oxygen plasma (Emitech K1050X plasma asher, UK). Co was deposited by sputtering (SC7640 sputter coater, Quarum Techologies Ltd., UK) at 1 kV for 20 s and 30 s with respect to the growth of HD and SHD SWNT networks. The substrate was heated from room temperature to 850 ^oC in 14 min under H_2 (BOC Gases, 99.95 %, UK) atmosphere at a flow rate of 150 sccm, followed by 1 min stabilization at 850 ^oC. The carbon feedstock, ethanol (Fisher, 99.99 %, UK) was then introduced *via* the flow of Ar (BOC Gases, 99.9995 % UK) (850 sccm) held at 0 ^oC. Growth was carried out for 10, 20 and 30 mins for LD, HD and SHD SWNT networks respectively. The system was left to cool under H_2 gas.

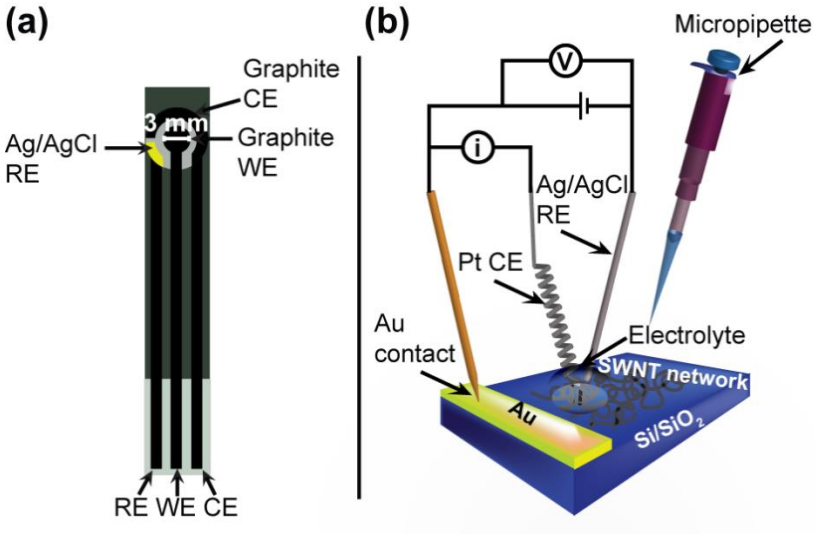

Figure 4.1 Schematic of the (a) three-electrode system of SPCE and (b) experimental setup for the EC analysis.

4.2.3 Single-walled carbon nanotube network electrodes and screen-printed carbon electrodes characterization

Field emission scanning electron microscopy (FE-SEM) images were acquired (n = 3) using a Zeiss Supra 55-VP at 1 kV acceleration voltage to visualize the SWNT networks with different densities and SPCEs. Micro-Raman spectra were recorded using a Renishaw inVia Raman microscope (514.5 nm Ar laser, 10 mW, n = 3).

4.2.4 Droplet experiments

Ohmic contact to the SWNT networks was achieved by evaporating Cr (3 nm) followed by Au (60 nm) through a shadow mask using a Moorfields MiniLab deposition system (Moorfield Associates, UK). To perform droplet measurements, SWNT networks were connected as the WE. A drop of electrolyte solution (~15 µL, 4 mm diameter) containing redox mediator was placed on the electrode surface fairly close to the Au band but without making contact (Figure 4.1b). An AgCl-coated Ag

wire acted as quasi-RE and a platinum wire was used as a CE. Both were positioned within the drop of solution to complete the circuit. EC measurements were conducted using a CH Instruments (Austin, TX; model 1040A) potentiostat. CV and DPV were used for the EC measurements. DPV scans were recorded at 50 ms pulse width, 20 mV potential step, 200 ms pulse period with an potential amplitude of 50 mV.

4.3 Results and discussion

4.3.1 Characterization of low, high and super high density single-walled carbon nanotube network electrodes and comparison with screen-printed carbon electrodes

All SWNT networks in this chapter have a connectivity greater than the metallic percolation threshold ($\rho_{th(\text{metallic})}$, 1.4 – 2.4 $\mu m_{SWNT}\ \mu m^{-2}$; based on typical SWNTs lengths of 7 – 12 μm) with sufficient mSWNT to mSWNT connections to act as an metallic electrode material.[33] Figure 4.2a is a typical FE-SEM image of a LD SWNT network, which has a density of 5 (±1) $\mu m_{SWNT}\ \mu m^{-2}$. For HD and SHD SWNTs, it is difficult to accurately determine the network density using microscopy owing to the aggregating of individual SWNT to bundles, evidenced by the obvious layering of CNTs with the increase of SWNT density (Figure 4.2b and c). The surface morphology of a SPCE is illustrated in Figure 4.2d showing uneven and rough graphite on the PVC substrate.

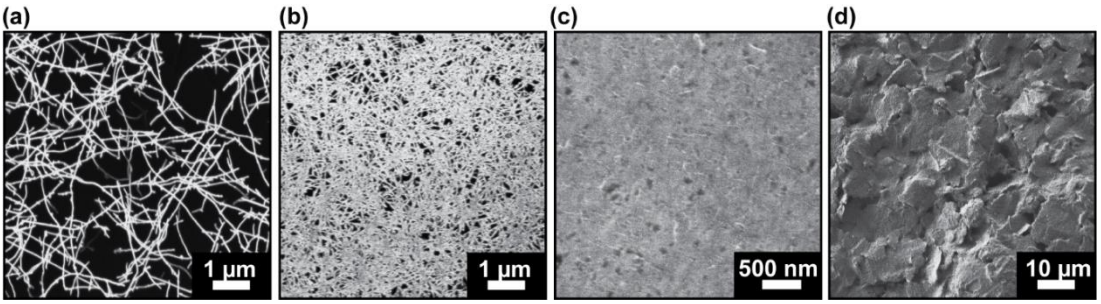

Figure 4.2 Typical FE-SEM images of (a) LD, (b) HD, (c) SHD SWNT networks and (d) SPCE.

Due to the aggregating effect observed in Figure 4.2b and c, the SWNT network density was estimated from the capacitance of the network, as the non-faradaic current would be reasonably expected to scale with the density of SWNTs. Typical data are shown in Figure 4.3 and summarized in Table 4.1. The capacitance values, *C*, of 60 ± 5 nF cm^{-2} (LD SWNT); 280 ± 15 nF cm^{-2} (HD SWNT); 400 ± 30 nF cm^{-2} (SHD SWNT) and 8600 ± 100 nF cm^{-2} (SPCE) were calculated from CVs presented in Figure 4.3, at 0 V versus Ag/AgCl in 8 % PEG 2K + 0.01 M PBS, using:

$$C = \frac{i_{average}}{vA_{geometric}} \tag{1}$$

where $i_{average}$ is the average current from forward and reverse sweep, v is the scan rate and $A_{geometric}$ is the geometrical area of the electrode. It is worth noting that the capacitances of the SWNT networks are 20 times (SHD), 30 times (HD) and 140 times (LD) lower than that of the SPCE. The HD SWNT network (Figure 4.2b) had an estimated density of ~20 μm_{SWNT} μm^{-2} calculated from the capacitance while the SHD SWNT network (Figure 4.2c) had an estimated density of ~30 μm_{SWNT} μm^{-2}.

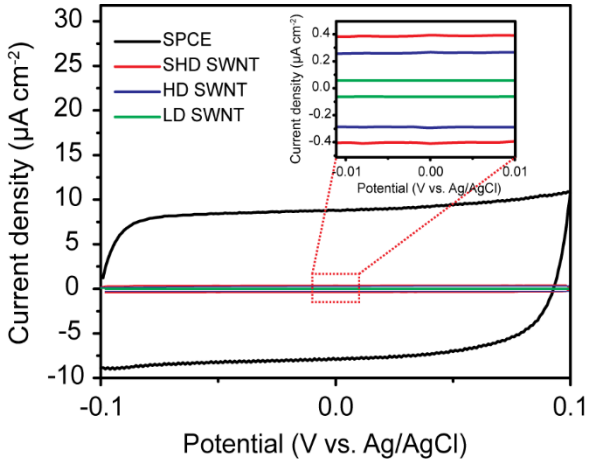

Figure 4.3 CVs for the capacitance examination in 8 % PEG 2K + 0.01 M PBS (100 mV s^{-1}) on SPCE (black), SHD (red), HD (blue) and LD (green) SWNT networks.

Figure 4.4 shows representative micro-Raman spectra of LD, HD and SHD SWNT networks and SPCE, with the wavenumber ranging from 100 to 2600 cm^{-1}. For the SWNT networks, the peaks marked with (*) at 303 cm^{-1}, 521 cm^{-1} and 963 cm^{-1} originate from the Si/SiO_2 substrate and serve as a reference against which other peaks can be compared. In all spectra the presence of the *G* peak (1585 cm^{-1}) indicates sp^2 carbon,[47] and radial breathing modes[48] (RBM, 100 to 350 cm^{-1}) positively identify the networks as SWNTs. It is clear that the intensity of *G* peak increased with the increased number of SWNTs in resonance with the Raman laser (*vide supra*).[48] The *D* peak at 1350 cm^{-1} originates from sp^3 carbon which can be found at defects or can be due to amorphous carbon.[49] The intensity difference of *G* peak to *D* peak is used as an indicator of the quality of SWNTs.[50] The *G* peak was *ca.* 40 times, 30 times and 20 times the intensity of *D* peak for the LD, HD and SHD network SWNTs, showing that the as-grown SWNTs had low intrinsic defect densities. In contrast, it is apparent that the *D* peak intensity of the SPCE is comparable with that of *G* peak which is possibly due to amorphous carbon and the binder that covered the SPCE surface.[51]

Table 4.1 Estimated values of the network density from capacitance of SWNT network electrodes and comparison to SPCE

Electrode	Capacitance (nF cm^{-2})	SWNT density estimated from capacitance (μm_{SWNT} μm^{-2})
LD SWNT	60 ± 5	~ 5 (determined from SEM presented in Figure 4.2a)
HD SWNT	280 ± 15	~ 20
SHD SWNT	400 ± 30	~ 30
SPCE	8600 ± 100	Not applicable

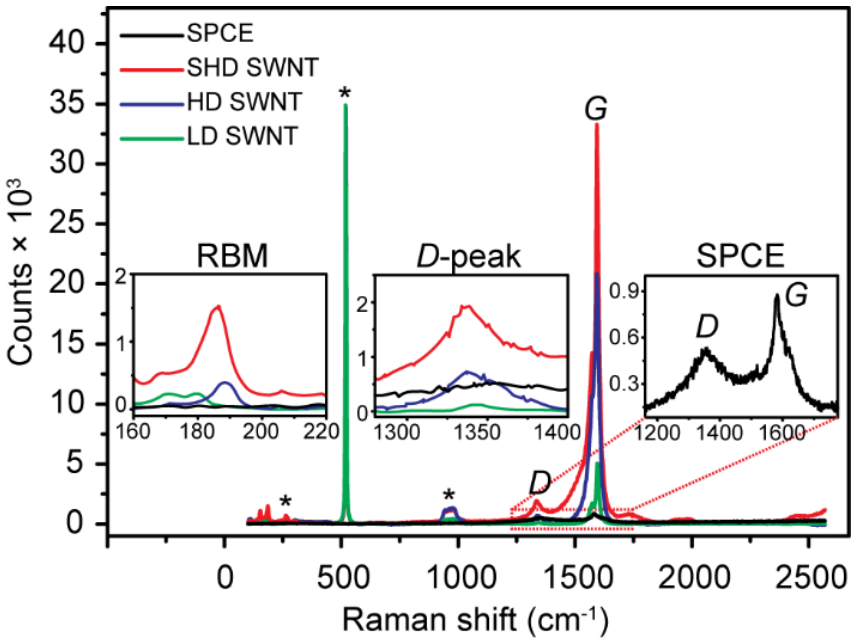

Figure 4.4 Micro-Raman spectra of SPCE (black), SHD (red), HD (blue) and LD (green) SWNT networks.

4.3.2 Evaluation of diffusion coefficients of solutions with and without polymers

Figure 4.5 shows typical CVs obtained for the oxidation of FcCOOH without (black) and with 8 % PEG 2K (red) using a Pt microdisk electrode (25 µm in diameter). The diffusion coefficient, *D*, can be estimated from:[52]

$$D = \frac{i_{lim}}{4nFcr} \tag{2}$$

where i_{lim} is the limiting current at the potential of 0.25 V, *n* is the number of electrons transferred, *F* is the Faraday constant, *r* is the radius of electrode and *c* is the concentration of the redox mediator. The value of *D* for FcCOOH without the presence of PEG was calculated to be 5.16×10^{-6} cm^2 s^{-1} from the limiting current for the oxidation of 1mM FcCOOH (~2.5 nA). The value of *D* for FcCOOH in PEG 2K was calculated to be 3.50×10^{-6} cm^2 s^{-1} (~1.7 nA).

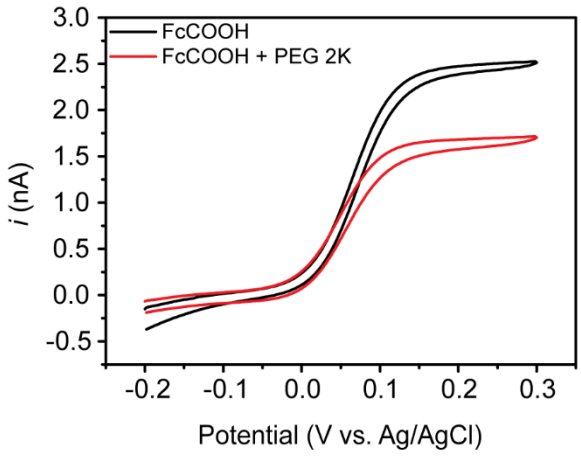

Figure 4.5 CVs for the oxidation of 1 mM FcCOOH and 0.01 M PBS (10 mV s^{-1}) using a Pt microdisk electrode (25 µm in dia.) without PEG (black) and with 8 % of PEG 2K (red).

4.3.3 Cyclic voltammetry response and detection limit of low, high and super high density single-walled carbon nanotube network electrodes compared to screen-printed carbon electrodes

CV was initially employed to analyze the oxidation of FcCOOH using SWNT network electrodes of different densities and the SPCE. Figure 4.6 shows typical CVs recorded at different concentrations of FcCOOH in 8 % PEG 2K (*w/w*) and 0.01 M PBS, at a scan rate of 100 mV s^{-1}. Interestingly, The CVs in Figure 4.6a recorded on a LD SWNT network show a linear dependence of peak current (i_p) on concentration in the range 25 to 100 nM (inset) for the oxidation of FcCOOH and the signal for the concentration of 25 nM FcCOOH is easily discernible. The good current response of the LD SWNT network is attributed to the low intrinsic background current. It is noteworthy that the current response for the LD network with surface coverage <1 % is still characteristic of a uniformly active electrode, due to the overlapping of diffusion fields between neighbouring SWNTs,[32] even in the more viscous solution (lower diffusion coefficient (D) of 3.50×10^{-6} cm^2 s^{-1}, Figure 4.5). The response for the concentration of 75 nM (HD SWNT (Figure 4.6b)) and 500 nM (SHD SWNT (Figure 4.6c)) is detectable. No redox current signal is detected at low concentration, *i.e.* 50 nM and 100 nM FcCOOH, for HD SWNT and SHD SWNT respectively. This behaviour is expected as the capacitance, or background current, scales with the SWNT network density which impairs the limit of detection. Further capacitive constraint was observed at SPCEs with a detectable concentration of 10 µM FcCOOH (Figure 4.6d). The peak to peak separations (ΔE_p) for FcCOOH on the different electrodes were 62 mV (100 nM; HD SWNT), 60 mV (1 µM; SHD SWNT) and 72 mV (100 µM; SPCE) which are

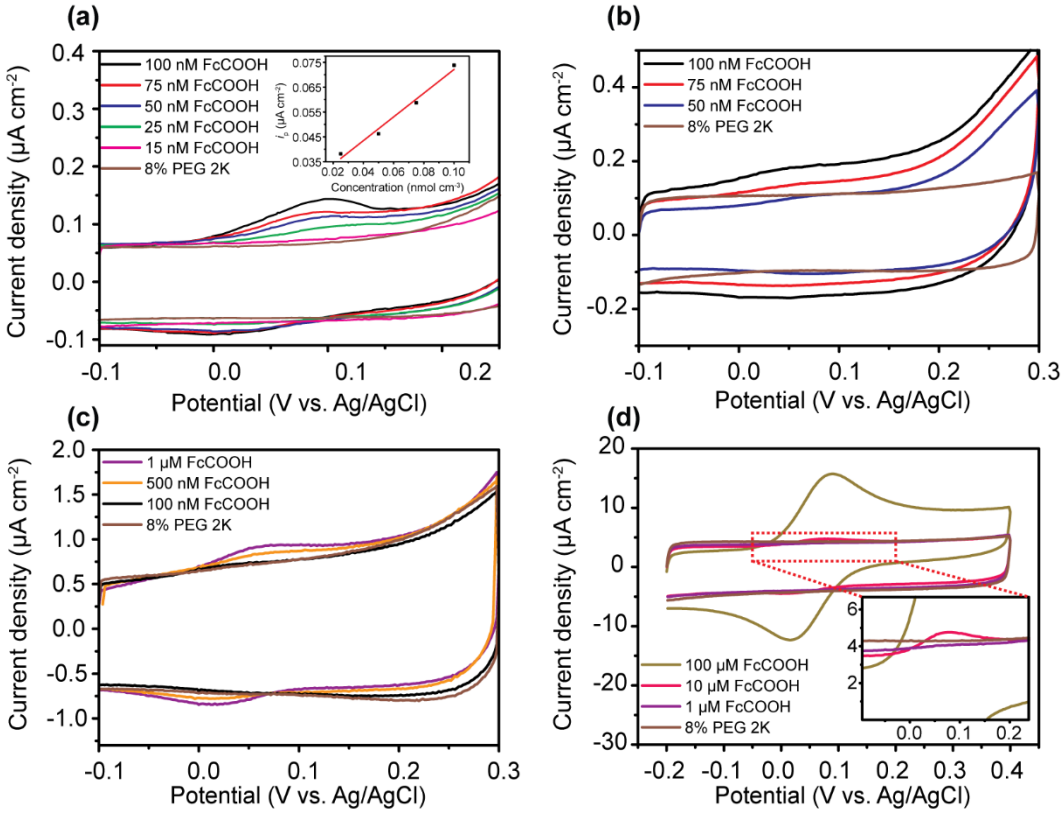

Figure 4.6 CVs for the oxidation of different concentrations of FcCOOH in 8% PEG 2K and 0.01 M PBS (100 mV s^{-1}) at (a) LD (Inset is the plot of i_p *vs.* Concentration), (b) HD, (c) SHD SWNT networks and (d) SPCE.

reasonably close to reversible behaviour, indicating fast ET for this one-electron oxidation system. However, ΔE_p for the LD SWNT network at 100 nM FcCOOH is 90 mV. Large ΔE_p is probably caused by a greater susceptibility to a blocking effect (attachment of PEG molecules to the surface) for the LD SWNT network, which decreases the overall ET kinetics in the sparse network,[46] despite the much higher intrinsic mass transport rate.[53]

4.3.4 Differential pulse voltammetry response of low, high and super high density single-walled carbon nanotube network electrodes and screen-printed carbon electrodes

DPV was employed to enhance the detection sensitivity for the oxidation of FcCOOH. As shown in Figure 4.7, the detecteable concentration was greatly enhanced for all electrodes, reaching 5 nM for LD SWNT (Figure 4.7a), 5 nM for HD SWNT (Figure 4.7b), 1 nM for SHD SWNT (Figure 4.7c) and 1 μM for SPCE (Figure 4.7d). The most striking observation is the substantially enhanced sensitivity of the SHD SWNT electrode with observable oxidative current response for a concentration of 1 nM FcCOOH (inset). This is due to the diminished capacitance current for SHD SWNT network . In contrast, the SPCE, possessing the highest capacitance current, did not reveal a particularly low detection limit owing to the complexity of graphite surface including organic oil, binder paste and other pollutants.[7]

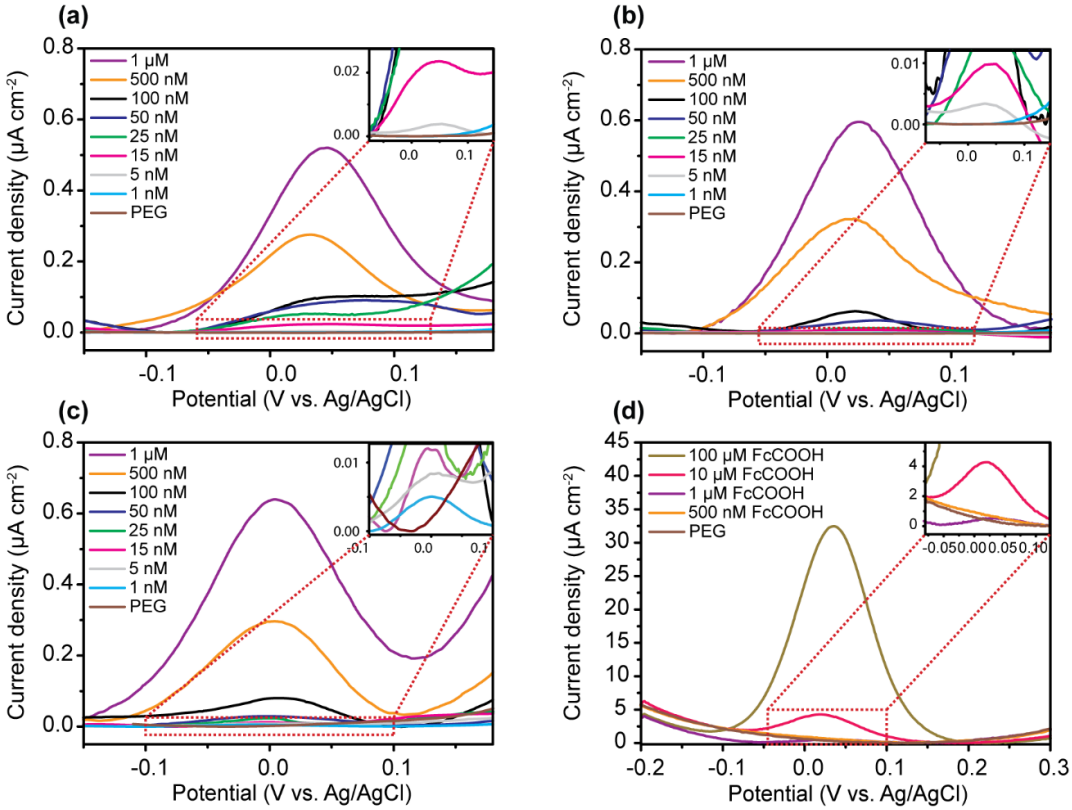

Figure 4.7 DPVs for the oxidation of different concentrations of FcCOOH in 8% PEG 2K and 0.01 M PBS at (a) LD, (b) HD, (c) SHD SWNT networks and (d) SPCE. Inset is the zoomed-in DPVs.

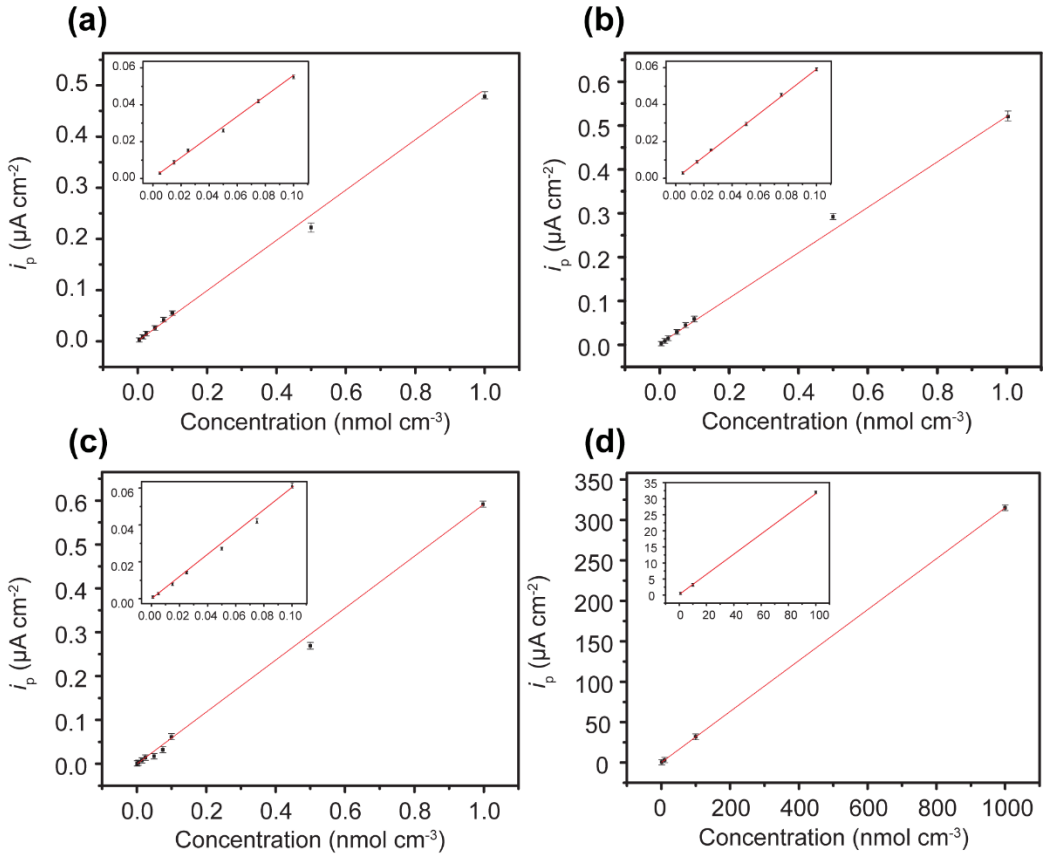

Figure 4.8 i_p as a function of FcCOOH concentration for (a) LD, (b) HD, (c) SHD SWNT networks and (d) SPCE. Note the different concentration ranges.

Figure 4.8 shows the i_p as a function of FcCOOH concentration in 8% PEG 2K and 0.01 M PBS at different electrodes. It can be seen that for all electrodes, peak currents increased with the increase of FcCOOH concentration. The gradient of the plot was 476 ± 5.38 A cm mol^{-1} (R^2 = 0.9957) for LD SWNTs, 579 ± 20.79 A cm mol^{-1} (R^2 = 0.9990) for HD SWNTs, 592 ± 2.09 A cm mol^{-1} (R^2 = 0.9989) for SHD SWNTs and 314 ± 9.83 A cm mol^{-1} (R^2 = 0.9990) for SPCE. LOD is often expressed as:[54]

$$LOD = \mu + 3\sigma \quad (3)$$

where μ and σ are the mean and standard deviation of the background response obtained from the current at the peak potential in the absence of FcCOOH (n = 4). The

LOD was calculated to be 1.29 ± 0.01 nM, 1.01 ± 0.04 nM, 0.99 ± 0.003 nM and 2.06 ± 0.06 μM, for LD SWNTs, HD SWNTs, SHD SWNTs and SPCE, respectively. Thus, the LD SWNT electrode gives a quantitative response that is ca. 1000 times lower than that obtained from the SPCE.

4.3.5 Surface fouling studies on electrodes

Albumin adsorbs onto the surface of SWNT networks leading to rapid fouling and blocking the electrode surface.[55] The extent of fouling on SWNT network electrodes with different densities and SPCE was investigated by recording fifteen consecutive CVs in 100 μM FcCOOH and 4 % albumin (*w/w),* which are shown in Figure 4.9. The LD SWNT network appears to be more susceptible to fouling than other electrodes, with a drop in i_p by 22 % (Figure 4.9a) compared to 10 % (HD SWNT network; Figure 4.9b), 5 % (SHD SWNT network; Figure 4.9c) and 11 % (SPCE; Figure 4.9d) over 15 scans. Interestingly, the SHD SWNT networks exhibit good stability with little change in i_p. Evidently, both the HD SWNTs and SHD SWNTs give far superior response to the SPCE in this medium. Further, the CV response at this concentration is somewhat resistive as the LD SWNT networks have an intrinsic resistivity which is most suited to low concentration.[56] The electrodes respond just as well over that 100 scans (FcCOOH oxidation in 8 % PEG 2K), as shown in Figure 4.10a-d, for LD, HD, SHD SWNT network and SPCE, respectively.

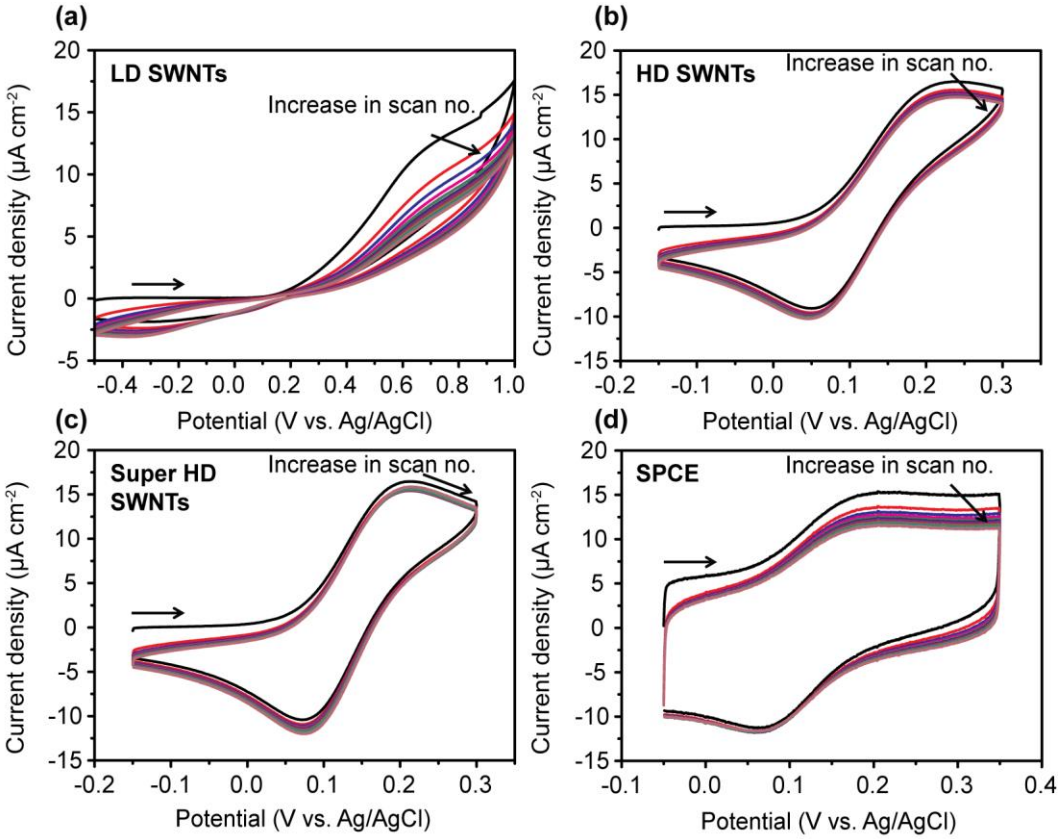

Figure 4.9 CVs of 15 consecutive cycles for the oxidation of 100 μM FcCOOH in 4 % albumin and 0.01 M PBS at (a) LD, (b) HD, (c) SHD SWNT networks and (d) SPCE, scan rate 100 mV s^{-1}.

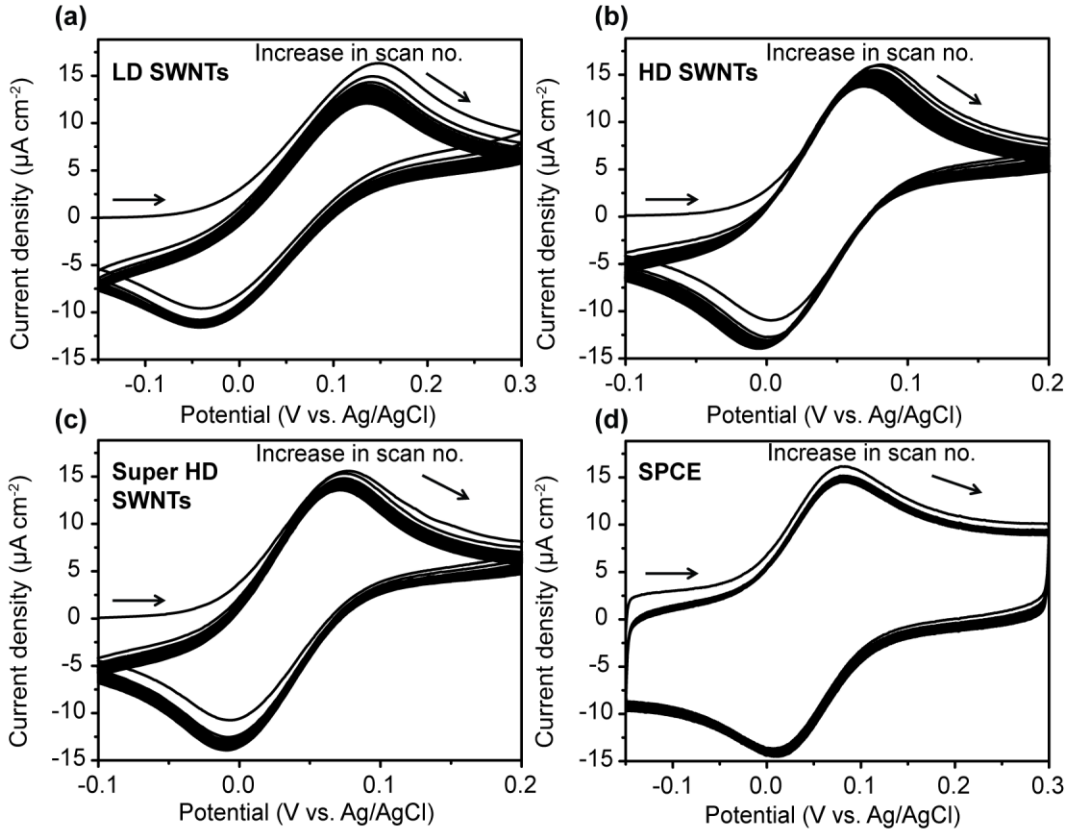

Figure 4.10 CVs of 100 consecutive cycles for the oxidation of 100 μM FcCOOH in 8 % PEG 2K and 0.01 M PBS at (a) LD, (b) HD, (c) SHD SWNT networks and (d) SPCE, scan rate 100 mV s^{-1}.

4.4 Conclusions

In this study, SWNT networks have been demonstrated to be effective for trace level detection measurements in complex media, outperforming SPCE in terms of detection sensitivity by up to 3 orders of magnitude. We systematically studied the oxidation of FcCOOH in the presence of PEG by CV and DPV techniques using SWNT network electrodes of different densities as well as SPCEs. DPV significantly improves the detection sensitivity owing to minimization of capacitance currents. It should be

emphasized that the novel nanomaterial of SHD SWNT network has been prepared successfully to a nearly complete surface coverage on an insulating substrate *via* cCVD growth. SHD SWNT networks showed a current response at concentration down to 1 nM FcCOOH when the capacitance current is eliminated by DPV. LD SWNT network electrodes have the lowest capacitance and exhibited good sensitivity with 25 nM FcCOOH using CV. However, it suffered from fouling effects that eventually impaired its detection sensitivity. SPCE possesses the highest capacitance current and did not reveal the high sensitivity using DPV due to the graphite surface complexity. The increased density of SWNT network and low charging current are the dominant factors for a superb electrode material that can be used in challenging biological media. SHD SWNT networks make exceptional electrodes with incredible detection sensitivity, facile electron transfer and less susceptible to blocking in the presence of albumin and PEG 2K.

4.5 References

1. Cai, H.; Cao, X. N.; Jiang, Y.; He, P. G.; Fang, Y. Z. Carbon Nanotube-Enhanced Electrochemical DNA Biosensor for DNA Hybridization Detection. *Anal. Bioanal. Chem.* **2003**, *375*, 287-293.

2. Chang, K. S.; Hsu, W. L.; Chen, H. Y.; Chang, C. K.; Chen, C. Y. Determination of Glutamate Pyruvate Transaminase Activity in Clinical Specimens Using a Biosensor Composed of Immobilized L-Glutamate Oxidase in a Photo-Crosslinkable Polymer Membrane on a Palladium-Deposited Screen-Printed Carbon Electrode. *Anal. Chim. Acta* **2003**, *481*, 199-208.

3. Dequaire, M.; Heller, A. Screen Printing of Nucleic Acid Detecting Carbon Electrodes. *Anal. Chem.* **2002**, *74*, 4370-4377.

4. Mann, T. S.; Mikkelsen, S. R. Antibiotic Susceptibility Testing at a Screen-Printed Carbon Electrode Array. *Anal. Chem.* **2008**, *80*, 843-848.

5. Wring, S. A.; Hart, J. P.; Bracey, L.; Birch, B. J. Development of Screen-Printed Carbon Electrodes, Chemically Modified with Cobalt Phthalocyanine, for Electrochemical Sensor Applications. *Anal. Chim. Acta* **1990**, *231*, 203-212.

6. Karuwan, C.; Wisitsoraat, A.; Phokharatkul, D.; Sriprachuabwong, C.; Lomas, T.; Nacapricha, D.; Tuantranont, A. A Disposable Screen Printed Graphene-Carbon Paste Electrode and Its Application in Electrochemical Sensing. *RSC Adv.* **2013**, *3*, 25792-25799.

7. Wang, J.; Tian, B. M.; Nascimento, V. B.; Angnes, L. Performance of Screen-Printed Carbon Electrodes Fabricated from Different Carbon Inks. *Electrochim. Acta* **1998**, *43*, 3459-3465.

8. Tiwari, J. N.; Vij, V.; Kemp, K. C.; Kim, K. S. Engineered Carbon-Nanomaterial-Based Electrochemical Sensors for Biomolecules. *ACS Nano* **2016**, *10*, 46-80.

9. Ishikawa, F. N.; Curreli, M.; Olson, C. A.; Liao, H. I.; Sun, R.; Roberts, R. W.; Cote, R. J.; Thompson, M. E.; Zhou, C. W. Importance of Controlling Nanotube Density for Highly Sensitive and Reliable Biosensors Functional in Physiological Conditions. *ACS Nano* **2010**, *4*, 6914-6922.

10. Song, Y. P.; Hu, H. F.; Feng, M.; Zhan, H. B. Carbon Nanotubes with Tailored Density of Electronic States for Electrochemical Applications. *ACS Appl. Mater. Inter.* **2015**, *7*, 25793-25803.

11. Dumitrescu, I.; Unwin, P. R.; Macpherson, J. V. Electrochemistry at Carbon Nanotubes: Perspective and Issues. *Chem. Commun.* **2009**, *45*, 6886-6901.

12. Dudin, P. V.; Unwin, P. R.; Macpherson, J. V. Electrochemical Nucleation and Growth of Gold Nanoparticles on Single-Walled Carbon Nanotubes: New Mechanistic Insights. *J. Phys. Chem. C* **2010**, *114*, 13241-13248.

13. Güell, A. G.; Ebejer, N.; Snowden, M. E.; McKelvey, K.; Macpherson, J. V.; Unwin, P. R. Quantitative Nanoscale Visualization of Heterogeneous Electron Transfer Rates in 2D Carbon Nanotube Networks. *P. Natl. Acad. Sci. USA* **2012**, *109*, 11487-11492.

14. Rutkowska, A.; Bawazeer, T. M.; Macpherson, J. V.; Unwin, P. R. Visualisation of Electrochemical Processes at Optically Transparent Carbon Nanotube Ultramicroelectrodes (OT-CNT-UMEs). *Phys. Chem. Chem. Phys.* **2011**, *13*, 5223-5226.

15. Luo, H. X.; Shi, Z. J.; Li, N. Q.; Gu, Z. N.; Zhuang, Q. K. Investigation of the Electrochemical and Electrocatalytic Behavior of Single-Wall Carbon Nanotube Film on a Glassy Carbon Electrode. *Anal. Chem.* **2001**, *73*, 915-920.

16. Paolucci, D.; Marcaccio, M.; Bruno, C.; Paolucci, F.; Tagmatarchis, N.; Prato, M. Voltammetric Quantum Charging Capacitance Behaviour of Functionalised Carbon Nanotubes in Solution. *Electrochim. Acta* **2008**, *53*, 4059-4064.

17. Zhao, J.; Yu, Y.; Weng, B.; Zhang, W.; Harris, A. T.; Minett, A. I.; Yue, Z.; Huang, X.; Chen, J. Sensitive and Selective Dopamine Determination in Human Serum with Inkjet Printed Nafion/MWCNT Chips. *Electrochem. Commun.* **2013**, *37*, 32-35.

18. Pujadó, M. P. *Carbon Nanotubes as Platforms for Biosensors with Electrochemical and Electronic Transduction*; Springer Berlin Heidelberg, 2012.

19. Papadimitriou, K. I.; Wang, C.; Rogers, M. L.; Gowers, S. A. N.; Leong, C. L.; Boutelle, M. G.; Drakakis, E. M. High-Performance Bioinstrumentation for Real-Time Neuroelectrochemical Traumatic Brain Injury Monitoring. *Front. Hum. Neurosci.* **2016**, *10*.

20. Marshall, M. W.; Popa, N. S.; Shapter, J. G. Measurement of Functionalised Carbon Nanotube Carboxylic Acid Groups Using a Simple Chemical Process. *Carbon* **2006**, *44*, 1137-1141.

21. Heller, I.; Kong, J.; Heering, H. A.; Williams, K. A.; Lemay, S. G.; Dekker, C. Individual Single-Walled Carbon Nanotubes as Nanoelectrodes for Electrochemistry. *Nano Lett.* **2005**, *5*, 137-142.

22. Fan, Y. W.; Goldsmith, B. R.; Collins, P. G. Identifying and Counting Point Defects in Carbon Nanotubes. *Nat. Mater.* **2005**, *4*, 906-911.

23. Dumitrescu, I.; Wilson, N. R.; Macpherson, J. V. Functionalizing Single-Walled Carbon Nanotube Networks: Effect on Electrical and Electrochemical Properties. *J. Phys. Chem. C* **2007**, *111*, 12944-12953.

24. Karst, U. Electrochemistry/Mass Spectrometry (EC/MS) – a New Tool to Study Drug Metabolism and Reaction Mechanisms. *Angew. Chem. Int. Edit* **2004**, *43*, 2476-2478.

25. Dudin, P. V.; Unwin, P. R.; Macpherson, J. V. Electro-Oxidation of Hydrazine at Gold Nanoparticle Functionalised Single Walled Carbon Nanotube Network Ultramicroelectrodes. *Phys. Chem. Chem. Phys.* **2011**, *13*, 17146-17152.

26. Bagheri, A.; Hosseini, H. Electrochemistry of Raloxifene on Glassy Carbon Electrode and Its Determination in Pharmaceutical Formulations and Human Plasma. *Bioelectroch.* **2012**, *88*, 164-170.

27. Adams, K. L.; Puchades, M.; Ewing, A. G. In Vitro Electrochemistry of Biological Systems. *Annu. Rev. Anal. Chem.* **2008**, *1*, 329-355.

28. Patel, A. N.; Tan, S. Y.; Miller, T. S.; Macpherson, J. V.; Unwin, P. R. Comparison and Reappraisal of Carbon Electrodes for the Voltammetric Detection of Dopamine. *Anal. Chem.* **2013**, *85*, 11755-11764.

29. Swamy, B. E. K.; Venton, B. J. Carbon Nanotube-Modified Microelectrodes for Simultaneous Detection of Dopamine and Serotonin in Vivo. *Analyst* **2007**, *132*, 876-884.

30. Rogers, M., et al. Simultaneous Monitoring of Potassium, Glucose and Lactate During Spreading Depolarisation in the Injured Human Brain – Proof of Principle of a Novel Real-Time Neurochemical Analysis System, Continuous Online Microdialysis (coMD). *J. Cereb. Blood Flow Metab.* **2016**, ASAP, **URI:** http://hdl.handle.net/10044/1/39579.

31. Zhang, X.; Ju, H.; Wang, J. *Electrochemical Sensors, Biosensors and Their Biomedical Applications*; Elsevier Science, 2011.

32. Bertoncello, P.; Edgeworth, J. P.; Macpherson, J. V.; Unwin, P. R. Trace Level Cyclic Voltarnmetry Facilitated by Single-Walled Carbon Nanotube Network Electrodes. *J. Am. Chem. Soc.* **2007**, *129*, 10982-10983.

33. E, S. P.; Miller, T. S.; Macpherson, J. V.; Unwin, P. R. Controlled Functionalisation of Single-Walled Carbon Nanotube Network Electrodes for the Enhanced Voltammetric Detection of Dopamine. *Phys. Chem. Chem. Phys.* **2015**, *17*, 26394-26402.

34. Dumitrescu, I.; Edgeworth, J. P.; Unwin, P. R.; Macpherson, J. V. Ultrathin Carbon Nanotube Mat Electrodes for Enhanced Amperometric Detection. *Adv. Mater.* **2009**, *21*, 3105-3109.

35. Sokol, W. F.; Evans, D. H. Suppression of Background Current in Differential Pulse Voltammetry with Solid Electrodes. *Anal. Chem.* **1981**, *53*, 578-580.

36. Cheemalapati, S.; Devadas, B.; Chen, S.-M. Highly Sensitive and Selective Determination of Pyrazinamide at Poly-L-Methionine/Reduced Graphene Oxide Modified Electrode by Differential Pulse Voltammetry in Human Blood Plasma and Urine Samples. *J. Colloid Interf. Sci.* **2014**, *418*, 132-139.

37. Yu, C. J.; Yowanto, H.; Wan, Y. J.; Meade, T. J.; Chong, Y.; Strong, M.; Donilon, L. H.; Kayyem, J. F.; Gozin, M.; Blackburn, G. F. Uridine-Conjugated Ferrocene DNA Oligonucleotides: Unexpected Cyclization Reaction of the Uridine Base. *J. Am. Chem. Soc.* **2000**, *122*, 6767-6768.

38. Krider, E. S.; Meade, T. J. Electron Transfer in DNA: Covalent Attachment of Spectroscopically Unique Donor and Acceptor Complexes. *J. Biol. Inorg. Chem.* **1998**, *3*, 222-225.

39. Holmlin, R. E.; Yao, J. A.; Barton, J. K. Dipyridophenazine Complexes of Os(II) as Red-Emitting DNA Probes: Synthesis, Characterization, and Photophysical Properties. *Inorg. Chem.* **1999**, *38*, 174-189.

40. Hillier, S. C.; Frost, C. G.; Jenkins, A. T. A.; Braven, H. T.; Keay, R. W.; Flower, S. E.; Clarkson, J. M. An Electrochemical Study of Enzymatic Oligonucleotide Digestion. *Bioelectroch.* **2004**, *63*, 307-310.

41. Yu, C. J.; Wan, Y. J.; Yowanto, H.; Li, J.; Tao, C. L.; James, M. D.; Tan, C. L.; Blackburn, G. F.; Meade, T. J. Electronic Detection of Single-Base Mismatches in DNA with Ferrocene-Modified Probes. *J. Am. Chem. Soc.* **2001**, *123*, 11155-11161.

42. Fu, J.; Fiegel, J.; Krauland, E.; Hanes, J. New Polymeric Carriers for Controlled Drug Delivery Following Inhalation or Injection. *Biomaterials* **2002**, *23*, 4425-4433.

43. Webster, R.; Didier, E.; Harris, P.; Siegel, N.; Stadler, J.; Tilbury, L.; Smith, D. PEGylated Proteins: Evaluation of Their Safety in the Absence of Definitive Metabolism Studies. *Drug Metab. Dispos.* **2007**, *35*, 9-16.

44. Jevsevar, S.; Kunstelj, M.; Porekar, V. G. PEGylation of Therapeutic Proteins. *Biotechnol. J.* **2010**, *5*, 113-128.

45. Pisal, D. S.; Kosloski, M. P.; Balu-Iyer, S. V. Delivery of Therapeutic Proteins. *J. Pharm. Sci.* **2010**, *99*, 2557-2575.

46. Cheng, T.-C., et al. Sensitivity of PEGylated Interferon Detection by Anti-Polyethylene Glycol (PEG) Antibodies Depends on Peg Length. *Bioconjugate Chem.* **2013**, *24*, 1408-1413.

47. Dresselhaus, M. S.; Dresselhaus, G.; Saito, R.; Jorio, A. Raman Spectroscopy of Carbon Nanotubes. *Phys. Rep.* **2005**, *409*, 47-99.

48. Dresselhaus, M. S.; Dresselhaus, G.; Jorio, A.; Souza, A. G.; Saito, R. Raman Spectroscopy on Isolated Single Wall Carbon Nanotubes. *Carbon* **2002**, *40*, 2043-2061.

49. Skakalova, V.; Kaiser, A. B.; Dettlaff, W. U.; Hrncarikova, K.; Roth, S. Effect of Chemical Treatment on Electrical Conductivity, Infrared Absorption, and Raman Spectra of Single-Walled Carbon Nanotubes. *J. Phys. Chem. B* **2005**, *109*, 7174-7181.

50. Jorio, A.; Saito, R.; Dresselhaus, G.; Dresselhaus, M. S. Determination of Nanotubes Properties by Raman Spectroscopy. *Philos. T. Roy. Soc. A* **2004**, *362*, 2311-2336.

51. Wang, S. C.; Chang, K. S.; Yuan, C. J. Enhancement of Electrochemical Properties of Screen-Printed Carbon Electrodes by Oxygen Plasma Treatment. *Electrochim. Acta* **2009**, *54*, 4937-4943.

52. Bard, A. J.; Faulkner, L. R. *Electrochemical Methods: Fundamentals and Applications*, 2nd ed.; Wiley, 2002.

53. Dumitrescu, I.; Dudin, P. V.; Edgeworth, J. P.; Macpherson, J. V.; Unwin, P. R. Electron Transfer Kinetics at Single-Walled Carbon Nanotube Electrodes Using Scanning Electrochemical Microscopy. *J. Phys. Chem. C* **2010**, *114*, 2633-2639.

54. Channon, R. B.; Newland, J. C.; Bristow, A. W. T.; Ray, A. D.; Macpherson, J. V. Selective Detection of Hydrazine in the Presence of Excess Electrochemically Active Pharmaceutical Ingredients Using Boron Doped Diamond Metal Nanoparticle Functionalised Electrodes. *Electroanal.* **2013**, *25*, 2613-2619.

55. Celik, E.; Liu, L.; Choi, H. Protein Fouling Behavior of Carbon Nanotube/Polyethersulfone Composite Membranes During Water Filtration. *Water Res.* **2011**, *45*, 5287-5294.

56. Snowden, M. E.; Edwards, M. A.; Rudd, N. C.; Macpherson, J. V.; Unwin, P. R. Intrinsic Electrochemical Activity of Single Walled Carbon Nanotube-Nafion Assemblies. *Phys. Chem. Chem. Phys.* **2013**, *15*, 5030-5038.

Chapter 5 Electrodeposition of nickel hydroxide nanoparticles on carbon nanotube electrodes: correlation of particle crystallography with electrocatalytic properties

The use of two different electrodeposition approaches to form nickel hydroxide, $Ni(OH)_2$, nanoparticles (NPs) of different crystallographic orientations on single-walled carbon nanotubes is demonstrated *via*: (i) the electrochemical generation of OH^- (~ mM), in the presence of Ni^{2+}, resulting in the formation of disordered α-phase $Ni(OH)_2$ NPs by precipitation (direct approach); (ii) the electrodeposition of Ni NPs that are converted to $Ni(OH)_2$ through potential cycling in alkaline media to form the more thermodynamically favourable, ordered β-phase $Ni(OH)_2$ NPs (indirect approach). NPs produced by the direct approach exhibit remarkable electrocatalytic activity towards both methanol and ethanol oxidation, exhibiting excellent specific activities (SA) of ~2.8 kA g^{-1} for 0.5 M methanol and ~3.7 kA g^{-1} for 0.5 M ethanol. In contrast, NPs produced by the indirect approach shows SA values about an order of magnitude lower. This study demonstrates the capability of electrochemistry for the tailored synthesis of $Ni(OH)_2$ nanostructures for electrocatalytic applications and a powerful, but simple, combinatorial approach for quick activity screening.

5.1 Introduction

The electrocatalytic oxidation of small organic molecules has attracted considerable interest for applications in different areas of electrochemical science, such as fuel cells[2] and electrochemical-based sensors.[3] Among these the electrochemical oxidation of methanol (MeOH) and ethanol (EtOH) have been active areas of research, especially to aid the development (and understanding) of direct alcohol-based fuel cells.[4] The most widely used catalysts for the alcohol oxidation reaction (AOR) are rather expensive and scarce metals such as platinum[5] and ruthenium.[6] There is thus a need to find alternative, cheaper materials, which perform as well, if not better, in terms of electrocatalytic activity.

Nickel hydroxide ($Ni(OH)_2$) is one such material that exhibits high electrochemical activity and cost effectiveness and so this electrode has been the focus of considerable attention.[7-11] A variety of different synthetic routes are available for the production of a wide range of different $Ni(OH)_2$ morphologies.[8, 12] The electrocatalytic activity of $Ni(OH)_2$ results from the oxidized form, NiOOH, owing to unpaired d electrons or empty d-orbitals[13-15] which are available to bond with adsorbed species and intermediates.

It is well known that the electrocatalytic activity of materials can be increased significantly when nanostructures, such as nanoparticles (NPs), are employed.[16, 17] Among electrocatalytic supports, carbon nanotubes (CNTs) have been shown to be extremely attractive for metal NPs[18, 19] and metal oxides[20] due to their exceptional intrinsic properties, such as chemical stability[21] and nanoscale dimensions.[22] Moreover, compared to the more traditional support materials, such as carbon black,

CNTs have been shown to offer an increased porosity and enhancement of the kinetic rate constant for the electrocatalytic process of interest (for similar metal NP loadings and carbon surface areas).[23-25] Several approaches have been adopted for depositing metal NPs onto nanotube electrodes, such as sol gel,[26] sonochemistry[27] and hydrothermal methods.[28] However, these methods can be time-consuming and challenging to use. In contrast, electrochemistry is both rapid and facile, and a good deal of control over the nucleation and growth of metal NPs can be achieved by varying the deposition potential and time.[29, 30]

The fabrication of $Ni(OH)_2$/CNT composite materials has often involved dispersing CNTs in solution followed by chemical precipitation of $Ni(OH)_2$.[31, 32] The typical methods for CNT growth are arc discharge,[33] laser ablation[34] and catalyzed chemical vapor deposition (cCVD).[35] Material produced by the first two methods has mainly been used in electrochemistry, but this contains large amounts of metal NPs and amorphous carbon, making the use of a clean-up procedure after growth mandatory.[36, 37] However, CNTs contain significant amount of metallic impurities, even after extensive purification processes,[38] and these clean-up procedures introduce considerable defects in the single-walled carbon nanotubes (SWNTs).[39] The electrochemical behavior of redox systems can be strongly affected by such impurities and defects, which are particularly problematic for fundamental studies of eletrocatalysis.[40] In contrast, CNTs grown using cCVD method have been shown to exhibit low defect density,[41] high crystallinity and are relatively free of metallic NPs.[42]

In principle, $Ni(OH)_2$ NP deposition can be driven electrochemically using two approaches: (i) the *direct approach*[43-47] where $Ni(OH)_2$ is precipitated from highly supersaturated solutions by electrochemically generating high concentrations of OH^-

at the electrode/electrolyte interface, in the presence of Ni^{2+}; and: (ii) the *indirect approach*, whereby Ni NPs are first electrodeposited by direct reduction of Ni^{2+} and subsequently electrochemically converted to $Ni(OH)_2$ by potential cycling in a basic electrolyte.[48-50] In this chapter we compare the two different procedures for $Ni(OH)_2$ NP deposition on SWNT electrodes in terms of both the resulting crystalline phase of the $Ni(OH)_2$ and electrocatalytic performance towards the EtOH oxidation reaction (EOR) and MeOH oxidation reaction (MOR).

The $Ni(OH)_2$/SWNTs are electrochemically interrogated using the microcapillary electrochemical method (MCEM),[29] which allows multiple electrochemical measurements to be made in different locations on the same electrode, thereby allowing a range of key parameters to be changed and investigated, without the need to make new electrodes and with minimal processing of the SWNTs. Although, SWNTs are attracting considerable attention as a support for electrocatalytic materials,[23, 50, 51] in the vast majority of cases, SWNT/NP composites are assessed by immobilizing, or producing, these structures on an electrode (typically glassy carbon)[50, 52, 53] which has its own intrinsic electroactivity. In contrast, our approach examines the behavior of the SWNT/NP materials alone and thus circumvents any problems and contributions that may arise from the need to use a further electrode support.

5.2 Experimental

5.2.1 Electrodeposition of $Ni(OH)_2$ on single-walled carbon nanotube network electrodes

All aqueous solutions were prepared using high purity Milli-Q reagent water (Millipore Corp.) with a resistivity of 18.2 MΩ cm at 25 °C. 10 mM nickel nitrate ($Ni(NO_3)_2$, Aldrich, 99.999%) and 10 mM nickel sulphate ($NiSO_4$, Aldrich, 99%) solutions were used for the electrodeposition of $Ni(OH)_2$ NPs for the direct and indirect approach, respectively, using a droplet method (Figure 5.1a).[54] Electrochemical measurements were carried out in a 3-electrode setup, with the SWNT network acting as the working electrode. Electrical contact to the Au band side contact was made *via* a pin. A drop of electrolyte solution (~15 µL, 4 mm diameter) was placed on the electrode surface, fairly close to the gold band but without making contact (Figure 5.1a). A platinum wire was used as a counter electrode (CE). On the timescale of electrodeposition procedure (5 seconds) there is little chance of any CE products reaching the working electrode (which is located at least 1 mm away from the end of the CE). AgCl-coated Ag wire acted as a quasi-reference electrode (QRCE), against which all potentials are quoted. This QRCE was found to be sufficiently stable under the experimental conditions and timescale.[55, 56] Both the Pt CE and AgCl-coated Ag wire QRCE were positioned within the droplet of solution to complete the circuit.

For the direct approach, precipitation of $Ni(OH)_2$ on the SWNT network electrode occurred by driving the electroreduction of nitrate (from dissolved $Ni(NO_3)_2$) at the SWNT electrode to form OH^- locally (equation 1).

$$NO_3^- + 7H_2O + 8e^- \rightleftharpoons NH_4^+ + 10OH^- \quad (1)$$

This concept is illustrated schematically in Figure 5.1b.[57] To produce NPs it was necessary to produce a high concentration of OH^-, leading to a highly supersaturated solution. This was achieved by driving the reduction process (1) at a negative driving potential of -1.5 V *vs*. Ag/AgCl, for 5 s.[13]

For the indirect approach, Ni metal NPs were first electrodeposited by applying a sufficiently negative reduction potential of -1.5 V *vs*. Ag/AgCl, for 5 s, in $NiSO_4$ solution, followed by oxidative potential cycling (+0.1 V to +0.5 V at 5 mV s^{-1} for 10 cycles) in 0.1 M KOH (Aldrich).

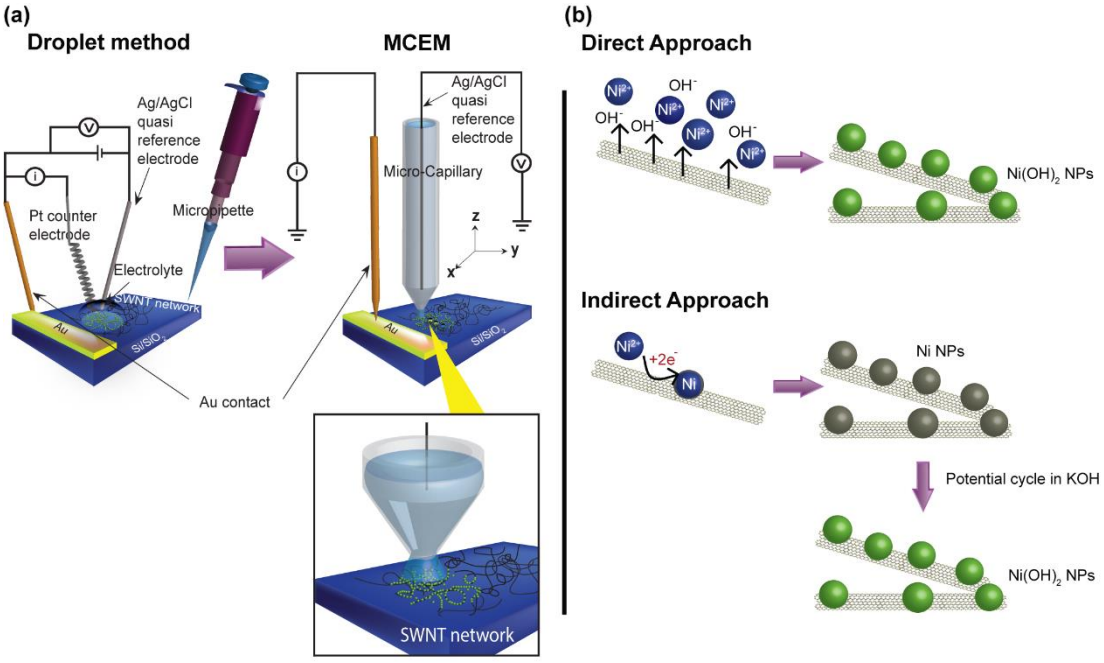

Figure 5.1 Experimental set-up for (a) the electrodeposition of NPs using the droplet method and microscopic electrocatalytic measurements using the MCEM. (b) Illustration showing $Ni(OH)_2$ NPs formation on a SWNT network electrode by both the direct (top) and indirect (bottom) approach.

5.2.2 Material characterization

Bare and functionalized SWNT networks were characterized using both field-emission scanning electron microscopy (FE-SEM: Zeiss Supra 55-VP, 5 kV acceleration voltage) and atomic force microscopy (AFM: tapping mode, Bruker-Nano Enviroscope). Micro-Raman spectra were recorded using a Renishaw inVia Raman microscope (514.5 nm Ar laser, 10 mW). For these techniques, three measurements (n = 3) were recorded per substrate. For high resolution transmission electron microscopy (HR-TEM) sample preparation, $Ni(OH)_2$ NPs were mechanically scratched from the growth substrate using a blade and dispersed in absolute EtOH (Fisher Scientific) solution. The suspension underwent sonication for 4 minutes and centrifugation for 15 minutes (Eppendorf, 10 000 rpm) to cause particle sedimentation. A drop of solution (3 µL), containing the sedimented particles, was then placed onto a lacey carbon TEM grid (Agar Scientific) and left until the EtOH had evaporated. HR-TEM was conducted (n = 3) using a JEM 2100 TEM (JEOL, LaB_6 filament, operated at 200 kV) equipped with energy-dispersive X-ray spectroscopy (EDS) and selected area electron diffraction (SAED) technique.

5.2.3 Electrocatalytic measurements

0.5 M MeOH (VWR, 99%) and 0.5 M EtOH (Fisher, 99.5%) were used for MOR and EOR, respectively, in 0.1 M KOH. All chemicals were used as received. Electrochemical measurements were performed using the MCEM, a localized electrochemical technique which has been described in detail previously.[29, 58] The electrochemical cell consisted of a borosilicate glass capillary (1.2 mm outer diameter, 0.69 mm internal diameter, Harvard Apparatus Ltd.), pulled to a sharp tip using a laser

pipet puller (P-2000, Sutter Instrument Co.). The end was polished to reveal an aperture in the range 60 – 62 μm (measured using optical microscopy for each capillary) and rendered hydrophobic on the outer walls through immersion in dichlorodimethylsilane (Fisher, ≥99%) for 90 s, with high purity Ar gas flowing through the capillary to prevent any internal silanization. The capillary was filled with the solution of interest and a Ag/AgCl wire as QRCE was inserted. The SWNT-$Ni(OH)_2$ substrate was connected as the working electrode and the capillary was manually lowered towards the electrode using an *x-y-z* micropositioner (Newport 433 series), with the aid of a camera (PixeLINK PL-B776U). A quick tap was applied to the micropositioner, once the capillary was close to the sample surface, so that an electrolyte meniscus formed on the SWNT network, without the capillary itself making contact with the electrode surface. Electrochemical measurements were made in a 2-electrode arrangement (due to the small currents, < 120 nA), for which the use of a QRCE gives adequate stability,[59, 60] using a potentiostat (CH Instruments, Austin, TX; model 730A).

5.3 Results and discussion

5.3.1 $Ni(OH)_2$ formation on single-walled carbon nanotube network electrodes

Typical FE-SEM and AFM images shown in Figures 5.2a and 5.2b, respectively, are of a representative pristine (bare) HD SWNT network with a measured SWNT density >>10 μm length of SWNT per μm^2. This density is more than sufficient to ensure that the SWNT network is above the metallic percolation threshold (1.4 – 2.4 μm_{SWNT} μm^{-2}; based on typical SWNTs lengths of 7 – 12 μm).[61] Figure 5.2c shows a representative

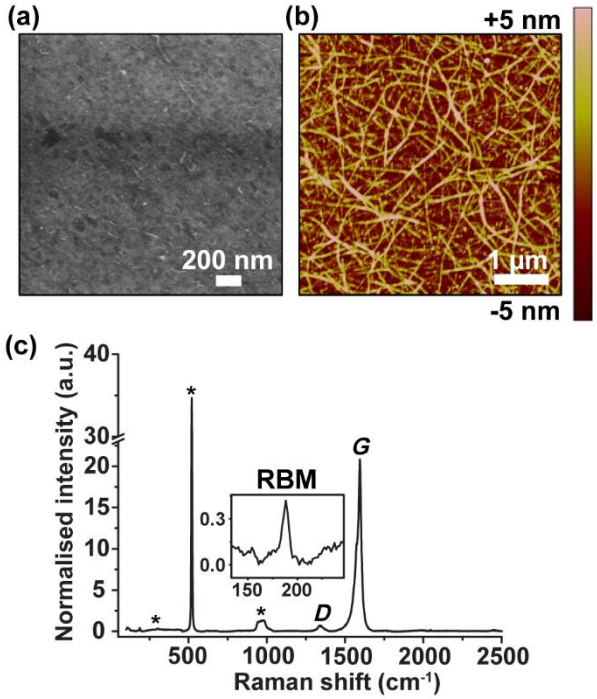

Figure 5.2 Typical (a) FE-SEM and (b) AFM images of a HD SWNT network. (c) Corresponding micro-Raman spectrum.

micro-Raman spectrum of a pristine HD SWNT network. The peaks marked with an (*) at 303 cm^{-1}, 521 cm^{-1} and 950 cm^{-1} originate from the Si/SiO_2 substrate and are used as a reference against which other peak intensities can be compared. The presence of radial breathing modes (RBM) between 100 and 350 cm^{-1} are clearly observed, confirming the presence of SWNTs. Moreover, the *G*-peak (1585 cm^{-1}, sp^2 graphitic carbon) was *ca*. 30 times the intensity of the *D*-peak (1350 cm^{-1}), indicating that the networks are of a high quality. The small *D*-peak could arise from defect sites or a small amount of amorphous carbon.

A typical current-time curve for a 5 s $Ni(OH)_2$ NPs deposition is shown in Figure 5.3a for direct deposition, with the electrodeposition current is due to OH^- production. A stable current is achieved after a short time which corresponds to a constant flux of electrogenerated OH^-. In the presence of Ni^{2+}, supersaturation of the

solution occurs resulting in $Ni(OH)_2$ formation. It is possible to calculate the relative saturation ratio, *S*:[13]

$$S = (a_{Ni^{2+}} a_{OH^-})/K_{sp} \quad (2)$$

where $a_{Ni^{2+}}$ and a_{OH^-} are the activities of Ni^{2+} and OH^- and K_{sp} of $Ni(OH)_2$ is 5.48×10^{-16} at 25°C.[62] Under constant flux conditions at the electrode surface, the electrogenerated OH^- concentration profile in the direction perpendicular to the electrode surface, can be calculated using equations (3) and (4):[63]

$$C - Co = \frac{jo\ l}{D}\{\frac{Dt}{l^2} + \frac{3x^2 - l^2}{6l^2} - \frac{2}{\pi^2}\sum_m^{\infty} \frac{(-1)^m}{m^2} \exp(-\frac{Dm^2\pi^2 t}{l^2}) \cos\frac{m\pi x}{l}\} \quad (3)$$

$$jo = \frac{i}{nF} \quad (4)$$

where *C* is the concentration and *C*o is initial concentration; *j*o is the flux and *i* is the current density during electrodeposition; *D* is the diffusion coefficient of OH^- ions (5.6×10^{-5} cm^2 s^{-1})[64], *l* is the separation of electrode surface and a parallel boundary (set as 0.22 cm; unrestricted diffusion from or to the electrode surface), *t* is time, *x* is distance from electrode and *m* is the number of points used (100) in the analytical expression. Using a time, *t* = 5 s, the resulting OH^- concentration profile is shown in Figure 5.3b (equations 3 and 4) along with the calculated *S* values (□), using equation 5.2, by approximating activity as concentration. The high OH^- concentrations generated close to the electrode surface (~2.5 mM), together with the bulk concentration of [Ni^{2+}] (10 mM), result in very high S values of 10^8-10^9, promoting high nucleation rates and the formation of $Ni(OH)_2$ NPs.[13] $Ni(OH)_2$ NPs can be seen to precipitate uniformly on the

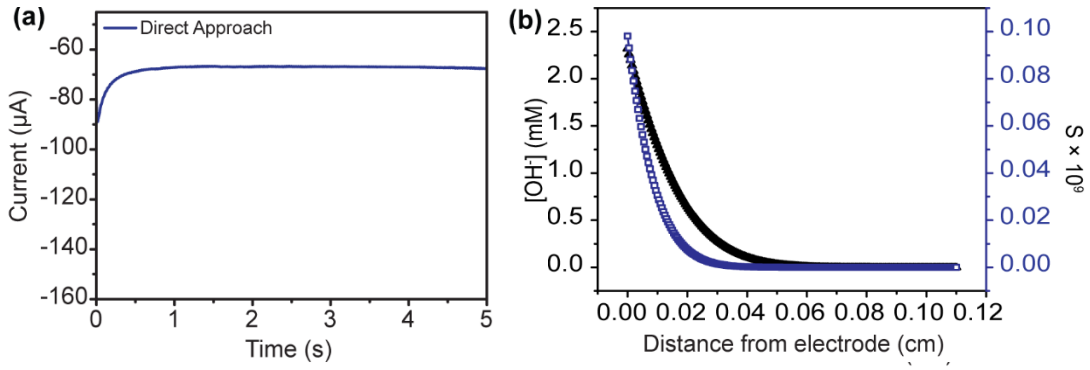

Figure 5.3 (a) A typical current-time curve recorded at a substrate potential of -1.5 V for 5 s in 10 mM $Ni(NO_3)_2$ for the direct approach. (b) Concentration profile of OH^- (▲) vs. distance from electrode surface for a time of 5 s and corresponding S values (□), calculated using equation 2.

multiply interconnected HD SWNT networks, as shown in the FE-SEM (Figure 5.4a) and AFM (Figure 5.4b) images. Cross-sectional AFM height analysis (Figure 5.4c) reveals NP heights in the range 3 – 12 nm.

For the indirect approach, typical FE-SEM and higher resolution AFM images of the SWNT electrode surface recorded after Ni electrodeposition, but prior to electrochemical cycling in basic electrolyte are shown in Figures 5.5(ai) and 5.5(bi) respectively. The Ni NPs were widely distributed over the HD SWNTs. Due to the

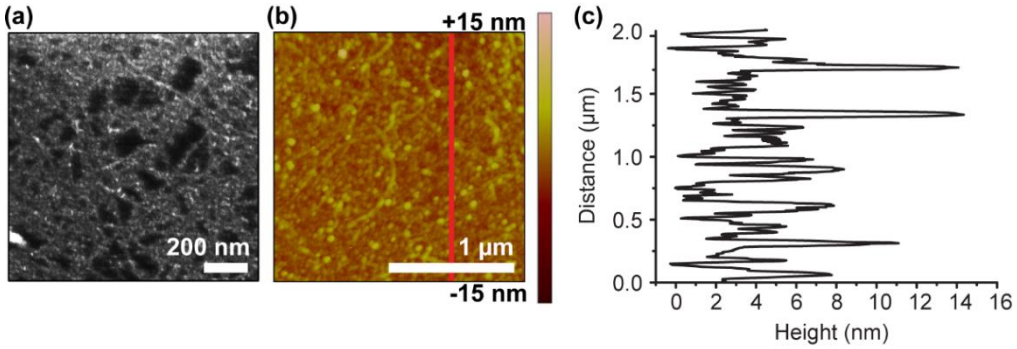

Figure 5.4 Typical (a) FE-SEM and (b) AFM images of a HD SWNT network electrode modified with $Ni(OH)_2$ (deposition parameters 5 s at -1.5 V *vs.* Ag/AgCl in 10 mM ($Ni(NO_3)_2$ solution). (c) AFM cross sectional height analysis (red line in b) of the NPs.

reduced lattice spacing and denser nature of the native metal, Ni NPs provide better contrast against the SWNTs in FE-SEM than the $Ni(OH)_2$ NPs (Figure 5.4a).[65] As determined by AFM, Ni NPs of heights in the range 3 – 25 nm were formed during the initial electrodeposition process. The Ni NPs were then converted to $Ni(OH)_2$ by potential cycling, in 0.1 M KOH, sweeping from +0.1 V to +0.5 V at a potential scan rate of 5 mV s^{-1}, as shown in Figure 5.6. The current decreased significantly for the first seven cycles as a result of the transformation of metal Ni to $Ni(OH)_2$ and remained relatively stable with further cycles.[66] Figures 5.5(a,b) show typical FE-SEM and

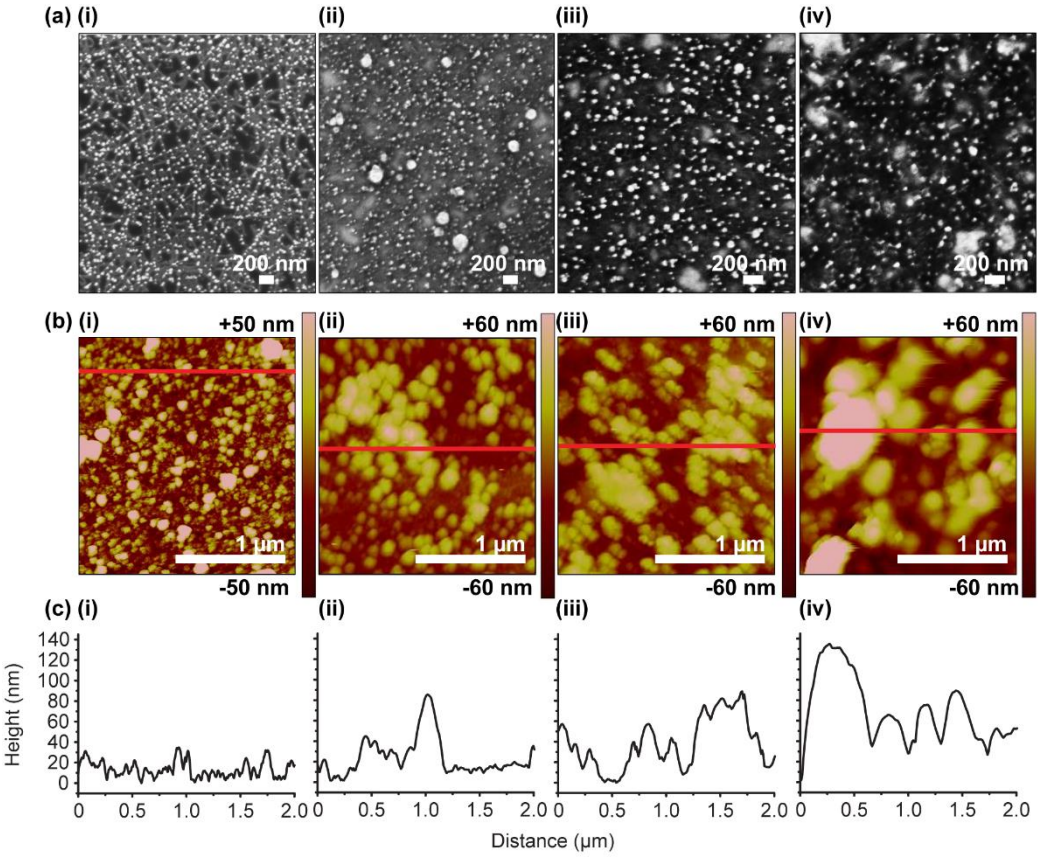

Figure 5.5 Typical (a) FE-SEM and (b) AFM images of HD SWNT network electrodes with Ni NPs (formed by electrodeposition at -1.5 V for 5 s in 10 mM $NiSO_4$ solution) (i) before and after (ii) 1 cycle, (iii) 10 cycles and (iv) 50 cycles in 0.1 M KOH. (c) Corresponding height cross sections of the NPs.

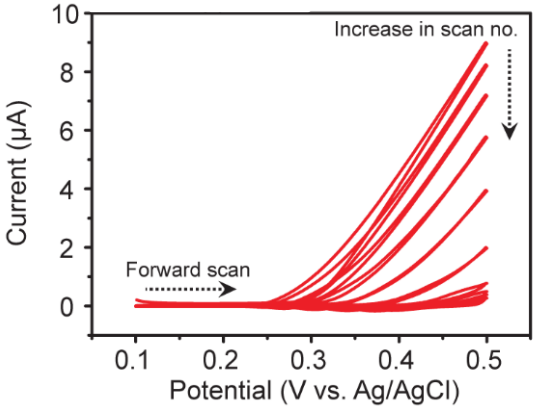

Figure 5.6 Repetitive CVs recorded in 0.1 M KOH on Ni NP deposited SWNT network electrode (indirect approach). The scan rate was 5 mV s^{-1}.

AFM images of the surface after (ii) 1 and (iii) 10 cycles. NPs of 6 – 75 nm and 25 – 80 nm in height were found after 1 and 10 cycles, respectively, clearly showing the size of the NPs increases with increasing cycle number (Figure 5.5c). However, it is difficult to determine the actual size of the NPs as there is evidence of NP agglomeration on the SWNTs. Hence, HR-TEM (*vide infra*) was carried out to provide a more detailed analysis of the NPs formed.

Note that further voltammetric cycling resulted in even larger NPs, as shown in Figure 5.5(a, b and c iv) where the Ni NPs were subjected to 50 voltammetric cycles in 0.1 M KOH. Particle heights of 40 – 130 nm were determined using AFM cross sectional analysis. These data indicate that an electrochemically-induced Ostwald-ripening or agglomeration process likely operates during potential cycling that has to be controlled to avoid particles becoming too large. For electrocatalytic studies, samples with smaller NPs were of interest (due to enhanced mass action), i.e. those formed after 10 cycles (*vide infra*).

HR-TEM analysis of the $Ni(OH)_2$ NPs is shown in Figures 5.7a-c (direct approach) and Figures 5.7d-f (indirect approach, 10 cycles). The preparation

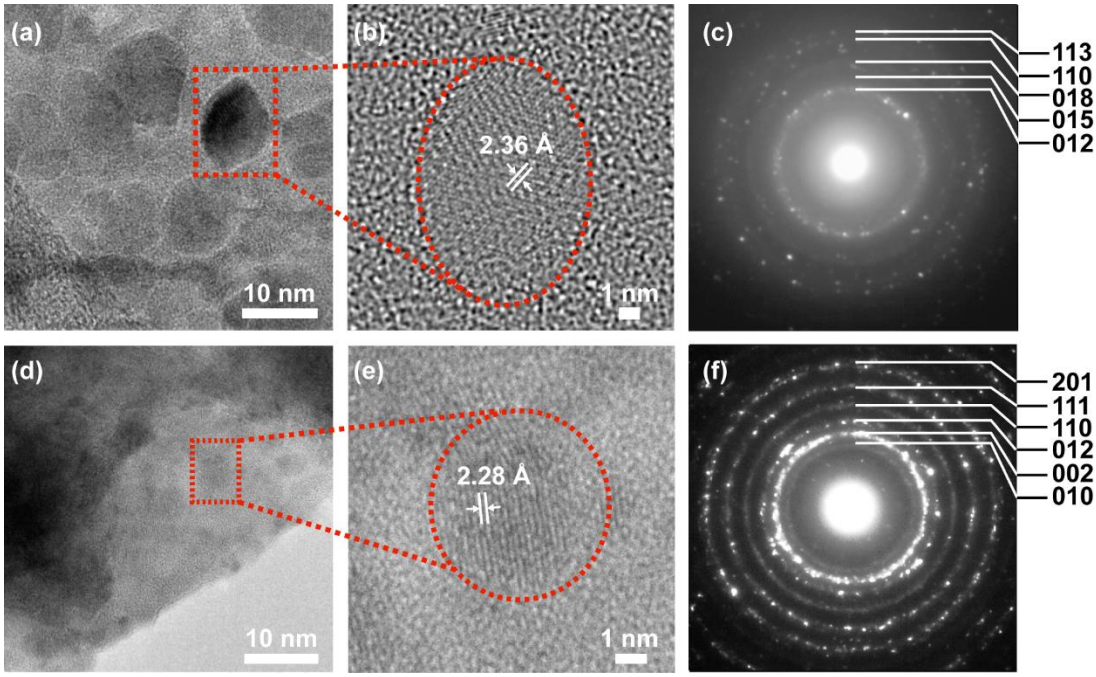

Figure 5.7 Typical (a, d) HR-TEM images and (c, f) SAED patterns of modified HD SWNT network electrode with $Ni(OH)_2$ NPs by the (a-c) direct and (d-f) indirect approaches.

procedure for HR-TEM analysis resulted in significant NP agglomeration (as shown in Figures 5.7a,d) but had the advantage that it was possible to focus on individual particles within the agglomerate to provide more information on individual NP size. For the direct approach, HR-TEM shows the smallest crystallites of $Ni(OH)_2$ were around 5 nm in diameter, whilst the typical size of $Ni(OH)_2$ NPs was 10 nm, as shown in Figures 5.7a-b, in agreement with the AFM data (Figure 5.4b,c). For the indirect approach, HR-TEM shows the smallest crystallites were *ca.* 3 nm in diameter, with a typical size of 5 nm observed, as shown in Figures 5.7d-e, indicating that the larger sized NPs observed by AFM analysis (Figures 5.5b, c (ii-iv)) are due to the agglomeration of smaller NPs.

SAED was performed on NP agglomerates that were in the holes of the supporting lacey carbon TEM grid, in order to avoid carbon background interference

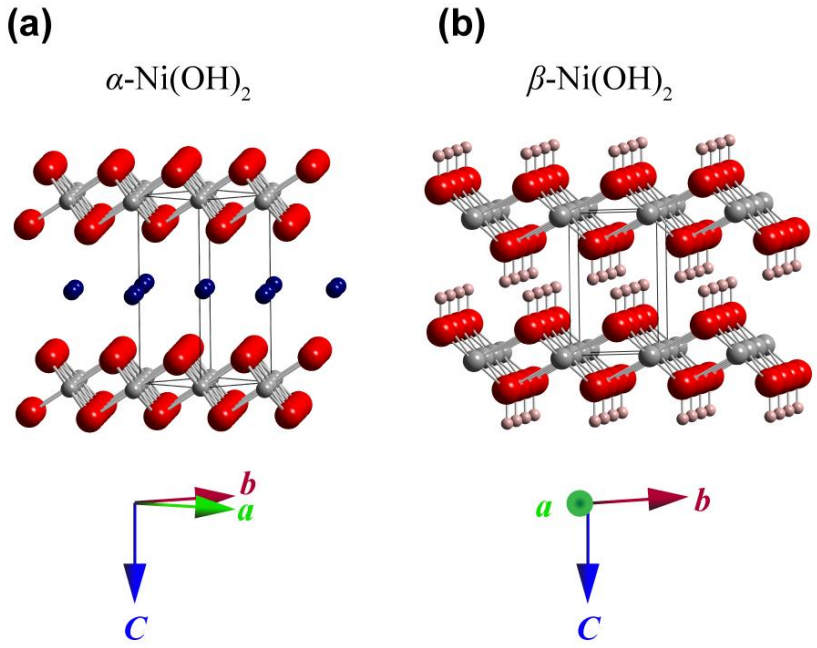

Figure 5.8 Schematic representation of (a) α-$Ni(OH)_2$ phase (small grey spheres, Ni^{2+}; large red spheres, OH^-; medium size blue spheres, H_2O positions) and (b) β-$Ni(OH)_2$ phase (medium grey spheres, Ni^{2+}; large red spheres, O^{2-}; small pink spheres, H^+). In the first structure, H^+ is omitted for clarity.[1]

in the TEM analysis. SAED of $Ni(OH)_2$ produced by the direct method indicated the formation of α-phase $Ni(OH)_2$ (Figure 5.7c; Joint Committee on Powder Diffraction Standards (JCPDS) 380715), whilst β-phase $Ni(OH)_2$ (Figure 5.7f; JCPDS 140117) was observed for the indirect method. Figure 5.8a and b show a schematic diagram representing the α and β phases of $Ni(OH)_2$, respectively.[1] Figure 5.8b clearly shows that the β phase (inter-sheet (001) distance, c_o = 4.60 Å) adopts a more close packed (de-hydrated) structure compared to the more disordered (c_o = 7.60 Å) hydrated α phase (Figure 5.8a).[1, 67, 68] For the direct approach, it is likely that the rapid precipitation process in the presence of Ni^{2+} and supersaturated concentrations of OH^- (generated electrochemically) is responsible for α-phase formation, favoring the formation of disordered α-$Ni(OH)_2$ (kinetically-driven process). For the indirect approach, as the initial electrodeposited metallic Ni has a face-centered cubic (close

packed) structure,[69] electrochemical conversion of Ni NPs to β-$Ni(OH)_2$ appears to be favored as β-phase $Ni(OH)_2$ has a similar close-packed structure. Furthermore, the slow process using potential cycling is also likely to favor the formation of the thermodynamically stable β-phase $Ni(OH)_2$.[1]

Figures 5.7b and e show the HR-TEM of a selected NP (n = 3) and the corresponding SAED images (Figures 5.7c and f); for an α-$Ni(OH)_2$ NP (b,c) and β-phase $Ni(OH)_2$ NP (e,f). Note the SAED sample size is ~ 675 nm and therefore the area around the NP is also sampled. From the HR-TEM images, lattice fringes indicate d spacings of 2.36 Å for the α-$Ni(OH)_2$ NP and 2.28 Å for the β-$Ni(OH)_2$ NP. These d spacings correspond to the (015) and (002) planes, identified using SAED, of the α and β phase $Ni(OH)_2$ NP, respectively, as provided by Figure 5.7c,f and the JCPDS.

5.3.2 Methanol oxidation reaction and ethanol oxidation reaction on $Ni(OH)_2$ nanoparticles modified single-walled carbon nanotube network electrodes

CVs were first recorded in the potential range +0.1 V to +0.55 V, on both the α and β phase $Ni(OH)_2$ modified SWNT electrodes (prepared by the direct and indirect approach, respectively) by cycling in 0.1 M KOH at 5 mV s^{-1} to estimate the amount of electroactive $Ni(OH)_2$, as shown in Figure 5.9. For both cases, the charge associated with Q_{ox} (oxidation of $Ni(OH)_2$; shaded area under the anodic peaks in Figure 5.9) is greater than the charge associated with Q_{red} (reduction of NiOOH), with Q_{ox} /Q_{red} values of 1.4 and 2.5 determined for the α-phase and β-phase $Ni(OH)_2$ NPs respectively. This is likely to be due to the fact that highly electrocatalytic NiOOH can also oxidize adsorbed OH^-, leading to the evolution of O_2 and reduction of NiOOH

back to $Ni(OH)_2$. This means there are less NiOOH sites available for electrochemical reduction on the return scan.[70] The effect, however, is small and we showed in our previous work[13] that the anodic charge was well correlated with the particle size and number, assuming volumetric conversion of $Ni(OH)_2$.

The amount of electroactive $Ni(OH)_2$ (Γ /mol cm^{-2}) is thus reasonably given by:

$$\Gamma = \frac{Q_{ox}}{nFA} \qquad (5)$$

where n is the number of electrons (n = 1), F is the Faraday constant and A is the area of the capillary opening. Given Q_{ox} values of 24.5 nC and 7.4 nC for the α-phase and β-phase $Ni(OH)_2$ respectively, Γ values of 9 ± 1 nmol cm^{-2} and 3 ± 1 nmol cm^{-2} were obtained. Given the slight enhancement of the charge on the forward sweep compared to the reverse sweep, these are maximum values for the amount of electrodeposited $Ni(OH)_2$, and hence the specific activity values that follow are minimum values.

For α-$Ni(OH)_2$ oxidation, the oxidation peak lies 60 mV less positive than that for β-$Ni(OH)_2$ oxidation. Upon oxidation the α-$Ni(OH)_2$ transforms to γ-NiOOH,[71] the

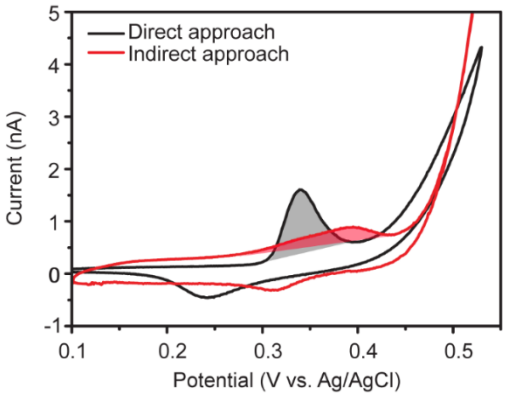

Figure 5.9 Typical CVs recorded using the MCEM with a capillary of 60 µm diameter in 0.1 M KOH, using a $Ni(OH)_2$ modified SWNT network electrode by the direct and indirect approaches. The potential scan rate is 5 mV s^{-1}.

latter has a higher oxidation state (+3.5)[72] and nearly identical c_o parameter to α-$Ni(OH)_2$.[73] In contrast, β-$Ni(OH)_2$ transforms to β-NiOOH (+3 oxidation state), which only slowly transforms to γ-NiOOH (with a resulting volume change) upon prolonged (repeated) cycling.[12] In order to maintain charge neutrality during redox cycling, it is important that ions/solvent molecules can penetrate the layered $Ni(OH)_2$ structure (Figure 5.8); thus, as ion/solvent transfer can occur more freely in the disordered α-$Ni(OH)_2$/γ-NiOOH phase structures than in the corresponding β-phase structures.[74] This could be a likely cause of the observed differences in the CV responses in Figure 5.9.

The two different $Ni(OH)_2$ structures were investigated for their electrocatalytic response towards the MOR and the EOR. CV measurements, at a potential scan rate of 5 mV s^{-1}, over the potential range +0.1 V to +0.55 V, were carried out in 0.5 M MeOH and 0.5 M EtOH, respectively in 0.1 M KOH. For comparison to literature values, currents were normalized by the mass of electroactive $Ni(OH)_2$ electrodeposited on the SWNT network electrode, to provide a value for specific activity (current / mass = A $g_{Ni(OH)_2}^{-1}$):

$$\text{specific activity} = \frac{inF}{Q_{ox}M_{Ni(OH)_2}} \qquad (6)$$

where i is the current and $M_{Ni(OH)_2}$ is the molar mass of $Ni(OH)_2$. The calculated masses of electroactive material were 23.6 pg and 7.0 pg for α-$Ni(OH)_2$ and β-$Ni(OH)_2$, respectively. Note that the MOR and EOR responses for pristine SWNT network electrodes were negligible, even when doubling the alcohol concentration to 1 M, as shown in Figures 5.10a (inset). These data indicate that a bare SWNT network

electrode is ineffective towards the electrochemical oxidation of alcohols, within this potential range.

For α-$Ni(OH)_2$, the forward scans in Figures 5.10a-b show a small anodic peak current (1) at +0.28 V and +0.31 V, followed by the appearance of larger (2) current peaks at +0.41 V and +0.48 V in the presence of EtOH and MeOH, respectively. For the reverse scan a cathodic peak current is observed at +0.20 V in both alcohols. Peak 1 is the characteristic signal for the oxidation of $Ni(OH)_2$ to NiOOH. The second larger current peak is due to the oxidation of the alcohol, catalyzed by NiOOH, occurring at +0.3 V and +0.33 V for EtOH and MeOH, respectively. Compared to cycling in 0.1 M KOH alone, Figure 5.10a shows *ca*. 40 times increase in the peak current density for the EOR, which equates to a specific activity of ~3.7 kA g^{-1} and *ca*. 30 times increase in the peak current density for the MOR, which is a specific activity of ~2.8

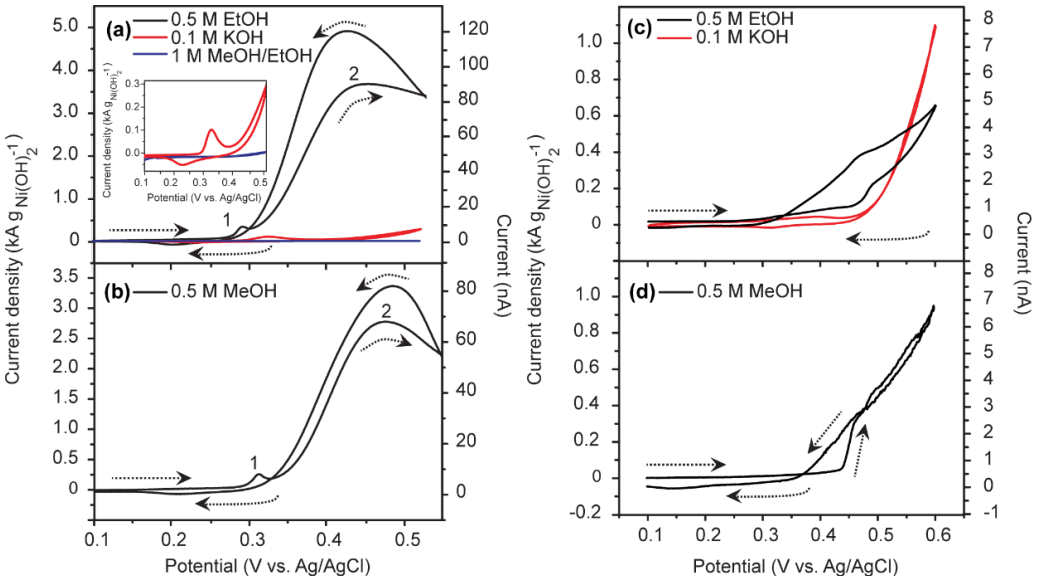

Figure 5.10 CVs at $Ni(OH)_2$ NP-modified SWNT network electrodes using the (a, b) direct and (c, d) indirect approach in a solution of 0.1 M KOH (red) with (a, c) 0.5 M EtOH and (b, d) 0.5 M MeOH (black). Inset: Magnification of the CVs of bare SWNT network electrode (blue) in 0.1 M KOH solution containing 1 M EtOH + 1 M MeOH and $Ni(OH)_2$/SWNT in 0.1 M KOH (red). The potential scan rate was 5 mV s^{-1}.

kA g^{-1} (Figure 5.10b). These values are higher than recent reports using nanostructured catalysts on carbon supports, as shown in Table 5.1. The small peak observed on the back scan for both the EOR and MOR, is attributed to the reduction of adsorbed intermediates (carbonaceous species not fully oxidized in the forward scan).[75]

For β-$Ni(OH)_2$, Figures 5.10c-d show the CVs recorded from +0.1 V to +0.60 V in the absence (0.1 M KOH only) and presence of 0.5 M EtOH (Figure 5.10c) and MeOH (Figure 5.10d). In contrast to the data in Figure 5.10a, it is not possible to differentiate between oxidation of the $Ni(OH)_2$ and oxidation of the alcohol, instead one single oxidation wave is seen, which itself is not clearly defined. Therefore, it is difficult to define precisely an onset potential for AOR, although the current can be seen to begin increasing from a ~ zero baseline *ca.* +0.34 V and +0.37 V in the presence of EtOH and MeOH, respectively. The CV characteristic is most likely due to the sluggish kinetics of the β-$Ni(OH)_2$ to β-NiOOH conversion and the oxidation of the alcohol. By taking the current at +0.47 V for the EOR and +0.45 V for the MOR, SA values of ~0.4 kA g^{-1} and ~0.3 kA g^{-1} are estimated for the EOR and MOR, respectively. These values are *ca.* 9 times smaller than for the NPs obtained by the direct approach. Cycling β-$Ni(OH)_2$ NPs reduces the catalytic efficiency even further,

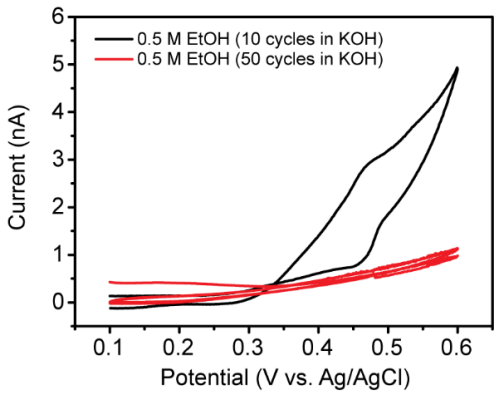

Figure 5.11 Typical CVs of 0.5 M EtOH in 0.1 M KOH at β-$Ni(OH)_2$/SWNT prepared by 10 (black) and 50 (red) potential cycles in 0.1 M KOH.

as shown by the CVs in Figure 5.11, for a β-$Ni(OH)_2$/SWNT in 0.5 M EtOH, with the electrode prepared by 50, rather than 10 potential cycles of electrodeposited Ni NPs in 0.1 M KOH (Figure 5.5vi).

Overall, it is apparent that α-$Ni(OH)_2$ produced by the direct approach exhibits faster kinetics and superior electrocatalytic (oxidizing) properties, compared to β-$Ni(OH)_2$ produced by the indirect approach. The improved performance of the α-phase over the β-phase could be due to several factors including: (i) the more disordered structure of α-$Ni(OH)_2$/γ-NiOOH which enables ion-solvent intercalation, maintaining charge neutrality during electrocatalysis;[76] (ii) γ-NiOOH has a higher oxidation state than β-NiOOH and, in principle, could act as a more effective electro-oxidation catalyst.[71-73]

Table 5.1 Nanostructured catalysts for MOR and EOR.

Electrode modification	Electrolyte, Scan rate	Maximum catalytic current (A $g_{Ni(OH)2}^{-1}$)		Ref.
		MeOH	EtOH	
Pt-Ru-Ni-P/Carbon supported	0.5 M H_2SO_4 and 0.5 M CH_3OH, 50 mV s^{-1}	459	-	[77]
Pt-TiO_2/Graphene composites	0.5 M H_2SO_4 and 1 M CH_3OH, 100 mV s^{-1}	1354	-	[78]
Pt-Ag/Glassy carbon electrode	0.5 M H_2SO_4 and 1 M CH_3OH, 50 mV s^{-1}	400	-	[79]
Pt-Ru/Carbon supported	0.1 M $HClO_4$ and 0.5 M CH_3OH	300	-	[80]
Pd-Ag/Graphene oxide	1 M KOH and 1 M CH_3OH, 1 M CH_2CH_3OH, 50 mV s^{-1}	600	1500	[81]

Cu-Pt-Pd/Carbon supported	0.5 M H_2SO_4 and 1 M CH_3OH, 1 M CH_2CH_3OH, 50 mV s^{-1}	700	1200	[82]
Pd-Cu-Sn/CNTs	1 M KOH and 0.5 M CH_3OH, 0.5 M CH_2CH_3OH, 50 mV s^{-1}	396	873	[83]
$Ni(OH)_2$/Boron-doped diamond	0.1 M KOH and 0.5 M CH_3OH, 0.5 M CH_2CH_3OH, 5 mV s^{-1}	990	1010	[13]
$Ni(OH)_2$/HD SWNT	0.1 M KOH and 0.5 M CH_3OH, 0.5 M CH_2CH_3OH, 5 mV s^{-1}	2800	3700	This work

5.4 Conclusions

The studies herein have revealed detailed information on the structure and electrocatalytic activity of $Ni(OH)_2$ NPs produced by two different electrochemical approaches on HD SWNT networks. For the direct approach, $Ni(OH)_2$ NPs were formed by electro-generating relatively high concentrations of OH^- at the electrode surface in the presence of Ni^{2+}. For the indirect approach, Ni NPs were first electrodeposited on the SWNTs and then electrochemically transformed to $Ni(OH)_2$ by potential cycling in alkaline media.

NP distribution was investigated using FE-SEM, whilst AFM was employed to provide quantitative information on NP size. AFM revealed individual NPs for the direct approach, of size in the range 3 – 12 nm. For the indirect approach, AFM indicated that NP aggregation was a potential problem, revealing a wide size distribution of 25 – 80 nm in the height of nanostructures. HR-TEM was used to provide higher resolution information on the NP deposits. This revealed typical NP

crystallites of sizes 10 nm and 5 nm for the direct and indirect approaches, respectively. The latter data supported the idea that the larger nanostructured material, as observed by AFM, was produced by the aggregation of smaller NPs.

A key part of our study was to determine the crystallography of individual NPs using SAED in the HR-TEM. It was possible to assign NPs formed by direct deposition to the disordered (hydrated) α-phase and those formed *via* indirect deposition to the ordered (de-hydrated) β-phase. The different phases formed by these methods can be rationalized because in the direct approach extremely high supersaturations are generated resulted in the immediate precipitation of the kinetically favored α-phase of $Ni(OH)_2$. In contrast, the potential cycling approach involves a slow conversion of Ni to $Ni(OH)_2$, leading to the more thermodynamically favored β-phase of $Ni(OH)_2$.

α-$Ni(OH)_2$ NPs formed *via* the direct approach, performed remarkably well in terms of the high specific activities for the MOR (~2.8 kA g^{-1}) and EOR (~3.7 kA g^{-1}), for 0.5 M of alcohol, compared to β-$Ni(OH)_2$ NPs for the MOR (~0.3 kA g^{-1}) and EOR (~0.4 kA g^{-1}) respectively. This difference was mainly attributed to the more disordered nature of α-$Ni(OH)_2$/γ-NiOOH, compared to β-$Ni(OH)_2$/β-NiOOH, leading to more ready ion-solvent intercalation during electrocatalysis in the former case. Furthermore, γ-NiOOH has a higher oxidation state than β-NiOOH which could make it more effective as a catalyst for electro-oxidation.

Finally, it is important to highlight the MCEM as approach to quickly screen electrocatalysts and that our studies have allowed the study of SWNT-$Ni(OH)_2$ nanostructured electrodes without any need for an additional support electrode so that

the intrinsic activity of this novel composite is investigated without complications from a substrate electrode.

5.5 References

1. Hall, D. S.; Lockwood, D. J.; Bock, C.; MacDougall, B. R., Nickel Hydroxides and Related Materials: A Review of Their Structures, Synthesis and Properties. *P. Roy. Soc. A Mat.* **2015**, *471*.

2. Ghenciu, A. F. Review of Fuel Processing Catalysts for Hydrogen Production in PEM Fuel Cell Systems. *Curr. Opin. Solid St. M.* **2002**, *6*, 389-399.

3. Wang, J.; Musameh, M. Carbon Nanotube/Teflon Composite Electrochemical Sensors and Biosensors. *Anal. Chem.* **2003**, *75*, 2075-2079.

4. Miller, T. S.; Sansuk, S.; E, S. P.; Lai, S. C. S.; Macpherson, J. V.; Unwin, P. R. Pt Nanoparticle Modified Single Walled Carbon Nanotube Network Electrodes for Electrocatalysis: Control of the Specific Surface Area over Three Orders of Magnitude. *Catal. Today* **2014**, *244*, 136-145.

5. Li, Y.; Gao, W.; Ci, L.; Wang, C.; Ajayan, P. M. Catalytic Performance of Pt Nanoparticles on Reduced Graphene Oxide for Methanol Electro-Oxidation. *Carbon* **2010**, *48*, 1124-1130.

6. Gao, M. R.; Sheng, W. C.; Zhuang, Z. B.; Fang, Q. R.; Gu, S.; Jiang, J.; Yan, Y. S. Efficient Water Oxidation Using Nanostructured α-Nickel-Hydroxide as an Electrocatalyst. *J. Am. Chem. Soc.* **2014**, *136*, 7077-7084.

7. Gong, M., et al. Nanoscale Nickel Oxide/Nickel Heterostructures for Active Hydrogen Evolution Electrocatalysis. *Nat. Commun.* **2014**, *5*, 4695.

8. Li, H. B.; Yu, M. H.; Wang, F. X.; Liu, P.; Liang, Y.; Xiao, J.; Wang, C. X.; Tong, Y. X.; Yang, G. W. Amorphous Nickel Hydroxide Nanospheres with Ultrahigh Capacitance and Energy Density as Electrochemical Pseudocapacitor Materials. *Nat. Commun.* **2013**, *4*, 1894.

9. Mu, Y.; Jia, D.; He, Y.; Miao, Y.; Wu, H.-L. Nano Nickel Oxide Modified Non-Enzymatic Glucose Sensors with Enhanced Sensitivity through an Electrochemical Process Strategy at High Potential. *Biosens. Bioelectron.* **2011**, *26*, 2948-2952.

10. Casas-Cabanas, M.; Canales-Vazquez, J.; Rodriguez-Carvajal, J.; Rosa Palacin, M. Deciphering the Structural Transformations During Nickel Oxyhydroxide Electrode Operation. *J. Am. Chem. Soc.* **2007**, *129*, 5840-5842.

11. Liu, J.; Chen, M.; Zhang, L.; Jiang, J.; Yan, J.; Huang, Y.; Lin, J.; Fan, H. J.; Shen, Z. X. A Flexible Alkaline Rechargeable Ni/Fe Battery Based on Graphene Foam/Carbon Nanotubes Hybrid Film. *Nano Lett.* **2014**, *14*, 7180-7187.

12. Oliva, P.; Leonardi, J.; Laurent, J. F.; Delmas, C.; Braconnier, J. J.; Figlarz, M.; Fievet, F.; Deguibert, A. Review of the Structure and the Electrochemistry of Nickel Hydroxides and Oxy-Hydroxides. *J. Power Sources* **1982**, *8*, 229-255.

13. Hutton, L. A.; Vidotti, M.; Patel, A. N.; Newton, M. E.; Unwin, P. R.; Macpherson, J. V. Electrodeposition of Nickel Hydroxide Nanoparticles on Boron-Doped Diamond Electrodes for Oxidative Electrocatalysis. *J. Phys. Chem. C* **2011**, *115*, 1649-1658.

14. Reim, R. E.; Vaneffen, R. M. Determination of Carbohydrates by Liquid-Chromatography with Oxidation at a Nickel(III) Oxide Electrode. *Anal. Chem.* **1986**, *58*, 3203-3207.

15. Dai, W.; Li, H.; Li, M.; Li, C.; Wu, X.; Yang, B. Electrochemical Imprinted Polycrystalline Nickel-Nickel Oxide Half-Nanotube-Modified Boron-Doped Diamond Electrode for the Detection of L-Serine. *ACS Appl. Mater. Inter*. **2015**, 7, 22858-22867.

16. Kraeutler, B.; Bard, A. J. Heterogeneous Photocatalytic Preparation of Supported Catalysts-Photodeposition of Platinum on TiO_2 Powder and Other Substrates. *J. Am. Chem. Soc.* **1978**, *100*, 4317-4318.

17. Kleijn, S. E. F.; Lai, S. C. S.; Koper, M. T. M.; Unwin, P. R. Electrochemistry of Nanoparticles. *Angew. Chem. Int. Ed.* **2014**, *53*, 3558-3586.

18. Li, W. Z.; Liang, C. H.; Zhou, W. J.; Qiu, J. S.; Zhou, Z. H.; Sun, G. Q.; Xin, Q. Preparation and Characterization of Multiwalled Carbon Nanotube-Supported Platinum for Cathode Catalysts of Direct Methanol Fuel Cells. *J. Phys. Chem. B* **2003**, *107*, 6292-6299.

19. Mu, Y. Y.; Liang, H. P.; Hu, J. S.; Jiang, L.; Wan, L. J. Controllable Pt Nanoparticle Deposition on Carbon Nanotubes as an Anode Catalyst for Direct Methanol Fuel Cells. *J. Phys. Chem. B* **2005**, *109*, 22212-22216.

20. Corso, B. L.; Perez, I.; Sheps, T.; Sims, P. C.; Gül, O. T.; Collins, P. G. Electrochemical Charge-Transfer Resistance in Carbon Nanotube Composites. *Nano Lett.* **2014**, *14*, 1329-1336.

21. Güell, A. G.; Ebejer, N.; Snowden, M. E.; McKelvey, K.; Macpherson, J. V.; Unwin, P. R. Quantitative Nanoscale Visualization of Heterogeneous Electron Transfer Rates in 2D Carbon Nanotube Networks. *P. Natl. Acad. Sci. USA* **2012**, *109*, 11487-11492.

22. Heller, I.; Kong, J.; Heering, H. A.; Williams, K. A.; Lemay, S. G.; Dekker, C. Individual Single-Walled Carbon Nanotubes as Nanoelectrodes for Electrochemistry. *Nano Lett.* **2005**, *5*, 137-142.

23. Kongkanand, A.; Kuwabata, S.; Girishkumar, G.; Kamat, P. Single-Wall Carbon Nanotubes Supported Platinum Nanoparticles with Improved Electrocatalytic Activity for Oxygen Reduction Reaction. *Langmuir* **2006**, *22*, 2392-2396.

24. Joo, S. H.; Choi, S. J.; Oh, I.; Kwak, J.; Liu, Z.; Terasaki, O.; Ryoo, R. Ordered Nanoporous Arrays of Carbon Supporting High Dispersions of Platinum Nanoparticles. *Nature* **2001**, *412*, 169-172.

25. Zhou, X.; Xia, Z.; Zhang, Z.; Ma, Y.; Qu, Y. One-Step Synthesis of Multi-Walled Carbon Nanotubes/Ultra-Thin $Ni(OH)_2$ Nanoplate Composite as Efficient Catalysts for Water Oxidation. *J. Mater. Chem. A* **2014**, *2*, 11799-11806.

26. Yang, M. H.; Yang, Y. H.; Liu, Y. L.; Shen, G. L.; Yu, R. Q. Platinum Nanoparticles-Doped Sol-Gel/Carbon Nanotubes Composite Electrochemical Sensors and Biosensors. *Biosens. Bioelectron.* **2006**, *21*, 1125-1131.

27. Zhang, X.; Zhang, B.; Li, X.-D.; Ma, L.-X.; Zhang, J.-W. Sonochemical Synthesis of Hollow Pt Alloy Nanostructures on Carbon Nanotubes with Enhanced Electrocatalytic Activity for Methanol Oxidation Reaction. *Int. J. Hydrogen Energ.* **2015**, *40*, 14416-14420.

28. Lu, Q. Y.; Gao, F.; Zhao, D. Y. One-Step Synthesis and Assembly of Copper Sulfide Nanoparticles to Nanowires, Nanotubes, and Nanovesicles by a Simple Organic Amine-Assisted Hydrothermal Process. *Nano Lett.* **2002**, *2*, 725-728.

29. Day, T. M.; Unwin, P. R.; Macpherson, J. V. Factors Controlling the Electrodeposition of Metal Nanoparticles on Pristine Single Walled Carbon Nanotubes. *Nano Lett.* **2007**, *7*, 51-57.

30. Miller, T. S.; Macpherson, J. V.; Unwin, P. R. Dual-Electrode Measurements in a Meniscus Microcapillary Electrochemical Cell Using a High Aspect Ratio Carbon Fibre Ultramicroelectrode. *J. Electroanal. Chem.* **2014**, *729*, 80-86.

31. Asgari, M.; Maragheh, M. G.; Davarkhah, R.; Lohrasbi, E. Methanol Electrooxidation on the Nickel Oxide Nanoparticles/Multi-Walled Carbon Nanotubes Modified Glassy Carbon Electrode Prepared Using Pulsed Electrodeposition. *J. Electrochem. Soc.* **2011**, *158*, K225-K229.

32. Xu, C.; Sun, J.; Gao, L. Large Scale Synthesis of Nickel Oxide/Multiwalled Carbon Nanotube Composites by Direct Thermal Decomposition and Their Lithium Storage Properties. *J. Power Sources* **2011**, *196*, 5138-5142.

33. Shi, Z. J.; Lian, Y. F.; Zhou, X. H.; Gu, Z. N.; Zhang, Y. G.; Iijima, S.; Zhou, L. X.; Yue, K. T.; Zhang, S. L. Mass-Production of Single-Wall Carbon Nanotubes by Arc Discharge Method. *Carbon* **1999**, *37*, 1449-1453.

34. Munoz, E.; Maser, W. K.; Benito, A. M.; Martinez, M. T.; de la Fuente, G. F.; Maniette, Y.; Righi, A.; Anglaret, E.; Sauvajol, J. L. Gas and Pressure Effects on the Production of Single-Walled Carbon Nanotubes by Laser Ablation. *Carbon* **2000**, *38*, 1445-1451.

35. Huang, S. M.; Woodson, M.; Smalley, R.; Liu, J. Growth Mechanism of Oriented Long Single Walled Carbon Nanotubes Using "Fast-Heating" Chemical Vapor Deposition Process. *Nano Lett.* **2004**, *4*, 1025-1028.

36. Hiura, H.; Ebbesen, T. W.; Tanigaki, K. Opening and Purification of Carbon Nanotubes in High Yields. *Adv. Mater.* **1995**, *7*, 275-276.

37. Yuge, R.; Toyama, K.; Ichihashi, T.; Ohkawa, T.; Aoki, Y.; Manako, T. Characterization and Field Emission Properties of Multi-Walled Carbon Nanotubes with Fine Crystallinity Prepared by CO_2 Laser Ablation. *Appl. Surf. Sci.* **2012**, *258*, 6958-6962.

38. Pumera, M., Carbon Nanotubes Contain Residual Metal Catalyst Nanoparticles Even after Washing with Nitric Acid at Elevated Temperature Because These Metal Nanoparticles Are Sheathed by Several Graphene Sheets. *Langmuir* **2007**, *23*, 6453-6458.

39. Rosca, I. D.; Watari, F.; Uo, M.; Akaska, T. Oxidation of Multiwalled Carbon Nanotubes by Nitric Acid. *Carbon* **2005**, *43*, 3124-3131.

40. Pumera, M.; Iwai, H. Multicomponent Metallic Impurities and Their Influence Upon the Electrochemistry of Carbon Nanotubes. *J. Phys. Chem. C* **2009**, *113*, 4401-4405.

41. Fan, Y. W.; Goldsmith, B. R.; Collins, P. G. Identifying and Counting Point Defects in Carbon Nanotubes. *Nat. Mater.* **2005**, *4*, 906-911.

42. Dumitrescu, I.; Wilson, N. R.; Macpherson, J. V. Functionalizing Single-Walled Carbon Nanotube Networks: Effect on Electrical and Electrochemical Properties. *J. Phys. Chem. C* **2007**, *111*, 12944-12953.

43. Pickett, D. F.; Maloy, J. T. Micro-Electrode Studies of Electrochemically Coprecipitated Cobalt Hydroxide in Nickel-Hydroxide Electrodes. *J. Electrochem. Soc.* **1978**, *125*, 1026-1032.

44. Corrigan, D. A. The Catalysis of the Oxygen Evolution Reaction by Iron Impurities in Thin-Film Nickel-Oxide Electrodes. *J. Electrochem. Soc.* **1987**, *134*, 377-384.

45. Jayashree, R. S.; Kamath, P. V. Nickel Hydroxide Electrodeposition from Nickel Nitrate Solutions: Mechanistic Studies. *J. Power Sources* **2001**, *93*, 273-278.

46. Streinz, C. C.; Hartman, A. P.; Motupally, S.; Weidner, J. W. The Effect of Current and Nickel Nitrate Concentration on the Deposition of Nickel-Hydroxide Films. *J. Electrochem. Soc.* **1995**, *142*, 1084-1089.

47. Hu, Y. N.; Scherson, D. A. Potential-Induced Plastic Deformations of Nickel Hydrous Electrodes in Alkaline Electrolytes: An in Situ Atomic Force Microscopy Study. *J. Phys. Chem. B* **1997**, *101*, 5370-5376.

48. Hopper, M. A.; Ord, J. L. Optical Study of Growth and Oxidation of Nickel Hydroxide Films. *J. Electrochem. Soc.* **1973**, *120*, 183-187.

49. Wolf, J. F.; Yeh, L. S. R.; Damjanovic, A. Anodic Oxide-Films at Nickel Electrodes in Alkaline-Solutions.1. Kinetics of Growth of the Beta-$Ni(OH)_2$ Phase. *Electrochim. Acta* **1981**, *26*, 409-416.

50. Deo, R. P.; Lawrence, N. S.; Wang, J., Electrochemical Detection of Amino Acids at Carbon Nanotube and Nickel-Carbon Nanotube Modified Electrodes. *Analyst* **2004**, *129*, 1076-1081.

51. Liao, S. J.; Holmes, K. A.; Tsaprailis, H.; Birss, V. I. High Performance PtRulr Catalysts Supported on Carbon Nanotubes for the Anodic Oxidation of Methanol. *J. Am. Chem. Soc.* **2006**, *128*, 3504-3505.

52. Luo, H. X.; Shi, Z. J.; Li, N. Q.; Gu, Z. N.; Zhuang, Q. K. Investigation of the Electrochemical and Electrocatalytic Behavior of Single-Wall Carbon Nanotube Film on a Glassy Carbon Electrode. *Anal. Chem.* **2001**, *73*, 915-920.

53. Paolucci, D.; Marcaccio, M.; Bruno, C.; Paolucci, F.; Tagmatarchis, N.; Prato, M. Voltammetric Quantum Charging Capacitance Behaviour of Functionalised Carbon Nanotubes in Solution. *Electrochim. Acta* **2008**, *53*, 4059-4064.

54. Bertoncello, P.; Edgeworth, J. P.; Macpherson, J. V.; Unwin, P. R. Trace Level Cyclic Voltarnmetry Facilitated by Single-Walled Carbon Nanotube Network Electrodes. *J. Am. Chem. Soc.* **2007**, *129*, 10982-10983.

55. Zhang, G.; Cuharuc, A. S.; Güell, A. G.; Unwin, P. R. Electrochemistry at Highly Oriented Pyrolytic Graphite (HOPG): Lower Limit for the Kinetics of Outer-Sphere Redox Processes and General Implications for Electron Transfer Models. *Phys. Chem. Chem. Phys.* **2015**, *17*, 11827-11838.

56. Cuharuc, A. S.; Zhang, G.; Unwin, P. R., Electrochemistry of Ferrocene Derivatives on Highly Oriented Pyrolytic Graphite (HOPG): Quantification and Impacts of Surface Adsorption. *Phys. Chem. Chem. Phys.* **2016**, *18*, 4966-4977.

57. Portemer, F.; Delahayevidal, A.; Figlarz, M., Characterization of Active Material Deposited at the Nickel-Hydroxide Electrode by Electrochemical Impregnation. *J. Electrochem. Soc.* **1992**, *139*, 671-678.

58. Dudin, P. V.; Unwin, P. R.; Macpherson, J. V. Electrochemical Nucleation and Growth of Gold Nanoparticles on Single-Walled Carbon Nanotubes: New Mechanistic Insights. *J. Phys. Chem. C* **2010**, *114*, 13241-13248.

59. Zhang, G. H.; Kirkman, P. M.; Patel, A. N.; Cuharuc, A. S.; McKelvey, K.; Unwin, P. R. Molecular Functionalization of Graphite Surfaces: Basal Plane Versus Step Edge Electrochemical Activity. *J. Am. Chem. Soc.* **2014**, *136*, 11444-11451.

60. Güell, A. G.; Meadows, K. E.; Dudin, P. V.; Ebejer, N.; Macpherson, J. V.; Unwin, P. R. Mapping Nanoscale Electrochemistry of Individual Single-Walled Carbon Nanotubes. *Nano Lett.* **2014**, *14*, 220-224.

61. E, S. P.; Miller, T. S.; Macpherson, J. V.; Unwin, P. R. Controlled Functionalisation of Single-Walled Carbon Nanotube Network Electrodes for the Enhanced Voltammetric Detection of Dopamine. *Phys. Chem. Chem. Phys.* **2015**, *17*, 26394-26402.

62. Lide, D. R. *Handbook of Chemistry and Physics*; CRC Press: Boca Raton, FL, 2009.

63. Crank, J. *The Mathematics of Diffusion*; Clarendon Press: Oxford, UK, 1975.

64. Breiter, M.; Hoffmann, K. Z. *Elektrochem.* **1960**, 64, 462.

65. Goldstein, J.; Newbury, D. E.; Echlin, P.; Joy, D. C.; Fiori, C.; Lifshin, E. *Scanning Electron Microscopy and X-Ray Microanalysis: A Text for Biologists, Materials Scientists, and Geologists*; Springer US: New York, 2013.

66. Fantini, M. C. A.; Gorenstein, A. Electrochromic Nickel-Hydroxide Films on Transparent Conducting Substrates. *Sol. Energ. Mater.* **1987**, 16, 487-500.

67. Song, Q. S.; Tang, Z. Y.; Guo, H. T.; Chan, S. L. I. Structural Characteristics of Nickel Hydroxide Synthesized by a Chemical Precipitation Route under Different pH Values. *J. Power Sources* **2002**, *112*, 428-434.

68. McEwen, R. S. Crystallographic Studies on Nickel Hydroxide and Higher Nickel Oxides. *J. Phys. Chem.* **1971**, *75*, 1782-1789.

69. Parks, E. K.; Zhu, L.; Ho, J.; Riley, S. J. The Structure of Small Nickel Clusters .2. Ni-16-Ni-28. *J. Chem. Phys.* **1995**, *102*, 7377-7389.

70. Ayeb, A.; Notten, P. H. L. The Oxygen Evolution Kinetics in Sealed Rechargeable NiMH Batteries. *Electrochim. Acta* **2008**, *53*, 5836-5847.

71. Cornilsen, B. C.; Shan, X. Y.; Loyselle, P. L. Structural Comparison of Nickel Electrodes and Precursor Phases. *J. Power Sources* **1990**, *29*, 453-466.

72. Kamath, P. V.; Dixit, M.; Indira, L.; Shukla, A. K.; Kumar, V. G.; Munichandraiah, N. Stabilized α-$Ni(OH)_2$ as Electrode Material for Alkaline Secondary Cells. *J. Electrochem. Soc.* **1994**, *141*, 2956-2959.

73. Kumar, V. G.; Munichandraiah, N.; Kamath, P. V.; Shukla, A. K. On the Performance of Stabilized α-Nickel Hydroxide as a Nickel-Positive Electrode in Alkaline Storage Batteries. *J. Power Sources* **1995**, *56*, 111-114.

74. French, H. M.; Henderson, M. J.; Hillman, A. R.; Vieil, E. Ion and Solvent Transfer Discrimination at a Nickel Hydroxide Film Exposed to LiOH by Combined Electrochemical Quartz Crystal Microbalance (EQCM) and Probe Beam Deflection (PBD) Techniques. *J. Electroanal. Chem.* **2001**, *500*, 192-207.

75. Maiyalagan, T.; Scott, K. Performance of Carbon Nanofiber Supported Pd-Ni Catalysts for Electro-Oxidation of Ethanol in Alkaline Medium. *J. Power Sources* **2010**, *195*, 5246-5251.

76. McBreen J. *Nickel Hydroxides. In Handbook of Battery Materials*; Wiley-VCH Verlag GmbH & Co.KGaA.: Weinheim, Germany, 2011.

77. Ma, Y.; Li, H.; Wang, H.; Mao, X.; Linkov, V.; Ji, S.; Gcilitshana, O. U.; Wang, R. Evolution of the Electrocatalytic Activity of Carbon-Supported Amorphous Platinum-Ruthenium-Nickel-Phosphorous Nanoparticles for Methanol Oxidation. *J. Power Sources* **2014**, *268*, 498-507.

78. Ye, L.; Li, Z.; Zhang, L.; Lei, F.; Lin, S. A Green One-Pot Synthesis of Pt/TiO_2/Graphene Composites and Its Electro-Photo-Synergistic Catalytic Properties for Methanol Oxidation. *J. Colloid Interf. Sci.* **2014**, *433*, 156-162.

79. Fu, G.-T.; Ma, R.-G.; Gao, X.-Q.; Chen, Y.; Tang, Y.-W.; Lu, T.-H.; Lee, J.-M. Hydrothermal Synthesis of Pt-Ag Alloy Nano-Octahedra and Their Enhanced Electrocatalytic Activity for the Methanol Oxidation Reaction. *Nanosc.* **2014**, *6*, 12310-12314.

80. Chen, D. J.; Sun, S. G.; Tong, Y. Y. J. On the Chemistry of Activation of a Commercial Carbon-Supported PtRu Electrocatalyst for the Methanol Oxidation Reaction. *Chem. Commun.* **2014**, *50*, 12963-12965.

81. Li, L.; Chen, M.; Huang, G.; Yang, N.; Zhang, L.; Wang, H.; Liu, Y.; Wang, W.; Gao, J. A Green Method to Prepare Pd-Ag Nanoparticles Supported on Reduced Graphene Oxide and Their Electrochemical Catalysis of Methanol and Ethanol Oxidation. *J. Power Sources* **2014**, *263*, 13-21.

82. Sieben, J. M.; Alvarez, A. E.; Comignani, V.; Duarte, M. M. E. Methanol and Ethanol Oxidation on Carbon Supported Nanostructured Cu Core Pt-Pd Shell

Electrocatalysts Synthesized via Redox Displacement. *Int. J. Hydrogen Energ.* **2014**, *39*, 11547-11556.

83. Zhu, F.; Ma, G.; Bai, Z.; Hang, R.; Tang, B.; Zhang, Z.; Wang, X. High Activity of Carbon Nanotubes Supported Binary and Ternary Pd-Based Catalysts for Methanol, Ethanol and Formic Acid Electro-Oxidation. *J. Power Sources* **2013**, *242*, 610-620.

Chapter 6 Nanoscale electrocatalysis of hydrazine electro-oxidation at blistered graphite electrodes

There is great interest in finding and developing new, efficient and more active electrocatalytic materials. Surface modification of highly oriented pyrolytic graphite (HOPG), through the introduction of surface "blisters", is demonstrated to result in an electrode material with greatly enhanced electrochemical (EC) activity. The increased EC activity of these blisters, which are produced by electro-oxidation in $HClO_4$, is revealed through the use of scanning electrochemical cell microscopy (SECCM) coupled with complementary techniques (optical microscopy, FE-SEM, Raman spectroscopy and AFM). The use of a linear sweep voltammetry (LSV)-SECCM scan regime allows for dynamic EC mapping, where a voltammogram is produced at each pixel, from which movies consisting of spatial EC currents at a series of applied potentials are produced. The measurements reveal significantly enhanced activity at blisters compared to the basal planes, with a significant cathodic shift of the onset potential for hydrazine oxidation reaction. The improved EC activity of the hollow structure of blistered graphite could be explained by the increased adsorption of protonated hydrazine at oxygenated defect sites, the ease of ion-solvent intercalation/de-intercalation and the susceptibility to N_2 nanobubble attachment (as a product of the reaction). This study highlights the capability of electrochemistry to tailor the surface structure of graphite and presents a new electrocatalyst for hydrazine electro-oxidation.

6.1 Introduction

There has been an intense push towards efficient and inexpensive alternatives to noble-metal electrocatalysts (*i.e.* platinum and ruthenium) for a wide range of applications.[1-4] Great efforts have been made in developing non-noble metals catalysts through means of surface modification, doping and alloying,[5, 6] with varying degrees of success.[7] Beyond metals, carbon-based materials, which have mainly used as supports for electrocatalysts,[8, 9] are receiving increasing attention as electrocatalysts in their own right.[7, 10-12] Carbon is an attractive proposition, due to the possibility of modification by doping and surface functionalization in a wide variety of ways.[13-15] This is particularly true of graphite which comprises stacked graphene layers with weak bonding energy of van der Waals force between the layers.[7]

While outer sphere redox processes and some more complex electron-proton coupled processes, occur readily at the basal structure of graphite,[16-21] electrocatalytic (bond-breaking) reactions often require additional efforts to promote the electrochemical (EC) activity. There are 3 broad and somewhat interrelated, approaches and effects to consider: (i) selective doping of sp^2 materials by various heteroatoms (*e.g.* N,[22] B,[23] S,[24] and P[25]); (ii) surface modification with different functional groups by chemical oxidation, or grafting;[26, 27] (iii) defects, which may promote electrocatalysis.[28, 29] An interesting way to introduce defects is by intercalation of anions (ClO_4^-, NO_3^- and SO_4^{2-}) during the EC oxidation of sp^2 carbon materials (*e.g.* graphite), which ultimately leads to delamination, followed by fracturing into a bubble-like blister structure (hollow interior) presented on the

graphite surface.[30-32] These are interesting structures, but their electrocatalytic properties have not been widely studied.

Herein, we investigate the electrocatalytic activity of blisters on an HOPG surface for hydrazine (N_2H_4) oxidation. Hydrazine is a high-energy fuel molecule, which has been investigated for the development of high power density direct hydrazine-air fuel cells.[33] Separately, hydrazine is a carcinogenic and hepatotoxic compound which affects liver and brain glutathione,[34] and the development of strategies for hydrazine detection is especially important, with EC detection showing promise.[35, 36]

High spatiotemporal resolution EC measurements provide major insight into the activity of functional electrode materials and our group has shown that scanning electrochemical cell microscopy (SECCM) is particularly promising for revealing nanoscale EC activity and topographic information at various substrates and is especially powerful when combined with other forms of microscopy, applied to the same area as EC mapping, in a correlative approach.[37-40] In this chapter, we use hopping voltammetric mode SECCM, in which a linear sweep voltammetry (LSV) measurement is performed at each location (pixel) of the defined scan area. These data can be processed to provide EC activity maps, comprising hundreds of spatially-resolved current measurements as a function of potential, that can be played back as a movie, from which potential resolved snapshots can be extracted and from which current-voltage curves, Tafel analysis, etc. can be performed at individual pixels. The use of complementary microscopy techniques applied to the same area, including optical microscopy, scanning electron microscopy (SEM), atomic force microscopy

(AFM) and micro-Raman, permits detailed investigations into structure-activity relationships of nanoscale features.

6.2 Experimental

6.2.1 Materials

All chemicals were used as received. Electrolyte solutions were prepared freshly using deionized water produced by a Purite Select HP system (resistivity of 18.2 MΩ cm at 25 ^{o}C) and $HClO_4$ (70 %, Sigma Aldrich). 5 mM Hydrazine (64 %, Acros Organics) was prepared in 0.1 M phosphate-buffered solution (PBS, pH 7.4). PBS was prepared in house from sodium phosphate dibasic heptahydrate ($Na_2HPO_4{\cdot}7H_2O$, Sigma-Aldrich, 98-102 %) and sodium dihydrogen orthophosphate dihydrate ($NaH_2PO_4{\cdot}2H_2O$, Fisher Scientific, 99-101 %). Pd wire (99.9 %, 0.25 mm diameter, Alfa Aesar) was used to make Pd-H_2 quasi-reference counter electrodes (QRCEs) and quasi-reference electrodes (QREs) as described elsewhere.[38] All reported potentials are against the reversible hydrogen electrode ($E_{\mathrm{Pd-H_2}} = 50$ mV $vs.$ RHE).[41] A high-quality AM-grade HOPG sample was used as a substrate, originating from Dr. A. Moore, Union Carbide (now GE Advanced Ceramics) and kindly provided by Prof. Richard L. McCreery (University of Alberta, Canada).

6.2.2 Droplet experiments

The EC formation of blisters was carried out in a 3-electrode setup, with freshly cleaved AM-grade HOPG acting as the working electrode (WE). Electrical contact to the WE was made via conductive Ag paint applied to electrometer head unit. A drop of electrolyte solution (~10 µL of 0.1 M $HClO_4$, ~ 4 mm dia.) was placed on the HOPG

surface (Figure 6.1a). A Pt wire (99.95 %, 0.6 mm thickness, Alfa Aesar) was used as a counter electrode (CE) and Pd-H_2 wire acted as a QRE. These positioned within the droplet of solution.[18, 42] The EC measurements were performed with a CHI 730 EC workstation (CH Instruments, TX, USA).[43, 44]

6.2.3 Hopping scanning electrochemical cell microscopy-linear sweep voltammetry experiments

Dual channel borosilicate theta capillaries (ID = 1.0 mm, OD = 1.5 mm, Harvard Apparatus, UK) were pulled using a laser pipette puller (P-2000, Sutter Instrument Co., USA) to produce nanopipettes with a diameter of around 400 nm (200 nm each channel). Nanopipettes were silanized using dichlorodimethylsilane (>99 %, Acros) to produce a hydrophobic outer surface, with Ar gas flowing through to prevent any internal silanization. This ensured confined aqueous meniscus contact during SECCM experiments.[37]

A schematic illustrating the hopping SECCM method is shown in Figure 6.1b. Briefly, a dual barrel nanopipette filled with 5 mM N_2H_4 solution and a Pd-H_2 wire in each channel, which act as QRCEs, functions as both a conductimetric cell and voltammetric cell. The nanopipette was approached towards the surface of the HOPG substrate until the meniscus just made contact (without contact from the nanopipette itself). The nanopipette was used to make a series of measurements by landing the meniscus at a set of predefined locations. Electrolyte residues from the SECCM meniscus (*vide infra*) were visualized after experiments using field emission-scanning electron microscopy (FE-SEM) (Supra 55-VP, Zeiss) to provide key information

about the meniscus size and location. The hopping distance between each pixel was 2 μm to avoid overlap of the probed areas (~ 900 nm in dia.).

High precision control of the meniscus contact was achieved by applying a bias voltage (V_2, 200 mV) between the two QRCEs to produce a direct ion current (I_{IC}) across the meniscus. The nanopipette was oscillated perpendicular to the surface (267 Hz, 14 nm peak-to-peak amplitude) to induce an alternating component (AC) to the ion current between two barrels when the meniscus came into contact with the surface. The AC signal, at the generated oscillation frequency, was detected using a lock-in amplifier (SR380, Stafford Research System) and the resulting AC ion current served as the feedback signal for positioning the nanopipette at a set distance from the electrode surface. The working electrode potential (E_s) was $-(V_1 + V_2/2)$ *vs.* Pd-H_2, against which all the EC currents of the substrate (I_{EC}) were measured using a custom built, high-sensitivity, current-to-voltage converter. The voltammetric scan rate was 500 mV s^{-1}, applied at each point of meniscus contact, giving a spatial array of voltammograms. Data analysis was performed in Matlab (R2014b, Mathworks Inc.) to provide I_{EC} spatial maps over a set of potentials which could also be presented as movies.[37, 45]

6.2.4 Micro-Raman and atomic force microscopy experiments

Micro-Raman spectroscopy (InVia Reflex Raman, Renishaw, UK) fitted with a solid state 532 nm laser and a 50× lens was used to determine the nature of the treated HOPG surface. For Raman mapping, the laser beam was raster-scanned across the area of interest, with spectra obtained every 0.8 μm and 1.0 μm over two predefined areas.

AFM imaging of the HOPG was carried out in air in tapping mode (Innova, Veeco-Bruker).

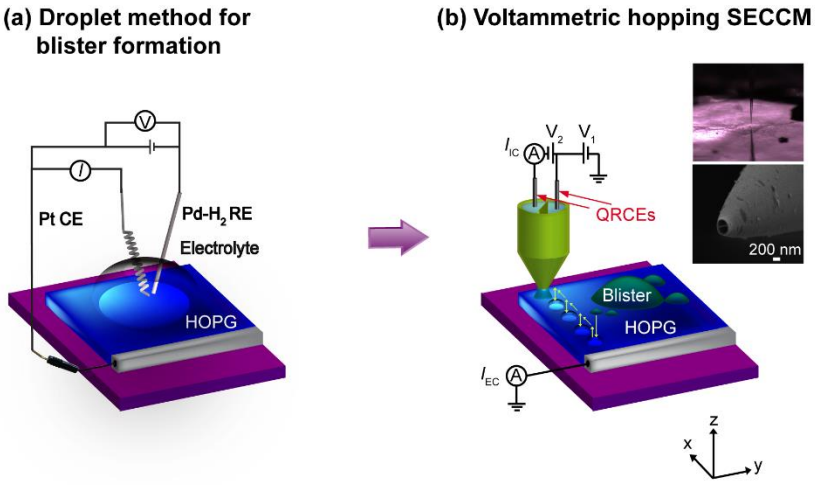

Figure 6.1 Experimental setup for (a) blister formation on HOPG using the droplet method (0.1 M $HClO_4$) and (b) nanoscopic electrocatalytic measurement using voltammetric hopping mode SECCM. For SECCM, a bias voltage (V_2) was applied between two QRCEs and the resulting ion conductance current (I_{IC}) was measured and used for nanopipette positioning. A substrate voltage (V_1) was applied to one of the QRCEs to control the working electrode potential (E_s = – (V_1 + V_2/2) *vs*. Pd-H_2) and the working electrode current (I_{EC}) was measured. Small amounts of residue were left on the surface after withdrawing the nanopipette from each position, which aided location identification by other techniques. The arrows show the movement of the nanopipette.

6.3 Results and discussion

6.3.1 Surface blistering of highly oriented pyrolytic graphite

Perchlorate (ClO_4^-) is known to intercalate into HOPG at anodic potentials, with the extent of intercalation depending on the potential applied and time scale.[30, 42, 46] Three consecutive cyclic voltammograms (CVs) were performed on freshly cleaved HOPG in 0.1 M $HClO_4$, with start and reverse potentials of 0.15 V_{RHE} and 2.35 V_{RHE},

respectively (25 mV s^{-1}). The insertion and removal of ClO_4^- ions is manifest as redox peaks, as shown in Figure 6.2a and the inset. For the first anodic scan of the CV, small oxidation peaks at 1.95 V_{RHE} (I), 2.12 V_{RHE} (II) and 2.22 V_{RHE} (III) are similar to those seen previously that were attributed to three different anion intercalation stages.[30-32, 47] A broad reduction peak at ca. 0.17 V_{RHE} on the reverse scan corresponds to de-intercalation of ClO_4^- from the graphite. The current magnitudes for the redox peaks increased and progressively shifted towards more cathodic values as the number of cycles increased, which can be attributed to more facile anion intercalation/de-intercalation.

On the anodic scan of the CV, ClO_4^- ions, along with solvent and acid molecules, are incorporated into the graphite lattice through defect sites, overcoming the weak interlayer van der Waals' interactions between the graphene layers.[32, 48] The intercalation process[31] can be described by:

$$C_x + ClO_4^- + yHClO_4 \rightleftharpoons C_x^+ClO_4^-(HClO_4)y + e^- \quad (1)$$

Irreversible side reactions involving graphite oxide formation and water electrolysis may also occur at anodic potentials. These reactions contribute to the anodic currents at relatively high positive potentials.[46] Surface quinone-hydroquinone redox reactions[49] may also occur at EC-functionalized graphite surface involving the alcohol and carbonyl groups that are formed at edge plane and defect sites.

Figure 6.2b shows an FE-SEM image of HOPG after oxidation in $HClO_4$ for three potential cycles (as defined above). The image reveals blisters along grain boundaries (GBs). The magnified FE-SEM image (Figure 6.2c) shows large blisters of irregular shapes, aligned along GBs with small blisters extending to the surrounding

GBs, consistent with previous studies.[30] The mechanism of blister formation on HOPG is shown schematically in Figure 6.2d.[30-32]

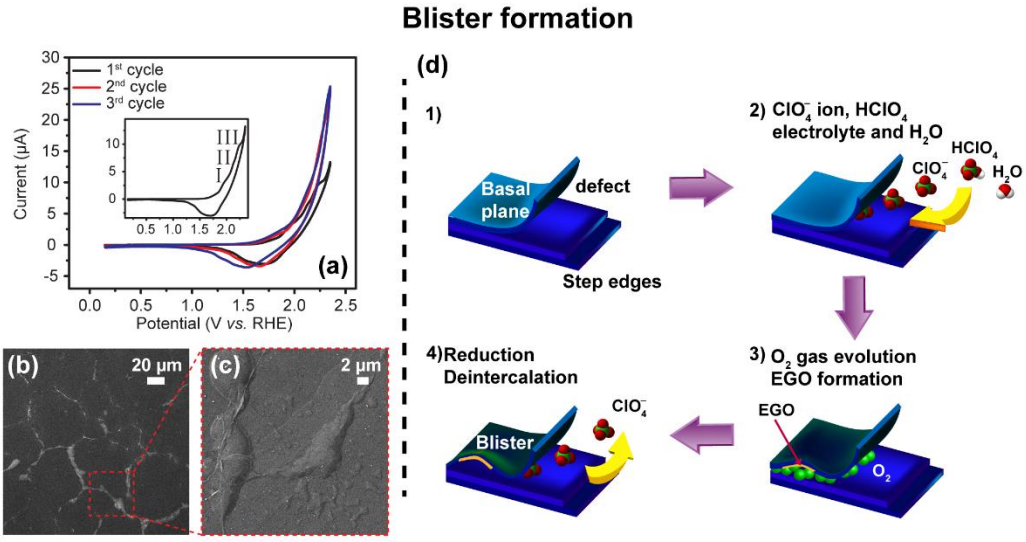

Figure 6.2 Three consecutive CVs recorded at HOPG in 0.1 M $HClO_4$ (25 mV s^{-1}). Peak positions on the potential scale (inset figure) are mentioned in the text. (b and c) Corresponding FE-SEM images recorded on a blistered region of HOPG after the measurement in (a). (d) Schematic depicting the formation of a blister on HOPG.[30-32] 1) The basal plane and surface defects (step edges and GBs) on HOPG electrode prior to electro-oxidation in 0.1 M $HClO_4$ solution. 2) Intercalation of ClO_4^- ions occurs along with the intercalation of $HClO_4$ and H_2O at defect sites during the anodic scanning of the electrode potential. 3) At more anodic potential (and/or more extensive electro-oxidation times), blister formation occurs due to mechanical stress, for example, from gas evolution. The orange colored area represents electrochemically formed graphite oxide (EGO). 4) Ions de-intercalate during the reverse scan (reduction reaction), leaving behind the blister.

Anion intercalation starts close to, or at, surface defects (Figure 6.2d (1)). Intercalation of anions (ClO_4^-) first expands the interlayer gap for efficient intercalation of the solvent molecules into the graphite lattice during the anodic scan of CV (Figure 6.2d (2)). Figure 6.2d (3) shows gas evolution (*e.g.* O_2 formation) from side reactions, occurring along with electrochemically generated graphite oxide (EGO). The

mechanical stress, originating from the gas evolution, in particular, induces surface blistering on HOPG. De-intercalation of anion occurs during the reverse scan of the CV (Figure 6.2d (4)).

6.3.2 Characterization of surface blisters on highly oriented pyrolytic graphite using atomic force microscopy and Raman microscopy

A typical AFM image of AM-grade HOPG recorded prior to EC cycling in 0.1 M $HClO_4$ is shown in Figure 6.3a. The HOPG surface is characterized by extensive flat terraces, with a few step edges clearly visible. The HOPG surface is dramatically changed after three repetitive voltammetric cycles in 0.1 M $HClO_4$ (same conditions as Figure 6.2a). Figure 6.3b shows two small blisters of circular shape, ca. 1.2 μm across and 10 – 14 nm in height (Figure 6.3d). Figure 6.3c shows a mixture of small and large blisters of irregular shape, ranging from 0.5 – 5 μm across and 10 – 90 nm in height (Figure 6.3e). The elongated shape of blisters could be due to the blister formation along the GBs and extension in those directions, resulting from the merging of several smaller blisters. Mechanical forces originating from gas evolution in the anodic oxidation process is known to result in blister growth.[31]

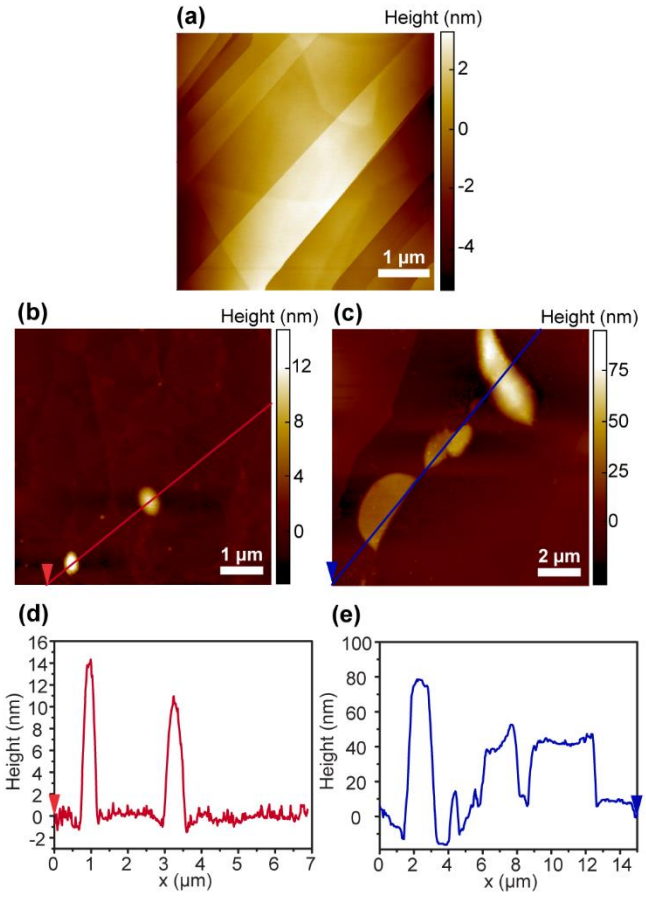

Figure 6.3 Typical AFM images of AM HOPG (a) before and after (b and c) voltammetric cycling 0.1 M $HClO_4$ (conditions as Figure 6.2a), leading to surface blistering. (d and e) Corresponding height cross sections of surface blistered regions. Note the different height scale bars.

Figure 6.4a(i) and b(i) show optical micrographs of two "blistered" areas on HOPG. Within these two regions are areas with basal planes and blisters and these were analyzed with micro-Raman spectroscopy in terms of *D* band intensity (Figures 6.4a(ii) and 6.4b(ii)) and *G*/*D* ratio (Figures 6.4a(iii) and 6.4b(iii)). The micro-Raman spectra in Figures 6.4a(iv-vi) and b(iv-vi) were normalized with respect to the intensity of the second-order double resonance (2*D*) at 2710 cm^{-1} to permit easy comparison. The *D*-peak at 1350 cm^{-1} originates from the breakup of hexagonal sp^2 carbon atoms in the graphitic planes.[50] The Raman maps in Figures 6.4a(ii) and b(ii) show a higher

intensity of the *D*-peak at blisters that are aligned along the GBs. Corresponding micro-Raman spectra of the *D*-peak intensity for the surface blistered region increases by ca. 360 % (Figure 6.4a(iv and vi) and ca. 870 % (Figure 6.4b(iv and vi)) relative to the basal plane region. Oxidation of HOPG in 0.1 M $HClO_4$ above 1.5 V evidently caused graphite lattice damage as indicated by the increased intensity of the *D*-peak.[46, 51] The intense line at 1565-1595 cm^{-1} is assigned to the *G*-peak, which is also indicative of sp^2 carbon.[52] The *G*-peak in Figures 6.4 a(iv-vi) show little, or no difference between the blister and basal planes, but the *G*-peak bands in Figures 6.4 b(iv and vi) are significantly broader than usual. This can be attributed to an EGO region produced during the anodic oxidation process that varies across different regions of the "blistered" HOPG, with the broader *G*-band response caused by a thicker EGO film.[53] Typically, EGO films contain many anionic sites and are highly permeable to small molecules.[54]

The same scenario is apparent for the intensity of the *G*-peak with respect to the intensity of the *D*-peak *i.e.* (i_G /i_D), which is often used for the evaluation of the defect density in graphite.[50] Clearly, the value of i_G /i_D decreases at the blistered area. It should be noted that blisters were found only inside the contact area of the droplet at the surface of the HOPG substrate in Figures 6.2b, indicating that they were generated by the EC process. Thus, these results show that the EC generation of graphitic blisters leads to a considerable alteration of local structure.

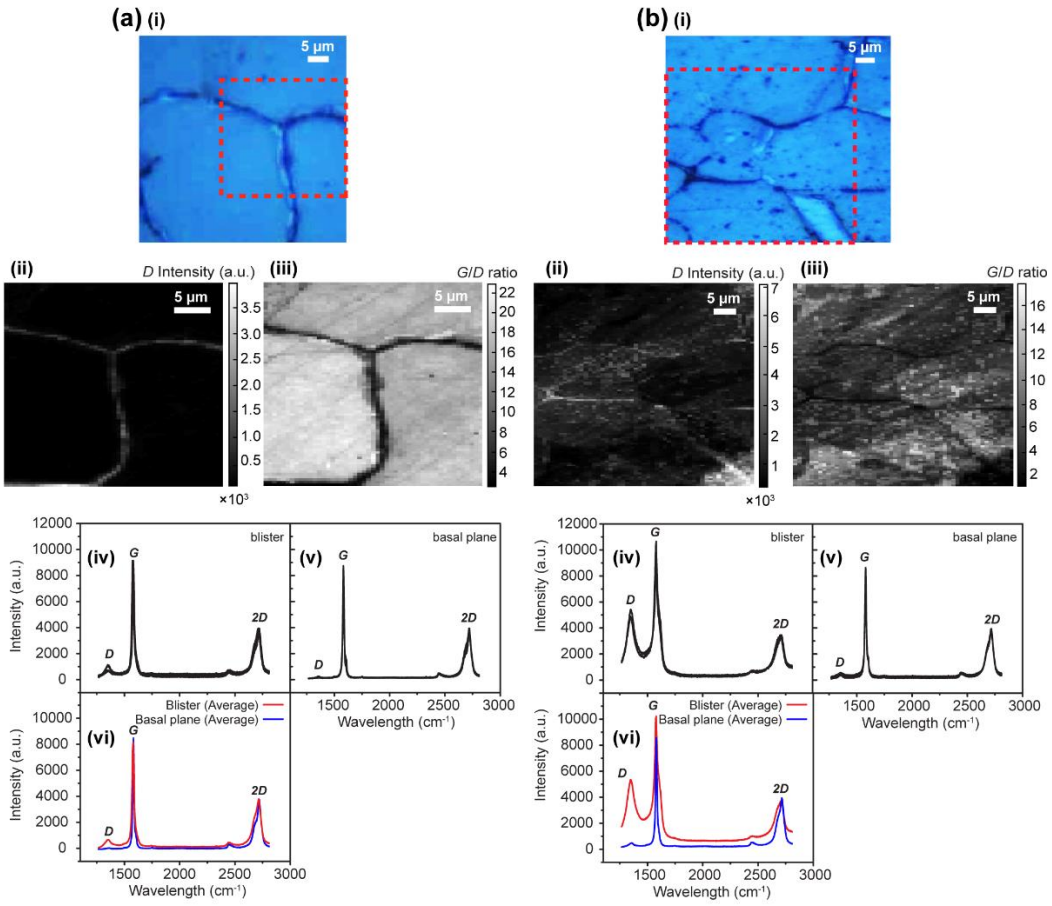

Figure 6.4 Optical micrographs (i) of two surface blistered regions (a and b) with corresponding micro-Raman maps of: (ii) i_D and (iii) i_G/i_D ratio, along with individual Raman spectra at (iv) blistered and (v) basal plane regions of an EC-treated HOPG surface. (vi) Averaged-spectra (n = 3 – 5) of the surface blistered region (red) and basal plane (blue) of the treated HOPG surface.

6.3.3 Scanning electrochemical cell microscopy imaging at the "blistered" highly oriented pyrolytic graphite for hydrazine oxidation

We first consider an area (40 μm × 30 μm) of an EC-treated HOPG surface consisting of blisters formed where two or more grains meet. The SECCM voltammetric scan regime provides a series of potential-resolved images of I_{EC} at a set of x-y coordinates from which an EC map at a given potential can be extracted, or a movie can be played.

Figures 6.5a shows an EC map at the most positive potential obtained from the SECCM-LSV movie file which contains 191 images (336 pixels), one image every 2.56 mV, with the potential scanned from 0.45 V_{RHE} to 2.35 V_{RHE}. FE-SEM performed after SECCM imaging showed meniscus residues with fairly consistent shape and size on the surface (Figure 6.5b), from which one can deduce that each measurement has a very similar local working electrode area. By coupling the SECCM measurement with FE-SEM applied to the same area, a detailed correlation of structure with electrocatalytic properties is revealed. The immediate and striking observation is that the EC map in Figure 6.5a shows relatively high EC activity at the blisters along the GBs (region 1), as compared to the basal plane area (region 2).

To analyze the EC behavior in detail, raw LSV data are extracted at two regions, 1 and 2 (Figures 6.5c), with LSVs from 5 individual pixels in each area (black), along with the resulting average LSV for each area (red). At a potential of 1.5 V_{RHE}, the peak current for hydrazine electro-oxidation in the blister (region 1) is ca. 1.3 nA. This current is significantly enhanced as compared to the basal plane (region 2) with peak current of ca. 0.5 nA, but at a much higher overpotential, ca. 2.05 V_{RHE}. Furthermore, that the onset potential for hydrazine electro-oxidation at a blister (ca. 0.8 V_{RHE}) is significantly shifted to a more cathodic potential when compared voltammetrey at the basal plane (ca. 1.6 V_{RHE}), indicating that this blister has greatly enhanced electrocatalytic activity for the electro-oxidation of hydrazine. Note that the limiting current is higher for the blistered graphite, as compared to a standard gold electrode in the same SECCM configuration (Figure 6.6). Furthermore, SECCM voltammetry at the basal graphite surface gives a limiting current similar to gold (albeit shifted cathodically by a large value). The higher current magnitude at the blister, is

most likely due to the electrowetting of the substrate by the meniscus during ions intercalation/deintercalation, driven by the applied potential.[42] Interestingly, however, the electroactivity of the blistered region lies between that of the gold electrode and basal plane graphite, highlighting how simple surface modification can impart significant electrocatalytic effects.

A Tafel map (Figure 6.5d) was obtained to highlight the different kinetic regimes across the treated HOPG surface. The voltammetric data were analyzed in the potential intervals from 0.65 to 1.10 V (blistered region) and 1.40 to 1.70 V (basal plane region) corresponding to the foot of the wave, where mass transport and, as such, concentration polarization could be neglected in each case. The Tafel slope was in the range 100 – 180 mV/decade (region 1) and 250 – 400 mV/decade (region 2). The Tafel slopes of the blistered region are superior to alternative carbon-based electrode catalyst, such as polypyrrole[55] or curcumin modified multi-walled carbon nanotubes[56] on a glassy carbon support. The charge transfer coefficient, α, was 0.33 – 0.59 in the blistered region which was determined from the Tafel slope, indicating a more or less one-electron process in the rate determining step, followed by processes amounting to the transfer of a further three electrons to give N_2 as a final product:[57, 58]

$$N_2H_5^+ \rightarrow N_2H_3(ads) + 2H^+ + e^- \quad (2)$$

$$N_2H_3(ads) \rightarrow N_2 + 3H^+ + 3e^- \quad (3)$$

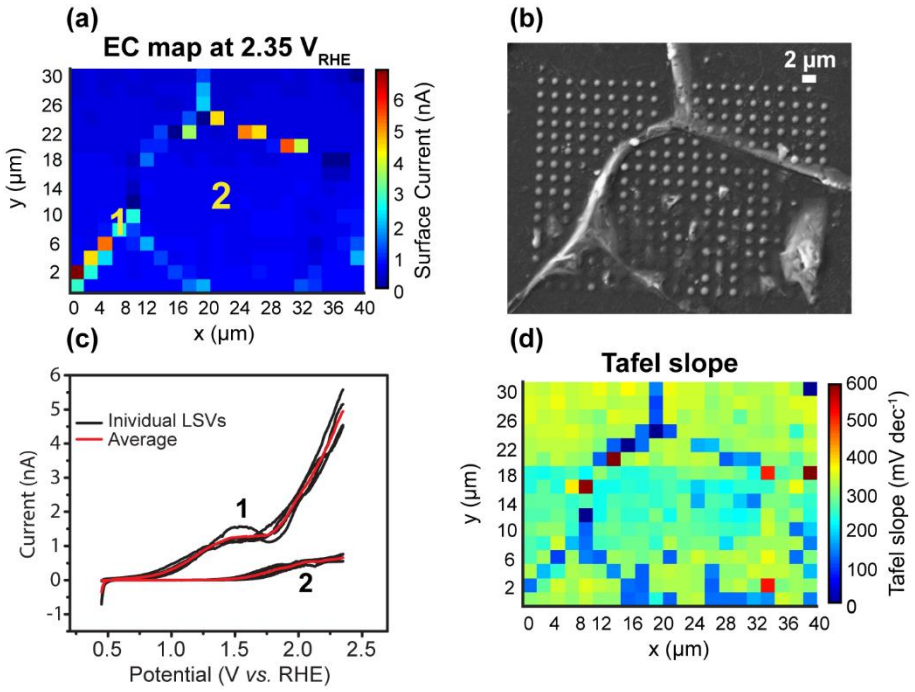

Figure 6.5 EC map of the modified HOPG substrate at (a) 2.35 V_{RHE} (5 mM N_2H_4). (b) FE-SEM image after SECCM imaging showing the locations of the individual pixels. (c) Individual LSVs (black, n = 5) and averaged LSV (red) for different regions marked in (a). (d) Tafel map (mV per decade) determined using data from 0.65 > E_s > 1.10 V_{RHE} (blister) and 1.40 > E_s > 1.70 V_{RHE} (basal plane).

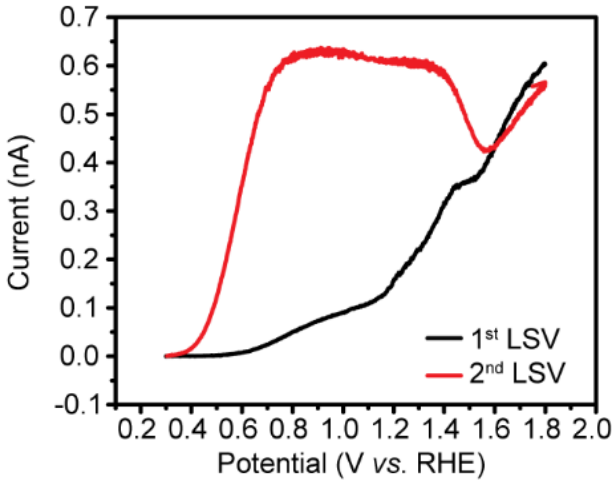

Figure 6.6 2 consecutive LSVs of hydrazine oxidation at a gold electrode in a SECCM setup. Electrolyte: 5 mM N_2H_4 in 0.1 M PBS. Scan rate: 500 mV s^{-1}.

To investigate further the influence of HOPG structure on hydrazine oxidation, SECCM imaging was performed in a different area (40 μm × 44 μm) of an acid modified HOPG sample, comprising small blisters and a relatively large blister along the GBs. The EC map in Figure 6.7a was extracted from an SECCM-LSV movie file in which the potential was scanned from 0.45 V_{RHE} to 2.1 V_{RHE} at each pixel (483 pixels with a hopping distance of 2 μm, Figure 6.7b). Strikingly, the EC map, shows high activity at the blisters present along the GBs, particularly noticeable at the circumference of the large spherical blister (Figure 6.7b). Raw LSV data for the hydrazine oxidation were extracted at two pixels, spot 1 and spot 2, (Figures 6.7c). At a potential of 1.5 V_{RHE}, the peak current of the hydrazine electro-oxidation was ca. 5.4 nA (spot 1) and ca. 1.8 nA (spot 2). These result reveals heterogeneous electroactivity within the blister structure, with the highest activity attributed to the blister edge.

For comparison, Figures 6.7d and 6.7e show individual LSVs (n = 5) and the averaged response for regions A and B, respectively. The EC behavior of the center of the blister (region A) is similar to the basal plane (region B) and displays low activity compared to the much more active regions of the blisters. Tafel analysis was performed on the SECCM scanned area and the resulting Tafel map is shown in Figure 6.7f. The analysis was in the potential range from 0.75 to 1.05 V (active region) and 0.90 to 1.30 V (less active region). The Tafel slope was 96±1 mV/decade (spot 1), 160±2 mV/decade (spot 2) and in the range 250 – 450 mV/decade (region A and B). These data again reveal the power of the SECCM voltammetric mode to highlight key areas of activity on an electrocatalytic surface and, in this case, to even pinpoint differences in activity within blisters.

At pH 7.4, hydrazine (p*K*a = 8.1)[59] is largely protonated and, the blistered region has a high density of negatively charged EGO film evident from the broader *G*-band (Figure 6.4b(iv)) and oxygen groups (–COOH, –OH, –CHO) formed during potential cycling in acid.[60] These groups on the modified graphite surface can act as potential sites to adsorb active species, leading to enhanced electron transfer kinetics.[61] Further, the more disordered nature of the blister (increased *D*-band in Figure 6.4a(vi) and 6.4b(vi)) compared to the basal surface, leads to more ready ion-solvent intercalation during electrocatalysis, which could be important for improving the EC activity. It should further be pointed out that N_2 nanobubbles can be formed during N_2H_4 electrooxidation and block the electrode surface.[62] The porous structure of blistered regions may aid the evolution of N_2 nanobubbles, resulting in enhancement of EC activity. Finally, and significantly, the electronic properties of graphite change dramatically by the introduction of defects,[63] in particular, resulting in a high density of state (DOS) near the Fermi level at defective graphite,[17, 52, 64] which would be expected to significantly enhance electrocatalysis.

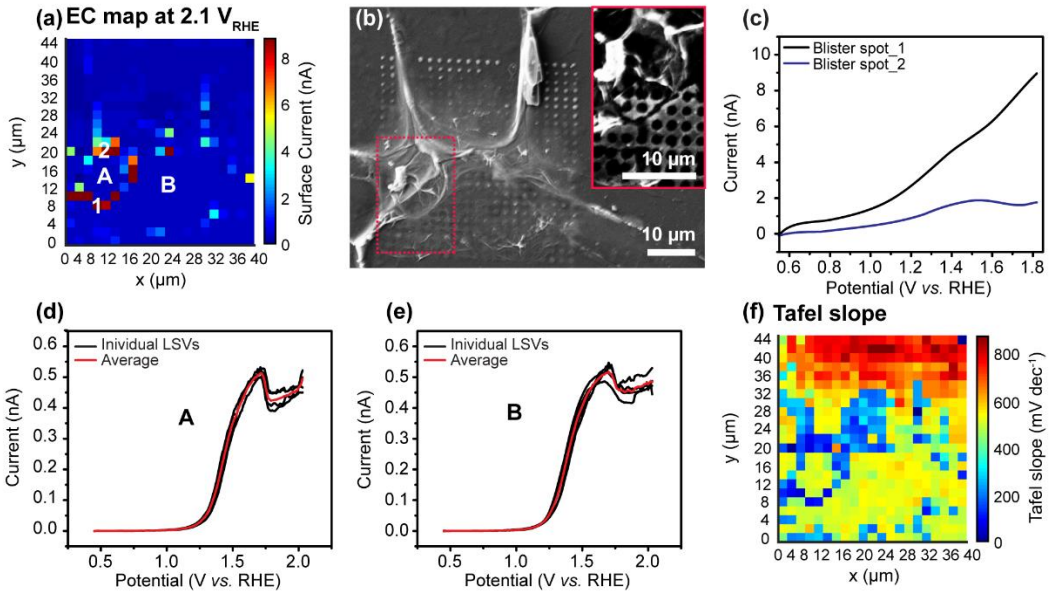

Figure 6.7 EC map of a modified HOPG substrate at (a) 2.1 V_{RHE} (5 mM N_2H_4) (b) FE-SEM image after SECCM imaging. LSV for different regions: (c) blister spots (1 and 2 in (a)), (d) Inner blister (A) (n = 5) and (e) basal plane (B) (n = 5). (f) Tafel map (mV per decade) determined using data from 0.75 > E_s > 1.05 V_{RHE} (blister) and 0.90 > E_s > 1.30 V_{RHE} (basal plane).

6.4 Conclusions

In this study, we have shown that surface blisters formed on HOPG (at GBs and step edges) during CV cycling in 0.1 M $HClO_4$ produces defect structures that have been characterized by FE-SEM and Raman microscopy. These structures show considerable electrocatalytic activity compared to basal HOPG areas on the same surface, as revealed by SECCM imaging. The use of the LSV-SECCM approach has enabled a potential sweep at every pixel of the scanned area, to provide detailed information on microscopic activity. The extensive data sets produced have allowed us to observe an earlier onset potential, higher peak current and smaller Tafel slope at the blistered area, all of which are indicative of enhanced electrocatalysis compared to the basal plane.

Several factors need to be considered to explain the dramatic effect of HOPG blisters on hydrazine electro-oxidation. These include enhanced adsorption of protonated hydrazine at the defect sites, the hollow nature of the blistered graphite that allows ion-solvent intercalation/de-intercalation during the electrocatalytic reaction and the porous structure of the blistered region that would be less susceptible to N_2 nanobubbles blocking access to the surface. Overall, the results show that electrochemistry is a powerful tool for engineering the surface properties of graphite to make an effective electrocatalyst and that state of the art EC imaging, in combination with other microscopy techniques allows detailed correlations between structure and activity to be drawn and explained.

6.5 References

1. Suntivich, J.; Gasteiger, H. A.; Yabuuchi, N.; Nakanishi, H.; Goodenough, J. B.; Shao-Horn, Y. Design Principles for Oxygen-Reduction Activity on Perovskite Oxide Catalysts for Fuel Cells and Metal-Air Batteries. *Nat. Chem.* **2011**, *3*, 546-550.

2. Chen, Z.; Higgins, D.; Yu, A.; Zhang, L.; Zhang, J. A Review on Non-Precious Metal Electrocatalysts for PEM Fuel Cells. *Energ. & Environ. Sci.* **2011**, *4*, 3167-3192.

3. Zheng, Y.; Jiao, Y.; Zhu, Y.; Li, L. H.; Han, Y.; Chen, Y.; Du, A.; Jaroniec, M.; Qiao, S. Z. Hydrogen Evolution by a Metal-Free Electrocatalyst. *Nat. Commun.* **2014**, *5*, 3783.

4. Li, C.; Han, X.; Cheng, F.; Hu, Y.; Chen, C.; Chen, J. Phase and Composition Controllable Synthesis of Cobalt Manganese Spinel Nanoparticles towards Efficient Oxygen Electrocatalysis. *Nat. Commun.* **2015**, *6*, 7345.

5. Sahraie, N. R.; Kramm, U. I.; Steinberg, J.; Zhang, Y.; Thomas, A.; Reier, T.; Paraknowitsch, J.-P.; Strasser, P. Quantifying the Density and Utilization of Active Sites in Non-Precious Metal Oxygen Electroreduction Catalysts. *Nat. Commun.* **2015**, *6*, 8618.

6. Wang, H.; Lee, H.-W.; Deng, Y.; Lu, Z.; Hsu, P.-C.; Liu, Y.; Lin, D.; Cui, Y. Bifunctional Non-Noble Metal Oxide Nanoparticle Electrocatalysts through Lithium-Induced Conversion for Overall Water Splitting. *Nat. Commun.* **2015**, *6*, 7261.

7. Zhang, J.; Li, H.; Guo, P.; Ma, H.; Zhao, X. S. Rational Design of Graphitic Carbon Based Nanostructures for Advanced Electrocatalysis. *J. Mater. Chem. A* **2016**, *4*, 8497-8511.

8. Novoselov, K. S. Nobel Lecture: Graphene: Materials in the Flatland. *Rev. Mod. Phys.* **2011**, *83*, 837-849.

9. Planeix, J. M.; Coustel, N.; Coq, B.; Brotons, V.; Kumbhar, P. S.; Dutartre, R.; Geneste, P.; Bernier, P.; Ajayan, P. M. Application of Carbon Nanotubes as Supports in Heterogeneous Catalysis. *J. Am. Chem. Soc.* **1994**, *116*, 7935-7936.

10. Trogadas, P.; Fuller, T. F.; Strasser, P. Carbon as Catalyst and Support for Electrochemical Energy Conversion. *Carbon* **2014**, *75*, 5-42.

11. Zhao, Y.; Nakamura, R.; Kamiya, K.; Nakanishi, S.; Hashimoto, K. Nitrogen-Doped Carbon Nanomaterials as Non-Metal Electrocatalysts for Water Oxidation. *Nat. Commun.* **2013**, *4*, 2390.

12. Zhao, J.; Deng, Q.; Bachmatiuk, A.; Sandeep, G.; Popov, A.; Eckert, J.; Ruemmeli, M. H. Free-Standing Single-Atom-Thick Iron Membranes Suspended in Graphene Pores. *Science* **2014**, *343*, 1228-1232.

13. Dai, L.; Xue, Y.; Qu, L.; Choi, H.-J.; Baek, J.-B. Metal-Free Catalysts for Oxygen Reduction Reaction. *Chem. Rev.* **2015**, *115*, 4823-4892.

14. Gao, C.; Guo, Z.; Liu, J.-H.; Huang, X.-J. The New Age of Carbon Nanotubes: An Updated Review of Functionalized Carbon Nanotubes in Electrochemical Sensors. *Nanoscale* **2012**, *4*, 1948-1963.

15. Balasubramanian, K.; Burghard, M. Chemically Functionalized Carbon Nanotubes. *Small* **2005**, *1*, 180-192.

16. Dudin, P. V.; Snowden, M. E.; Macpherson, J. V.; Unwin, P. R. Electrochemistry at Nanoscale Electrodes: Individual Single-Walled Carbon Nanotubes (SWNTs) and SWNT-Templated Metal Nanowires. *ACS Nano* **2011**, *5*, 10017-10025.

17. Unwin, P. R.; Güell, A. G.; Zhang, G. Nanoscale Electrochemistry of Sp^2 Carbon Materials: From Graphite and Graphene to Carbon Nanotubes. *Acc. Chem. Res.* **2016**, ASAP, **DOI:** 10.1021/acs.accounts.6b00301.

18. Zhang, G.; Cuharuc, A. S.; Güell, A. G.; Unwin, P. R. Electrochemistry at Highly Oriented Pyrolytic Graphite (HOPG): Lower Limit for the Kinetics of Outer-Sphere Redox Processes and General Implications for Electron Transfer Models. *Phys. Chem. Chem. Phys.* **2015**, *17*, 11827-11838.

19. Zhang, G. H.; Kirkman, P. M.; Patel, A. N.; Cuharuc, A. S.; McKelvey, K.; Unwin, P. R. Molecular Functionalization of Graphite Surfaces: Basal Plane Versus Step Edge Electrochemical Activity. *J. Am. Chem. Soc.* **2014**, *136*, 11444-11451.

20. Patel, A. N.; McKelvey, K.; Unwin, P. R. Nanoscale Electrochemical Patterning Reveals the Active Sites for Catechol Oxidation at Graphite Surfaces. *J. Am. Chem. Soc.* **2012**, *134*, 20246-20249.

21. Patel, A. N.; Collignon, M. G.; O'Connell, M. A.; Hung, W. O. Y.; McKelvey, K.; Macpherson, J. V.; Unwin, P. R. A New View of Electrochemistry at Highly Oriented Pyrolytic Graphite. *J. Am. Chem. Soc.* **2012**, *134*, 20117-20130.

22. Wang, H.; Maiyalagan, T.; Wang, X. Review on Recent Progress in Nitrogen-Doped Graphene: Synthesis, Characterization, and Its Potential Applications. *ACS Catal.* **2012**, *2*, 781-794.

23. Panchokarla, L. S.; Subrahmanyam, K. S.; Saha, S. K.; Govindaraj, A.; Krishnamurthy, H. R.; Waghmare, U. V.; Rao, C. N. R. Synthesis, Structure, and

Properties of Boron- and Nitrogen-Doped Graphene. *Adv. Mater.* **2009**, *21*, 4726-4730.

24. Yang, Z.; Yao, Z.; Li, G.; Fang, G.; Nie, H.; Liu, Z.; Zhou, X.; Chen, X. a.; Huang, S. Sulfur-Doped Graphene as an Efficient Metal-Free Cathode Catalyst for Oxygen Reduction. *ACS Nano* **2012**, *6*, 205-211.

25. Liu, Z.-W.; Peng, F.; Wang, H.-J.; Yu, H.; Zheng, W.-X.; Yang, J. Phosphorus-Doped Graphite Layers with High Electrocatalytic Activity for the O_2 Reduction in an Alkaline Medium. *Angew. Chem. Int. Edit* **2011**, *50*, 3257-3261.

26. Delamar, M.; Hitmi, R.; Pinson, J.; Saveant, J. M. Covalent Modification of Carbon Surfaces by Grafting of Functionalized Aryl Radicals Produced from Electrochemical Reduction of Diazonium Salts. *J. Am. Chem. Soc.* **1992**, *114*, 5883-5884.

27. Greenwood, J.; Phan, T. H.; Fujita, Y.; Li, Z.; Ivasenko, O.; Vanderlinden, W.; Van Gorp, H.; Frederickx, W.; Lu, G.; Tahara, K.; Tobe, Y.; Uji-i, H.; Mertens, S. F. L.; De Feyter, S. Covalent Modification of Graphene and Graphite Using Diazonium Chemistry: Tunable Grafting and Nanomanipulation. *ACS Nano* **2015**, *9*, 5520-5535.

28. Byers, J. C.; Güell, A. G.; Unwin, P. R. Nanoscale Electrocatalysis: Visualizing Oxygen Reduction at Pristine, Kinked, and Oxidized Sites on Individual Carbon Nanotubes. *J. Am. Chem. Soc.* **2014**, *136*, 11252-11255.

29. Shen, A.; Zou, Y.; Wang, Q.; Dryfe, R. A. W.; Huang, X.; Dou, S.; Dai, L.; Wang, S. Oxygen Reduction Reaction in a Droplet on Graphite: Direct Evidence That the Edge Is More Active Than the Basal Plane. *Angew. Chem. Int. Edit* **2014**, *53*, 10804-10808.

30. Hathcock, K. W.; Brumfield, J. C.; Goss, C. A.; Irene, E. A.; Murray, R. W. Incipient Electrochemical Oxidation of Highly Oriented Pyrolytic-Graphite: Correlation between Surface Blistering and Electrolyte Anion Intercalation. *Anal. Chem.* **1995**, *67*, 2201-2206.

31. Goss, C. A.; Brumfield, J. C.; Irene, E. A.; Murray, R. W. Imaging the Incipient Electrochemical Oxidation of Highly Oriented Pyrolytic Graphite. *Anal. Chem.* **1993**, *65*, 1378-1389.

32. Alliata, D.; Kotz, R.; Haas, O.; Siegenthaler, H. In Situ AFM Study of Interlayer Spacing During Anion Intercalation into HOPG in Aqueous Electrolyte. *Langmuir* **1999**, *15*, 8483-8489.

33. Sanabria-Chinchilla, J.; Asazawa, K.; Sakamoto, T.; Yamada, K.; Tanaka, H.; Strasser, P. Noble Metal-Free Hydrazine Fuel Cell Catalysts: EPOC Effect in

Competing Chemical and Electrochemical Reaction Pathways. *J. Am. Chem. Soc.* **2011**, *133*, 5425-5431.

34. Zhou, W. H.; Xu, L.; Wu, M. J.; Xu, L. J.; Wang, E. Determination of Hydrazines by Capillary Zone Electrophoresis with Amperometric Detection at a Platinum Particle-Modified Carbon-Fiber Microelectrode. *Anal. Chim. Acta* **1994**, *299*, 189-194.

35. Channon, R. B.; Joseph, M. B.; Bitziou, E.; Bristow, A. W. T.; Ray, A. D.; Macpherson, J. V. Electrochemical Flow Injection Analysis of Hydrazine in an Excess of an Active Pharmaceutical Ingredient: Achieving Pharmaceutical Detection Limits Electrochemically. *Anal. Chem.* **2015**, *87*, 10064-10071.

36. Chen, C.-H.; Jacobse, L.; McKelvey, K.; Lai, S. C. S.; Koper, M. T. M.; Unwin, P. R. Voltammetric Scanning Electrochemical Cell Microscopy: Dynamic Imaging of Hydrazine Electro-Oxidation on Platinum Electrodes. *Anal. Chem.* **2015**, *87*, 5782-5789.

37. Ebejer, N.; Güell, A. G.; Lai, S. C. S.; McKelvey, K.; Snowden, M. E.; Unwin, P. R. Scanning Electrochemical Cell Microscopy: A Versatile Technique for Nanoscale Electrochemistry and Functional Imaging. *Annu. Rev. Anal. Chem.* **2013**, *6*, 329-351.

38. Aaronson, B. D. B.; Chen, C.-H.; Li, H.; Koper, M. T. M.; Lai, S. C. S.; Unwin, P. R. Pseudo-Single-Crystal Electrochemistry on Polycrystalline Electrodes: Visualizing Activity at Grains and Grain Boundaries on Platinum for the Fe^{2+}/Fe^{3+} Redox Reaction. *J. Am. Chem. Soc.* **2013**, *135*, 3873-3880.

39. Güell, A. G.; Cuharuc, A. S.; Kim, Y.-R.; Zhang, G.; Tan, S.-Y.; Ebejer, N.; Unwin, P. R. Redox-Dependent Spatially Resolved Electrochemistry at Graphene and Graphite Step Edges. *ACS Nano* **2015**, *9*, 3558-3571.

40. Güell, A. G.; Meadows, K. E.; Dudin, P. V.; Ebejer, N.; Macpherson, J. V.; Unwin, P. R. Mapping Nanoscale Electrochemistry of Individual Single-Walled Carbon Nanotubes. *Nano Lett.* **2014**, *14*, 220-224.

41. Vasile, M. J.; Enke, C. G. The Preparation and Thermodynamic Properties of a Palladium-Hydrogen Electrode. *J. Electrochem. Soc.* **1965**, *112*, 865-870.

42. Zhang, G.; Walker, M.; Unwin, P. R. Low-Voltage Voltammetric Electrowetting of Graphite Surfaces by Ion Intercalation/Deintercalation. *Langmuir* **2016**, *32*, 7476-7484.

43. Bertoncello, P.; Edgeworth, J. P.; Macpherson, J. V.; Unwin, P. R. Trace Level Cyclic Voltammetry Facilitated by Single-Walled Carbon Nanotube Network Electrodes. *J. Am. Chem. Soc.* **2007**, *129*, 10982-10983.

44. E, S. P.; Liu, D.; Lazenby, R. A.; Sloan, J.; Vidotti, M.; Macpherson, J. V.; Unwin, P. R. Electrodeposition of Nickel Hydroxide Nanoparticles on Carbon Nanotube Electrodes: Correlation of Particle Crystallography with Electrocatalytic Properties. *J. Phys. Chem. C* **2016**, *120*, 16059-16068.

45. Ebejer, N.; Schnippering, M.; Colburn, A. W.; Edwards, M. A.; Unwin, P. R. Localized High Resolution Electrochemistry and Multifunctional Imaging: Scanning Electrochemical Cell Microscopy. *Anal. Chem.* **2010**, *82*, 9141-9145.

46. Alsmeyer, D. C.; McCreery, R. L. In Situ Raman Monitoring of Electrochemical Graphite-Intercalation and Lattice Damage in Mild Aqueous Acids. *Anal. Chem.* **1992**, *64*, 1528-1533.

47. Dresselhaus, M. S.; Dresselhaus, G. Intercalation Compounds of Graphite. *Adv. Phys.* **1981**, *30*, 139-326.

48. Schnyder, B.; Alliata, D.; Kotz, R.; Siegenthaler, H. Electrochemical Intercalation of Perchlorate Ions in HOPG: An SFM/LFM and XPS Study. *Appl. Surf. Sci.* **2001**, *173*, 221-232.

49. Choo, H. S.; Kinumoto, T.; Nose, M.; Miyazaki, K.; Abe, T.; Ogumi, Z. Electrochemical Oxidation of Highly Oriented Pyrolytic Graphite During Potential Cycling in Sulfuric Acid Solution. *J. Power Sources* **2008**, *185*, 740-746.

50. Dresselhaus, M. S.; Jorio, A.; Souza Filho, A. G.; Saito, R. Defect Characterization in Graphene and Carbon Nanotubes Using Raman Spectroscopy. *Philos. T. Roy. Soc. A* **2010**, *368*, 5355-5377.

51. Maeda, Y.; Okemoto, Y.; Inagaki, M. Electrochemical Formation of Graphite-Sulfuric Acid Intercalation Compounds on Carbon-Fibers. *J. Electrochem. Soc.* **1985**, *132*, 2369-2372.

52. Zhong, J.-H.; Zhang, J.; Jin, X.; Liu, J.-Y.; Li, Q.; Li, M.-H.; Cai, W.; Wu, D.-Y.; Zhan, D.; Ren, B. Quantitative Correlation between Defect Density and Heterogeneous Electron Transfer Rate of Single Layer Graphene. *J. Am. Chem. Soc.* **2014**, *136*, 16609-16617.

53. Alsmeyer, Y. W.; McCreery, R. L. Surface-Enhanced Raman-Spectroscopy of Carbon Electrode Surfaces Following Silver Electrodeposition. *Anal. Chem.* **1991**, *63*, 1289-1295.

54. McCreery, R. L. Advanced Carbon Electrode Materials for Molecular Electrochemistry. *Chem. Rev.* **2008**, *108*, 2646-2687.

55. Majidi, M. R.; Jouyban, A.; Asadpour-Zeynali, K. Electrocatalytic Oxidation of Hydrazine at Overoxidized Polypyrrole Film Modified Glassy Carbon Electrode. *Electrochim. Acta* **2007**, *52*, 6248-6253.

56. Zheng, L.; Song, J. F. Curcumin Multi-Wall Carbon Nanotubes Modified Glassy Carbon Electrode and Its Electrocatalytic Activity towards Oxidation of Hydrazine. *Sensor Actuat. B-Chem.* **2009**, *135*, 650-655.

57. Harrison, J. A.; Khan, Z. A. Oxidation of Hydrazine on Platinum in Acid Solution. *J. Electroanal. Chem.* **1970**, *28*, 131-138.

58. Harrison, J. A.; Khan, Z. A., Oxidation of Hydrazine in Alkaline Solution at Platinum and Mercury. *J. Electroanal. Chem.* **1970**, *26*, 1-11.

59. Zhang, C. H.; Wang, G. F.; Ji, Y. L.; Liu, M.; Feng, Y. H.; Zhang, Z. D.; Fang, B. Enhancement in Analytical Hydrazine Based on Gold Nanoparticles Deposited on ZnO-MWCNTS Films. *Sensor Actuat. B-Chem.* **2010**, *150*, 247-253.

60. E, S. P.; Miller, T. S.; Macpherson, J. V.; Unwin, P. R. Controlled Functionalisation of Single-Walled Carbon Nanotube Network Electrodes for the Enhanced Voltammetric Detection of Dopamine. *Phys. Chem. Chem. Phys.* **2015**, *17*, 26394-26402.

61. Su, C.; Loh, K. P. Carbocatalysts: Graphene Oxide and Its Derivatives. *Acc. Chem. Res.* **2013**, *46*, 2275-2285.

62. Chen, Q.; Wiedenroth, H. S.; German, S. R.; White, H. S. Electrochemical Nucleation of Stable N2 Nanobubbles at Pt Nanoelectrodes. *J. Am. Chem. Soc.* **2015**, *137*, 12064-12069.

63. Banhart, F.; Kotakoski, J.; Krasheninnikov, A. V. Structural Defects in Graphene. *ACS Nano* **2011**, *5*, 26-41.

64. Deng, D.; Novoselov, K. S.; Fu, Q.; Zheng, N.; Tian, Z.; Bao, X. Catalysis with Two-Dimensional Materials and Their Heterostructures. *Nat. Nanotechnol.* **2016**, *11*, 218-230.

Chapter 7 Visualization of Redox Activity of Li_2O_2 in non-aqueous media: conformal layer *vs.* toroid structure

Given their high theoretical capacity and energy density, non-aqueous Li-O_2 batteries are subjected as one of the most promising alternatives to Li-ion batteries. However, there is a gap in fundamental knowledge with regards to the cathode surface of such devices in part due to a lack of existing high resolution techniques. Herein, we report a strong relationship between the surface structure and electrochemical activity of Li_2O_2 using scanning electrochemical cell microscopy (SECCM), a droplet based technique that employs a dual-barrel nanopipette containing unique gel polymer electrolyte, coupled with complementary techniques (field emission-scanning electron microscopy, Raman spectroscopy and atomic force microscopy). The measurements reveal heterogeneous behavior at the nanoscale with significantly enhanced activity at toroidal Li_2O_2 structures when compared to the conformal layer.

7.1 Introduction

Lithium (Li) oxygen batteries are considered to be a key power source for future electric transportation and renewable energy applications.[1-4] However, there are still formidable scientific and technical challenges in developing effective Li-O_2 batteries,[5, 6] of which passivation of the cathode during the discharge process due to the build-up of a wide bandgap insulator on the Li_2O_2 layer is critical.[7, 8] Very recent work suggests that Li_2O_2 toroid structures improve the charge transport limitations,[9] thus understanding structure-activity of Li_2O_2 layers would be hugely beneficial. There are huge efforts to develop techniques for the investigation of physicochemical processes in batteries,[10-12] but there has been relatively little work on nanoscale electrochemical (EC) probe mapping of battery materials, which has the power to reveal considerable information on battery electrodes.[13] Our group has shown that scanning electrochemical cell microscopy (SECCM) is able to resolve EC activity at the nanoscale for a variety of systems,[14-16] and further that structure–activity correlations can be revealed through the combination of microscopic techniques which are applied to the same area as EC mapping.[17-20] in correlative microscopy approach. This is the strategy we use herein to obtain key information on Li_2O_2 conformal layer versus toroid structure.

7.2 Experimental

7.2.1 Materials

All chemicals were used as received. Anhydrous electrolyte was prepared using dimethyl sulfoxide (DMSO) (Sigma-Aldrich, analytical reagent). 0.1 M Lithium

perchlorate ($LiCO_4$) (Sigma-Aldrich, 99.99 %) was prepared in DMSO bubbled with O_2 gas (BOC Gases, U.K., 99.5 %). All solvents were dried for several days using freshly activated molecular sieves (4 Å). A gel polymer electrolyte containing the cross-linker (4, 7, 10-trioxa-1, 13 tridecanediamine; Sigma-Aldrich; 97 %) and polymer matrix (home-made poly-glycidyl methacrylate (PGMA)), tetrabutylammonium hexafluorophosphate ($TBAPF_6$) (Sigma-Aldrich, ≥99 %) was used for SECCM imaging.

7.2.2 Li_2O_2 growth

Chronoamperometry in O_2 saturated 0.1 M $LiClO_4$ DMSO was used for the Li_2O_2 product growth on a gold substrate (prepared by evaporating Cr (3 nm) followed by Au (60 nm) using a Moorfields MiniLab deposition system (Moorfield Associates)). The anhydrous DMSO electrolyte shows a broad peak in the linear sweep voltammetry (LSV) at 1.87 V_{Li/Li^+} and a distinct shoulder at 1.62 V_{Li/Li^+} (Figure 7.1a). The peak at 1.87 V_{Li/Li^+} is attributed to surface EC growth of Li_2O_2 layer and the peak at 1.62 V_{Li/Li^+} is attributed to solution-mediated growth of Li_2O_2 toroid.[9] Typical current-time curves for a 10 s deposition at 1.87 V_{Li/Li^+} are shown in Figure 7.1b. All the electrolyte preparations and CV measurements were conducted in an argon-filled glovebox.

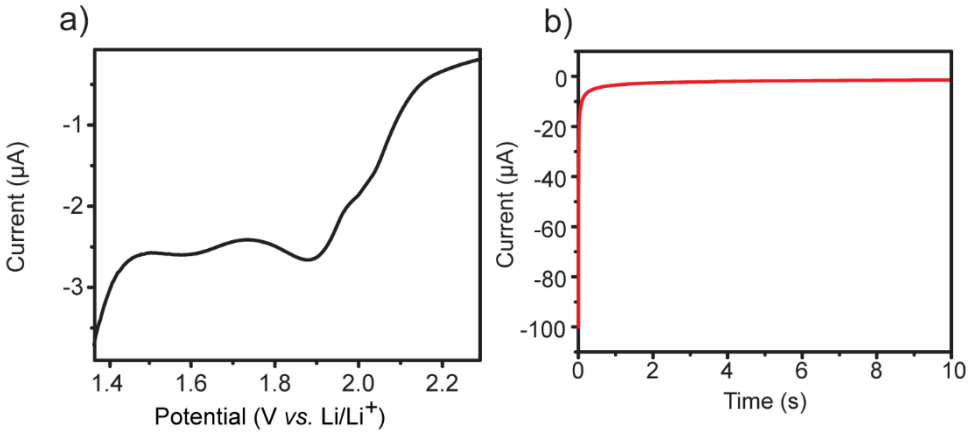

Figure 7.1 (a) Typical LSV recorded in O_2 saturated 0.1 M $LiClO_4$ DMSO on gold substrate. The scan rate was 100 mV s^{-1}. (b) Typical current-time curves recorded at a substrate potential of 1.87 $V_{Li/Li+}$ for 10 s.

7.2.3 Field emission-scanning electron microscopy, micro-Raman and atomic force microscopy experiments

The sample was characterized before and after SECCM imaging using field emission-scanning electron microscopy (FE-SEM, Zeiss Supra 55-VP, 1 kV acceleration voltage). Micro-Raman spectroscopy (InVia Reflex Raman, Renishaw, UK) equipped with a solid state 633 nm laser and a 50× lens was used to determine the nature of the Li_2O_2 surface. AFM imaging of the Li_2O_2 surface was carried out in air using a tapping mode scan (Innova, Veeco-Bruker).

7.2.4 Poly (glycidyl methacrylate)

A solution of glycidyl methacrylate monomer (50 mL, 0.376 mol) and AIBN initiator (400 mg, 2.44 mmol) in MeCN (50 mL) was deoxygenated by bubbling with N_2 for 30 min. Concurrently, a vessel containing the CoBF (1 mg) catalyst was similarly evacuated of oxygen by purging with N_2 for 30 min. The solution of the monomer and

initiator was cannulated into the vessel containing CoBF and the resulting solution was heated at 65 °C and stirred for 23 hours. Samples were taken periodically for conversion and molecular weight analysis. The resulting polymer was purified by dialysis against MeCN and finally isolated by concentration in vacuo.

7.2.5 Gel-polymer electrolyte

The cross-linker, 4,7,10-trioxa-1,13-tridecanediamine (50 mol% with respect to epoxide) was added to a solution of poly(glycidyl methacrylate) (10 % w/w) in $LiClO_4$/DMSO electrolyte solution (0.1 M). The resulting solution was added to both barrels of a dual barrel nanopipette, which was suspended in an empty glass vial prior to curing by indirect heating at 80 °C in an oil bath. Gel formation and conductivity were confirmed by microscopy and using a conductivity sensor (1063 µS cm^{-1}, Mettler Toledo), respectively.

7.2.6 Hopping scanning electrochemical cell microscopy-cyclic voltammetry experiments

Dual channel borosilicate theta capillaries (ID = 1.0 mm, OD = 1.5 mm, Harvard Apparatus, UK) were pulled using a laser pipette puller (P-2000, Sutter Instrument Co., USA) to produce nanopipettes with a diameter of ca. 140 nm (70 nm each channel; Figure 7.2). The dual barrel nanopipettes were filled with the gel polymer electrolyte and a Ag/AgCl wire in each channel, which act as QRCEs. The nanopipette was approached towards the substrate surface until the meniscus just made contact, making a series of measurements by landing the meniscus at a set of predefined locations (hopping distance of 3 µm). Electrolyte residues from the SECCM meniscus

were inspected after experiments using FE-SEM (Supra 55-VP, Zeiss) to provide detail information about the droplet size and location.

Great control of the meniscus contact was conducted by applying a bias voltage (V_2, 200 mV) between the two QRCEs to produce a direct ion cucrrent (I_{IC}) across the meniscus. The nanopipette was oscillated perpendicular to the surface (276 Hz, 14 nm peak-to-peak amplitude) to induce an alternating component (AC) to the ion current between two barrels when the meniscus came into contact with the surface. The AC signal was detected using a lock-in amplifier (SR380, Stafford Research System) and the resulting AC ion current acted as the feedback signal to position the nanopipette at a set distance from the electrode surface. A substrate voltage (V_1) was applied to one of the QRCEs to control the working electrode potential ($E_{app} = -(V_1 + V_2/2)$ *vs.* Ag/AgCl; $E_{Ag/AgCl} = 2.82\ V\ vs.\ Li/Li^+$) and the working electrode current (I_{EC}) was measured using a custom built current-to-voltage converter. The voltammetric scan rate was 1 V s^{-1}. Data analysis was performed in Matlab (R2014b, Mathworks Inc.) to produce I_{EC} spatial maps over a set of potentials and can be presented as movie.

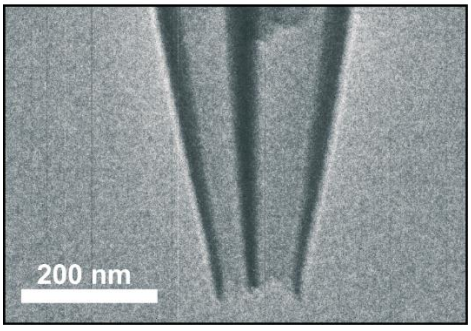

Figure 7.2 High resolution transmission electron microscopy (HR-TEM) image of pulled dual channel nanopippette for SECCM imaging.

7.3 Results and discussion

In this chapter, we introduce EC mapping of a Li_2O_2 formed cathode, a product of the discharge process of Li-O_2 batteries (*vide infra*), using scanning SECCM in a controlled atmospheric environment (Figure 7.3a). Previous studies with SECCM have employed aqueous solutions[16, 21] or ionic liquid,[22, 23] which stable meniscus contact from a pipette with a wide variety of structures. However, typical organic solvents tend to wet the surface, making meniscus contact unstable. Therefore, a gel polymer electrolyte was used to reduce the wetting issue of the SECCM meniscus DMSO on the substrate by trapping the liquid component in a polymer matrix whilst still maintaining the properties of a good electrolyte.[24, 25] A hopping mode protocol was employed with two CVs performed, at each image pixel upon contact between the meniscus and surface, in order to produce EC maps with varying potential (Figure 7.3b). The combination of topographical mapping with CVs allows for the correlation of EC activity correlated with the morphology of the substrate. EC images with varying applied potentials (E_{app}) were constructed from the CVs at each hop (*e.g.* pixel), providing a video consisting of 1800 EC images (potential resolution of 5.12 mV). The use of field emission-scanning electron microscopy (FE-SEM), *applied to the same area scanned with SECCM*, together with complementary multi-microscopic techniques (atomic force microscopy (AFM) and Raman spectroscopy) allowed for a detailed investigation into the individual toroidal and layered structure of Li_2O_2 particles for the first time, establishing the presence of a significantly enhanced EC activity on the Li_2O_2 toroid structures.

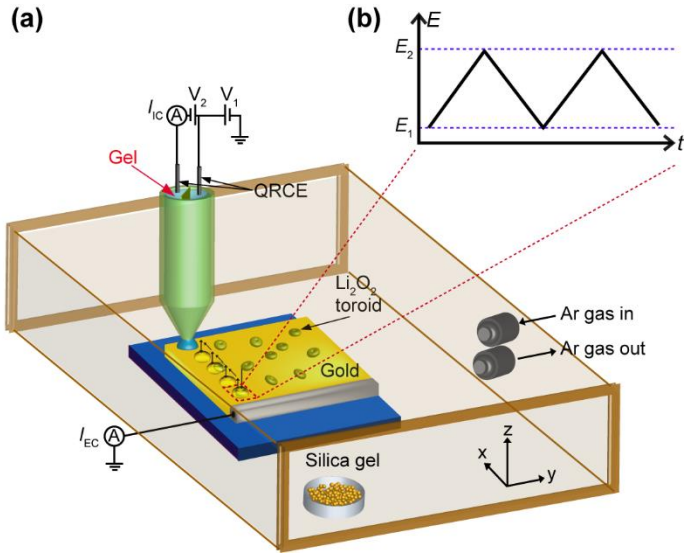

Figure 7.3 (a) Schematic of EC measurement using voltammetric hopping mode SECCM in the Ar environmental chamber. (b) CV measurements at every pixel of a pre-defined scanned area.

7.3.1 Li_2O_2 growth and characterization

A gold support electrode was chosen instead of carbon-based electrode, which is commonly used as cathode in Li-O_2 battery, to prevent Li_2CO_3 formation at the cathode resulting from carbon decomposition.[26, 27] The Li_2O_2 surface was prepared by driving the oxygen reduction reaction (ORR) during the discharge process (at 1.87 V_{Li/Li^+} for 10 s, in O_2 saturated 0.1 M $LiClO_4$ DMSO (Figure 7.1)) in Li-O_2 battery and equation of the reaction is given by:[9, 28]

$$2Li^+ + 2e^- + O_2 \rightleftharpoons Li_2O_2 \quad (1)$$

The high Gutmann donor number (DN) of DMSO (DN = 30) encourages the ORR to form Li_2O_2 *via* a solution-mediated mechanism,[9, 29] in which the solubility of the superoxide is improved ($LiO_2^* \rightarrow Li^+(sol) + O_2^-(sol)$), leading to micrometer-sized Li_2O_2 (e.g Li_2O_2 toroid) growth.[9]

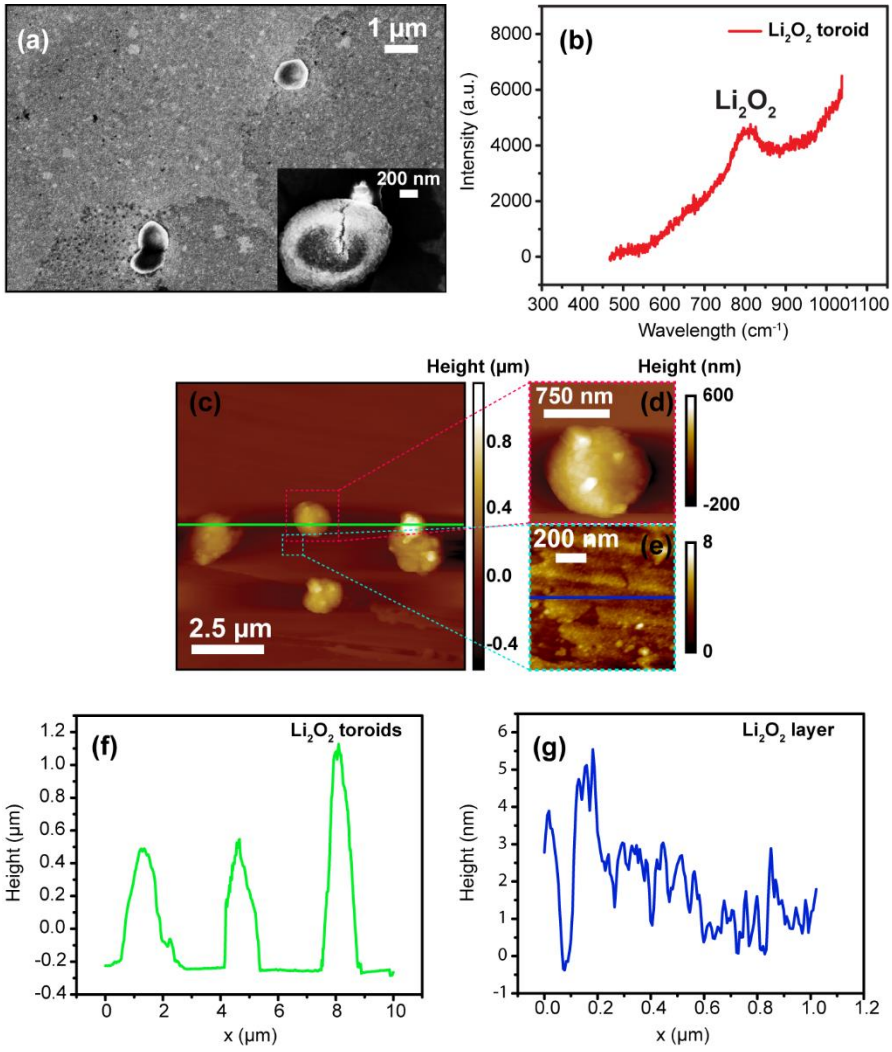

Figure 7.4 (a) FE-SEM images after Li_2O_2 products (Li_2O_2 toroids on top of thin Li_2O_2 layer) growth on gold substrate (conditions as Figure 7.1) and inset is FE-SEM image of the toroid with higher magnification. (b) Typical micro-Raman spectra of Li_2O_2 toroid. (c) Typical AFM image of Li_2O_2 toroids on Li_2O_2 layer. A magnified AFM image of (d) a spherical Li_2O_2 toroid, illustrating a nanocrystalline aggregate structure and (e) the Li_2O_2 layer. Corresponding height cross sections of surface Li_2O_2 particles: (f) toroidal and (g) layer structure.

Li_2O_2 toroids (1 – 1.5 µm in diameter) form on top of the uniform thin Li_2O_2 layer and are shown in FE-SEM image (Figure 7.4a), resulting in a density of Li_2O_2 toroid of 0.05 particles μm^{-2}. An FE-SEM image of a Li_2O_2 toroid with higher magnification (inset) shows its nanocrystalline, aggregated toroidal structure (this

structure is likely grown on the defect sites of the homogeneous Li_2O_2 film[9]). The micro-Raman spectra in Figure 7.4b was collected in the range 460 to 1040 cm^{-1} on Li_2O_2 toroid, confirmed the presence of Li_2O_2 on the gold surface giving a peak at 805 cm^{-1} which is attributed to the O – O stretch vibrations of Li_2O_2.[29-31]

AFM was utilized to pursue the substrate morphology (Figure 7.4c-e). It shows two Li_2O_2 toroids of circular shape at the center and two elongated shape of Li_2O_2 toroids at the right and left end of the image (Figure 7.4c). The latter could be due to the blister formation at the defects followed by the continuous agglomeration of smaller Li_2O_2 crystals, resulting in the formation of larger Li_2O_2 toroidal structures. A magnified AFM image of the Li_2O_2 toroid in Figure 7.4d inset elucidates a rough, aggregated morphology, which is made up of numerous nanosize Li_2O_2 particles. In contrast, Figure 7.4e illustrates a relatively homogenous layer of Li_2O_2 particles on the gold substrate. The corresponding line profile from Figure 7.4f shows the toroids exhibit a diameter of 1.2 – 2.0 μm and are in the range of 0.5 – 1.1 μm in height. The conformal layer of Li_2O_2 exhibits thickness of 0.5 – 5.5 nm (Figure 7.4g).

7.3.2 Gel polymer electrolyte

A suitable gel polymer electrolyte formulation was prepared to enable the pre-gel solution to flow down through the nanopipette, forming a suitably conductive meniscus, prior to curing. To this end, a low molecular weight, poly(glycidyl methacrylate) (PGMA) was synthesized by catalytic chain transfer polymerization. Using this technique the molecular weight ($M_{n,SEC}$) was limited to 1900 g mol^{-1} equating to an average degree of the polymerization (DP_n) of 12. Thus, the viscosity of the polymer matrix in solutions of the electrolyte (0.1 M tetrabutylammonium

hexafluorophosphate ($TBAPF_6$)) remained low, facilitating flow through the nanopipette and the pendent epoxide functional group was predisposed for cross-linking using a *bis*-amine reagent (4,7,10-trioxa-1,13-tridecanediamine). To establish optimal gel formulation, the loading of the polymer matrix in the electrolyte (1-10 % w/w) and the concentration of cross-linker relative to epoxide groups (1-50 mol%) was varied. A formulation consisting of PGMA (10 % w/w), cross-linker (50 mol% with respect to epoxide) and 0.1 M $TBAPF_6$/DMSO was found to be optimum with a high conductivity of 1063 μS cm^{-1}. Addition of this formulation to both barrels of a dual barrel nanopipette yielded a gel-polymer electrolyte loaded probe after curing for 8 hours at 60 °C in the Ar environment glovebox. DMSO was chosen, herein, as a suitable aprotic solvent for EC measurement due to its prominent physical properties (e.g. including low viscosity (1.948 cP), high conductivity (2.11 mS cm^{-1}) and high DN), resulting in remarkable stability of Li^+ and good oxygen diffusion ability.[9, 32, 33] For these reasons, DMSO has been utilized in recent studies for high performance rechargeable Li-O_2 batteries which offer improvements in discharge capacity and charge potential.[30, 32]

7.3.3 Scanning electrochemical cell microscopy imaging at the Li_2O_2 products

The SECCM mapping area was 42 μm × 45 μm (Figure 7.5a) considering the Li_2O_2 toroid density on the surface (*vide supra*) to investigate EC activity of both Li_2O_2 toroids and thin Li_2O_2. The hopping distance between each pixel was 3 μm to avoid overlap of the meniscus areas (~ 2.5 μm in diameter) resulting 240 pixels within the scanning area. Figure 7.5b shows a FE-SEM image conducted after SECCM imaging

and shows that the size and shape of meniscus was reasonably consistent on the substrate throughout the entire scanning, confirming the presence of a fairly similar local working electrode area at each pixel. The topographical image (Figure 7.5a) shows the location of Li_2O_2 toroids with height of 1 – 1.5 μm in agreement with FE-SEM and AFM topographic analysis (Figure 7.4). Moreover, a magnified FE-SEM image (Figure 7.5c) of the scanned area after SECCM experiments showing Li_2O_2 toroids provides excellent agreement with the SECCM topographical image (Figure 7.5a).

A series of EC images at different E_{app} were generated with the potential swept from 3.12 V_{Li/Li^+} to 0.22 V_{Li/Li^+} (negative direction) followed by being scanned positively to 4.72 V_{Li/Li^+} with this cycle being run twice. This yielding an EC video consisting of 1800 images at different E_{app}). The potential range was determined to allow for electrochemically investigating the discharge/charge process in Li-O_2 battery as the net EC reaction of Li-O_2 battery is described as:

$$2Li + O_2 + 2e^- \rightleftharpoons Li_2O_2 \quad (2)$$

with the forward process corresponding to discharge process (reduction) and the backward reaction describing charge process (oxidation).[33-35]

For an in-depth comparison of the Li_2O_2 toroids and the thin Li_2O_2 layer, CV data were extracted (Figure 7.5d) and averaged, from 4 individual pixels at the two distinct regions, according to results from topographical image (Figure 7.5a), presented. The first cycle of the CVs in both toroidal shaped and layered Li_2O_2 structure show either little or no peak at 2.39 V_{Li/Li^+} (Figure 7.5e) due to the absence of Li^+ in the solution, so consequently there is no further Li_2O_2 formation. The

oxidation of the Li_2O_2 toroid was observed at 3.59 V_{Li/Li^+} followed by the further oxidation of the Li_2O_2 layer at 4.12 V_{Li/Li^+}, producing Li ions and oxygen due to Li_2O_2 oxidation. The low charge potential of Li_2O_2 toroids is relatively easy to oxidize with facile charge transport across the surface as compared to the layered structure of Li_2O_2.[36] At the second CV cycle on Li_2O_2 toroid, a relatively high I_p at 2.39 V_{Li/Li^+} appeared (Figure 7.5f) by forming Li_2O_2 products (forward process of equation 1) due to the ORR in the presence of Li^+ and O_2 in the meniscus, generated from the oxidation process during the first CV. The thin Li_2O_2 layer, on the other hand, showed marginal change at 2.39 V_{Li/Li^+} between two CV cycles. The oxidation process of the Li_2O_2 toroid in second cycle occurs with a similar process to the first cycle.

The higher discharge capacity while forming Li_2O_2 toroids (3.3 Ah cm^{-2}) on the gold electrode, when compared to the thin Li_2O_2 film (0.8 Ah cm^{-2}) is due to the blocking of the charge transfer through the conformal thin layer (Figure 7.6), which is in a good agreement with recent studies.[30, 37] EC images at 2.39 V_{Li/Li^+} (Figure 7.5f) shows an evident contrast of EC activity for Li_2O_2 formation between the Li_2O_2 toroid and the Li_2O_2 layer. Two EC images, charge process (oxidation) extracted from the video (at E_{app} = 3.59 and 4.12 V_{Li/Li^+}) (Figure 7.5g and 7.5h, respectively) illustrate the higher EC activity present on Li_2O_2 toroids compared to thin Li_2O_2 film. The results show that the Li_2O_2 oxidation occurs at relatively lower overpotential with a significantly high current generated (*ca*. 9 times increase in the I_p for oxidation process) at the toroidal structure, compared to Li_2O_2 layered structure. Hence, toroidal Li_2O_2 structures boost the charging capability of the cathode material. The low current magnitude at the Li_2O_2 layer, is most likely due to the poor electrical conductivity of wide bandgap insulator Li_2O_2 layer, which hampers the charge transfer between the

surface/electrolyte once the build-up of Li_2O_2 occurs.[7, 8, 38-40] The striking observation of the significantly high oxidation current in Li_2O_2 toroid is attributed to the charging efficiency at comparatively low overpotentials, highlighting the toroidal structure of Li_2O_2 can impart significant the capability of battery materials.

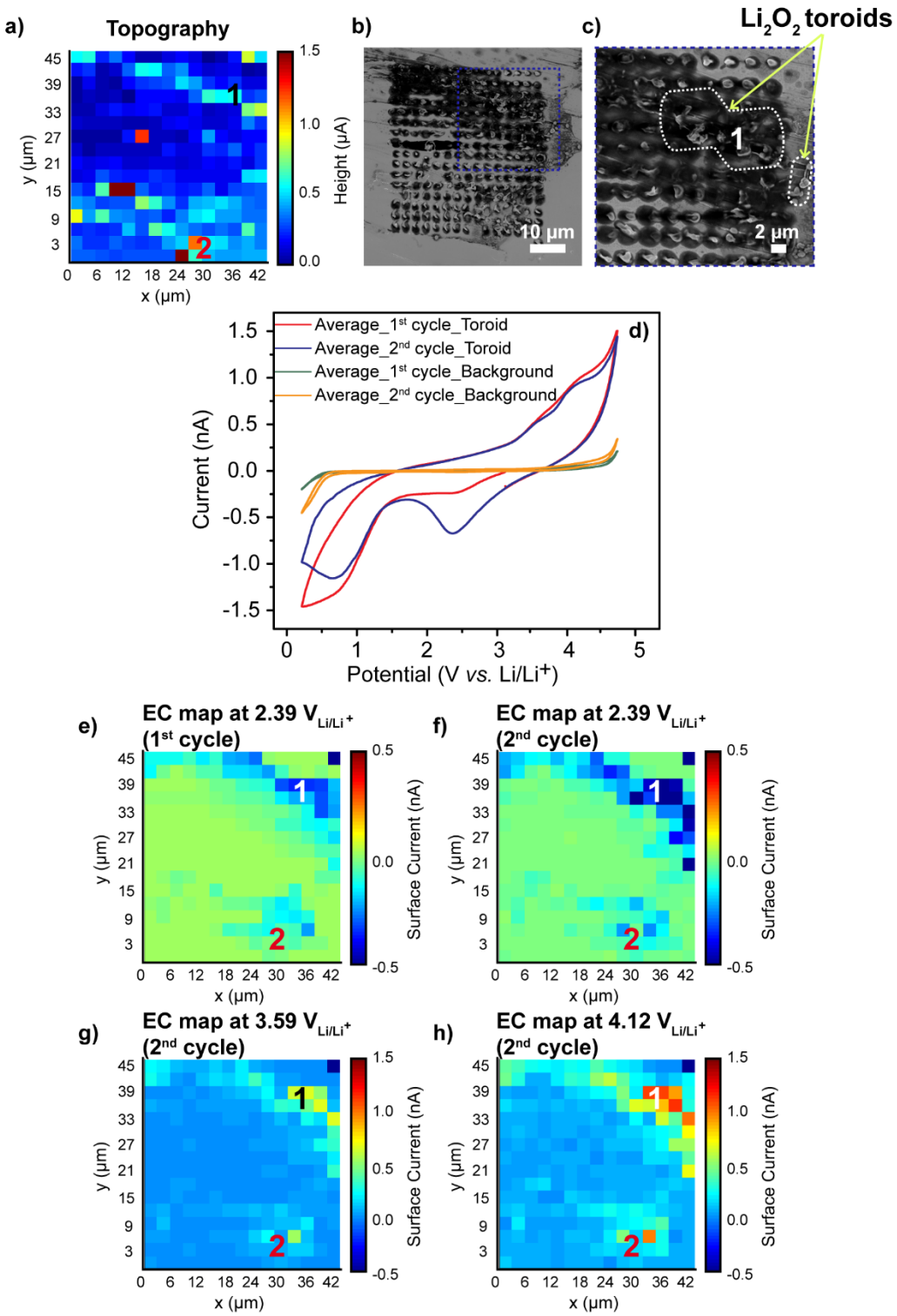

Figure 7.5(a) Topography simultaneously generated with the EC measurements using voltammetric hopping mode SECCM in the Ar environmental chamber. (b) FE-SEM image after SECCM imaging showing the locations of the individual pixels. (c) Magnified FE-SEM image after SECCM imaging at region 1. (d) Averaged CVs (n = 4) for Li_2O_2 toroid (1st cycle (red); 2nd cycle (blue)) and Li_2O_2 layer (1st cycle (green); 2nd cycle (orange)). EC map of the Li_2O_2 modified gold substrate (conditions as Figure 7.1) at 2.39 V_{Li/Li^+} for (e) first and (f) second cycle. EC map different oxidation potential at (g) 3.59 V_{Li/Li^+} and (g) 4.12 V_{Li/Li^+} for second cycle.

One explanation for this phenomenon is that the incomplete surface blocking of the toroidal structure of Li_2O_2 (space remaining between each particle) allowing the continuing flow of charge for longer discharge times. In contrast, the early cell death and low EC activity of Li_2O_2 layer structure is attributed to the termination of electron flow with the increased of thickness of Li_2O_2 conformal layer.

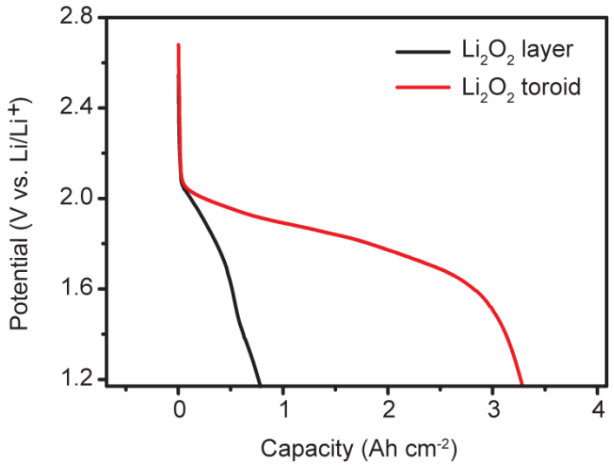

Figure 7.6 Galvanostatic discharge curves at the current density of 30 μA cm^{-2} for both the Li_2O_2 layered (black) and toroidal (red) structure in 0.1 M $LiClO_4$ DMSO.

Furthermore, the efficiency under charging (η_{charge}) is calculated by the ratio of Q_{red} to Q_{ox}. The Coulombic efficiency of the Li_2O_2 toroid is ca. 80 % and the Li_2O_2

layer is ca. 45 %. The relatively high η_{charge} of Li_2O_2 toroid suggests that toroidal structure is a promising battery material, with this study yielding key insights into the role of the electrode structure on the overall battery performance.

7.4 Conclusions

In this study, we have shown that Li_2O_2 product formed on a gold substrate (toroidal and layer structure) during chronoamperometry in O_2 saturated 0.1 M $LiClO_4$ DMSO, which have been characterized by FE-SEM, AFM and Raman microscopy. Li_2O_2 toroidal are promising structures showing 9 times increase of the redox current magnitude and 80 % of η_{charge} as compared to Li_2O_2 layer on the same surface, which is revealed by SECCM imaging. The unique gel polymer organic electrolyte in dual barrel nanopipette for SECCM-CV approach in combination with other microscopy techniques has enabled a potential sweep at every pixel of the pre-defined scanned area and allows for detailed correlations of structure-activity on interesting electrode materials. The results show that electrochemistry is a powerful tool for elucidating the surface properties of Li_2O_2 to improve the performance of cathode materials for the design of effective Li-O_2 battery.

7.5 Future work

The remaining challenge is to investigate the inclusions of redox mediator (tetrathiafulvalene) as electrocatalyst in gel electrolyte to alleviate the large overpotential during recharging process (oxidation of the Li_2O_2 product at the cathode).

7.6 References

1. Lu, Y.-C.; Xu, Z.; Gasteiger, H. A.; Chen, S.; Hamad-Schifferli, K.; Shao-Horn, Y. Platinum−Gold Nanoparticles: A Highly Active Bifunctional Electrocatalyst for Rechargeable Lithium−Air Batteries. *J. Am. Chem. Soc.* **2010**, *132*, 12170-12171.

2. Black, R.; Adams, B.; Nazar, L. F. Non-Aqueous and Hybrid Li-O_2 Batteries. *Adv. Energ. Mater.* **2012**, *2*, 801-815.

3. Bruce, P. G.; Freunberger, S. A.; Hardwick, L. J.; Tarascon, J. M. Li-O_2 and Li-S Batteries with High Energy Storage. *Nat. Mater.* **2012**, *11*, 19-29.

4. Lu, Y.-C.; Gallant, B. M.; Kwabi, D. G.; Harding, J. R.; Mitchell, R. R.; Whittingham, M. S.; Shao-Horn, Y. Lithium-Oxygen Batteries: Bridging Mechanistic Understanding and Battery Performance. *Energ. & Environ. Sci.* **2013**, *6*, 750-768.

5. Christensen, J.; Albertus, P.; Sanchez-Carrera, R. S.; Lohmann, T.; Kozinsky, B.; Liedtke, R.; Ahmed, J.; Kojic, A. A Critical Review of Li/Air Batteries. *J. Electrochem. Soc.* **2012**, *159*, R1-R30.

6. Girishkumar, G.; McCloskey, B.; Luntz, A. C.; Swanson, S.; Wilcke, W. Lithium – Air Battery: Promise and Challenges. *J. Phys. Chem. Lett.* **2010**, *1*, 2193-2203.

7. Luntz, A. C.; Viswanathan, V.; Voss, J.; Varley, J. B.; Norskov, J. K.; Scheffler, R.; Speidel, A. Tunneling and Polaron Charge Transport through Li_2O_2 in Li-O_2 Batteries. *J. Phys. Chem. Lett.* **2013**, *4*, 3494-3499.

8. Radin, M. D.; Siegel, D. J., Charge Transport in Lithium Peroxide: Relevance for Rechargeable Metal-Air Batteries. *Energ. & Environ. Sci.* **2013**, *6*, 2370-2379.

9. Aetukuri, N. B.; McCloskey, B. D.; Garcia, J. M.; Krupp, L. E.; Viswanathan, V.; Luntz, A. C. Solvating Additives Drive Solution-Mediated Electrochemistry and Enhance Toroid Growth in Non-Aqueous Li-O_2 Batteries. *Nat. Chem.* **2015**, *7*, 50-56.

10. Huang, R.; Ikuhara, Y. Stem Characterization for Lithium-Ion Battery Cathode Materials. *Curr. Opin. Solid State Mater. Sci.* **2012**, *16*, 31-38.

11. Chueh, W. C.; El Gabaly, F.; Sugar, J. D.; Bartelt, N. C.; McDaniel, A. H.; Fenton, K. R.; Zavadil, K. R.; Tyliszczak, T.; Lai, W.; McCarty, K. F. Intercalation Pathway in Many-Particle $LiFePO_4$ Electrode Revealed by Nanoscale State-of-Charge Mapping. *Nano Lett.* **2013**, *13*, 866-872.

12. Baddour-Hadjean, R.; Pereira-Ramos, J.-P. Raman Microspectrometry Applied to the Study of Electrode Materials for Lithium Batteries. *Chem. Rev.* **2010**, *110*, 1278-1319.

13. Takahashi, Y., et al. Nanoscale Visualization of Redox Activity at Lithium-Ion Battery Cathodes. *Nat. Commun.* **2014**, *5*.

14. Güell, A. G.; Cuharuc, A. S.; Kim, Y.-R.; Zhang, G.; Tan, S.-y.; Ebejer, N.; Unwin, P. R. Redox-Dependent Spatially Resolved Electrochemistry at Graphene and Graphite Step Edges. *ACS Nano* **2015**, *9*, 3558-3571.

15. Unwin, P. R.; Güell, A. G.; Zhang, G. Nanoscale Electrochemistry of Sp^2 Carbon Materials: From Graphite and Graphene to Carbon Nanotubes. *Acc. Chem. Res.* **2016**, ASAP, **DOI:** 10.1021/acs.accounts.6b00301.

16. Chen, C.-H.; Jacobse, L.; McKelvey, K.; Lai, S. C. S.; Koper, M. T. M.; Unwin, P. R. Voltammetric Scanning Electrochemical Cell Microscopy: Dynamic Imaging of Hydrazine Electro-Oxidation on Platinum Electrodes. *Anal. Chem.* **2015**, *87*, 5782-5789.

17. Ebejer, N.; Güell, A. G.; Lai, S. C. S.; McKelvey, K.; Snowden, M. E.; Unwin, P. R. Scanning Electrochemical Cell Microscopy: A Versatile Technique for Nanoscale Electrochemistry and Functional Imaging. *Annu. Rev. Anal. Chem.* **2013**, *6*, 329-351.

18. Aaronson, B. D. B.; Chen, C.-H.; Li, H.; Koper, M. T. M.; Lai, S. C. S.; Unwin, P. R. Pseudo-Single-Crystal Electrochemistry on Polycrystalline Electrodes: Visualizing Activity at Grains and Grain Boundaries on Platinum for the Fe^{2+}/Fe^{3+} Redox Reaction. *J. Am. Chem. Soc.* **2013**, *135*, 3873-3880.

19. Güell, A. G.; Cuharuc, A. S.; Kim, Y.-R.; Zhang, G.; Tan, S.-y.; Ebejer, N.; Unwin, P. R. Redox-Dependent Spatially Resolved Electrochemistry at Graphene and Graphite Step Edges. *ACS Nano* **2015**, *9*, 3558-3571.

20. Güell, A. G.; Meadows, K. E.; Dudin, P. V.; Ebejer, N.; Macpherson, J. V.; Unwin, P. R. Mapping Nanoscale Electrochemistry of Individual Single-Walled Carbon Nanotubes. *Nano Lett.* **2014**, *14*, 220-224.

21. Byers, J. C.; Güell, A. G.; Unwin, P. R. Nanoscale Electrocatalysis: Visualizing Oxygen Reduction at Pristine, Kinked, and Oxidized Sites on Individual Carbon Nanotubes. *J. Am. Chem. Soc.* **2014**, *136*, 11252-11255.

22. Aaronson, B. D. B.; Garoz-Ruiz, J.; Byers, J. C.; Colina, A.; Unwin, P. R. Electrodeposition and Screening of Photoelectrochemical Activity in Conjugated Polymers Using Scanning Electrochemical Cell Microscopy. *Langmuir* **2015**, *31*, 12814-12822.

23. Aaronson, B. D. B.; Lai, S. C. S.; Unwin, P. R. Spatially Resolved Electrochemistry in Ionic Liquids: Surface Structure Effects on Triiodide Reduction at Platinum Electrodes. *Langmuir* **2014**, *30*, 1915-1919.

24. Stephan, A. M. Review on Gel Polymer Electrolytes for Lithium Batteries. *Eur. Polym. J.* **2006**, *42*, 21-42.

25. Song, J. Y.; Wang, Y. Y.; Wan, C. C. Review of Gel-Type Polymer Electrolytes for Lithium-Ion Batteries. *J. Power Sources* **1999**, *77*, 183-197.

26. McCloskey, B. D.; Speidel, A.; Scheffler, R.; Miller, D. C.; Viswanathan, V.; Hummelshoj, J. S.; Norskov, J. K.; Luntz, A. C. Twin Problems of Interfacial Carbonate Formation in Nonaqueous Li-O_2 Batteries. *J. Phys. Chem. Lett.* **2012**, *3*, 997-1001.

27. Peng, Z. Q.; Freunberger, S. A.; Chen, Y. H.; Bruce, P. G. A Reversible and Higher-Rate Li-O_2 Battery. *Science* **2012**, *337*, 563-566.

28. Shao, Y.; Park, S.; Xiao, J.; Zhang, J.-G.; Wang, Y.; Liu, J. Electrocatalysts for Nonaqueous Lithium–Air Batteries: Status, Challenges, and Perspective. *ACS Catal.* **2012**, *2*, 844-857.

29. Zhang, Y.; Zhang, X.; Wang, J.; McKee, W. C.; Xu, Y.; Peng, Z. Potential-Dependent Generation of O_2^- and LiO_2 and Their Critical Roles in O_2 Reduction to Li_2O_2 in Aprotic Li–O_2 Batteries. *J. Phys. Chem. C* **2016**, *120*, 3690-3698.

30. Johnson, L.; Li, C. M.; Liu, Z.; Chen, Y. H.; Freunberger, S. A.; Ashok, P. C.; Praveen, B. B.; Dholakia, K.; Tarascon, J. M.; Bruce, P. G. The Role of LiO_2 Solubility in O_2 Reduction in Aprotic Solvents and Its Consequences for Li-O_2 Batteries. *Nat. Chem.* **2014**, *6*, 1091-1099.

31. Yang, J.; Zhai, D.; Wang, H.-H.; Lau, K. C.; Schlueter, J. A.; Du, P.; Myers, D. J.; Sun, Y.-K.; Curtiss, L. A.; Amine, K. Evidence for Lithium Superoxide-Like Species in the Discharge Product of a Li-O_2 Battery. *Phys. Chem. Chem. Phys.* **2013**, *15*, 3764-3771.

32. Xu, D.; Wang, Z. L.; Xu, J. J.; Zhang, L. L.; Zhang, X. B. Novel DMSO-Based Electrolyte for High Performance Rechargeable Li-O_2 Batteries. *Chem. Commun.* **2012**, *48*, 6948-6950.

33. Laoire, C. O.; Mukerjee, S.; Abraham, K. M.; Plichta, E. J.; Hendrickson, M. A. Influence of Nonaqueous Solvents on the Electrochemistry of Oxygen in the Rechargeable Lithium-Air Battery. *J. Phys. Chem. C* **2010**, *114*, 9178-9186.

34. Ogasawara, T.; Debart, A.; Holzapfel, M.; Novak, P.; Bruce, P. G. Rechargeable Li_2O_2 Electrode for Lithium Batteries. *J. Am. Chem. Soc.* **2006**, *128*, 1390-1393.

35. Laoire, C. O.; Mukerjee, S.; Abraham, K. M.; Plichta, E. J.; Hendrickson, M. A. Elucidating the Mechanism of Oxygen Reduction for Lithium-Air Battery Applications. *J. Phys. Chem. C* **2009**, *113*, 20127-20134.

36. Aurbach, D.; McCloskey, B. D.; Nazar, L. F.; Bruce, P. G. Advances in Understanding Mechanisms Underpinning Lithium–Air Batteries. *Nat. Energy* **2016**, *1*, 16128.

37. Gao, X. W.; Chen, Y. H.; Johnson, L.; Bruce, P. G. Promoting Solution Phase Discharge in Li–O_2 Batteries Containing Weakly Solvating Electrolyte Solutions. *Nat. Mater.* **2016**, *15*, 882-888.

38. Viswanathan, V.; Thygesen, K. S.; Hummelshoj, J. S.; Norskov, J. K.; Girishkumar, G.; McCloskey, B. D.; Luntz, A. C. Electrical Conductivity in Li_2O_2 and Its Role in Determining Capacity Limitations in Non-Aqueous Li–O_2 Batteries. *J. Chem. Phys.* **2011**, *135*, 214704.

39. Albertus, P.; Girishkumar, G.; McCloskey, B.; Sanchez-Carrera, R. S.; Kozinsky, B.; Christensen, J.; Luntz, A. C. Identifying Capacity Limitations in the Li/Oxygen Battery Using Experiments and Modeling. *J. Electrochem. Soc.* **2011**, *158*, A343-A351.

40. Radin, M. D.; Siegel, D. J., Charge Transport in Lithium Peroxide: Relevance for Rechargeable Metal-Air Batteries. *Energ. & Environ. Sci.* **2013**, *6*, 2370-2379.

Chapter 8 Conclusions

The work in this thesis has investigated the fundamental electrochemical (EC) properties (electrocatalysis and electroanalysis) of key electrodes (single-walled carbon nanotube (SWNT), highly oriented pyrolytic graphite (HOPG) and Li_2O_2 cathode material) using both microscopic and nanoscopic imaging techniques.

In chapter 3, catalyzed chemical vapour deposition (cCVD) grown single-walled carbon nanotube (SWNT) electrodes were employed for dopamine (DA) oxidation. DA detection was improved by controllably tuning the density of SWNTs followed by chemical functionalization. High density (HD) SWNT networks exhibited faster electron transfer (ET) for DA electro-oxidation and were less susceptible to blocking than low density (LD) SWNT networks. Defects, most likely functionalized carboxylic acid groups, were introduced on the SWNTs by using a 3 M nitric acid treatment at 70 ^{o}C. It was found that acid treatment resulted in the cutting of the SWNTs, leading to the gradual etching away at cut ends. SWNT electrodes that were subjected to acid treatment for 2 hours exhibited remarkably fast kinetics with only minor susceptibility towards surface fouling from DA oxidation products. For longer treatment times, the increased level of SWNTs etching reduced the amount of available sites for ET, leading to slower overall kinetics. This study provided conclusive evidence that the advantages brought about by acid treatment were not offset by decreasing the density of the SWNT networks. Hence, a balance must be attained between defect creation and etching in order to improve the electrode performance.

In chapter 4, we demonstrated the use of carbon electrodes (SWNTs of different densities (LD, HD, super HD (SHD) SWNTs) and commercial screen printed carbon electrode (SPCE)) for trace level detection of ferrocenecarboxylic acid (FcCOOH) in complex aqueous media (polyethylene glycol (PEG) and albumin). When using cyclic voltammetry (CV), the current response for 25 nM FcCOOH in PEG 2K was observed only with LD SWNTs due to the low capacitance current. The detection sensitivity of FcCOOH was further improved to 1 nM FcCOOH using differential pulse voltammetry (DPV) on SHD SWNT electrode. SWNTs surpassed SPCEs using both CV and DPV, with a detection limit 3 orders of magnitude lower than that of SPCEs. LD SWNTs showed small deterioration of EC response with continuous cycling, while SHD SWNTs performed as well as SPCEs, showing little deterioration over 100 voltammetric sweeps (0.1 V s^{-1}). These studies showed that SWNT network electrodes exhibit impressive detection sensitivity, stability and relatively low background current. Patterned growth of SWNT networks on an insulating Si/SiO_2 substrate was then carried out (results not presented herein) to provide a device containing a planar arrangement of the 3-electrode setup, which offers opportunities for detecting low concentrations of analytes.

In chapter 5, the electrodeposition of nickel hydroxide, $Ni(OH)_2$, nanoparticles (NPs) was performed on pristine HD SWNTs using two approaches: (i) direct precipitation of $Ni(OH)_2$ by EC generation of OH^- radicals in the presence of Ni^{2+}; and (ii) indirect approach in which the native Ni NPs were first electrodeposited and then electrochemically oxidized in the presence of 0.1 M KOH. The two different $Ni(OH)_2$ structures formed by the two different mechanisms (direct and indirect) were confirmed by transmission electron microscopy (TEM). The electrocatalytic behaviour (methanol oxidation reaction (MOR) and ethanol oxidation reaction (EOR))

of $Ni(OH)_2$ NPs was elucidated using the microcapillary EC method (MCEM) which allowed multiple EC measurements to be made on the same electrode in different locations. The results showed that simple synthesis of $Ni(OH)_2$ NPs on SWNT network electrodes by the direct approach produced an electrode with remarkable electrocatalytic activity for both the MOR and the EOR, exhibiting excellent current density (~2.8 kA g^{-1} for 0.5 M methanol and ~3.7 kA g^{-1} for 0.5 M ethanol). These values are approximately 9 times higher than that obtained from the NPs produced by the indirect approach and are much higher as compared to recent reports using other nanostructured catalysts.

In chapter 6, the relationship between the surface properties and EC activity of surface "blistered" HOPG, produced after electro-oxidation in $HClO_4$, was revealed using scanning electrochemical cell microscopy (SECCM) coupled with complementary techniques (optical microscopy, field emission scanning electron microscopy (FE-SEM), Raman spectroscopy and atomic-force microscopy (AFM)). EC data were presented as a movie, consisting of EC currents at a series of applied surface potential values, illustrating subtle differences in the electrode activity between blisters and basal planes. These measurements showed an enhanced current response at the blister area with an apparent cathodic shift of the onset potential for hydrazine oxidation. Thus, the more disordered structure, the blister, was excellent in catalyzing hydrazine oxidation in contrast to the basal surface. The improved EC activity of the hollow structure of blistered graphite is thought to be due to a combination of three processes: the increased adsorption of protonated hydrazine at the defect sites; the ease of ion-solvent intercalation/de-intercalation and a lower susceptibility to the N_2 nanobubble fouling effect. The results highlighted the

capability of electrochemistry for tailoring the surface structure of graphite and presented a new electrocatalyst for hydrazine electro-oxidation.

In chapter 7, we investigated the fundamental redox activity of Li_2O_2 products in non-aqueous media, diversifying the range of materials that can be studied by SECCM. Both toroidal and layered structures of Li_2O_2 were formed on a gold substrate using chronoamperometry in O_2 saturated 0.1 M $LiClO_4$ dimethyl sulfoxide (DMSO) solution. An SECCM-CV approach was performed in a dual-barrel nanopipette filled with a unique home-made gel polymer organic electrolyte (polymer matrix, cross linker and organic electrolyte), enabling a potential sweep at every pixel of the pre-defined scanned area, coupled with other microscopy techniques. The results provided detailed correlations on structure-activity of the electrode material. The results showed that toroidal Li_2O_2 exhibits approximately 9 times the redox current and *ca.* 80 % of the charge efficiency of the layer structure. This work provides a fundamental understanding of the cathode material for effective Li-air batteries.

In summary, this thesis has advanced understanding of nanostructured electrode materials and proposed novel methodologies for structure-activity studies and wide applications.